Development of two-photon polymerization-based protocols for the investigation of neuronal mechanobiology

Sharaf, A.M.S.E.

DOI
10.4233/uuid:84827e4f-d718-4d1d-b9ed-fb106a272520

Publication date
2025

Document Version
Final published version

Citation (APA)
Sharaf, A. M. S. E. (2025). *Development of two-photon polymerization-based protocols for the investigation of neuronal mechanobiology*. [Dissertation (TU Delft), Delft University of Technology]. https://doi.org/10.4233/uuid:84827e4f-d718-4d1d-b9ed-fb106a272520

Important note
To cite this publication, please use the final published version (if applicable).
Please check the document version above.

Development of two-photon polymerization-based protocols for the investigation of neuronal mechanobiology

Development of two-photon polymerization-based protocols for the investigation of neuronal mechanobiology

Dissertation

for the purpose of obtaining the degree of doctor
at Delft University of Technology
by the authority of the Rector Magnificus prof.dr.ir. T.H.J.J. van der Hagen
chair of the Board for Doctorates
to be defended publicly on
Monday 24 March, 2025 at 17.30 o'clock
by

Ahmed SHARAF

Master of Science in Chemical Engineering
Technische Universiteit Delft, the Netherlands
born in Giza, Egypt

This dissertation has been approved by the promotors.

Composition of the doctoral committee:

Rector Magnificus	Chairman
Prof. dr. U. Staufer	Delft University of Technology, promoter
Dr. A. Accardo	Delft University of Technology, copromoter

Independent members*:*

Prof. dr. P.G. Steeneken	Delft University of Technology
Prof. C. Vieu	LAAS-CNRS, France
Prof. dr. L. Moroni	Maastricht University, the Netherlands
Dr. R. Luttge	Eindhoven University of Technology, the Netherlands
Prof. dr. M. Langelaar	Delft University of Technology, Reserve member

Keywords: two-photon polymerization, neuromechanobiology, nanopillars, autofluorescence suppression, confinement, hydrogel

Printed by: Proefschriften Printen

Cover design: Confocal microscopy images of immature neuron-like cells differentiated from SH-SY5Y cells cultured on a microcage (in the middle of the page) and microgrooves (at the top and bottom).

ISBN: 978-90-835161-7-2

An electronic version of this dissertation is available at
http://repository.tudelft.nl

TU Delft Delft University of Technology

Summary

Fundamental neuronal studies are concerned with the investigation and understanding of the behaviour of cells in response to certain chemical or physical cues. The field of study concerned with physical cues and their effect on neurons is referred to as neuronal mechanobiology or neuromechanobiology. These cues include properties such as the geometry (i.e. 2D vs. 3D substrates), topography (i.e. roughness of the substrate), and stiffness of the substrate, which can affect migration, phenotypic expression, and neurite outgrowth of neurons. In recent years, the study of mechanobiology has witnessed substantial developments due to our increasing ability to fabricate (physiologically) relevant environments that simulate specific features of the native extracellular matrix (ECM). Specifically, within micro and nano-fabrication techniques, two-photon polymerization (2PP) gained a lot of traction and proved to be a versatile method for the fabrication of microstructures to be used in mechanobiological studies. The technology of 2PP allows indeed the fabrication of specifically designed complex 3D microstructures with a resolution that can reaches down to 50 nm in feature size in a reproducible manner with relative ease.

In this dissertation, I present multiple microfabrication and processing protocols developed specifically for mechanobiological studies of neurons and microglia (part of the glial cells category), two of the most abundant cell types in the brain. The physical variables investigated in the fabricated microstructures were topography, geometry (**Chapter 2 & 4**) and stiffness (**Chapter 2 & 5**). Moreover, I developed protocols for the suppression of the autofluorescence of the microstructures since this issue has been a consistent bottleneck in the field due to the fact that it hampers fluorescence microscopy characterization of cells (**Chapter 3**), which is a standard method in cell biology.

Topography and geometry were the first properties to be investigated in terms of their effect on primary microglia (**Chapter 2**). These cells are the main line of defence against foreign bodies and neuronal debris in the central nervous system and they contribute to the brain's homeostasis. When cultured *in vitro* on stiff 2D petri dishes, microglia exhibit a flat amoeboid phenotype which is drastically different from the resting ramified phenotype present in a healthy brain when they are not activated by a foreign agent (e.g. cell debris or invading pathogens). This phenotypic change is a result of the lack of resemblance of the culture environment in terms of topography, stiffness, and geometry from the native neuronal ECM. In our study, arrays of nano and micropillars (diameters = 0.29–1.06 µm) of effective shear moduli in the range (0.25-14.6 MPa) were fabricated via 2PP from acrylate-based monomers and used to investigate the effect of topography on the phenotypic expression of primary microglia of rhesus macaque primates. The topography and stiffness are a closer match to the native brain ECM (Young's modulus, E = 0.1-1 kPa) than conventional polystyrene 2D petri dishes (E ≈ 3 GPa). Our results showed that microglia cultured on nanopillars expressed more cells featuring a ramified phenotype and even exhibited more ramifications per cell compared to those cultured on the flat substrate. Additionally, 3D microcages with nano and micropillar decorations were fabricated via an innovative fabrication method to approach the 3-dimensionality of the ECM. Microglia cultured on such micropillar decorated microcages colonized the higher sections of the cages compared to undecorated cages. This possibly signifies that the filopodia of the cells interacted with the nano and micropillars which are of a similar scale as that of the filopodia. A major problem faced in this study was the prominent autofluorescence of the microstructures. This was especially an issue since a crucial quantitative analysis method in such studies is the staining of cells for specific proteins and then investigating the samples using fluorescence or confocal microscopy. The autofluorescence of the microstructures systematically blocked at least one fluorescent emission wavelength (usually either the 410–475 nm (blue), or 495–550 nm (green) channels) during the analysis. This triggered us to develop a protocol for tackling this problem.

In **Chapter 3**, I elaborate on a protocol describing our attempt to supress the autofluorescence of 2PP-fabricated microstructures. The methods of choice were photobleaching and coating with an autofluorescence quencher known as Sudan Black B (SBB). These solutions were chosen due to their applicability to different photocrosslinkable materials and the relative ease of use, making a systematic study for both of them a valuable contribution to the 2PP community. I used four acrylate and silicone-based photoresins that are widely employed in the field of 2PP (IP-Dip, IP-L, IP-S, and IP-PDMS). The fabricated microstructures were microchannels (diameter = 30 μm) and microcages (dimensions = 100x100x100 μm^3). Both methods featured an autofluorescence suppression in the range of 33-95%. As a proof of principle, we cultured SH-SY5Y human neuroblastoma cell line on the structures and differentiated them for 3 days. For the chosen geometries, bleaching was the preferrable method of choice since, especially for the microchannels, SBB absorbed all photons coming from the microstructures as well as those coming from the cell staining.

I then utilised the results of the previous study to further investigate the effect of mechanical confinement of 2.5D microgrooves and 3D microchannels on the expression of the mechanotransductive protein Yes-Associated Protein (YAP), and the outgrowth of neurites of neurons (**Chapter 4**). In that regard, I fabricated cylindrical microgrooves and microchannels of diameters ranging from 5 to 30 μm. This study falls under the investigation of geometry on the behaviour of immature neurons. YAP is a protein that has been shown to be affected by the configuration of the cytoskeleton and focal adhesions which are in turn affected by mechanical and geometric cues of the substrate. This protein shuttles from the cytoplasm to the nucleus and it is of special importance in the developing brain since it has the ability to affect cell survival, proliferation, neuronal differentiation, and neuronal necrosis in Alzheimer's patients. The cells employed in this study were immature neuron-like derived SH-SY5Y cells and human immune pluripotent stem cells (hiPSCs) derived neurons. The results showed that for SH-SY5Y-neuron-like-derived cells, there was a maximum of YAP nuclear/cytoplasmic (N/C) ratio in the 2.5D microgrooves at the 10 μm grooves while this maximum moved to the 20 μm grooves in the 3D microchannels indicating the sensitivity of the cells to changes in the mechanical environment. As for the length of neurites, on average there was an inversely proportional relationship between their length and YAP N/C ratio. In case of hiPSC-derived neurons cultured in 2.5D microgrooves, the trend of YAP was similar to that of SH-SY5Y cells in terms of having a maximum although it was at the 20 μm grooves. Overall, our results indicate that mechanical confinement at a scale close to the size of the nuclei or smaller has an adverse effect on YAP N/C ratio possibly due to excessive elongation of the nucleus together with increased mechanical axial stress on actin filaments in the cytoskeleton.

In **Chapter 5**, we attempted to fabricate microstructures that would feature stiffness close to that of the neuronal ECM. Traditionally, materials used to fabricate soft structures with E in the kPa range are hydrogels. However, hydrogels are substantially cumbersome in handling due to their mechanical properties in terms of softness and swelling. On the other hand, photoresins utilised in 2PP to produce microstructures with high structural integrity have E in the GPa range which is significantly different from that of the ECM of the brain. Therefore, we developed a protocol in which we fabricated microstructures with a stiff core made by a 2PP photoresin and a soft shell made from a hydrogel via free radical polymerization of a precursor solution. This protocol aimed at creating a novel and simple way for fabricating a stiff, easy to handle structure with a soft hydrogel layer able to mimic the stiffness of the native neuronal ECM. The photoresin used for the core of the structure was chosen to be IP-S (an acrylate based polymer) and the hydrogel chosen for the shell was polyethylene glycol methacrylate (PEGMA). We attempted to coat the IP-S with micrometric layers of PEGMA hydrogel (E = 0.43 kPa). The structures of choice were microcages (dimensions = 80x80x80 μm^3) and pedestals (dimensions = 100x100x50 μm^3). The study showed that growing a homogenous micrometric layer (~ 1 μm in thickness) of PEGMA on top of the pedestals was possible and highly reproducible. As for the microcages, the layers of hydrogel were growing inhomogeneously.

We could also observe clogging of the pores of the microcages by layers of the hydrogel. The results show that there is potential for this method to produce the required structures at a microscale, but there needs to be more technical development on the hydrogel layers formation in order to ensure the presence of homogenous layers on 3D structures.

The protocols outlined in this dissertation were either directly applied in studies of neuronal mechanobiology or can be used by other groups in the field as a step towards developing their own studies. These protocols contribute therefore to further developing our understanding of neuronal behaviour within *in vitro* environments.

Samenvatting

Fundamentele neuronale studies houden zich bezig met het onderzoeken en begrijpen van het gedrag van cellen als reactie op bepaalde chemische of fysieke signalen. Het vakgebied dat zich bezighoudt met fysieke signalen en hun effect op neuronen wordt neuronale mechanobiologie of neuromechanobiologie genoemd. Deze signalen omvatten eigenschappen zoals de geometrie (d.w.z. 2D versus 3D substraten), topografie (d.w.z. ruwheid van het substraat) en stijfheid van het substraat, die migratie, fenotypische expressie en neuritenuitgroei van neuronen kunnen beïnvloeden. De afgelopen jaren heeft de studie van mechanobiologie aanzienlijke ontwikkelingen doorgemaakt vanwege ons toenemende vermogen om (fysiologisch) relevante omgevingen te fabriceren die specifieke kenmerken van de natuurlijke extracellulaire matrix (ECM) simuleren. Specifiek, binnen micro- en nanofabricagetechnieken, heeft twee-fotonenpolymerisatie (2PP) veel aanhang gekregen en bleek het een veelzijdige methode te zijn voor de fabricage van microstructuren voor gebruik in mechanobiologische studies. De technologie van 2PP maakt het inderdaad mogelijk om relatief eenvoudig en op een reproduceerbare manier specifiek ontworpen complexe 3D-microstructuren te fabriceren met een 50 nm resolutie.

In dit proefschrift presenteer ik meerdere microfabricage- en verwerkingsprotocollen die specifiek zijn ontwikkeld voor mechanobiologische studies van neuronen en microglia (onderdeel van de categorie gliacellen), twee van de meest voorkomende celtypen in de hersenen. De fysieke variabelen die werden onderzocht in de gefabriceerde microstructuren waren topografie, geometrie (**hoofdstuk 2 en 4**) en stijfheid (**hoofdstuk 2 en 5**). Bovendien heb ik protocollen ontwikkeld voor het onderdrukken van de autofluorescentie van de microstructuren, aangezien dit probleem een consistent knelpunt is in het veld omdat het de karakterisering van cellen met behulp van fluorescentiemicroscopie belemmert (**hoofdstuk 3**), wat een standaardmethode is in de celbiologie.

Topografie en geometrie waren de eerste eigenschappen die werden onderzocht in termen van hun effect op primaire microglia (**hoofdstuk 2**). Deze cellen vormen de belangrijkste verdedigingslinie tegen vreemde lichamen en neuronaal afval in het centrale zenuwstelsel en dragen bij aan de homeostase van de hersenen. Wanneer microglia *in vitro* worden gekweekt op stijve 2D-petrischalen, vertonen ze een plat amoeboïde fenotype dat drastisch verschilt van het rustende vertakte fenotype dat aanwezig is in een gezonde hersenen wanneer ze niet worden geactiveerd door vreemde lichamen (bijv. celafval of binnendringende pathogenen). Deze fenotypische verandering is het resultaat van het gebrek aan gelijkenis van de kweekomgeving in termen van topografie, stijfheid en geometrie van de oorspronkelijke neuronale ECM. In onze studie werden arrays van nano- en micropillars (diameters = 0,29-1,06 µm) met effectieve schuifmoduli in het bereik (0,25-14,6 MPa) vervaardigd via 2PP uit op acrylaat gebaseerde monomeren en gebruikt om het effect van topografie op de fenotypische expressie van primaire microglia van rhesus-apen te onderzoeken. De topografie en stijfheid komen beter overeen met de oorspronkelijke ECM van de hersenen (Young's modulus, E = 0,1-1 kPa) dan conventionele polystyreen 2D petrischalen (E ≈ 3 GPa). Onze resultaten toonden aan dat microglia gekweekt op nanopillars meer cellen met een vertakt fenotype tot expressie brachten en zelfs meer vertakkingen per cel vertoonden in vergelijking met die gekweekt op het vlakke substraat. Bovendien werden 3D microkooien met nano- en micropillardecoraties vervaardigd via een innovatieve fabricagemethode om de 3-dimensionaliteit van de ECM te benaderen. Microglia gekweekt op dergelijke met micropillar versierde microkooien koloniseerden de hogere delen van de kooien in vergelijking met niet-gedecoreerde kooien. Dit betekent mogelijk dat de filopodia van de cellen interageerden met de nano- en micropillars die van een vergelijkbare schaal zijn als die van de filopodia. Een groot probleem in deze studie was de prominente autofluorescentie van de microstructuren. Dit was vooral een probleem omdat een cruciale kwantitatieve analysemethode in dergelijke studies het kleuren van cellen voor specifieke eiwitten is en vervolgens het onderzoeken van de monsters met behulp van fluorescentie- of confocale microscopie. De autofluorescentie van de microstructuren blokkeerde systematisch ten minste één fluorescerende

emissiegolflengte (meestal de 410-475 nm (blauw) of 495-550 nm (groen) kanalen) tijdens de analyse. Dit was voor ons aanleiding om een protocol te ontwikkelen om dit probleem aan te pakken.
In **Hoofdstuk 3** werk ik een protocol uit dat onze poging beschrijft om de autofluorescentie van 2PP-gefabriceerde microstructuren te onderdrukken. De gekozen methoden waren fotobleken en coaten met een autofluorescentie-quencher die bekendstaat als Sudan Black B (SBB). Deze oplossingen werden gekozen vanwege hun toepasbaarheid op verschillende fotocrosslinkbare materialen en het relatieve gebruiksgemak, waardoor een systematische studie voor beide een waardevolle bijdrage aan de 2PP-gemeenschap is. Ik heb vier acrylaat- en siliconengebaseerde fotoresins gebruikt die veel worden gebruikt in het veld van 2PP (IP-Dip, IP-L, IP-S en IP-PDMS). De vervaardigde microstructures waren microkanalen (diameter = 30 µm) en microkooien (afmetingen = 100x100x100 μm^3). Beide methoden vertoonden een autofluorescentie-onderdrukking in het bereik van 33-95%. Als bewijs van het principe kweekten we SH-SY5Y humane neuroblastoomcellijn op de structuren en differentieerden ze gedurende 3 dagen. Voor de gekozen geometrieën was bleken de voorkeursmethode, omdat SBB, met name voor de microkanalen, alle fotonen absorbeerde die afkomstig waren van de microstructuren en die afkomstig waren van de celkleuring.
Vervolgens gebruikte ik de resultaten van de vorige studie om het effect van mechanische opsluiting van 2,5D-microgroeven en 3D-microkanalen op de expressie van het mechanotransductieve eiwit Yes-Associated Protein (YAP) en de uitgroei van neurieten van neuronen verder te onderzoeken (**Hoofdstuk 4**). In dat opzicht heb ik cilindrische microgroeven en microkanalen met diameters variërend van 5 tot 30 µm gefabriceerd. Deze studie valt onder het onderzoek naar geometrie op het gedrag van onvolgroeide neuronen. YAP is een eiwit waarvan is aangetoond dat het wordt beïnvloed door de configuratie van het cytoskelet en focale adhesies die op hun beurt worden beïnvloed door mechanische en geometrische signalen van het substraat. Dit eiwit pendelt van het cytoplasma naar de kern en is van speciaal belang in de zich ontwikkelende hersenen omdat het de celoverleving, proliferatie, neuronale differentiatie en neuronale necrose bij Alzheimerpatiënten kan beïnvloeden. De cellen die in deze studie werden gebruikt, waren onvolgroeide neuronachtige afgeleide SH-SY5Y-cellen en van humane immuunpluripotente stamcellen (hiPSC's) afgeleide neuronen. De resultaten toonden aan dat voor SH-SY5Y-neuron-achtige afgeleide cellen, er een maximum was van YAP nucleaire/cytoplasmatische (N/C) ratio in de 2.5D microgroeven bij de 10 µm groeven terwijl deze maximum naar de 20 µm groeven in de 3D microkanalen bewoog, wat de gevoeligheid van de cellen voor veranderingen in de mechanische omgeving aangeeft. Wat betreft de lengte van neuriten, was er gemiddeld een omgekeerd evenredige relatie tussen hun lengte en YAP N/C ratio. In het geval van hiPSC-afgeleide neuronen gekweekt in 2.5D microgroeven, was de trend van YAP vergelijkbaar met die van SH-SY5Y cellen in termen van het hebben van een maximum, hoewel deze zich bevond bij de 20 µm groeven. Over het geheel genomen geven onze resultaten aan dat mechanische opsluiting op een schaal die dicht bij de grootte van de kernen of kleiner ligt, een negatief effect heeft op de YAP N/C-verhouding, mogelijk als gevolg van overmatige verlenging van de kern samen met verhoogde mechanische axiale spanning op actinefilamenten in het cytoskelet.
In **Hoofdstuk 5** probeerden we microstructuren te fabriceren die een stijfheid zouden hebben die dicht bij die van de neuronale ECM ligt. Traditioneel worden hydrogels gebruikt om zachte structuren te fabriceren met E in het kPa-bereik. Hydrogels zijn echter aanzienlijk lastig te hanteren vanwege hun mechanische eigenschappen in termen van zachtheid en zwelling. Aan de andere kant hebben fotoresines die in 2PP worden gebruikt om microstructuren met een hoge structurele integriteit te produceren E in het GPa-bereik, wat aanzienlijk verschilt van die van de ECM van de hersenen. Daarom hebben we een protocol ontwikkeld waarin we microstructuren fabriceerden met een stijve kern gemaakt door een 2PP-fotoresine en een zachte schil gemaakt van een hydrogel via vrije radicalenpolymerisatie van een precursoroplossing. Dit protocol was gericht op het creëren van een nieuwe en eenvoudige manier om een stijve, gemakkelijk te hanteren structuur te fabriceren met een zachte

hydrogellaag die de stijfheid van de oorspronkelijke neuronale ECM kan nabootsen. De fotoresin die werd gebruikt voor de kern van de structuur werd gekozen als IP-S (een op acrylaat gebaseerd polymeer) en de hydrogel die werd gekozen voor de schil was polyethyleenglycolmethacrylaat (PEGMA). We probeerden de IP-S te coaten met micrometrische lagen PEGMA-hydrogel (E = 0,43 kPa). De gekozen structuren waren microkooien (afmetingen = 80x80x80 μm^3) en voetstukken (afmetingen = 100x100x50 μm^3). De studie toonde aan dat het mogelijk en zeer reproduceerbaar was om een homogene micrometrische laag (~ 1 µm dik) PEGMA bovenop de voetstukken te laten groeien. Wat de microkooien betreft, groeiden de lagen hydrogel niet homogeen. We konden ook verstopping van de poriën van de microkooien door lagen van de hydrogel waarnemen. De resultaten tonen aan dat er potentieel is voor deze methode om de vereiste structuren op microschaal te produceren, maar er meer technische ontwikkeling moet plaatsvinden op het gebied van de vorming van hydrogellagen om de aanwezigheid van homogene lagen op 3D-structuren te garanderen.
De protocollen die in dit proefschrift worden beschreven, werden ofwel direct toegepast in studies van neuronale mechanobiologie of kunnen door andere groepen in het veld worden gebruikt als een stap in de richting van het ontwikkelen van hun eigen studies. Deze protocollen dragen daarom bij aan de verdere ontwikkeling van ons begrip van neuronaal gedrag binnen *in vitro*-omgevingen.

Contents

List of abbreviations

2PP	Two-photon polymerization
ADC#	Alternative design channel of # µm diameter
APTES	(3-Aminopropyl)triethoxysilane
AUC	Area under the curve
CAD	Computer-aided design
CNS	Central nervous system
D#	Day # of differentiation
DI	Deionized
DiLL	Dip-in laser lithography
ECM	Extracellular matrix
FA	Focal adhesion
G#	Grooves of # µm diameter
C#	Channels of # µm diameter
HMDS	Hexamethyldisilazane
hiPSCs	human-induced pluripotent stem cells
I184	Irgacure 184
IPA	Isopropanol
LAP	Lithium phenyl-2,4,6-trimethylbenzoylphosphinate
MAP2	microtubule-associated protein 2
MAPTMS	3-(Trimethoxysilyl)propyl methacrylate
MRTFA	Myocardin-related transcription factor A
NA	Numerical aperture
N/C	Nuclear/cytoplasmic
PDMS	Polydimethylsiloxane
PEGMA	Poly(ethylene glycol) methacrylate
PGMEA	Propylene glycol monomethyl ether acetate
SBB	Sudan Black B

v/v	volume/volume
w/v	weight/volume
YAP	Yes-associated protein

1

Introduction

Introduction

The native environment of the cell, commonly referred to as the extracellular matrix (ECM), is ripe with multiple biochemical and physical cues that control the behaviour of the cells and direct their survival, migration, and proliferation among other things in health and disease. Neurons residing in the brain which is part of the central nervous system (CNS) also have their own specific ECM therein. While traditionally, biologists have focused on the use of biochemical cues in the form of compounds added to culture media, more recently, the importance and study of physical cues gained significant attention. These cues include mechanical aspects found in the ECM such as geometry, topography and stiffness. The field of study concerned with the physical cues affecting cellular fate is referred to as mechanobiology. A subset of this field is the one concerned with neurons and can be referred to as neuromechanobiology.

There are two types of cells in the brain, neurons and glia. Neurons communicate and receive information [1] while glia, such as microglia and astrocytes, perform supportive roles of neurons in the brain [2]. The ECM in the brain is a special one in which the stiffness of the tissue is the softest in the body with a Young's modulus (E) in the range of 0.1-1 kPa [3]. The geometry and topography of the neuronal and glial ECM is also highly complex. These properties are in stark contrast to those of 2D planar petri dishes made from glass (E ~ 70 GPa) [4] or polystyrene (E ~ 3 GPa) [5]. In order to investigate the effect of these cues on neurons and glia, researchers have conducted multiple studies *in vitro* with various cell types trying to mimic certain physical aspects of the ECM to induce different responses in the cells. To achieve that, multiple microfabrication technologies were used such as conventional electron beam lithography [6], stereolithography [7], electrospinning [8], bioprinting [9], or two-photon polymerization (2PP) [10]. The technology of 2PP, which is a 3D printing direct laser writing (DLW) technique, is of special interest due to its high precision, reproducibility, freedom of design, and high resolution (up to 50 nm) [11,12]. In 2PP, a photosensitive resin (commonly known as a photoresin) is subjected to a near infrared (NIR) laser of a 780 nm wavelength via an objective to fabricate a preprepared microstructure designed via a computer-aided design (CAD) software. The laser polymerizes line by line (in the horizontal direction) and layer by layer (in the vertical direction) of the photoresin in order to fabricate the microstructure. Multiple studies have employed 2PP to fabricate microstructures used in investigations relating to neuromechanobiology. For example, there were studies investigating the effect of ridges on the alignment of neuronal processes [13,14]. Other studies involved fabricating 3D micro-towers to foster the formation of neuronal networks or the guidance of neuronal processes [15,16]. Microcages were printed by others from stiff [17] and soft [18] materials to investigate the effect of 3D environments on the growth of neurons. In addition, researchers have printed micropillars to fabricate microelectrode arrays for *in vitro* neuronal tissue recordings [19].

Although 2PP has proven to be of high utility and multiple benefits in the field of neuromechanobiology, there are still some substantial shortcomings of the technique and materials used. To list a few of which, most photoresins used have E in the range of giga Pascals [20,21]. This constitutes a problem since soft structures are required to obtain a biomimetic environment of the brain ECM. When resorting to soft photoresins of E in the kilo Pascal range, hydrogels are often used, but the main problem is the difficulty of handling these materials due to their soft mechanical properties. Another major obstacle is the autofluorescence of the fabricated microstructures due to the fact that fluorescence microscopy is one of the vital characterization methods. Autofluorescence of the microstructures represents an undesired background signal [22]. Finally, there is an inherent problem to 2PP which relates to the speed of the technique. This technology is especially slow with higher resolutions. In cell studies, however, large areas of fabricated microstructures are required to obtain sensible statistical data. As a result of these shortcomings, innovative microfabrication and processing protocols should be developed to overcome them.

In light of the problem statements mentioned above, the main research question of this research work is *how to develop robust protocols for the fabrication of physiologically relevant and reproducible neural microenvironments by employing two-photon polymerization technique?* This query can be split into a series of sub-research questions

ranging from the effect of topography and stiffness on neural cells, to the development of protocols enabling autofluorescence suppression, to the effect of mechanical confinement in neuromechanobiology and the development of hybrid biomaterials for light assisted additive manufacturing.

To address such questions, in this thesis, a number of fabrication protocols and postprocessing techniques involving 2PP as the central technology are elaborated along with the relevant neuronal or glial *in vitro* studies conducted. All work in this thesis is published except for Chapter 5. In **Chapter 2**, the effect of geometry, topography and stiffness on the phenotypic expression of primate primary microglia are investigated. An innovative method of exploiting the effective shear modulus of nanopillar arrays to reduce the stiffness of the culture environment is elaborated. In **Chapter 3**, the problem of autofluorescence of microstructures is addressed and solutions for its suppression are exhibited therein. **Chapter 4** presents a study in which printing of microgrooves and microchannels with diameters as small as 5 µm is achieved over large areas for the study of the effect of confinement on protein expression of immature neurons. Finally, **Chapter 5** exhibits novel protocols of microfabrication and material manipulation to make microstructures with a stiff core and a soft overlying layer of hydrogel thereby addressing the issue of handling microstructures made solely from soft hydrogels. In addition, a short protocol of fabricating electrically conductive 3D microarchitectures is exhibited.

2

Two-photon polymerization of 2.5D and 3D microstructures fostering a ramified resting phenotype in primary microglia

Microglia are the resident macrophages of the central nervous system and contribute to maintaining brain's homeostasis. Current 2D "petri-dish" in vitro cell culturing platforms employed for microglia, are unrepresentative of the softness or topography of native brain tissue. This often contributes to changes in microglial morphology, exhibiting an amoeboid phenotype that considerably differs from the homeostatic ramified phenotype in healthy brain tissue. To overcome this problem, multi-scale engineered polymeric microenvironments are developed and tested for the first time with primary microglia derived from adult rhesus macaques. In particular, biomimetic 2.5D micro- and nano-pillar arrays (diameters = 0.29–1.06 μm), featuring low effective shear moduli (0.25–14.63 MPa), and 3D micro-cages (volume = 24 × 24 × 24 to 49 × 49 × 49 μm^3) with and without micro and nano-pillar decorations (pillar diameters = 0.24–1 μm) were fabricated using 2PP. Compared to microglia cultured on flat substrates, cells growing on the pillar arrays exhibit an increased expression of the ramified phenotype and a higher number of primary branches per ramified cell. The interaction between the cells and the micro-pillar-decorated cages enables a more homogenous 3D cell colonization compared to the undecorated ones. The results pave the way for the development of improved primary microglia in vitro models to study these cells in both healthy and diseased conditions.

The contents of this chapter have been published in:

- A. Sharaf, B. Roos, R. Timmerman, G.-J. Kremers, J.J. Bajramovic, A. Accardo, *Two-Photon Polymerization of 2.5D and 3D Microstructures Fostering a Ramified Resting Phenotype in Primary Microglia*, Frontiers in Bioengineering and Biotechnology 10 (2022).
- A. Sharaf, R. Timmerman, J. Bajramovic, A. Accardo, *In vitro microglia models: the era of engineered cell microenvironments*, Neural Regeneration Research, 18(8): 1709-1710 (2023).

2.1. Introduction

As briefly mentioned in the introduction, cell culture methods used nowadays for *in vitro* studies, mostly use stiff Petri dishes featuring a 2D planar geometry. This type of environment does not recapitulate the properties of the ECM within which cells reside in the human body (i.e., in an *in vivo* environment). This is especially true for cells in the CNS which includes the brain and spinal cord. The ECM of the CNS is made up of a complex 3D network of multiple macromolecules that are entangled together. Features in the ECM can be as small as 9 nm [23]. In terms of stiffness, brain tissue is among the softest tissues in the body with a Young's modulus ranging from 0.1 to 1 kPa [3]. In comparison, the Young's moduli of traditional Petri dishes made of polystyrene or glass are roughly 3 GPa or 70 GPa, respectively [4,5]. Cells in the CNS largely fall under one of two categories, neurons and glia (or glial cells) [24]. Microglia, in particular, are the macrophages of the CNS, and play a key role in innate immune responses [25,26]. These cells have a vital role in tissue repair as they contribute to resistance to infections and maintain the homeostasis (i.e., normal function and stable state) of the brain by clearing foreign bodies and cellular debris, such as damaged axons and dead neurons through phagocytosis, which is translated from Latin as "cell eating" [27–29].

When cultured *in vitro*, microglia show different morphologies [30] and gene regulation [31] from their *in vivo* counterparts (Fig. 2.1A). In terms of morphology, the ramified phenotype, which is a characteristic of homeostatic microglia [32,33], is rarely seen *in vitro* since primary microglia mostly show either round, globular-like or flat, amoeboid-like, morphologies [30]. This shows a stark difference from the abundance of ramified microglia, with their small somas and long branches [33], that can be found in a homeostatic brain [32]. Due to these discrepancies in terms of morphology and behavior and due to the major role played by microglia in brain homeostasis and disease, biomimetic, *in vitro* models must be devised to study these cells in a physiologically relevant context.

The guidance of microglia morphology and phenotype via engineered microenvironments can take place by exploiting four different parameters: substrate geometry, topography (e.g., roughness), stiffness, and biochemical coating (Fig. 2.1B) [34]. Fabrication of these microenvironments for *in vitro* studies can be performed via multiple techniques such as electrospinning (Fig. 2.1C-i) [35–37], chemical vapor deposition (CVD) (Fig. 2.1C-ii) [38], and 2PP (Fig. 2.1C-iii) [10,39] to name a few.

There are multiple examples of studies focusing on using micro- and nanotopographies to alter the morphology and phenotypic expression of microglia [23,35,40,41]. These features are sensed by microglia via lamellipodia and filopodia in a process known as mechanosensing [42–44]. The results of these studies in general indicate that micro- and nanotopographies may increase microglial polarization and the production of anti-inflammatory cytokines, thereby inducing a more homeostatic behavior. The reason is hypothesized to be the resemblance of such features to the native ECM in the CNS [23]. For instance, a decade ago, excimer laser processing of thin hydrogenated amorphous silicon films deposited by plasma-enhanced chemical vapor deposition on glass substrates already enabled the formation of silicon micro and nano-structures (between 2 nm and 2.3 µm) resulting in substrates with various roughness which influenced the morphology of a murine microglial cell line (BV-2) [40]. On amorphous flat silicon, BV-2 cells tended to adopt a rounded morphology with flat protrusions whereas in the presence of laser-processed silicon micro- and nano-structures, these cells displayed a more elongated, bipolar shape. More recently, electrospinning, the widely employed technique for the fabrication of cell scaffolds, which is able to generate polymeric nanofibers using electric fields, was employed to assess the response of primary microglia (which have a higher pre-clinical relevance compared to the BV-2 cell line), isolated from Wistar rat pups [35], in presence of poly(trimethylene carbonate-co-ε- caprolactone) (P(TMC-CL)) fibers. A comparison between flat P(TMC-CL) films and P(TMC-CL) fibers showed that cells cultured on P(TMC-CL) films were larger and featured an increased circularity compared to microglia cultured on fibers. This can be considered as an indication of a more pro-inflammatory profile. However, when media from the primary microglia culture was introduced to astrocytes, astrogliosis was not exacerbated, signifying that microglia were not activated. Thus, it is important to mention that the association between microglia activation states and the display of distinct

morphologies are not always linked. In another recent work, the addition of conditioned medium of BV-2 microglia grown within 3D graphene foams obtained by CVD promoted neurosphere formation, which was not observed when neurons were exposed to conditioned medium from 2D cultured microglia, suggesting possible applications in the field of regenerative medicine [38].

Another critical factor in affecting cell behavior is the stiffness of a substrate. Cells have the ability to sense the mechanical strength of their surrounding environment. Studies performed on macrophages have shown the various and inconsistent effects of substrate stiffness on the morphology and cytokine expression of these cells [45–48]. While some results show the polarization of microglia on softer substrates [46], others show the opposite [47].

Instead of using a soft material like hydrogels, a rather innovative way of obtaining a surface with relatively low stiffness is by utilizing the geometrical properties of large pillar arrays of stiff materials to affect the effective shear modulus of the array. The effective shear modulus of a pillar array can be explained as the shear modulus experienced by the cell as it moves over the array. Pillars with large aspect ratios result in arrays with lower effective shear moduli since long and slender pillars bend more readily in the direction of the force exerted by a cell. This reduction in the effective shear modulus was shown to significantly enhance the differentiation of human embryonic stem cells into endoderm cells [49]. The main advantage of such method lies in the relative ease of fabrication of pillar arrays made of stiff materials while still being able to achieve a stiffness low enough to approach the one of brain tissue. In addition, these patterns provide a unique discrete type of topography resembling that of the native ECM [23].

While each of the aforementioned fabrication methods has its own advantages, 2PP especially stands out due to its extremely high resolution (~50–200 nm) [11,12], ability to fabricate complex 3D geometries using CAD models, and high reproducibility. The most significant limitation of 2PP is the relatively long printing time hindering the upscaling of the technology [50]. Multiple polymeric, hydrogel or composite materials were employed in combination with 2PP to fabricate micro- and nano-patterns as well as 3D structures for *in vitro* cellular studies involving neuroblastoma, glioblastoma, prostate cancer, murine cerebellar granule, chondrocytes, macrophages, neuronal and stem cells [13,15,18,51–59].

To date, there has been no study exploring the effect of topography and stiffness on primary microglia derived from primates. Further, in terms of biomimicry of the native 3D environment of microglia, to the best of our knowledge, there has been no study employing free standing 3D structures including micro- and nanometric features as an added step of attaining resemblance to the *in vivo* 3D environment. To address these gaps in the field, in the current study, we tackle the research question of whether it is possible to foster the ramified resting phenotype in rhesus macaque primary microglia cells by culturing them on polymeric micro- and nano-pillar arrays, fabricated by 2PP, and exploiting the geometrical and mechanical cues of these patterns (Fig. 2.1D). We hypothesize that by approaching the topography and the stiffness of the ECM in the CNS (where the brain features, respectively, protein fibers of tens to hundreds of nm diameter [23] and a Young's modulus of 0.1–1 kPa), a biomimetic *in vitro* microenvironment can be created, thereby inducing the expression of the ramified phenotype of microglia, characteristic of a healthy brain. In addition, we investigate the effect of coating the microstructures with laminin since it is one of the most abundant proteins in the ECM of the brain [23] and has been shown to affect the morphology of microglia cultured *in vitro* [60,61]. In an attempt to take our investigation further, we use 2PP to fabricate 3D micro-cages decorated with micro- and nano-pillars to provide the cells with a well-structured three-dimensional environment, and we assess their effect on the phenotypic expression of microglia.

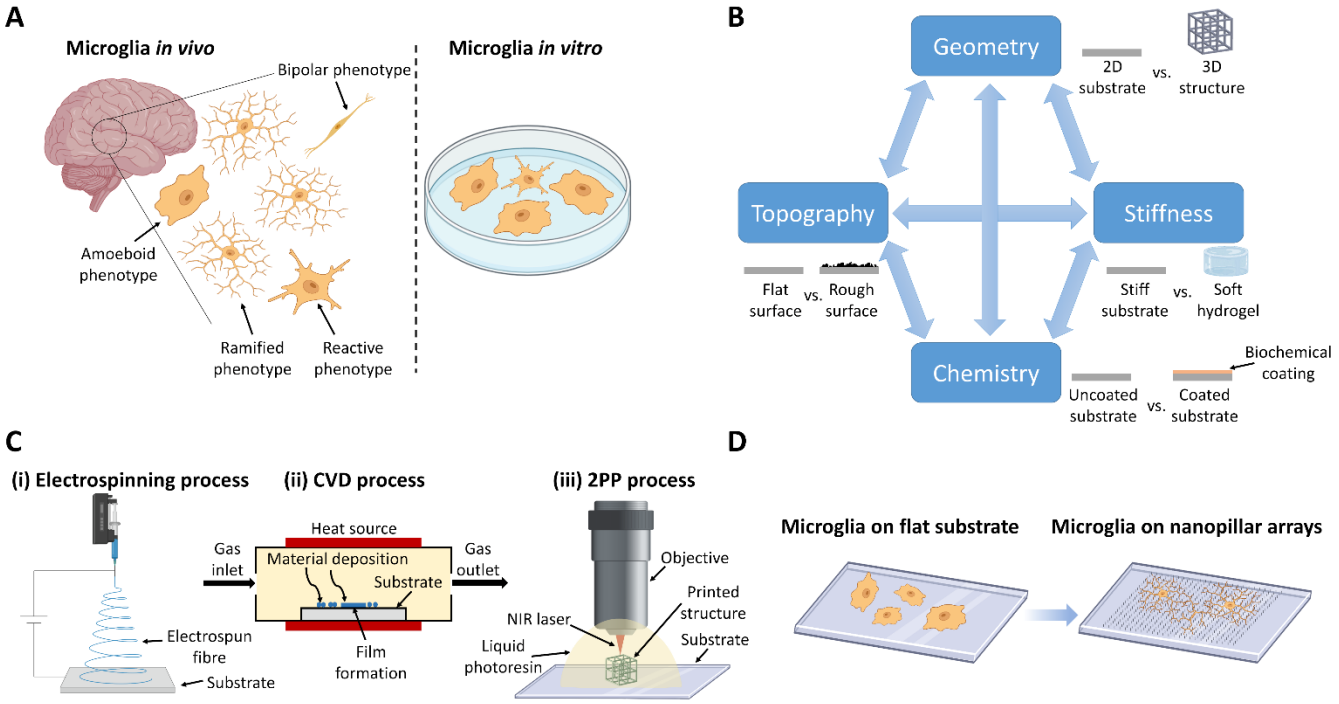

Fig. 2.1. Schematic representation of the various features of *in vitro* microenvironments, the processes used to fabricate them, and their effect on microglia. (A) Microglia phenotypes observed *in vivo* and *in vitro*. (B) Overview of the parameters of *in vitro* microglia engineered microenvironments and their interplay therein. (C) Examples of processes employed to fabricate *in vitro* engineered microglia microenvironments (i) electrospinning, (ii) chemical vapor deposition (CVD), and (iii) 2PP. (D) An example of the effect of engineered microenvironments where nanopillar arrays, providing a topography and stiffness that resemble those of the native cell environment, fostered the expression of a ramified phenotype in primate-derived microglia compared to the amoeboid one on flat surfaces. Created with BioRender.com.

2.2. Materials and methods

2.2.1. Design of 2D Pedestals and 2.5D Micro and Nano-Pillar Arrays

All the structures employed for cell culturing were designed using SOLIDWORKS 2019 (DASSAULT SYSTEMES), a 3D CAD modelling software. Three types of structures were designed, herein referred to as 2D, 2.5D, and 3D. The 2D structure was a pedestal ($l \times w \times h = 130 \times 130 \times 20$ µm^3) mainly used to test the viability of cells on the material employed for printing (Appendix A, Fig. A1.A). Pedestals were designed to cover a total area of 400×400 µm^2 on each substrate by printing arrays of 3×3 pedestals with an interspacing of 5 µm. The 2.5D category included the micro-pillar (MP) and nano-pillar (NP) arrays (Appendix A, Fig. A1.B). All pillar arrays were designed to cover a total area of 500×500 µm^2. The micro-pillars were designed to have a diameter (d) of 1 µm, a height (h) of 2.5 µm, and an inter-pillar spacing (p) of 1 µm (edge-to-edge). Two versions of the nanopillar arrays were designed (NP1 and NP2). NP1 arrays were designed to be directly printed on the substrate while NP2 ones were designed to be printed on top of a pedestal of $500 \times 500 \times 5$ µm^3 dimensions ($l \times w \times h$) to increase the stability of the pillars. The designed dimensions of the pillars in both NP1 and NP2 arrays, were the same ($d = 0.2$ µm, $h = 2.5$ µm, $p = 1$ µm).

2.2.2. Design of the 3D Cages

Concerning the 3D category, five structures in total were designed. The structures were cuboidal micro-cages of two different sizes. They were designed to either have no decoration, a micro-pillar decoration, or a nano-pillar decoration on their beams (Appendix A, Fig. A1.C). The small cage (SC) and micropillar-decorated small cage (SC-MP) structures were designed to have a volume of 25 × 25 × 25 μm^3 (L×W×H) and to be printed in arrays of 7 × 7 cages in order to cover a total area of 500 × 500 μm^2. Concerning the SC-MP, the pillar diameter and height were designed to be 1 and 2.5 µm, respectively. The angular spacing (θ) was 30°, and the lateral pillar spacing (δ) was 1 µm. On the other hand, the big cage (BC), micro-pillar-decorated big cage (BC-MP), and nano-pillar-decorated big cage (BC-NP) structures were designed to have a volume of 50 × 50 × 50 μm^3 (L × W × H) and to be printed in arrays of 5 × 5 cages in order to cover a total area of 550 × 550 μm^2. All the beams of the cages, whether small or big, were cylindrical in shape (D = 5 µm). The micro-pillars on the BC-MP were designed to have a diameter of 1 µm while nano-pillars on the BC-NP structures had a diameter of 0.2 µm. All pillars were designed to have a height of 2.5 µm, an angular spacing (θ) of 30°, and a lateral pillar spacing (δ) of 1 µm.

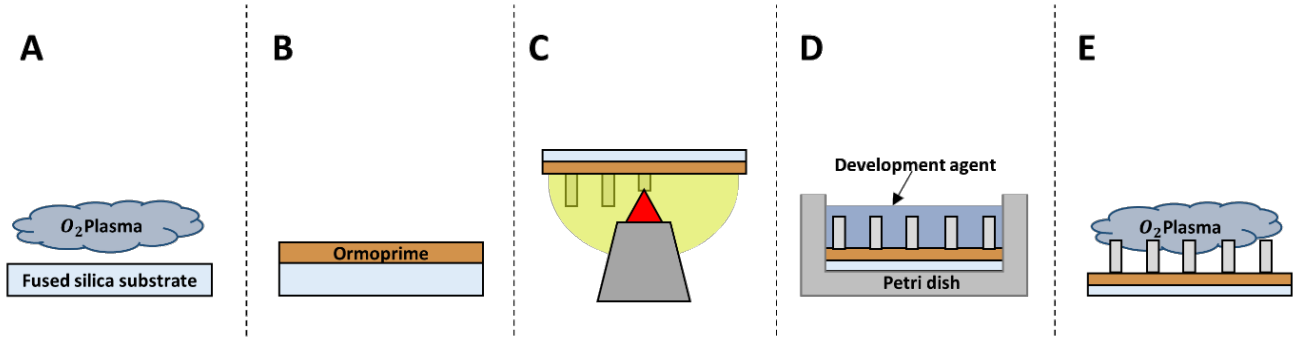

Fig. 2.2. Schematic representation of the fabrication process of the structures. (A) Oxygen plasma cleaning of the substrate. (B) Spin coating of the adhesion promoter Ormoprime® 08. (C) 2PP printing of the structures. (D) Chemical development of the structure. (E) Oxygen plasma functionalization of the polymer surface.

2.2.3. Preparation of the Substrate

All structures were printed on 25 × 25 × 0.7 mm3 (l × w × h) fused silica substrates (Nanoscribe GmbH & Co. KG) and, unless otherwise mentioned, all chemicals were purchased from Sigma-Aldrich. Before printing, the substrates (Young's modulus ≈72 GPa [62]) were first cleaned with acetone and iso-propanol using a lint-free wipe and then dried with an air-gun. The samples were then further cleaned and activated using a Diener oxygen plasma cleaner for 5 min at 80Wwith a gas flow rate of 5 cm3/min (Fig. 2.2A). The substrates were coated with OrmoPrime® 08 (Microresist Technology GmbH) to increase adhesion of the structures. Multiple droplets of OrmoPrime® 08 were cast and spincoated (spin-coating speed = 4,000 rpm, time = 60 s, acceleration = 1,000 rpm/s) on top of the substrate to achieve a coating thickness of 130 ± 15 nm (Fig. 2.2B). The substrates were then baked on a hot plate for 5 min at 150°C to harden the coating. Finally, the substrates were placed in the sample holder, and one droplet of the negative tone IP-Dip photoresist (Nanoscribe GmbH & Co. KG) was deposited in the middle of the substrate before printing.

2.2.4. Printing Parameters

The structures were printed employing the Nanoscribe Photonic Professional GT+ setup, with a femtosecond pulsed laser working at a wavelength of 780 nm (Nanoscribe GmbH & Co. KG). A 63x objective with a numerical aperture (NA) of 1.4 was operated in Dip-in Laser Lithography (DiLL) mode in order to polymerize the IP-Dip photoresist (Fig. 2.2C shows for simplicity only the pillars structures). The 3D models of the structures were imported into Describe (the proprietary software of Nanoscribe GmbH & Co. KG) as (.stl) files where they were

split into horizontal lines (hatching lines) and vertical layers (slices) since printing takes place in a layer-by-layer fashion in the vertical direction where each layer is made up of multiple horizontal lines. Hatching and slicing distances for all structures (2D, 2.5D, and 3D) were 0.2 and 0.25 µm respectively except for the nano-pillars on the BC-NP scaffolds where the hatching and slicing were 0.1 and 0.2 µm respectively. Afterwards, the printing parameters (i.e., laser power and scanning speed) were optimized for each structure. The
pedestals were printed at a laser power of 42.5mW (85% of a maximum power of 50 mW) and scanning speed of 60 mm/s. There were two versions of the micro-pillar arrays depending on the printing parameters (MP1 and MP2). The MP1 arrays were printed at a laser power of 42.5mW and a scanning speed of 60 mm/s while the MP2 ones were printed at a laser power of 35mW (70% of a maximum power of 50 mW) and a scanning speed of 30 mm/s. Similarly, the laser power and scanning speeds employed to manufacture NP1 and NP2 arrays were 42.5 mW and 60 mm/s, and 35mW and 30 mm/s respectively. The printing parameters of all 3D cages were 35mW and 30 mm/s. The corresponding light intensity values [63] are summarized in Table A1 in Appendix A together with additional parameters of the employed laser source.

2.2.5. Sample development and post-processing

Once the printing process was completed, the substrates with polymerized structures were carefully placed horizontally in a borosilicate Petri dish filled with propylene glycol methyl ether acetate (PGMEA) for 25 min to dissolve the unpolymerized resin. This was followed by submersion in a Petri dish with isopropanol (IPA) for 5 min to rinse off the excess PGMEA. The samples were then submersed for 30 s in Novec™ 7100 Engineered Fluid, which has lower surface energy than iso-propanol resulting in a decrease of collapsed nano-pillars as a result of mechanical stresses caused by wet-to-dry transitions (Fig. 2.2D). Post-processing of the IP-Dip structures was performed by plasma activation using the Diener oxygen plasma cleaner for 20 s at 80W with a gas flow rate of 5 cm3/min (Fig. 2.2E). This would additionally activate the surface of the polymeric structures to increase the adhesion of the biochemical coating and/or the cells to the structures.

2.2.6. Mechanical Characterization of the

Structures In order to assess the Young's modulus of the material, a series of four compression tests were performed using the FEMTOTOOLS nanomechanical testing system FT-NMT03 (Appendix A, Fig. A2.A,B). The 2D pedestal structure was used for this test. The compression test was performed at a displacement of 10% of the height of the structure. The employed probe was a flat silicon one, model FT-S200,000, had a tip size of 50 × 50 µm^2 and a force range of 200,000 ± 0.5 µN. To confirm that the Young's modulus of the material does not change significantly at the nanoscale, an Atomic Force Microscope (Bruker JPK Nanowizard 4) was employed to measure the mechanical properties of a single nano-pillar since the probes of the FT-NMT03 were too large in size to perform such a measurement. This was accomplished with a pillar bending test, using the cantilever tip to bend the nanopillars (cantilever stiffness 14.4 N/m) (Appendix A, Fig. A2.C,D), resulting in a force versus displacement diagram from which the spring constant of the structure was derived [64]. Using beam deflection theory, and assuming a cylindrical shaped cantilever beam with an external force at the tip, the Young's modulus was obtained. The calculation of the effective shear moduli of the micro- and nano-pillar arrays was achieved by using Eq. 1 [49].

$$\bar{G} = \frac{3}{16}\left(\frac{D}{L}\right)^2 fE \quad (1)$$

Where $\bar{G}$ is the effective shear modulus, *D* and *L* are the diameter and height of the pillar respectively, *f* is the surface coverage (surface area covered by pillars per total surface area of the array), and *E* is the Young's modulus of the bulk material.

2.2.7. Sample Sterilization

The substrates with or without structures were transferred to a 6- well plate. Within the 6-well plate, the substrates were then washed twice for 5 min with a large volume (~4 ml/well) of 70% ethanol. Finally, the substrates were washed five times for 1 min with sterile demi-water or phosphate buffer saline (PBS).

2.2.8. Laminin Coating of the Substrates

Some samples were coated with laminin to observe the effect of a biochemical coating on the phenotypic expression of microglia. To coat the samples with laminin, 10 mg/ml working solution of laminin was prepared in Dulbecco's Modified Eagle Medium/ Nutrient Mixture F-12 (DMEM/F-12) (Gibco). Then the solution was cast to cover the entire surface of the fused silica substrate (~500 ml/substrate). For uncoated substrates, DMEM/F-12 was cast to cover the entire surface of the fused silica substrate (~500 ml/substrate). The substrates were then incubated at 37°C and 5% CO2 for 2 h. The freshly coated substrates were then used for further experiments.

2.2.9. Primary Microglia Cell Isolation

Primary microglia were derived from isolated brain tissue (white matter) of adult rhesus macaque (Macaca mulatta) donors that were free from neurological diseases. All animals were outbred at the breeding colony of the Biomedical Primate Research Centre (BPRC). The BPRC has been recognized by the Dutch Ministry of Agriculture, Nature and Food Quality for performing animal experiments under the veterinary control number 7962. No animals were sacrificed for the exclusive purpose of the initiation of microglia cell cultures. Better use of experimental animals contributes to the priority 3Rs program of the BPRC. There were 6 donors in total with various ages and genders. The overview of donors is reported in Table A2 in Appendix A.
Microglia isolations were initiated from cubes (~4.5 g) of frontal subcortical white matter tissue that were depleted of meninges and blood vessels manually. The tissue was chopped into cubes of less than 2 mm2 by using gentle MACS™ C tubes (Miltenyi Biotec, Bergisch Gladbach, Germany) and then
incubated at 37°C for 20 min in PBS containing 0.25% (w/v) trypsin (Gibco Life Technologies, Bleiswijk, the Netherlands), 1 mg/ml bovine pancreatic DNAse I (Sigma-Aldrich, Saint Louis, MO) and mixed every 5 min. The supernatant was discarded (no centrifugation), the pellet was washed and passed over a 100 mm nylon cell strainer (Falcon; Becton Dickinson Labware Europe) and centrifuged for 7 min at 524 g. The pellet was re-suspended in 22% (v/v) Percoll, 37mM NaCl and 75% (v/v) myelin gradient buffer (5.6mM NaH2PO4, 20mM Na2 HPO4, 137mM NaCl, 5.3 mM KCl, 11mM glucose, 3 mM bovine serum albumin (BSA) Fraction V, pH 7.4). A layer of myelin gradient buffer was added on top, and this gradient was centrifuged at 1,561 g for 25 min (minimal brake). The pellet was washed and centrifuged for 7 min at 524 g.

2.2.10. Microglia Cell Culture

Primary microglia cells were plated at a density of 50,000 cells/cm2 on either uncoated or laminin coated substrates with or without structures in serum medium (SM) comprised of 1:1 v/v DMEM (high glucose)/HAM F10 Nutrient mixture (Gibco) supplemented with 10% v/v heat-inactivated FBS (TICO Europe, Amstelveen, the Netherlands), 2mM glutamax, 50 units/ml penicillin and 50 mg/ml streptomycin (all from Gibco). After overnight incubation at 37°C in a humidified atmosphere containing 5% CO2, the unattached cells and debris were removed by washing with PBS twice and replaced by fresh SM medium supplemented with 20 ng/ml (≥4 units/ml) M-CSF (PeproTech, London, United Kingdom). At day 4, cells were washed twice with PBS and replaced by serum-free microglial (SFM) culture medium comprised of DMEM/F12 (Gibco) supplemented with 0.5 mM glutamax, 50 units/ml penicillin, 50 mg/ml streptomycin, 5 mg/ml N-acetyl cysteine, 5 mg/ml insulin, 100 mg/ml apotransferrin, 100 ng/ml sodium selenite, 20 ng/ml (≥4 units/ ml) M-CSF, 12.5 ng/ml TGF-β (Miltenyi Biotec, Bergisch Gladbach, Germany), 1.5 mg/ml ovine wool cholesterol (Avanti Polar Lipids, Alabaster, AL), 1 mg/ml heparan sulfate (Galen Laboratory Supplies, North Haven, CT), 0.1 mg/ml oleic acid (Cayman Chemical, Ann Arbor,

MI), 1 ng/ml gondoic acid (Cayman Chemical). All cells were kept in culture for a total of 15 days without passaging. From day 4, half of the medium was replaced by a fresh SM medium containing new growth factors every 2–3 days.

2.2.11. Scanning Electron Microscope

Imaging To prepare cells for scanning electron microscope (SEM) imaging, a fixation protocol was carried out. First, the medium was removed and the cells were washed twice with PBS (Gibco). Second, the cells were fixed with 2% paraformaldehyde (PFA) (Affymetrix, Santa Clara, CA) in PBS for 30 min at room temperature. The PFA was removed and the cells were washed with PBS twice. The PFA fixated samples were then post-fixed with 2% glutaraldehyde (GA) (Agar Scientific, Stansted, United Kingdom) in PBS for 2 h. Then the fixative was removed and the samples were dehydrated in distilled water for 2 × 5 min, followed by 50% ethanol in distilled water for 15 min, 70% ethanol in distilled water for 20 min, and lastly in 96% ethanol in distilled water for 20 min. The ethanol was then removed from the sample and hexamethyldisilazane (HMDS) was used for further drying to reduce membrane rupture of the cells. Firstly, two parts of 96% ethanol were used on one part HMDS for 15 min. Secondly, one part of 96% ethanol on one part HMDS for 15 min. Thirdly, one part of 96% ethanol on two parts HMDS for 15 min. Pure HMDS was then used for 20 min, twice. Lastly, the HMDS was removed and the sample was air-dried for 2 h.
In order to visualize the structures and the morphology of the cells, SEM imaging was carried out using a JEOL JSM-6010LA SEM (JEOL (Europe) BV) in high-vacuum with an accelerating voltage of 10 kV. Prior to imaging the samples, they were sputtered with a nanometric layer of gold using a JEOL JFC-1300 auto-fine sputter coater at a current of 20 mA for a duration of 30 s. The samples were roughly 25 mm away from the gold source. An additional sputtering step at a 45° angle was performed in order to ensure a homogeneous metal coating also along sidewalls.

2.2.12. Immunofluorescence and Confocal

Imaging The cells grown on substrates were fixed for 30 min at room temperature in 2% PFA, washed with PBS and PBS +0.02% Tween20 respectively, and a-specific binding was blocked by incubation for 30 min in PBS containing 2% normal goat serum. Samples were incubated overnight at 4°C with
CX3CR1 antibody (1:400, Abcam, Cambridge, United Kingdom) in PBS containing 0.1% BSA, washed
with PBS +0.02% Tween20, and incubated for 1 h at room temperature with goat anti-rabbit Alexa 647 (1:250, Jackson ImmunoResearch Laboratories, Weste Grove, PA) (red channel) in PBS containing 0.1% BSA. This antibody was used to stain and visualize the cellular membrane of microglia. After extensive washes with PBS, the substrates were incubated in 2 mM Hoechst 33342 (Thermo Fisher Scientific™, blue channel, nuclei) for 10 min, washed with PBS twice and then stored in PBS. A Leica SP5 confocal microscope (Mannheim, Germany) was used in combination with the Leica LAS-AF software. The employed excitation wavelengths were 405 nm, 488 and 633 nm in presence of a Leica Microsystems HC APO L 20.0x/1.00W lens with a working distance of 1.95 mm and NA of 1.0, in water dipping mode. Samples were submersed in PBS during all imaging sessions. The step size of the z-stacks was 250 nm. Both Fiji [65] and Imaris (Oxford Instruments) were employed for the 3D reconstructions of the z-stacks.

2.2.13. Quantitative and Statistical Analysis of Microglia

The phenotype distribution of microglia was quantified by analyzing the morphology of the cells. This was achieved by using the multi-point selection tool in Fiji. To determine the degree of ramification of ramified cells (i.e., the degree of complexity and number of ramified branches that a cell has), Sholl analysis was carried out on both SEM and immunofluorescence images. First, the perimeter of the cell was traced with the Neurite tracer tool in Fiji and skeletonized. Then, using the Sholl analysis, concentric circles were drawn around the center of the cell, with a radial increment of 5 µm. This tool measures the number of intersections that the body and branches of

the cell have at each concentric circle. The number of intersections is plotted against the distance from the cell center. A high amount of intersections translates to a high degree of ramification of the cells. The area under the curve (AUC) obtained from a Sholl plot was also used as an indication of the degree of ramification of ramified cells. The larger the area, the more ramified a cell is. Furthermore, the counting of primary branches was performed by the use of the multi-point selection tool (Fiji) on the same cells that were investigated for the Sholl analysis. No less than two donors were used for all studies performed on fused silica substrates and 2.5D structures with 1-3 samples per donor, and with a minimum of three samples per study ($n \geq 3$).
To obtain the volumetric occupancy of the cells in the 3D cages, we assumed a volume of $60 \times 60 \times 60\ \mu m^3$ around each cage and counted all cells within that volume and then divided the number of cells by said volume to obtain a cell density (cells per mm^3). This was only performed for the BC structures since the cells completely enwrapped the SC structures leaving no room for such analysis. Lastly, cell occupancy and distribution in the bigger 3D structures were assessed and compared. The cells were counted in the fluorescent images extracted from z-stacks of the 3D cages using the multi-point selection tool in Fiji and an in-house code developed in MATLAB (MathWorks®). Cages were split into 15 µm thick sections (0–60 µm range) and cells were counted within each section. For 3D structure studies, one donor was used with a minimum of two samples per study. Results are reported as means and standard deviations. All means are calculated by first calculating the means for samples used with each individual donor and then averaging all results from all donors. Microsoft Excel was the main tool employed to obtain means and standard deviations.

2.3. Results and discussion

2.3.1. Fabrication of the Micro- & Nano-Structures

Nano-Structures Multi-scale structures were fabricated using 2PP to investigate the effect of geometry and mechanical cues on primary microglial morphology. The overview of the fabrication process is depicted in Fig. 2.2 and detailed in section 2.2.2. SEM images of all printed structures are shown in Figure 2.2. The developed structures consisted of square pedestals (Fig. 2.3A), micro-pillar arrays (Fig. 2.3B), nano-pillar arrays (Fig. 2.3C,D), small cuboidal cages (Fig. 2.3E), big cuboidal cages (Fig. 2.3F), micro-pillar-decorated small cages (Fig. 2.3G), micro-pillar-decorated big cages (Fig. 2.3H), and nano-pillar-decorated big cages (Fig. 2.3I). A higher magnification SEM micrograph of the micro- and nano-pillars decorating cuboidal cages is reported in Fig. A3 in Appendix A.
As mentioned in section 2.2.1, NP1 arrays (Fig. 2.3C) were directly printed on the substrate while NP2 ones (Fig. 2.3D) were printed on top of a pedestal to prevent the pillars from falling over since the forces of surface tension proved to have major detrimental effects on the stability of the pillars after the printing process. The SC and SC-MP structures were designed to have a size smaller than the cell soma, but comparable to that of the nucleus while the BC, BC-MP, and BC-NP structures were designed to have sizes larger than the cell soma. For more information regarding the design, fabrication and dimensions of the structures, the reader is referred to the Materials and Methods section. Table A3 in Appendix A shows the actual measured dimensions of the 2D and 2.5D structures. For the pedestal, an average of 5% difference between measured dimensions and nominal ones was noticed. For micro-pillars in the MP1 arrays, the average shrinkage in the x-y and in the z-directions was 3 and 21.2%, respectively. Pillars in the MP2 arrays, however, exhibited an average increase of 6% in measured dimensions in the x-y direction compared to the nominal ones. In the z-direction, there was an average shrinkage of ~25%. For the nano-pillars, in the NP1 array, an average enlargement of 95% in the x-y direction and an average shrinkage of 24% in the z-direction were noticed. Pillars in the NP2 array displayed an average enlargement of 45% in the x-y direction and shrinkage of ~27% in the z-direction. The difference in measured dimensions from designed ones can be attributed to the shrinkage of IP-Dip post development [66] and the high sensitivity of sub-micrometric structures to the printing parameters as well as the hatching and slicing parameters. The main reason for this is the increase in the voxel size when using a higher laser power. For the 3D cages, a similar difference in printed dimensions was observed.

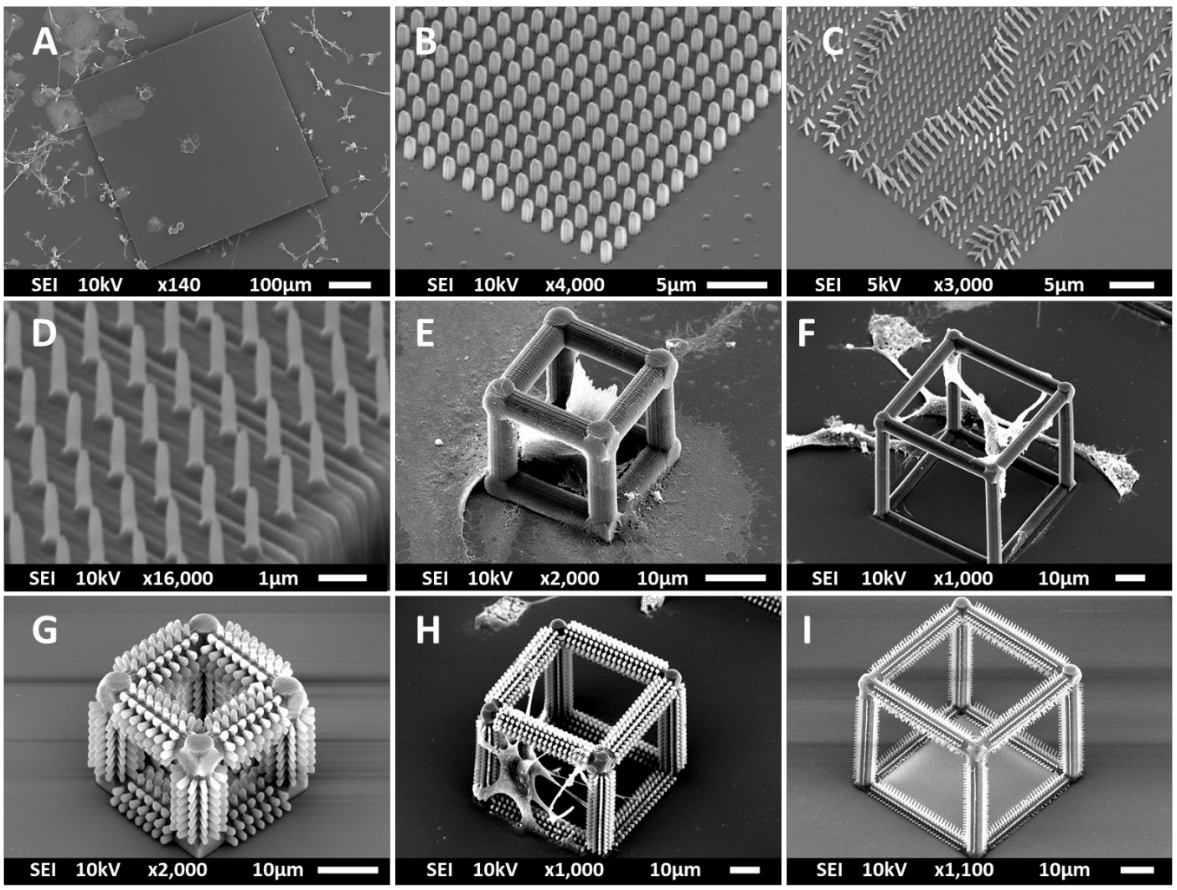

Fig. 2.3. SEM images (at a 45° angle) of (A) the pedestal; (B) micro-pillar array (MP1); (C) nano-pillar array (NP1); (D) nano-pillar array (NP2). The printing of a supporting pedestal for the nano-pillars prevented the collapse of pillars after development. (E) Small cage (SC). (F) Big cage (BC). (G) Small cage with micro-pillar decoration (SC-MP). (H) Big cage with micro-pillar decoration (BC-MP). (I) Big cage with nano-pillar decoration (BC-NP).

Table A4 in Appendix A shows the actual dimensions of the cages and their micro- or nano-pillars decorations. No major challenges were faced in printing 3D structures with the exception of the BC-NP. Since the hatching and slicing distances were different for the cage (hatching distance = 0.2 µm, slicing distance = 0.25 µm) and the nano-pillar decoration (hatching distance = 0.1 µm, slicing distance = 0.2 µm), the entire structure could not be printed directly in one run. Therefore, we proposed a method in which the beams of the cage were printed first and then the pillars were printed on top of them using multiple (.stl) files (Fig. 2.4). This printing technique, however, required the elements of the cage to be printed separately to avoid shadowing effects caused by the top part of the cage, thereby hindering the printing of pillars on the bottom and side beams. The cage was split into three sections, the bottom (consisting of four horizontal beams), the middle (consisting of four vertical beams), and the top (consisting of four horizontal beams). Each section was printed separately and then the pillars were printed on the respective section.

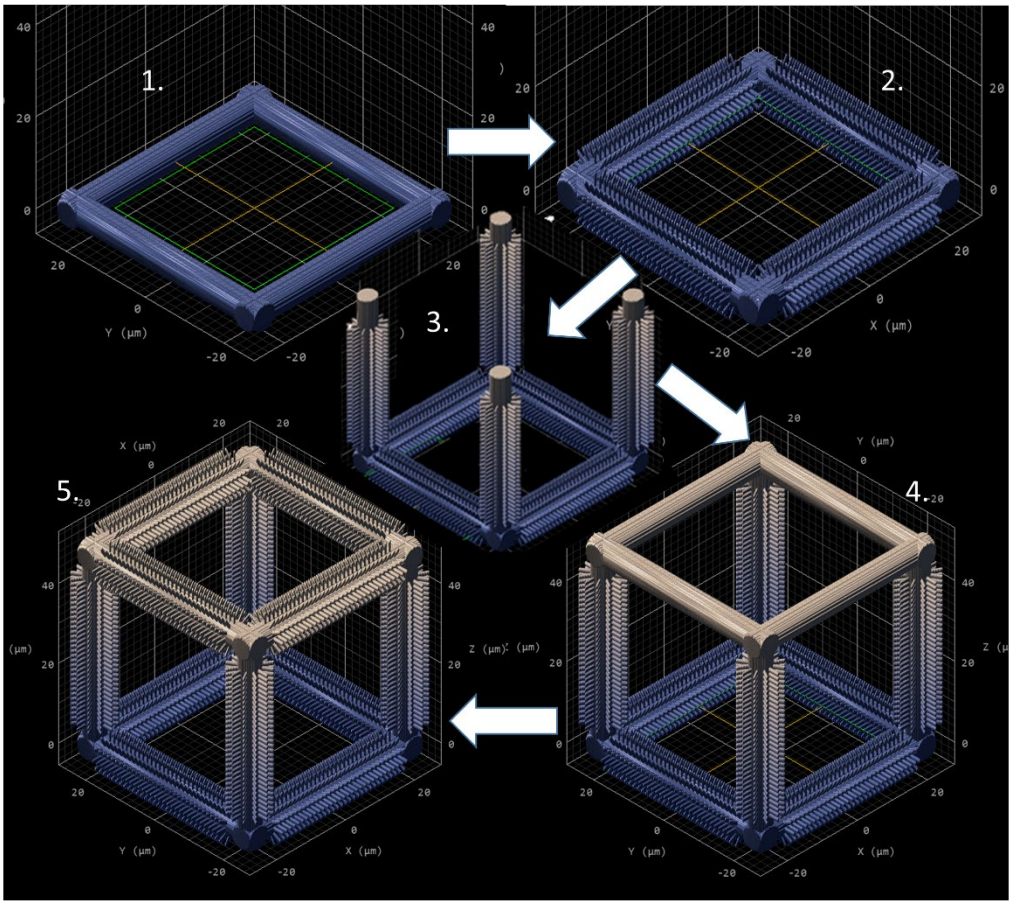

Fig. 2.4. Sequential printing technique of the BC-NP, using five steps. (1) Base printed. (2) Pillars printed on the base. (3) Vertical beam with pillars printed. (4) Top printed. (5) Pillars printed on the top. CAD model generated by Describe (Nanoscribe GmbH).

2.3.2. Mechanical Characterization of the IP-Dip

Structures The Young's modulus of IP-Dip (pedestal structure), which is known to have a dependence from writing parameters [67], was measured by compression testing using the FEMTOTOOLS nanomechanical testing system. The Young's modulus was determined to be 1.28 ± 0.18 GPa and 1.07 ± 0.06 GPa ($n > 3$) in presence of the writing parameter sets (42.5mW and 60 mm/s; 35mW and 30 mm/s) employed respectively for printing the pedestals, MP1, and NP1 arrays; the MP2, NP2 arrays, and the 3D cages. By means of a pillar bending test using an atomic force microscope (AFM), the Young's modulus was determined to be 1.80 ± 0.18 GPa ($n > 3$). Using Eq. 1 (see section 2.2.6), the effective shear moduli of MP1, MP2, NP1, and NP2 arrays were calculated to be 11.4, 14.63, 0.91, and 0.25 MPa respectively, therefore much lower than the intrinsic Young's modulus of IP-Dip and closer to the one of the brain tissue.

2.3.3. Classification of Microglial Phenotypes *In vitro*

In the *in vivo* environment of human brain white matter, there are four main phenotypes of microglia, namely ramified, primed, reactive and amoeboid [33]. The ramified phenotype (also known as the "resting" state of microglia) is the most abundant in a healthy brain [32]. This phenotype is characterized by multiple extensively

ramified processes acting as sensors that search for chemical or physical cues indicating the presence of a foreign body or cellular debris. Ramified microglia have the smallest cell body (area ≈ 16 μm^2), but the longest processes (total process length ≈ 430 µm). On average, the number of primary processes is five. Both primed and reactive microglia have on the other hand larger cell bodies, but fewer processes than the ramified ones. The amoeboid phenotype is the phagocytic state of microglia that isolates and then phagocytoses cellular debris or foreign bodies. This phenotype has a flat morphology, a wide cell body, and a maximum of two unbranched primary processes [33].

As already pointed out earlier, the phenotypes of microglia observed *in vitro* are substantially different from their *in vivo* counterparts, both morphologically and functionally [30,68,69]. Therefore, it was not possible to use a conventional *in vivo* classification of microglia to describe our findings. Based on our observations of microglial morphology *in vitro*, we proposed a more relevant phenotypic classification. We included four categories within this classification, namely flat amoeboid, globular, non-amoeboid, and bi-polar (Appendix A, Fig. A4 depicts representative SEM images of all *in vitro* phenotypes). The flat amoeboid category includes cells with a wide soma and few to no processes. This phenotype is similar to the one found *in vivo* except that the *in vitro* phenotype is more round and spread out over the surface (diameter ≈ 40 µm) as compared to the *in vivo* counterpart (diameter ≈ 12 µm). The globular phenotype includes cells that are almost spherical in shape. Such morphology should not be confused with that of dead cells, as the cell membrane is still completely intact. The bi-polar phenotype includes rod-shaped (polarized) cells. The last category is the nonamoeboid one and it consists of cells of two phenotypes, the ramified and the non-ramified ones. Ramified microglia look morphologically like the *in vivo* counterpart in terms of ramified branching that spread in multiple directions. A cell is considered ramified if it has at least three primary branches and a branch is considered primary if its length is equal to the minimum Feret diameter of the cell soma (i.e., the smallest diameter measured across the soma in all given directions). Non-ramified microglia are cells that resemble the ramified cell in morphology as they have multiple branches but not as long or branched as the ramified phenotype. This phenotype resembles the morphology of reactive *in vivo* microglia. The reason of gathering these two phenotypes in one category is their morphological resemblance and the absence of a robust and detailed method to discriminate between truly ramified cells and ramified-like cells based only on morphology in an *in vitro* cell culture.

2.3.4. Effect of Laminin Coating on Microglial Phenotype

Primary microglia from five rhesus macaque donors were isolated and cultured on fused silica substrates in the presence or absence of laminin coating to investigate the effect of laminin on the expression of a ramified phenotype in microglia (Appendix A, Fig. A5 shows representative confocal microscopy images of microglia grown on uncoated and laminin-coated substrates). For each donor, 1-3 samples were used. As depicted in Fig. 2.5A,B, there is not a remarkable difference between laminin coated and uncoated substrates in terms of fostering a ramified phenotype ($n_{samples}$ = 11 and n_{cells} > 1,000 for the uncoated substrates, $n_{samples}$ = 9 and n_{cells} > 1,000 for the laminin-coated substrates). The percentage of ramified cells on the uncoated substrates was 9.0 ± 8.39% (roughly 40.9% of the non-amoeboid phenotype) while on the laminin coated ones, it was 7.61 ± 3.29% (roughly 40.5% of the non-amoeboid phenotype, Fig. 2.5B). An additional observation was the increased complexity of the ramified microglia on the uncoated substrates shown by the higher average number of primary branches per ramified microglial cell (Fig. 2.5C) ($n_{samples}$ = 9 and $n_{ramified\_cells}$ > 30 for the uncoated substrates, $n_{samples}$ = 9 and $n_{ramified\_cells}$ > 30 for the laminin-coated substrates). It is noteworthy that the high standard deviation in this data is mainly due to the large donor-to-donor variance present in an outbred colony and to the limited number of tissue donors necessary to initiate primary cell cultures, as further explained in the following section.

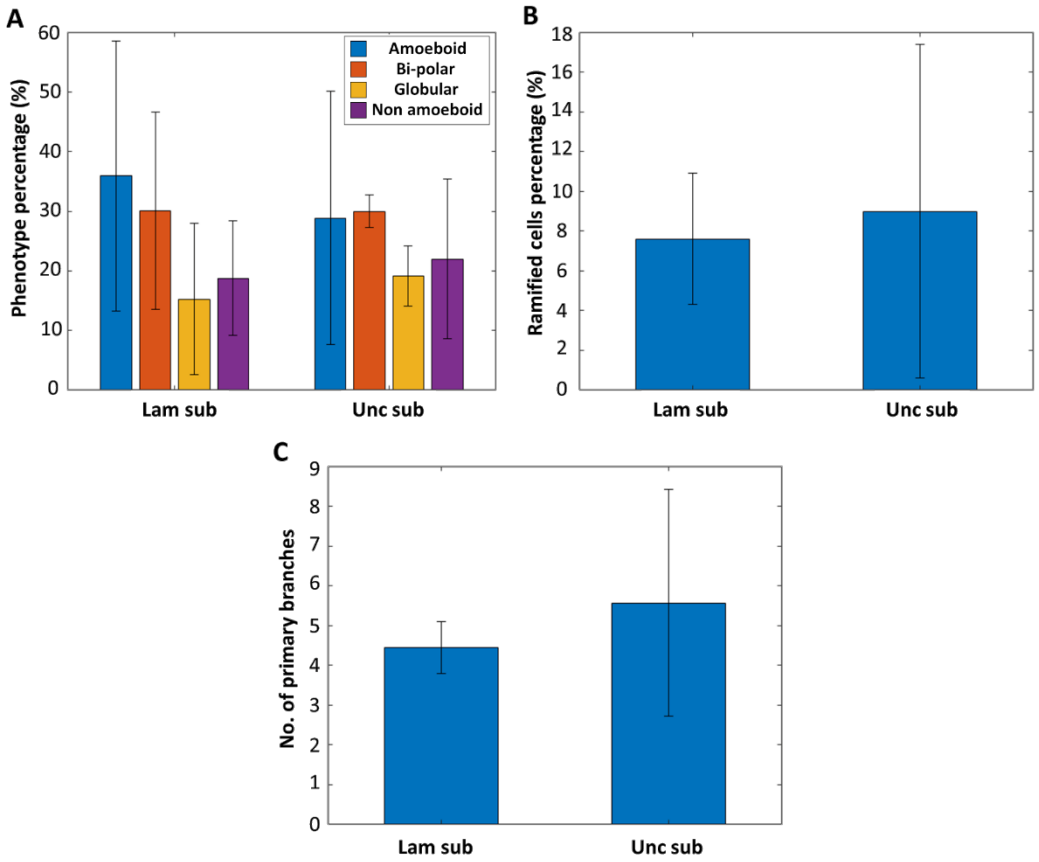

Fig 2.5. (A) The phenotype distribution of microglia cultured on laminin-coated fused silica substrates (Lam sub) and uncoated substrates (Unc sub) ($n_{samples}$ = 11 and n_{cells} > 1,000 for the uncoated substrates, $n_{samples}$ = 9 and n_{cells} > 1,000 for the laminin-coated substrates). (B) Percentage of ramified cells on laminin-coated versus uncoated substrates. (C) Number of primary branches per ramified cell for ramified microglia cultured on laminin-coated versus uncoated substrates ($n_{samples}$ = 9 and $n_{ramified\_cells}$ > 30 for the uncoated substrates, $n_{samples}$ = 9 and $n_{ramified\_cells}$ > 30 for the laminin-coated substrates).

In general, these results indicate that a laminin coating, which can feature some inhomogeneous distribution over the substrate, does not promote the expression of a ramified phenotype, which belongs to the non-amoeboid category (as explained in section 2.3.3). These results are in line with literature as it has been shown in multiple studies that laminin specifically increases a microglial amoeboid pro-inflammatory phenotype while simultaneously decreasing the expression of a ramified or resting phenotype [60,61,70]. For example, Pietrogrande et al. found that culturing BV2 cells and primary murine microglia on laminin coated substrates increased the phagocytic activity and expression of pro-inflammatory cytokines as well as decreased the branching of the cells when compared to culturing on uncoated substrates. These results were corroborated by *in vivo* experiments of murine microglia [70]. In a study performed by Tam et al., primary murine amoeboid microglia cultured *in vitro* were even shown to phagocytose the laminin coating on the substrate [61].

2.3.5. Effect of Micro- and Nano-Pillar Arrays on Microglial Phenotype

In order to investigate the effect of surface topography on the expression of a ramified resting phenotype in microglia, we performed *in vitro* experiments comparing the phenotype and morphology of primary microglia cultured on flat fused silica substrates, micro-pillar arrays, and nano-pillar arrays. Fig. 2.6A,B show representative

confocal images of microglia cultured on flat substrates and micro-pillars respectively. The high autofluorescence of IP-Dip specifically in the blue channel can be clearly noticed in Figure 2.5B. Neither flat substrates nor 2.5D- 3D structures were coated with laminin in these experiments in light of the observations reported in section 2.3.4. A total of two donors were used for this study with 1-3 samples per donor. The results showed a clear difference in phenotypic differentiation when culturing microglia on nano-pillar arrays as compared to micro-pillars or flat substrates ($n_{samples}$ = 4 and n_{cells} > 300 for the substrates, $n_{samples}$ = 4 and n_{cells} > 300 for the micro-pillar arrays, $n_{samples}$ = 3 and n_{cells} > 300 for the nano-pillar arrays). While the percentage of non-amoeboid cells on flat substrates was 31.3 ± 12.3% and on micro-pillar arrays was 26.8 ± 4.14%, it increased to 58.4 ± 34.7% on the nano-pillar arrays. On the other hand, the flat amoeboid phenotype percentage decreased from 26.1 ± 5.9% on the flat substrate and 32.7 ± 6.7% on the micro-pillar arrays to 16.8 ± 9.56% on the nano-pillar arrays. The percentage of the bi-polar phenotype showed a consistent decline also since the percentage was 30.5 ± 1.34% on the flat substrate, 23.4 ± 5.1% on the micro-pillar arrays, and 15.5 ± 7.76% on the nano-pillar ones. Finally, the percentage of globular phenotype was rather consistent on all substrates as its percentage was 12.3 ± 5.03% on the flat substrate, 17.1 ± 15.9% on the micro-pillar arrays, and 12.3 ± 17.4% on the nano-pillar arrays (Fig. 2.6C).
Moreover, Fig. 2.6D illustrates that the ramified phenotype is on average overexpressed when using nano-pillars compared to flat substrates or micro-pillar arrays. A total of 42.8 ± 38.4% of cells cultured on nano-pillar arrays were ramified (approximately 73.3% of non-amoeboid cells). On the other hand, only 15.6 ± 9.31% of cells on flat substrates (approximately 49.8% of nonamoeboid cells) and 15.2 ± 3.2% of cells on micro-pillar arrays (approximately 56.7% of non-amoeboid cells) expressed a ramified morphology. As a quantitative measure of the degree of complexity of the cells (i.e., the branching degree of the cell), Sholl analysis was performed. Briefly, this analysis is based on the counting of the intersections of the body and branches of the cell with concentric contour lines that have a common origin at the center of the cell. The result is displayed as the distance between an intersection and the cell center. In the Sholl analysis (Fig. 2.6E), we show that ramified cells grown on the flat substrate are the least complex cells with the fewest number of branches, followed by ramified cells cultured on the micro-pillars. The cells cultured on the nano-pillars are the most complex, indicated by the highest amount of intersections. This is also confirmed by the AUC values extracted from the Sholl plot. The AUC value for ramified cells cultured on the flat substrate was 345 ± 12.4 arbitrary units (a.u.), while the values for those cultured on micro-pillars and nano-pillars were 373 ± 46.0 a.u. and 408 ± 33.9 a.u. respectively (Fig. 2.6F). In terms of primary branches per ramified cell, a similar upward trend is reported in Fig. 2.6G. The graph shows an average of 4.70 ± 0.14 branches/cell for cells cultured on flat substrates. The number of branches is higher for ramified cells cultured on micro-pillar arrays showing 5.85 ± 1.06 branches/cell. Ramified cells cultured on nano-pillar arrays had on average 6.36 ± 0.34 branches/cell ($n_{samples}$ = 3 and $n_{ramified\_cells}$ = 15 for the flat substrates, $n_{samples}$ = 3 and $n_{ramified\_cells}$ = 15 for the micropillar arrays, $n_{samples}$ = 3 and $n_{ramified\_cells}$ = 13 for the nano-pillar arrays). More information about the Sholl analysis, AUC, and primary branches counting can be found in section 2.2.13.

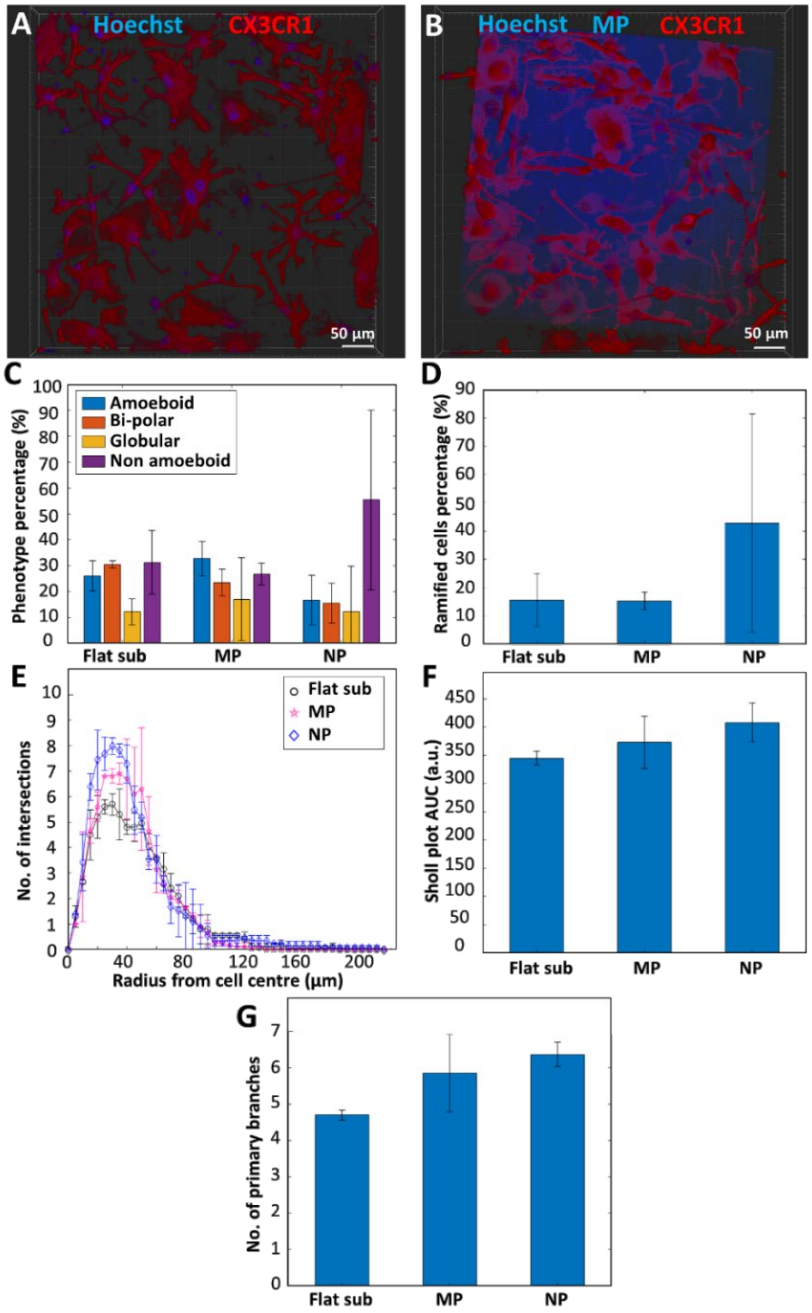

Fig. 2.6. Representative confocal microscopy images of primary microglia (maximum projection) cultured on (A) a fused silica substrate; (B) micro-pillar arrays. Blue is Hoechst 33342 staining (nucleus) and IP-Dip micro-pillars. Red is CX3CR1 (cell membrane). (C) Phenotype distribution of primary microglia cultured on flat fused silica substrates (Flat sub), micro-pillar (MP), and nano-pillar (NP) arrays ($n_{samples}$ = 4 and n_{cells} > 300 for the substrates, $n_{samples}$ = 4 and n_{cells} > 300 for the micro-pillar arrays, $n_{samples}$ = 3 and n_{cells} > 300 for the nano-pillar arrays). (D) Percentage of ramified cells. (E) Sholl analysis of ramified cells showing the complexity of the cells by indicating the number of intersections the cells have with the concentric contours. (F) Area under the curve (AUC) calculated from the Sholl plot. Larger AUC corresponds to a more complex ramified cell. (G) Number of primary branches per ramified cell ($n_{samples}$ = 3 and $n_{ramified\_cells}$ = 15 for the flat substrates, $n_{samples}$ = 3 and $n_{ramified\_cells}$ = 15 for the micro-pillar arrays, $n_{samples}$ = 3 and $n_{ramified\_cells}$ = 13 for the nano-pillar arrays).

Concerning the high standard deviation in our results, we would like to underline the exploratory nature of our work, which was primarily aimed at investigating if and how micro- and nanostructures could affect microglial morphological features. It is important to mention that technical and practical considerations, pertaining to the production times of micro- and nanostructures and to the availability of tissue donors to initiate primary cell cultures, impede repetitive use of micro- and nanostructures in donor numbers required to obtain statistical significance. In addition, the tissue donors come from an outbred colony of non-human primates, further contributing to increased donor-donor variability.
The observations pointed out in Fig. 2.5 were corroborated by SEM characterization of fixed and dehydrated cells that showed the difference in microglial phenotype and morphology when cultured on a flat substrate (Fig. 2.7A), micro-pillar arrays (Fig. 2.7B,C), and nano-pillar arrays (Fig. 2.7D–G).

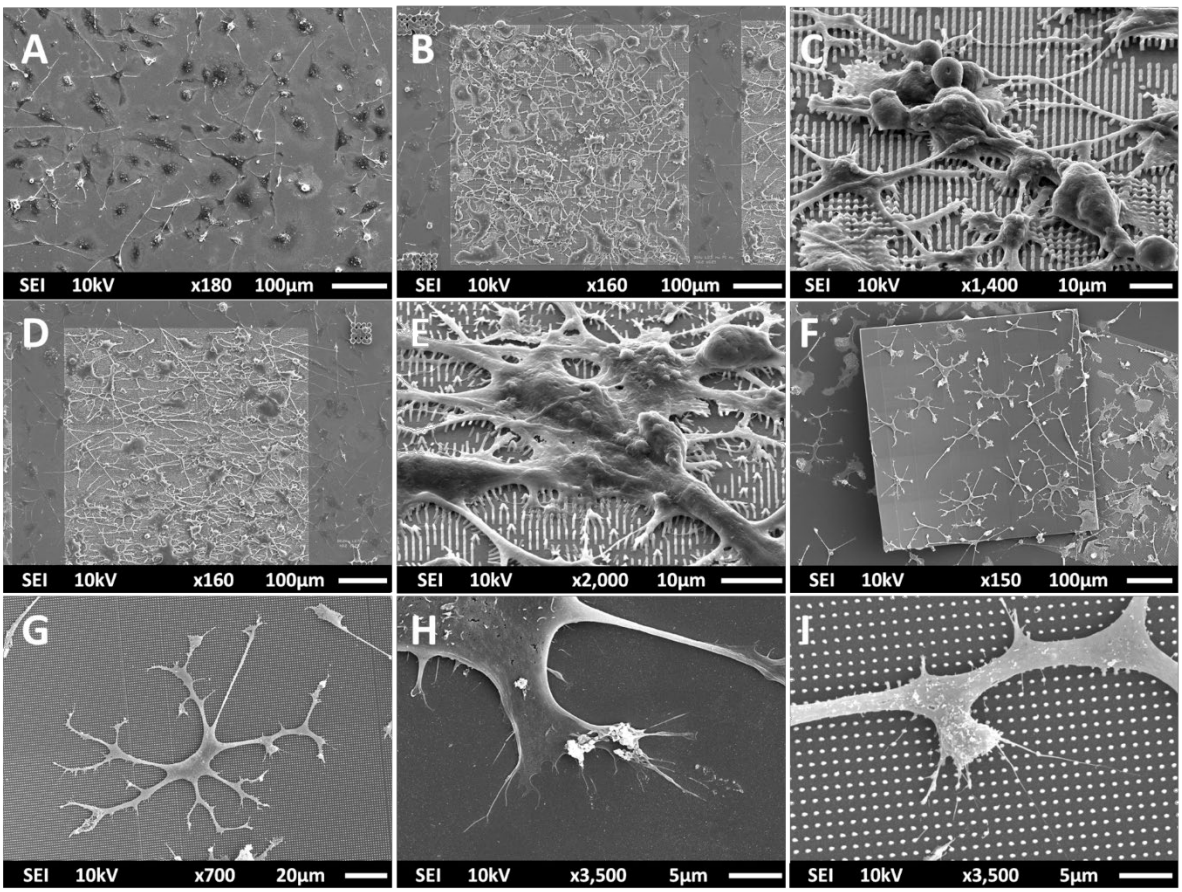

Fig. 2.7. SEM images of primary microglia on: (A) a flat fused silica substrate; (B,C) micro-pillar arrays; (D,E) NP1 nano-pillar arrays (pillars printed directly on the substrate); (F,G) NP2 nano-pillar arrays (pillars printed on a pedestal). Ramified microglia were noticed on both NP patterns, but pillars of NP2 had higher structural integrity compared to those on NP1 due to the support of the pedestal. Interaction of microglial filopodia with (H) the flat substrate; (I) nano-pillar arrays (NP2). (C,E) images are acquired at a 45° angle.

On flat substrates, an abundance in the amoeboid phenotype was noticed in contrast to micro- and nano-pillar arrays. An increased number of ramified cells and primary branches per cell were noticed on the pillar arrays. Overall, no phenotypic differences were noticed between microglia cultured on NP1 (Fig. 2.7D,E) and those cultured on NP2 (Fig. 2.7F,G). The processes of the ramified cells showed strong adhesion and wrapping of the

pillars, especially in the nano-pillars configuration. In some cases, the forces applied on the pillars were strong enough to detach them. This was particularly observed in NP1 patterns (Fig. 2.7E). The introduction of a supporting pedestal in NP2 patterns however improved the stability of the nano-pillars (Fig. 2.7G showing a highly ramified cell). In addition to the extensive branching of microglia noticed on the micro- and nano-pillar arrays, a plethora of connections between the cells were also observed alluding to the positive effect of these patterns on the intercellular communication and network formation (Appendix A, Fig. A6). The interaction between the filopodia and the different structures was evident. We observed that the membrane at the end of the primary branch of the ramified microglia on the flat fused silica substrate is flatter and more spread out (Fig. 2.7H) as compared to the membrane on the branches of the ramified microglia cultured on the micro- and nano-pillar arrays (Fig. 2.7I). The filopodia on the pillar arrays seem to only extend from pillar to pillar and avoid attaching to the fused silica substrate that lies underneath. Therefore, we hypothesize that the pillars have a guidance effect on the filopodia and hence on the direction of growth of the microglial branches.

The larger number of ramified microglia, their primary processes and the noticeable interaction of filopodia with the structures for the cells cultured on micro- and, especially, nanopillars can possibly be explained by the low effective shear modulus of the arrays and the high number of anchoring points, providing better support for the cells to exert forces on. The diameters of the pillars were in the range of 300 nm to 1 µm which is close to the range of diameters of filopodia (100–300 nm) [71], thereby inducing an efficient interaction with them which associate to the preferential growth of ramified cells with multiple protrusions. In addition, it is also hypothesized that the discrete geometry of micro- and nano-pillar arrays provides a biomimetic environment for the microglia since the pointed heads of the pillars resemble the multitude of the micro- and nanometric intersections found in the ECM as a result of the elaborate network of proteins from which the ECM is made. Such protein filaments have diameters in the range of 9–300 nm [23,72]. Focal adhesions formed on these discretized intersections in the ECM are usually smaller and much scarcer than those formed on 2D flat substrates as shown for mesenchymal stem cells among other cell types in 3D environments [73–75]. As mentioned by Kim et al., it is thought that culturing microglia on structures of similar size ranges as the proteins of the ECM reduces inflammatory responses of the cells since the mechanical cues presented to them are somewhat similar to their native *in vivo* environments [23]. These biomimetic structures are thought to stimulate the production of certain proteins and transcription factors that aid cell adhesion and define the morphology and phenotype of cells [76–79]. The effective shear modulus (0.25–14.63 MPa) of the pillars which is closer to the Young's modulus of brain tissue (0.1–1 kPa) [3] compared to the bulk Young's modulus of the fused silica substrate (~72 GPa) [62] also plays a fundamental role in the increase of ramified microglia. Based on our results, we conclude that the lower the effective shear modulus, the more ramified microglia are present and the higher the degree of ramification of these cells is observed.

Our results are supported by other studies, performed on non-primate derived cells, that utilized a nanotopography to stimulate the growth of a ramified microglial phenotype resembling microglia *in vivo* [35,80–82]. In the study conducted by Song et al., modified bacterial cellulose nanofibril substrates were shown to increase the complexity of primary rat microglia (i.e., the degree of ramification) by a factor of 1.7 when compared to cells cultured on flat glass substrates [81]. Pires et al. showed in their study an increase in microglial ramification upon culturing primary rat microglia on poly (trimethylene carbonate-co-1-caprolactone) electrospun fibers of 200 nm–2 µm diameters [35]. When it comes to the effect of stiffness on the morphology of microglia however, the literature shows some contradiction. In a study performed by Blaschke et al., rat primary microglia were shown to a have less round and more polar morphology and express more anti-inflammatory cytokines when cultured on a soft polydimethylsiloxane (PDMS) substrate (Young's modulus = 0.6 kPa) versus a stiffer one (Young's modulus = 1.2 MPa) [46]. On the other hand, Dudiki et al. showed in their study that when culturing murine primary microglia on fibronectin-coated hyaluronic acid-based hydrogels of 60 and 600 Pa Young's moduli, the bipolarization of the cells increased by approximately 3 times on the stiffer hydrogel [47]. Nouri-Goushki et al.

emphasized the importance of effective shear modulus when showing the positive effect of the height of nano-pillar arrays on polarization of murine macrophages [57].
Taken together, our results suggest that the resemblance of our 2.5D nano-pillar arrays to the adhesion discrete sites in 3D environments and the more biomimetic effective shear modulus of these arrays, affects the formation and sizes of focal adhesions and hence the morphology and phenotypic expression of primary microglia derived from adult rhesus macaques. It should be noted that the interplay between the effective shear modulus and the topography of the pillar arrays as well as the effect of each of them on the morphology of microglia should be further investigated. It is not possible to claim one or the other as the main reason for the increased number of the analyzed ramified microglia cells.

2.3.6. Culture of Microglia in 3D Polymeric Scaffolds

To provide a biofidelic environment for primary microglia cultured *in vitro*, 3D polymeric scaffolds were fabricated by 2PP at different scales. Microglia were cultured on undecorated 25 × 25 × 25 μm^3
small cages, small micro-pillar decorated cages, 50 × 50 × 50 μm^3 big cages, micro-pillar decorated big cages, and finally nano-pillar decorated big cages (Fig. 2.8). SEM characterization studies were
performed on microglia from three donors of which 1 was used for cell scaffold-occupancy assessment. An interesting discrepancy in the behavior of microglia cultured on small versus big cages was qualitatively observed. Microglia displayed a flat amoeboid-like morphology in presence of the SC (Fig. 2.8A) and SC-MP cages (Fig. 2.8B) and tried to enwrap them in a manner very reminiscent of phagocytosis. In addition, detachment of multiple small cages was noticed which may have been caused by the forces applied by microglia on the cages. When cultured on big cages, the cells wrapped around single beams of BC (Fig. 2.8C), BC-MP (Fig. 2.8D), and BC-NP (Fig. 2.8E,F) showing multiple phenotypes and extending their processes from one end to the other within each cage.
The phagocytosis of the SC and SC-MP may be explained by the fact that the size of the amoeboid phenotype of the microglia used in this study was measured to be roughly 40 µm which means that the area of this phenotype is larger than that of SC, but smaller than that of BC. Previous works also show that the current predominant opinion regarding the sizes of foreign bodies that can be phagocytosed by a single macrophage is between 500 nm and 10 µm [83,84]. Bodies larger than 10 µm but smaller than 100 µm may also be phagocytosed and digested by large assemblies of macrophages referred to as foreign body giant cells. Another possibility however is that macrophages may adhere to these relatively larger bodies and try to degrade them by producing multiple enzymes. It is not clear, however, why the microglia did not form bigger agglomerates to attempt phagocytosis of the BC and its variants. One possible reason is the large area and volume of the cages that hindered the cells from wholly engulfing them. Therefore, they wrapped around single beams instead. As for the other cell morphologies identified in the bigger cages, a possible explanation may be the increased points of contact provided by both the 3D geometry of the structure and the micro- and nano-pillars decoration. This hypothesis is supported by the study of Tylek et al. in which human monocyte-derived macrophages were cultured on poly (ε-caprolactone) micro-fibers with varying pore sizes (40–100 µm) and showed increased polarization in the smaller pores [85]. It has to be noted though that the difference in material, stiffness, and cell type must be kept in mind when making such comparisons. In addition, there is some inconsistency in literature regarding the effect of pore sizes on macrophages as it has been shown in other studies that larger pore sizes induce a more polarized morphology of macrophages while smaller ones confine them to a round shape [86,87]. In light of this, further studies focusing on the effect of a softer scaffold with a similar geometry on the phenotype of microglia would be needed.

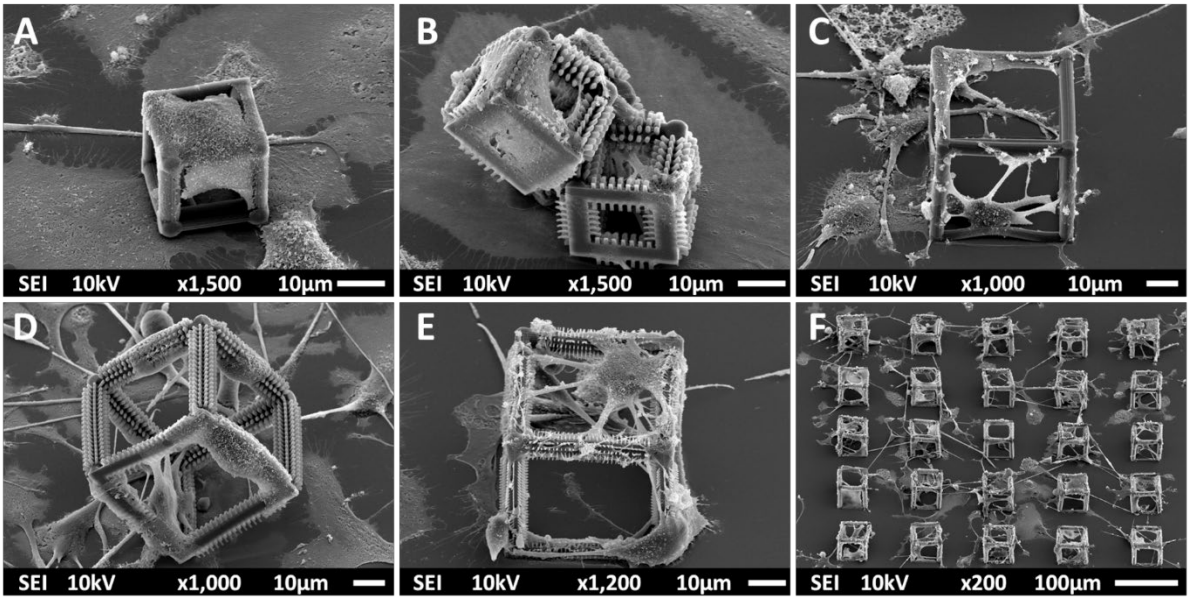

Fig. 2.8. SEM images (taken at a 45° angle) of primary microglia cultured on (A) SC; (B) SC-MP; (C) BC; (D) BC-MP; (E) and (F) BC-NP. An amoeboid-like morphology of microglia was observed when cultured on SC and SC-MP. Cells seemed to attempt to enwrap the cages. In presence of the bigger cages, multiple phenotypes were noticed. Detachment of the cages was observed especially for the smaller ones.

An additional investigation of the interaction of filopodia with the micro- and nano-features of the cages was performed using SEM imaging (Fig. 2.9). The filopodia mostly extend in multiple directions with respect to the hatching lines of the undecorated BC (Fig. 2.9A–C). The most predominant direction is along the hatching lines (Fig. 2.9C). This indicates that these lines act as topographical guidance cues to the filopodia. A possible reason for such a preference in growth direction can be the proximity of the size of hatching lines (hatching distance = 200 nm) to that of filopodia [71]. Another possible reason is the confinement of focal adhesions to these nanometric ridges [88]. Similar results were found in multiple studies such as that of Fujita et al. where filopodia of mesenchymal stem cells showed a preference towards extending along nanometric ridges instead of perpendicular to them [89]. In that study, they also pointed that the formation of longer and more stable focal adhesions in the longitudinal direction could be one of the main reasons why the filopodia chose to grow specifically in that direction. An interesting change was observed in the interaction of microglia and their filopodia with the pillars on the beams of BC-MP (Fig. 2.9D–F). The filopodia on the BC-MP extend in multiple directions bridging distances between pillars and do not strictly follow the hatching lines on the cage especially in regions where there is a high density of micro-pillars (Fig. 2.9E,F).

This can be explained by the fact that the micro-pillars represent a competing guidance cue for the filopodia, specifically, providing an anchor for the movement of the cells. This observation suggests that filopodia, once in contact with the pillars, specifically choose to refrain from interacting with the undecorated surface. When cultured on the BC-NP structure, microglia exhibited an increased interaction with the nanopillars (Fig. 2.9G–I). Once again, in high density regions of pillars, the membranes of the cells stretched mainly over the pillars with little to no interaction with the underlying hatching lines (Fig. 2.9H,I) proving that these pillars indeed represent a mechanical cue involved in the guidance and growth of the cells. What seems to be membrane rupture was noticed however when the cells wrapped around the nanopillars decorating the beams of BC-NP (Fig. 2.9I) which is a known problem that is thought to occur due to the dehydration step performed during the preparation of the samples for SEM imaging [90–92]. These results show that our HMDS protocol was only partially successful in preventing membrane rupture. Further optimization of the dehydration of cells should be carried out in future

studies to completely eliminate this undesirable effect. An alternative explanation of the observation in Figure 2.8I is that these extensions maybe filopodia wrapping around single nano-pillars.

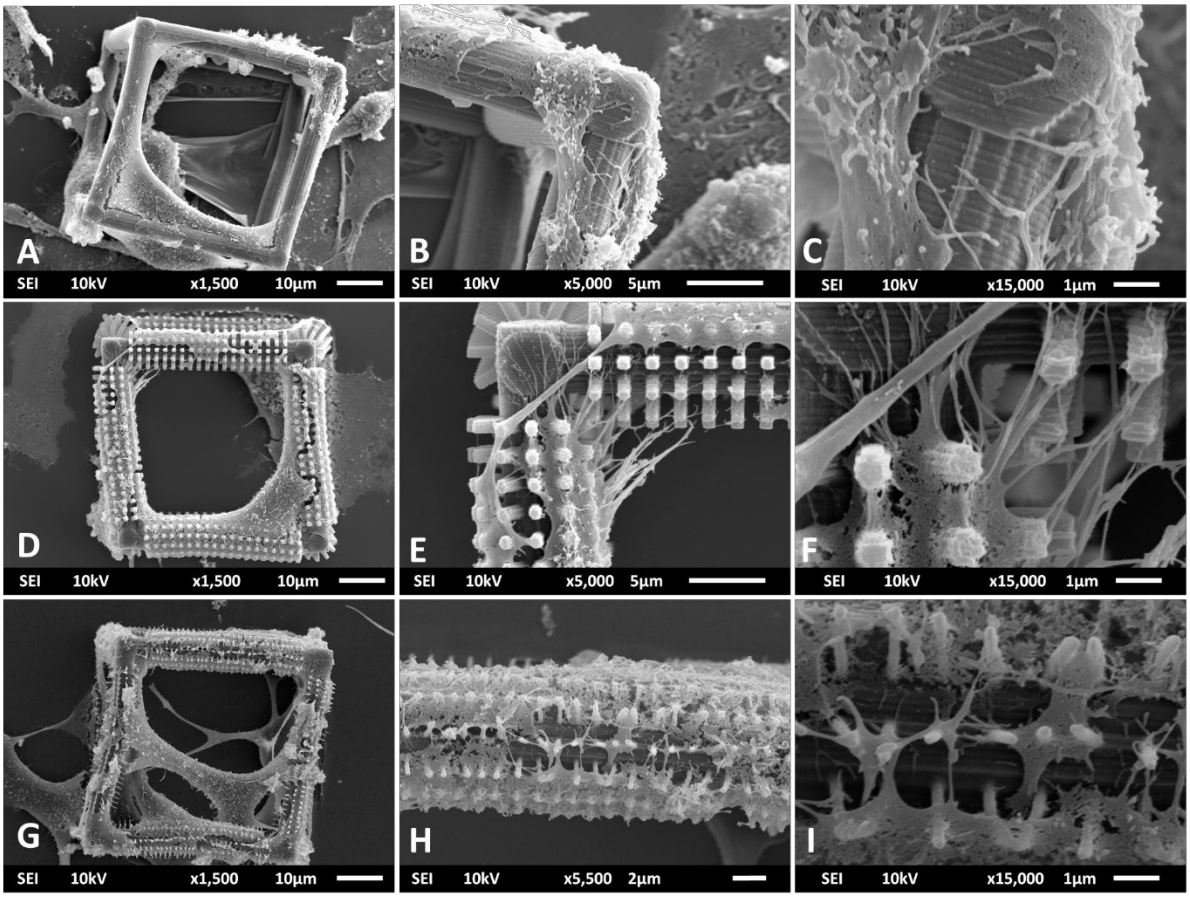

Fig. 2.9. SEM images showing the interaction of primary microglia and their filopodia with the micro- and nanometric features of the BC (A–C), BC-MP (D–F), and BC-NP (G–I). (C) Filopodia guided by the nano-grooves formed by the hatching lines in the BC. (F) Micro-pillars acting as a competing guidance cue to the filopodia. (I) Nano-pillars providing a mechanical cue and a platform of growth for the cells.

The overall degree of occupation of cells within the bigger cages was measured as well using z-stacks of the fluorescence images obtained by confocal microscopy (Fig. 2.10A). It was expressed in terms of occupied volume of cells per cage (Fig. 2.10B) (for each structure type $n_{samples} = 2$, $n_{cages} > 25$, $n_{cells} > 100$). The results show an increase in colonization of the cages when laminin is used as a coating. On average, laminin-coated cages had twice as many cells as compared to uncoated cages. More specifically, the laminin-coated BC had on average 3.5 ± 1.61 × 104 cells/mm3, which is higher than the uncoated BC which had on average 1.92 ± 1.28 × 104 cells/mm3. The laminin coated BC-MP had on average 2.67 ± 1.56 × 104 cells/ mm3 which was also higher than the uncoated BC-MP 1.43 ± 8.52 × 104 cells/mm3. The laminin-coated BC-NP had 3.77 ± 1.39 × 104 cells/mm3 while the uncoated BC-NP had 1.96 ± 1.06 × 104 cells/mm3. This positive effect of laminin coating on the colonization of the cages maybe explained by the added resemblance to the ECM that such a biochemical coating provide since laminin is a major component in the ECM of the CNS [23]. The structures present a large surface area with many micro- and nanometric features, grooves, and crevices consisting of micro- and nano-pillars in addition to hatching lines and slices produced by the 2PP process. We hypothesize that this surface area, acting as a basin, can be the

reason for the accumulation of laminin on these structures, thereby attracting microglia to colonize them. In an attempt to quantify the interaction of microglia with the 3D bigger cages, we investigated which region of the cages were most densely populated (for each structure type $n_{samples}$ = 2, n_{cages} > 25, n_{cells} > 100). The cages were split up into four sections depending on their height, namely 0–15, 15–30, 30–45, and 45–60 µm. The degree of cell colonization is expressed as the percentage of microglia occupying each section of the cages (Fig. 2.10C). A comparison between laminin-coated cages and uncoated cages is presented in the figure as well. It can be clearly seen that the percentage of microglia situated at the bottom of the cages was higher for undecorated cages regardless of the coating with laminin. For pillar-decorated cages, and especially micro-pillar-decorated ones, the distribution of cells throughout the height of the cages was more uniform. Even though this part of the study was performed using cells from only one donor, a clear difference can be seen in the way cells interact with and migrate up the beams of the decorated cages. It appears that providing the cells with anchor points in the form of pillars increases their possible points of contact and hence facilitates migrating towards the upper regions of the cages. It can also be argued that since the micro-pillars are larger and less fragile than the nano-pillars, they would provide more stable anchor points for the cells. These results are in line with those of Leclech et al. where neurons where shown to migrate faster in an *in vitro* environment of micro-pillars [93]. Bugnicourt et al. also showed how neurites of murine hippocampal neurons featured faster growth when cultured on nano-pillars [94].

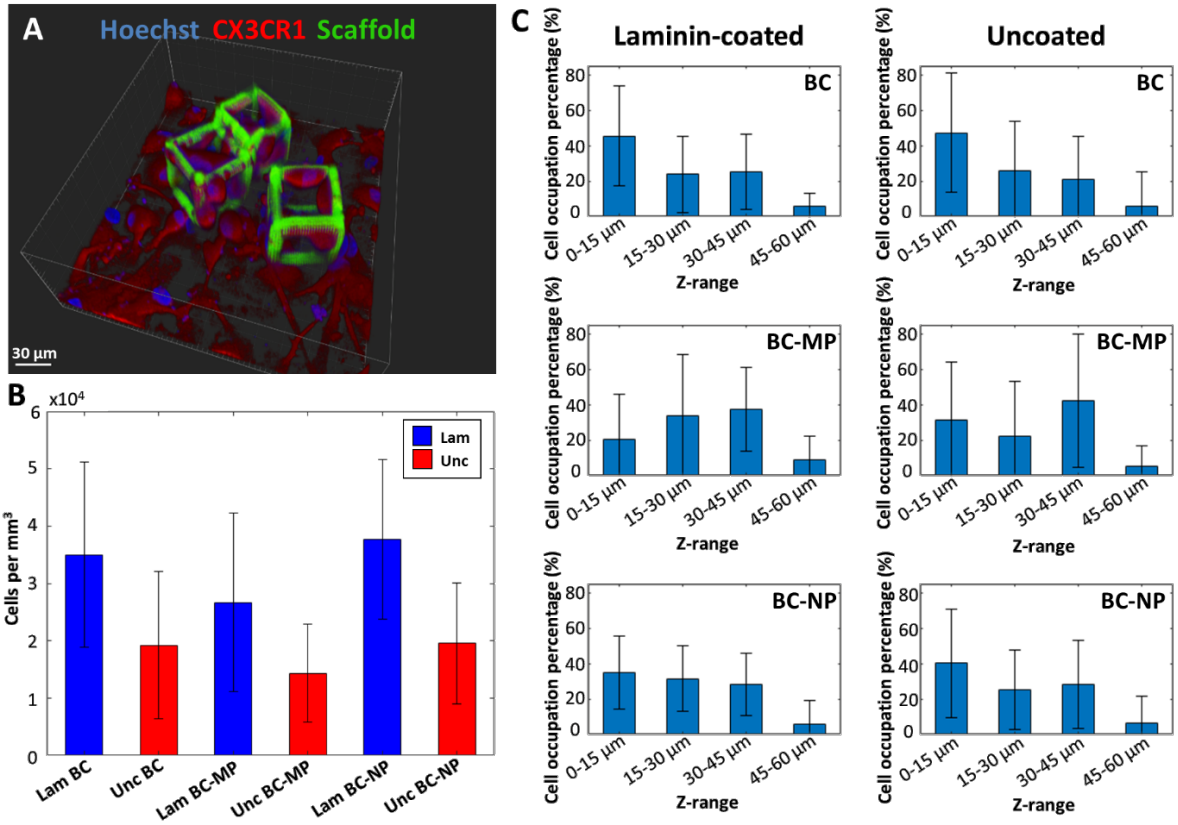

Fig. 2.10. (A) 3D reconstruction of a fluorescence z-stack obtained by confocal microscopy of BC-MP cages with microglia. Blue is Hoechst 33342 staining (nucleus) and red is CX3CR1 (cell membrane). (B) Volumetric occupancy of microglia in laminin-coated (blue) and uncoated (red) cages. Laminin coating resulted in doubling the occupancy of cages as compared to uncoated ones for decorated and undecorated cages alike. (C) Microglia distribution along the height of the BC, BCMP, and BC-NP for laminin-coated and uncoated samples. Microglia were shown to colonize the mid and top sections of decorated structures compared to the undecorated ones (for each structure type $n_{samples}$ = 2, n_{cages} > 25, n_{cells} > 100).

2.4. Conclusions

In the current study, we proposed the fabrication of 2.5D micro- and nano-pillars and 3D micro-cages to study the effects of engineered microenvironments on the phenotype of primary microglia derived from brain tissue of adult primates (rhesus macaques). The arrays of pillars were manufactured using 2PP technology with a stiff thermosetting polymer. They have the advantage of being easily fabricated due to the high stiffness of the material while providing a surface with a low effective shear modulus that better resembles the stiffness of brain tissue. In addition, they provide a discrete type of topography that is thought to also mimic that of the ECM and hold dimensions in the range of filopodia processes.

For the first time, we report how primate-derived primary microglia cultured on nano-pillar arrays, show on average an increase in the numbers of cells characterized by a ramified resting phenotype as compared to cells cultured on flat stiff substrates. This ramified morphology is associated with a homeostatic phenotype. However, further gene or protein expression analysis should be carried out to confirm the homeostatic function of these cells. Regarding morphological features, it is important to note that the percentage of the flat amoeboid phenotype also simultaneously decreased in presence of micro- and nanopillars. Moreover, we fabricated 3D micro-cages, decorated with micro- or nano-pillars, and employed them as scaffolds in order to emulate the three-dimensional spatial configuration of the native environment of microglia cells. Smaller cages were shown to be enwrapped by microglia, while cages of larger size than the average size of the cell body promoted the expression of multiple microglia phenotypes. Interestingly, cell colonization was affected by both laminin coating, which increased cellular occupation of the cages, and pillar decoration of the beams of the cages. Cells cultured on micro-pillar decorated cages especially showed a higher affinity to occupy the mid and upper sections of the cages suggesting a strong interaction between the microglia filopodia and the pillars. Future studies will be conducted to disentangle the effect of topography from that of substrate stiffness on the morphology and phenotypic expression of microglia. Additionally, it will be important to use our approach in presence of primary microglia from different species and compare the obtained results with the ones reported here. Moreover, as we pointed out, the problem of autofluorescence of the microstructures represented an obstacle in terms of characterization via confocal microscopy due to the strong background signal. Systematic solutions for this obstacle specifically are elaborated in the study presented in **chapter 3**. In conclusion, the proposed approach paves the way for a series of investigations, which can include co-culture studies involving microglia and other neuronal lineages in both healthy and diseased states.

In terms of future perspectives, engineered microglia cell culture models can help to overcome the limitations of conventional 2D plastic/glass culture ware approaches. These models have a pivotal role in better understanding fundamental neuromechanobiology processes but also for the development of more physiologically relevant *in vitro* drug screening platforms, which can be employed to test therapeutic targets when dealing with neurodegenerative diseases. By having culture models which better resemble the morphology and phenotype of cells in living tissues, it is theoretically possible to lower the amount of *in vivo* animal experiments and the time required to discover new drugs as well as related costs. The developed engineered microglia models are still very minimalistic, however, as they are usually composed of only one cell type while the brain niche features a highly heterogeneous population of cells (including neurons, brain endothelial cells, and glial cells). It will therefore be of paramount importance to assess the behavior of microglia cultured in the presence of other central nervous system cell types within such engineered microenvironments, especially for the development of *in vitro* disease models such as Alzheimer's disease and Parkinson's disease models. A second important point is to observe the behavior of microglia within even more complex tissue-like structures such as neural spheroids and organoids but in a "biomechanically controlled" configuration. Indeed, one of the main limitations of these widely employed 3D cell assemblies is that they rapidly develop a necrotic core which is detrimental for long-term studies. In the near future, we aim to merge scaffold-free and scaffold-based strategies in order to control the growth of pre-formed mini-neural-organoids seeded within meso-scale (mm or cm-sized) engineered porous microenvironments and facilitate the diffusion of nutrients to prevent early formation of necrotic cores. Another aspect, which needs to

be further developed, is the compatibility between the current scaffolds technology and some relevant characterization techniques employed in cell biology, and particularly microglia, such as gene expression analysis, to confirm the homeostatic phenotype of these cells. To reach this goal, one solution is to integrate bio-inert coatings on the flat substrate (onto which the engineered structures are manufactured) enabling the cells to adhere only to the developed architectures and allowing therefore reliable functional and gene expression analyses (which would otherwise be polluted by inputs coming from the cells adhering to the flat substrate). The technical challenge, in this case, is to ensure that the bio-inert coating does not hinder the adhesion of the engineered structures to the substrate as this would lead to delamination issues. As soon as such needs can be addressed, it is foreseeable that these engineered microenvironments will become an indispensable actor in the neuroscientific landscape and that unexplored neuromechanobiological mechanisms will be unveiled, which will be beneficial for both diagnostic and therapeutic applications [34].

3

Suppression of auto-fluorescence from high-resolution 3D polymeric architectures fabricated via two-photon polymerization for cell biology applications

2PP has provided the field of cell biology with the opportunity to fabricate precisely designed microscaffolds for a wide range of studies, from mechanobiology to in vitro disease modelling. However, a multitude of commercial and in-house developed photosensitive materials employed in 2PP suffers from high auto-fluorescence in multiple regions of the spectrum. In the context of in vitro cell biological studies, this is a major problem since one of the main methods of characterization is fluorescence microscopy of immunostained cells. This undesired auto-fluorescence of microscaffolds affects the efficiency of such an analysis as it often overlaps with fluorescent signals of stained cells rendering them indistinguishable from the scaffolds. Here, we propose two effective solutions to suppress this auto-fluorescence and compare them to determine the superiority of one over the other: photo-bleaching with a powerful UV point source and auto-fluorescence quenching via Sudan Black B (SBB). The materials used in this study were all commercially available, namely IPL, IP-Dip, IP-S, and IP-PDMS. Bleaching was shown to be 61.7–92.5% effective in reducing auto-fluorescence depending on the material. On the other hand, SBB was shown to be 33–95.4% effective. The worst result in presence of SBB (33%) was in combination with IP-PDMS since the adsorption of the material on IP-PDMS was not sufficient to fully quench the auto-fluorescence. However, auto-fluorescence reduction was significantly enhanced when activating the IP-PDMS structures with oxygen plasma for 30 s. Moreover, we performed a cell culture assay using a human neuroblastoma cell line (SH-SY5Y) to prove the effectiveness of both methods in immunofluorescence characterization. SBB presented a lower performance in the study especially in presence of 2PP-fabricated microchannels and microcages, within which the differentiated SH-SY5Y cells migrated and extended their axon-like processes, since the SBB obstructed the fluorescence of the stained cells. Therefore, we concluded that photo-bleaching is the optimal way of auto-fluorescence suppression. In summary, this study provides a systematic comparison to answer one of the most pressing issues in the field of 2PP applied to cell biology and paves the way to a more efficient immunofluorescence characterization of cells cultured within engineered in vitro microenvironments.

The contents of this chapter have been published in:

- A. Sharaf, J.P. Frimat, G.J. Kremers, A. Accardo, Suppression of auto-fluorescence from high-resolution 3D polymeric architectures fabricated via two-photon polymerization for cell biology applications, Micro and Nano Engineering 19 (2023) 100188.

3.1. Introduction

As laid out in the previous chapters, 2PP is a true asset as a microfabrication technique in the field of neuromechanobiology. There is a large degree of freedom of design of microstructures fabricated for *in vitro* studies using this technique. To perform such *in vitro* studies, one of the main techniques of characterization is fluorescence microscopy such as epifluorescence, confocal, two-photon, light-sheet or super-resolution microscopy. In order for this technique to be most efficient, there has to be minimal fluorescent background noise from any structures the cells are cultured on. In other words, the structures need to be non-auto-fluorescent. Unfortunately, auto-fluorescence is an intrinsic feature of multiple photoresins used in 2PP. This hinders the full capacity of analysis that can be carried out when using fluorescence microscopy since there is an area of the emission spectrum that is blocked by the auto-fluorescence of the fabricated scaffolds. Strong emission of the structures renders the visualization and therefore the analysis of stained cells challenging. This becomes especially a problem when working with 3D complex architectures since their large volumes lead to strong fluorescence emission, thereby shadowing the signal coming from stained cells [95,96]. To mitigate this problem, multiple solutions have been devised by different research groups. These solutions can be divided into pre-processing or post-processing ones. An effective pre-processing solution consists of eliminating the auto-fluorescence of a photoresin before fabricating the structure (i.e.: before exposing it to the NIR laser). Since, usually, the auto-fluorescent component of a photoresin is the photoinitiator, this is achieved by substituting the photoinitiator with a non-auto-fluorescent one [97] or one with very weak auto-fluorescence [15]. This method can be very effective in eliminating the majority of auto-fluorescence, however it has the disadvantage of being an ad-hoc solution which requires a lot of trial and error for each monomer solution. Post-processing solutions, on the other hand, come into effect after the fabrication of the structure. The two major methods within this category are photo-bleaching and auto-fluorescence quenching. Photo-bleaching takes place by exposing the structures to ultraviolet (UV) light for an extended amount of time [59] while quenching is achieved through coating the structures with a fluorescence-quenching material that absorbs emitted photons from the structures, such as Sudan Black B (SBB), one of the most commonly used fluorescence quenchers [96–98]. Even though there have been examples in literature of successfully using such solutions of post-processing to eliminate the auto-fluorescence of 2PP-fabricated structures, there have been no systematic studies on the effect of each of these solutions compared to the other.

In the current study, we present a comparison of bleaching and quenching of the auto-fluorescence of multiple commercial photoresins (IP-L, IP-Dip, IP-S, and IP-PDMS) widely used in 2PP. In order to achieve this purpose in the most efficient manner, square pedestals designs were chosen due to the low fabrication time and because they enabled the most uniform way of testing the auto-fluorescence and the mechanical strength of the selected materials. The structures are characterized by scanning electron microscopy (SEM) and confocal microscopy. In addition, characterization of the mechanical strength of the structures after bleaching is also reported. Finally, as a proof of principle, human neuroblastoma cells (SH-SY5Y cell line) are cultured and stained on multiple 3D microscaffolds, fabricated by 2PP and treated with the aforementioned methods, to compare their efficiency as solutions to the problem of auto-fluorescence.

3.2. Materials and Methods

3.2.1. Materials

Four proprietary acrylate based photoresins of Nanoscribe GmbH & Co. KG were used, namely IP-L, IP-Dip, IP-PDMS, and IP-S. Fused silica and indium tin oxide (ITO)-coated soda lime substrates were purchased from Nanoscribe GmbH & Co. KG as well and used as substrates for 2PP fabrication of the polymeric microstructures. SBB was purchased from Alfa Aesar. All other materials were purchased from Sigma-Aldrich.

3.2.2. Design of microstructures

Concerning auto-fluorescence and mechanical characterization measurements, pedestals of dimensions 30x30x20 μm^3 (lxwxh) were designed. The only exception was the mechanical characterization of IP-PDMS structures. For these measurements, pedestals of dimensions 150x150x20 μm^3 (lxwxh) were designed. For cell culture studies, rectangular microchannels (inner channel dimensions were wxh = 30x30 μm^2 and channel length = 100 µm), and 3D microcages with circular pores of 30 µm diameter and total volume of 120x120x120 μm^3 were designed (see Fig. B1 in Appendix B). For IP-L, IP-Dip, and IP-S, the top wall thickness of the microchannels was 3 µm and the one of the intermediate wall was 4 µm while for IP-PDMS these thicknesses had to be increased to 10 µm and 18 µm, respectively, to increase structural stability due to increased shrinkage of the material.

3.2.3. Fabrication of microstructures

All substrates used for printing were first cleaned with acetone and IPA before any treatment. Microstructures were printed using the Photonic Professional GT+ (PPGT+) 2PP printer, which is a setup of Nanoscribe GmbH & Co. KG. The printer is equipped with a pulsed femtosecond fibre laser with a pulse duration of roughly 80 fs, a repetition rate of 80 MHz, a wavelength of 780 nm, and a maximum power of 50 mW. IP-Dip structures were printed on fused silica substrates (lxwxh = 25x25x0.7 mm) via a 63x Zeiss objective with NA of 1.4. IP-L, IP-PDMS, and IP-S were printed on soda lime substrates coated with ITO (lxwxh = 25x25x0.7 mm) via a 25x Zeiss objective (NA=0.8). Printing of all structures took place in DiLL configuration (where the lens is immersed into the photoresin) and Galvo mode (where movement of the laser in the x-y dimensions is performed with the assistance of a set of galvanometric mirrors). Structures of all 4 materials used for cell culture were printed on silanized substrates to improve their adhesion to the substrates especially during the cell culture period since dipping the samples into cell culture medium may result in the delamination of the structures from the substrates. IP-Dip and IP-PDMS pedestals were also printed on silanized substrates for enhanced adhesion. For silanization, the cleaned substrates were activated in a Diener Femto oxygen plasma cleaner at 100 W for 5 min with a flowrate of 5 cm^3/min and a pressure of ~0.2 mbar and then submerged in a 3-(Trimethoxysilyl)propyl methacrylate (MAPTMS) solution (2% v/v in ethanol) for 1 h. The substrates were then rinsed with acetone, blow dried with an air gun, and stored in a petri dish wrapped with parafilm away from light. All silanized substrates were used within one month after the silanization process. Directly before printing, the silanized substrates were cleaned with an acetone-wetted lint free wipe and blow dried with an air gun.
All structures were designed in SOLIDWORKS (Dassault Systemes), saved as “stl” files, and then imported into Describe (the proprietary software of Nanoscribe GmbH & Co. KG). In Describe, the structures were cut into vertical slices and horizontal hatching lines since 2PP printing is achieved in a line-by-line fashion (see Table B1 in Appendix B for printing parameters of all structures including laser intensities [63]). After printing, IP-L, IP-Dip, and IP-S structures were developed in PGMEA for 1 h horizontally in a glass petri dish. This was followed by 2 min of gentle stirring by hand, before submerging the samples in IPA for 5 min followed by gentle stirring by hand for 2 min. Finally, the samples were blow dried with an air gun and stored in the dark until further use. IP-PDMS structures were developed in IPA for 30 min horizontally in a glass petri dish followed by gentle stirring by hand for 2 min. Afterwards, they were moved into a fresh IPA bath for 1 min, followed by gentle stirring by hand for 2 min. The samples were then left to air dry for a few minutes and stored in the dark until further use.

3.2.4. Bleaching treatment

Structures were bleached by using an upright UV point source (Bluepoint 4 Ecocure Honle UV technology) at a distance of 1 cm from the sample for 2 h at 100% power. The diameter of the point source was 8 mm and had a power of 10,000 mW/cm^2 at the emitting surface. The spectrum of emission ranged from 300 to 600 nm with a maximum intensity at ~375 nm. During the exposure, the substrates were covered within an aluminium foil enclosure since the reflective properties of aluminium maximize the efficiency of UV exposure.

3.2.5. SBB treatment

Treatment for auto-fluorescence quenching was performed by dipping the samples in a 0.3% w/v solution of the fluorescence quencher SBB in 70% ethanol for 2 h [97,98]. Afterwards, the samples were rinsed multiple times with ethanol before drying with an air gun.
For IP-PDMS, an additional step of plasma pre-treatment was added to enhance the adhesion of SBB to the material. The structures were exposed to oxygen plasma at 100 W for 30 s with a flowrate of 5 cm^3/min and a pressure of ~0.2 mbar in a Diener Femto plasma cleaner. They were then directly dipped in SBB solution as already mentioned.

3.2.6. SEM characterization

To prepare the samples for SEM characterization, they were first sputter coated with a nanometric layer of gold using a JEOL JFC-1300 auto-fine sputter coater. A JEOL JSM-6010LA SEM (JEOL (Europe) B.V.) in high-vacuum was employed for morphological characterization.

3.2.7. Fluorescence measurement

Fluorescence emission spectra of the pedestals was measured by a Leica SP5 confocal microscope (Mannheim, Germany). The excitation wavelength was 405 nm. The top layer of each structure was imaged with a Leica Microsystems HC APO L 20.0x/1.00 W lens (NA=1.0), in water dipping mode. The samples were submerged in deionized (DI) water while imaging. The images were taken with a scanning speed of 700 Hz at a resolution of 1024x1024 pixels and zoom 5x, resulting in a pixel size of 0.144x0.144 µm. The power of the laser was kept at 10% and the gain at 638 V for all measurements. The spectral range of measurement spanned from 410 to 750 nm of emission wavelength with 9.19 nm increments using a bandwidth of 10 nm. For UV-bleached samples, measurements were performed 1, 4, and 6 days after bleaching on 3 different sets of pedestals to study the effect of time on bleaching. The results of these measurements with respect to time are shown in Appendix B, while the results shown in the main text are the ones acquired 1 day after bleaching.
For each sample of each material, whether untreated, photo-bleached or SBB-treated, the fluorescence of 5 pedestals was measured (number of samples (pedestals) = n = 5). To measure the fluorescence of a pedestal, Fiji software [65] was used. First, a square of 250x250 pixels was drawn around each pedestal. The “Mean gray” value was specified then as a required measurement in the “Set Measurements” window. Via the command “Multi measure”, the “Mean gray” value of each pedestal was measured at each wavelength range of emission. In addition, the background signal was evaluated by performing the same procedure, but with a 125x125 pixels drawn at a random region away from the sample. A MATLAB (MathWorks®) code was developed to analyse the data. After importing the results, the background signal was subtracted from all signals and the average of the “Mean gray” values for all 5 pedestals was calculated and then plotted against the emission wavelengths. The maximum values of auto-fluorescence were then calculated along with the standard deviation.

3.2.8. Mechanical characterization

To measure the Young’s moduli of IP-L, IP-Dip, and IP-S before and after UV-bleaching, a FEMTOTOOLS nanomechanical testing system FT-NMT03 was employed to perform compression tests. A Si probe with a 50x50 μm^2 flat punch head with a force range of 200,000 ± 0.5 µN was used for all measurements. Again, the pedestals were used for these measurements. The stiffness of UV-bleached samples were measured within 24 h from bleaching. A compression of roughly 2 µm was chosen for all pedestals. The speed of compression was 0.25 µm/s for all samples. The stiffness of 5 pedestals per material were measured before and after UV bleaching. To obtain the stiffness of each pedestal from the generated Force-Displacement curve, the slope of only the first linear part of the loading curve was evaluated using an in-house developed MATLAB code with the assistance of the polyfit

function. The average stiffness was then calculated for each condition and the Young's modulus was extracted by using the equation $E = kL/A$ where E is the Young's modulus (Pa), k the stiffness (N/m), L the height of the pedestal (m), and A the area of the pedestal (m^2). The standard deviation was then calculated and the data plotted. All data analysis was performed by using the MATLAB code.

The Young's modulus of IP-PDMS was measured by nanoindentation since the material was too soft to be compressed with a FEMTOTOOLS Si probe. A Piuma Nanoindenter (Optics11 Life) was used to perform the nanoindentation. A probe of 42.7 N/m stiffness and a tip radius of 24.5 μm was utilised. The depth of indentation was roughly 1 μm. As aforementioned, the IP-PDMS pedestals fabricated for this specific measurement were of 150x150x20 μm^3 (lxwxh) dimensions since the smaller pedestals used for the other 3 materials were too small for the dimensions of the probe used for nanoindentation. UV-bleached samples were measured within 24 h from bleaching. The Young's moduli of 5 pedestals of the material before and after UV bleaching were tested. The Piuma Nanoindeter modelling tool employed the Johnson-Kendall-Roberts (JKR) model for adhesive materials in order to evaluate the Young's moduli of the samples. The results were then imported into a MATLAB code to calculate the Young's moduli average and standard deviation and plot the data.

3.2.9. Cell culture

SH-SY5Y human neuroblastoma cells (Sigma-Aldrich, 94030304) were cultured in Dulbecco's Modified Eagle's Medium (DMEM)/F-12 media (1:1) (Thermo Fisher Scientific, 10565018) supplemented with 10% fetal bovine serum (FBS, Sigma-Aldrich F7524) and 1% penicillin/streptomycin and grown in an incubator at 37 °C, 5% CO_2. When cell confluency was reached, trypsin (×1) was used to harvest the cells and centrifuged at 900 rpm for 5 min. The microstructures (microchannels and microcages) were enclosed in a well of 1x1 cm^2 area made of PDMS and placed on the substrate. A 100 μL droplet containing 50,000 cells was seeded on all the structures within the PDMS wells placed on all samples. Following the seeding, the cells were exposed to 10 μM retinoic acid (Sigma-Aldrich, R2625) for 3 days in DMEM/F-12 media to differentiate the cells into immature neuron-like cells. Following 3 days of differentiation, cells were fixed in 4% paraformaldehyde solution for 25 min prior to staining.

3.2.10. Immunofluorescence Staining and confocal imaging

Following fixation in 4% paraformaldehyde for 25 min, cells were permeabilized for 10 min at room temperature (RT) using 0.1% Triton X-100 in Phosphate Buffer Saline solution (PBS). Subsequently, cells were blocked for 30 min at RT using 1% bovine serum albumin (BSA) in PBS. Primary antibodies against paxillin (Sigma-Aldrich, SAB4502553) were diluted 1:200 in 1% BSA and incubated for 1.5 h at RT to visualize focal adhesions. Secondary antibody (Sigma-Aldrich, SAB3700937-Anti-Rabbit IgG (H+L)-Texas Red® antibody) was then diluted 1:500 in 1% BSA and incubated at RT for 2 h. Phalloidin staining for F-actin in the cytoskeleton was used (Thermo Fisher Scientific, ActinGreen 488 ReadyProbes, R37110). Cell nuclei were stained using Hoechst 33342 (Thermo Fisher Scientific, NucBlue Live ReadyProbes, R37605). For both actin and Hoechst, 2 drops per mL in PBS were added and incubated for 25 min. Samples were washed 3 times with PBS afterwards and stored in PBS in the dark until imaging.

Samples were imaged using a Leica SP5 confocal microscope with a Leica Microsystems HC APO L 20.0x/1.00 W lens (NA=1.0) in water dipping mode. The samples were kept in PBS while imaging. Laser sources of wavelengths 405, 488, and 561 were employed, all at 10% power. The wavelength ranges of the emission filters were 410-475 nm, 495-550 nm, and 570-750 nm for the 405, 488, and 561 nm excitation lines, respectively. Acquisition was performed in parallel for all three channels. The gain was kept at 638 V for all images and the zoom at 3.5x. These imaging parameters were kept constant to facilitate the comparison between untreated and treated samples. Z-stacks were obtained at a resolution of 1024x1024 pixels, a scanning speed of 700 Hz, and a step size of 0.5 μm resulting in a pixel size of 0.206x0.206 μm. All z-stacks were processed using Fiji [65] or Imaris Viewer software (Oxford Instruments).

3.3. Results and Discussion

3.3.1. Microstructures fabrication

Two-photon polymerized pedestals were fabricated using 4 different commercial acrylate resins. Optical microscope images of the fabricated pedestals are shown in Fig. 3.1. As aforementioned, the 4 materials are IP-L (Fig. 3.1a), IP-Dip (Fig. 3.1b), IP-S (Fig. 3.1c) and IP-PDMS (Fig. 3.1d). Minimal shrinkage was observed for the pedestals. These structures were used for fluorescence and mechanical characterization. Fig. 3.2 shows representative SEM images of the 3D structures fabricated for cell culture studies. The images shown are only of IP-L (Fig. 3.2a,b) and IP-PDMS (Fig. 3.2c,d). These structures included rectangular microchannels and 3D free standing microcages made of periodic circular pores. Both structures posed no problems when fabricated with IP-L, IP-Dip, or IP-S even with a 3 µm thick wall of the channels. When employing IP-PDMS, however, this wall thickness turned out to be too thin to withstand the significant shrinkage of this specific resin. Therefore, the top wall thickness of the channels had to be increased to 10 µm and the intermediate wall thickness to 18 µm to guarantee a high enough structural integrity. Additionally, the 3D microcages shrunk substantially and showed some minor deformations compared to those made of IP-L, IP-Dip, or IP-S. No changes to the design of the microcages were necessary however.

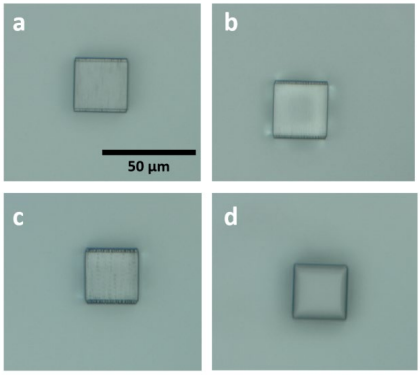

Fig. 3.1. Optical microscopy images of (a) IP-L pedestal, (b) IP-Dip pedestal, (c) IP-S pedestal, and (d) IP-PDMS pedestal.

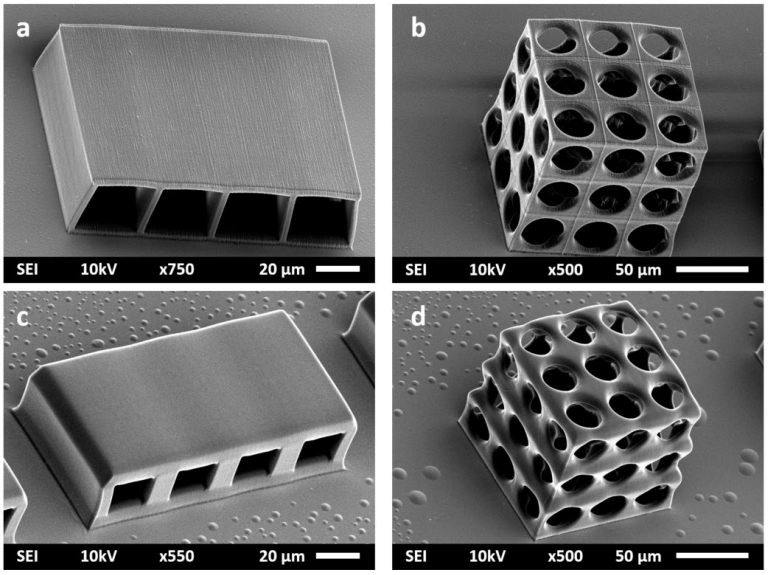

Fig. 3.2. Representative SEM images of (a) IP-L rectangular microchannels, (b) IP-L microcage, (c) IP-PDMS rectangular microchannels, and (d) IP-PDMS microcages.

3.3.2. Auto-fluorescence suppression

In order to suppress the auto-fluorescence of all IP materials, the effect of bleaching versus coating with SBB (an auto-fluorescence quencher) was assessed. All materials were bleached by a UV point source for 2 hours or treated by submerging in a solution of SBB for 2 hours. The UV point source had an emission range of 300-600 nm as mentioned previously (section 3.2.4). This range of emission guaranteed the excitation of the photoinitiators within the photoresins under investigation since their peak absorption wavelength is at roughly 390 nm. Moreover, the specific choice of the UV point source was dictated by the fact that one of the main points of the study is to provide an easy-to-use, efficient and inexpensive method for suppressing the auto-fluorescence of 2PP-fabricated microstructures.

Fig. 3.3 shows representative optical microscope images of IP-L (Fig. 3.3a-d) and IP-PDMS (Fig. 3.3e-j) printed structures before and after treatment with SBB. The morphology of bleached structures did not show a significant change from the untreated ones (data not shown). After treatment with SBB, a noticeable black tint of the IP-L structures can be observed indicating the deposition of SBB on top of them (Fig. 3.3b,d). These results were similar to those of IP-Dip and IP-S structures (see Fig. B2 in Appendix B). The case for IP-PDMS was not the same since SBB adhered very poorly to these structures upon submerging them in the solution without any prior treatment

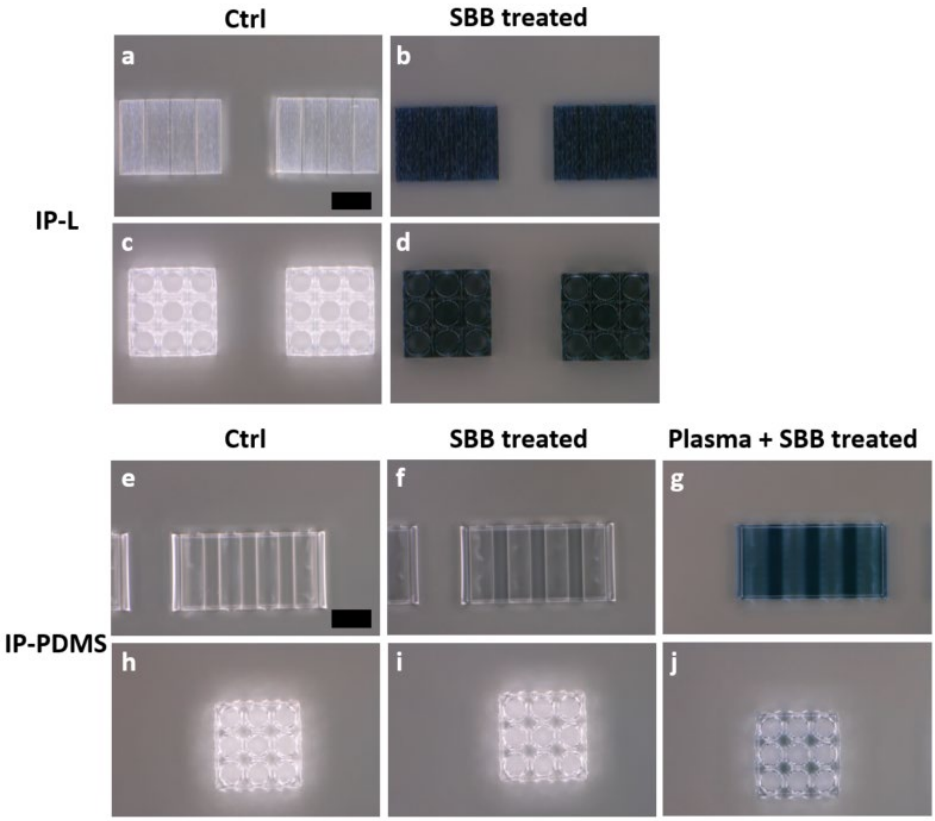

Fig. 3.3. Optical microscope images of (a,c) untreated IP-L fabricated structures (i.e. controls), (b,d) SBB treated IP-L structures, (e,h) Untreated IP-PDMS fabricated structures, (f,i) SBB treated IP-PDMS fabricated structures, (g,j) IP-PDMS structures pre-treated with oxygen plasma for 30 s and then treated with SBB. Scale bar = 50 μm.

(Fig. 3.3f,i). A possible reason for this maybe the fact that IP-PDMS structures are more hydrophobic than the other materials leading to the formation of a meniscus of the solvent at the surface of the structures thereby hindering the SBB from coming into contact with the IP-PDMS. Another reason could be a significant inertness

and/or smoothness of the surfaces of structures fabricated with IP-PDMS compared to the other resins. To test the validity of these hypotheses, we treated the IP-PDMS structures with oxygen plasma for 30 s prior to submerging them in the SBB solution. The results showed a significant enhancement in the deposition and adherence of SBB to the IP-PDMS structures indicated by the darker colour observed in the treated structures (Fig. 3.3g,j). Hence, we conclude that increasing the hydrophilicity, reactivity, and surface roughness of the IP-PDMS structures can lead to better interaction with SBB. It should be noted that SEM images of IP-L and IP-PDMS structures were taken before and after SBB treatment (see Fig. B3 in Appendix B). However, it was impossible to recognize any morphological difference between the treated and untreated samples.

The effect of both treatment methods on the auto-fluorescence of all 4 materials is shown in Fig. 3.4. The structures used for the comparison shown in Fig. 3.4 were pedestals (see the Materials and Methods section for more details). For each configuration (i.e.: control, bleached, SBB treated, and plasma+SBB treated), the emission spectra of 5 pedestals were measured (n=5). All results are shown as relative auto-fluorescence intensity (I) with a 100% denoting the highest signal value among all configurations for one specific material. A comparison between the auto-fluorescence of all materials over a wavelength spectrum of 410 to 750 nm clearly showed that IP-Dip is the most auto-fluorescent among all four materials (see Fig. B4 in Appendix B). The wavelength range at which the signal is maximal for all materials was 465-475 nm. In general, it can be concluded that all materials are highly fluorescent in the blue (400-500 nm) and green (500-600 nm) channels especially, while the fluorescence tapers off towards the red region of the spectrum (600-800 nm). The difference in signal intensity between IP-Dip and other materials may be attributed to the type of photoinitiators used in combination with the different printing parameters employed for each material. Fig. 3.4a indicates the effect of bleaching and SBB treatment on IP-L structures. Both treatments turned out to be very effective in eliminating fluorescence, but the SBB treatment was slightly more effective.

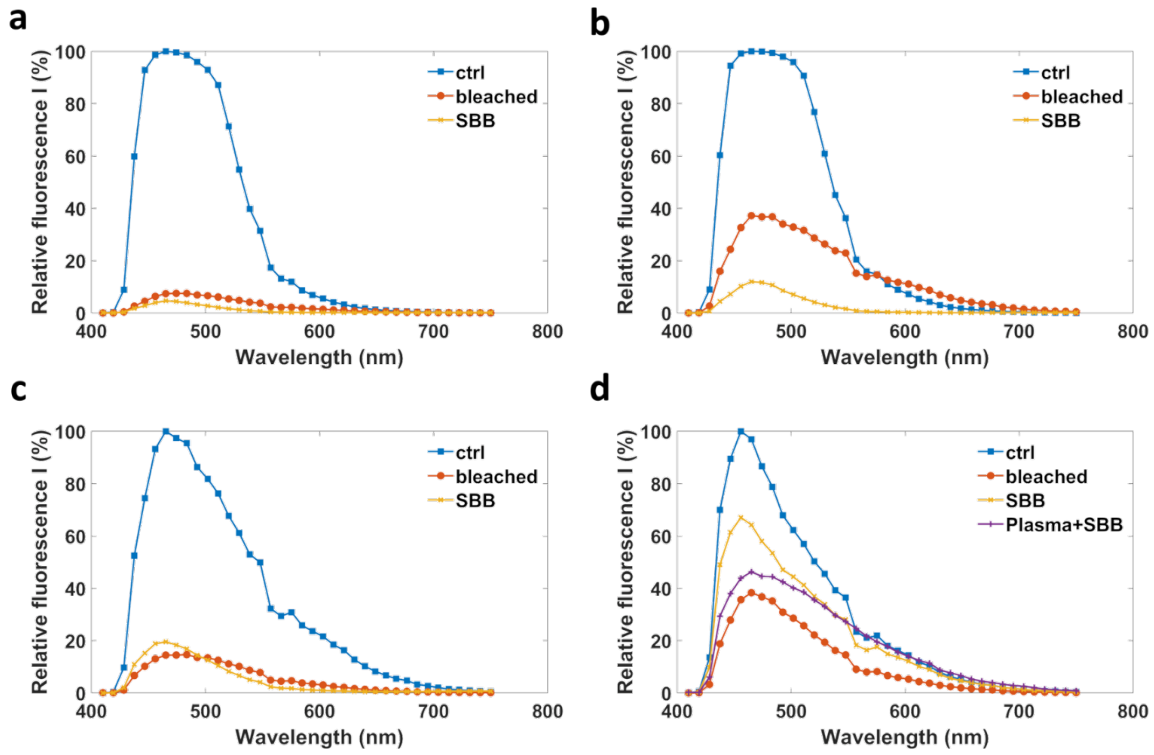

Fig. 3.4. Relative auto-fluorescence intensity (I) of treated and untreated structures made of respectively (a) IP-L, (b) IP-Dip, (c) IP-S, and (d) IP-PDMS. For each condition n=5 pedestals.

Bleaching decreased the maximum fluorescence intensity by 92.5% ± 0.5 while SBB decreased it by 95.4% ± 0.7. For IP-Dip, the reduction in maximum fluorescence with bleaching turned out to be 62.8% ± 10.2 while with SBB treatment it was 88% ± 4.2 (Fig. 3.4b). An interesting observation, in the data reported in Fig. 3.4b is that the bleached sample seems to have a slightly higher auto-fluorescence than the control in the spectral region of 575-750 nm. A similar phenomenon, known as photoconversion, is an invaluable tool in the fields of single-molecule super resolution imaging and dynamic imaging. This mechanism is observed for multiple fluorescent proteins (FPs) such as mKate (which is converted from red to green fluorescence) [99,100] and Dendra2 (which is converted from green to red fluorescence) [101]. In the context of our investigation, we hypothesize that the increase in fluorescence in the red region of the spectrum for IP-Dip may indicate the creation of new fluorescent species as a result of photo-bleaching. This hypothesis is supported by the fact that the auto-fluorescent component of IP-Dip is the photoinitiator. Therefore, bleaching may be cleaving the molecules of the photoinitiator and creating other molecules with different conformations that results in their increased fluorescence in the red part of the spectrum while simultaneously decreasing their fluorescence in the blue-green region of the spectrum [101]. Although we cannot ultimately conclude if our observations are directly correlated to the photoconversion phenomenon, to the best of our knowledge, this is the first time that this behaviour is reported for a photosensitive resin.

As for IP-S, bleaching was 85.3% ± 2.1 effective while SBB showed a comparable result of 80.5% ± 2.6 (Fig. 3.4c). For IP-PDMS on the other hand, bleaching was 61.7% ± 2.3 effective while SBB was only 33% ± 1.5 effective (Fig. 3.4d). The reason for such a small effect of SBB may be attributed to the poor adhesion of the material on the surface of IP-PDMS structures. Upon examining structures that were pre-treated with plasma, the efficiency of SBB increased to 53.7% ± 10.4 confirming the improved adhesion of SBB to the structures. These results show on average that the two solutions are comparable for all four materials. Fig. 3.5 shows representative confocal microscopy images of pedestals of all materials with and without the mentioned treatments. All images were taken at an emission wavelength range of 465-475 nm which corresponds to the maximum intensity of auto-fluorescence signal for all materials. The images clearly show the reduction in auto-fluorescence upon employing UV-bleaching or SBB treatment.

In addition to this investigation, we conducted a study to determine the effect of aging after bleaching the auto-fluorescence of the materials. It has been shown for some FPs, such as Cyan fluorescent proteins, that regaining fluorescence is possible after bleaching if they are kept in a dark environment for a short amount of time [102]. For this reason, we assessed the auto-fluorescence signal after 1, 4, and 6 days of UV-bleaching. Different samples were used for each day. The results showed no significant change in the auto-fluorescence signal with respect to time (see Fig. B5 in Appendix B).

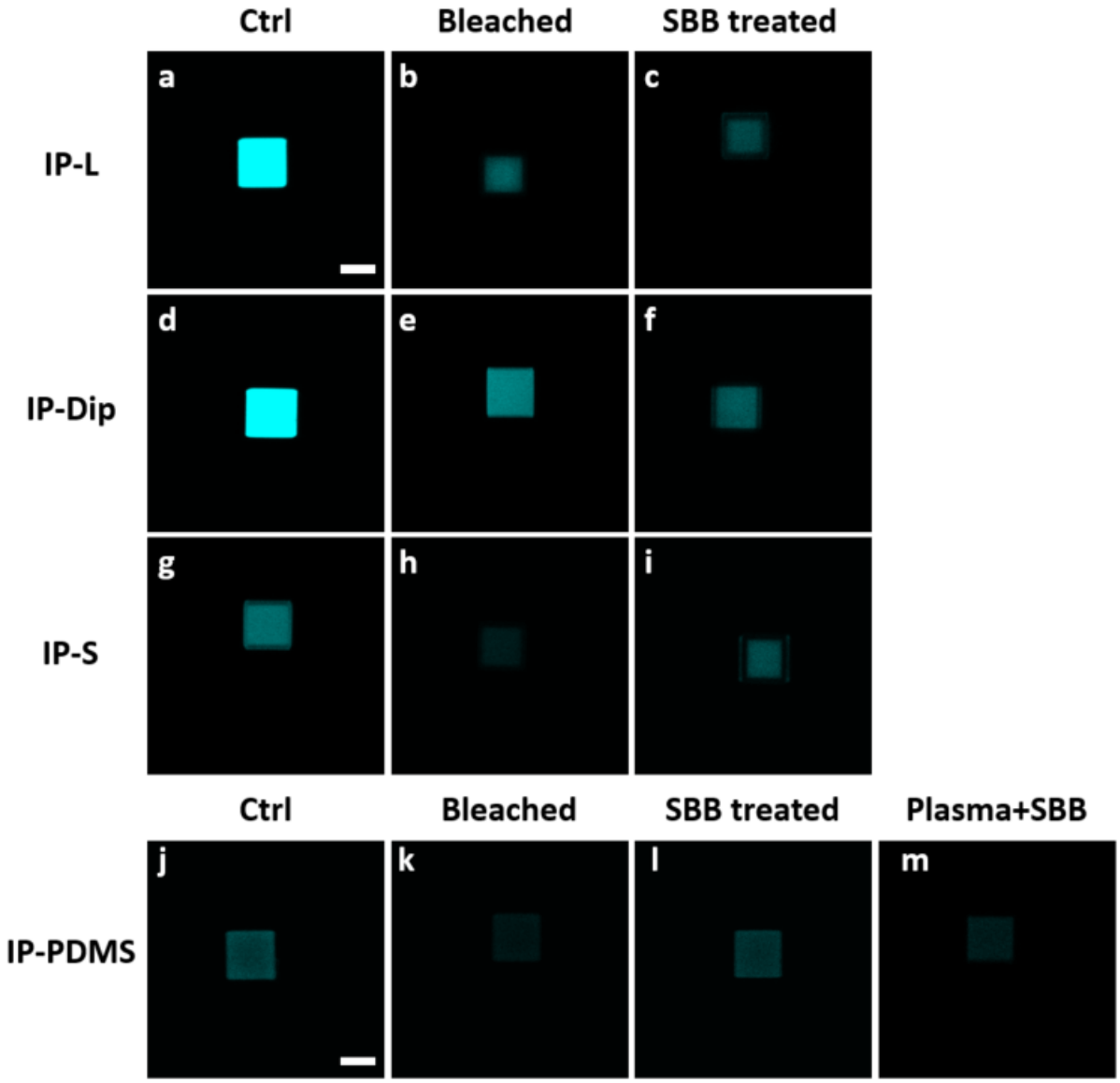

Fig. 3.5. Confocal microscopy images of pedestals fabricated from IP-L (a-c), IP-Dip (d-f), IP-S (g-i), and IP-PDMS (j-m). The effect of bleaching and SBB treatment is shown for each material. All images were acquired at an emission wavelength range of 465-475 nm (the wavelength range at which the auto-fluorescence signal was maximum). Scale bar = 20 µm.

3.3.2. Mechanical characterization

The Young's moduli (E) of all four materials before and after bleaching were measured by compression testing (for IP-L, IP-Dip, and IP-S) or nanoindentation (for IP-PDMS). Fig. 3.6 shows the change in E for all materials. For IP-L, E was evaluated to be 1.75 GPa ± 0.04 for the control sample and 3.26 GPa ± 0.28 for the bleached one (Fig. 3.6a). As for IP-Dip, E increased from 3.07 GPa ± 0.28 for the control sample to 4.1 GPa ± 0.29 for the bleached sample

(Fig. 3.6b). For IP-S, E increased from 2.95 GPa ± 0.12 to 3.35 GPa ± 0.09 for the control and bleached samples respectively (Fig. 3.6c).

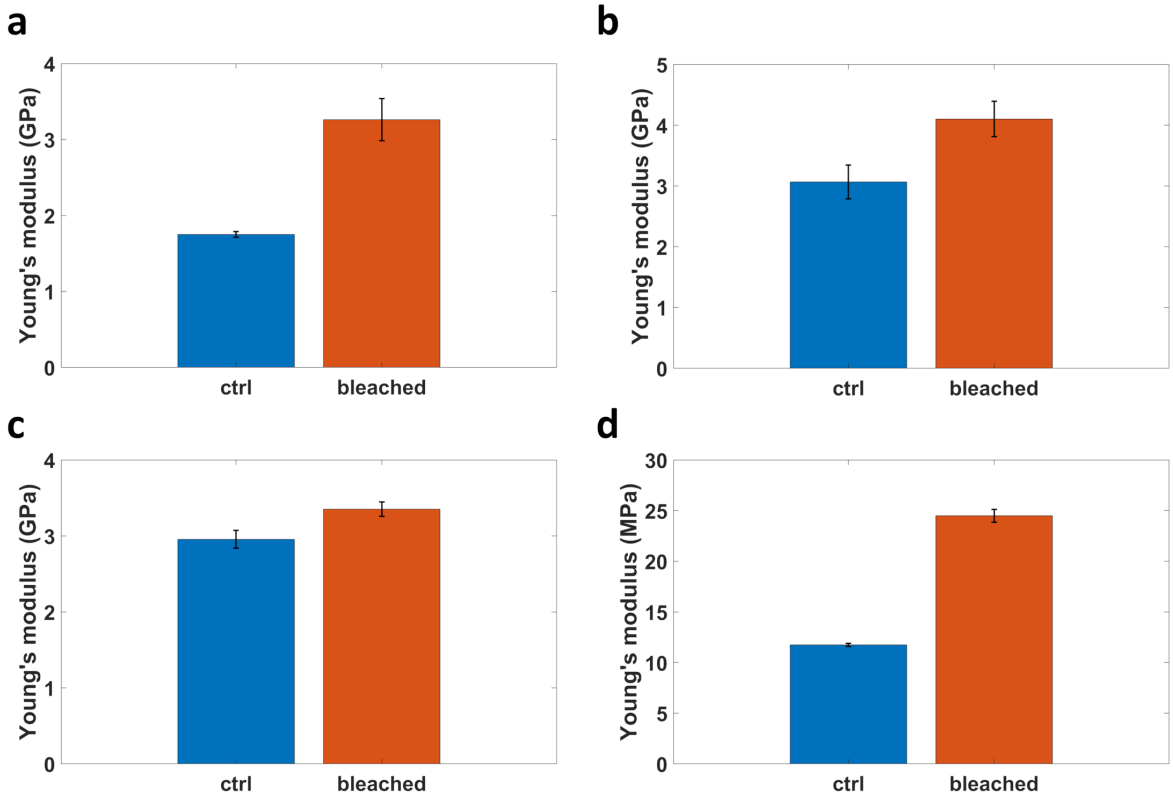

Fig. 3.6. A comparison of the Young's moduli of untreated (control) samples versus bleached samples of (a) IP-L, (b) IP-Dip, (c) IP-S, and (d) IP-PDMS. For each condition n=5 pedestals.

The Young's modulus of IP-PDMS increased approximately two fold from 11.74 MPa ± 0.16 for the control to 24.5 MPa ± 0.63 for the bleached samples (Fig. 3.6d). The increase in E is not surprising since the photoinitiator and some residual monomers remain within the solid structures even after development. Exposure to a UV light source excites these photoinitiaor molecules thus resuming the polymerization and crosslinking reaction leading to a stiffer structure with more crosslinks and a higher elastic modulus. This characterization is important as the elastic modulus of a biomaterial can have an influence on cell fate [103,104]. It is noteworthy that the mechanical characterization was only carried out for UV bleached samples and not SBB-treated ones owing to the fact that SBB treatment is a mere surface treatment resulting in the deposition of a nanometric layer on the surface of the structures. Therefore, SBB treatment is not expected to affect any of the intrinsic mechanical properties of the materials.

3.3.3. Visualization of stained cells

In order to validate our results in the context of cell biology applications, we conducted a study in which the proposed fluorescence suppression solutions were employed on the materials cultured with SH-SY5Y human neuroblastoma cells. The cells were cultured on the control and treated structures, differentiated for 3 days, and then stained for Hoechst (blue nucleus staining), phalloidin (green actin staining for the cytoskeleton), and paxillin (red staining for visualization of focal adhesions). Fig. 3.7 shows a comparison between the results for cells cultured in the 3D rectangular microchannels. The intermediate section of the structure along the z-axis is shown

in the figure in the blue, green, and red channels. All imaging acquisitions represented in Fig. 3.7 were performed using the same laser power and gain. We associate any overlap that maybe observed in the emission of the green and blue channels to the fact that the acquisition was performed in parallel for all three channels (blue, green, and red). All treated polymeric structures enabled a significant enhancement in visualization of the cells. Nonetheless, bleached structures showed to be superior to SBB coated ones since the SBB absorbed the fluorescence of the staining of the cells. This explanation is supported by the fact that the peak emissions of Hoechst 33342, ActinGreen 488, and Texas Red are 460, 518, and 615 nm, respectively, which clearly fall well within the spectral region of absorption of SBB [105]. The only material for which SBB did not cause such a problem was IP-PDMS due to the poor adhesion of the SBB to that specific material. To further illustrate the difference between untreated and treated microchannels in terms of cell visualization, we show representative 3D reconstructions of the structures in Fig. B6 and zoomed-in images of the intermediate sections of the microchannels in Fig. B7, acquired at optimized imaging parameters for each configuration, in Appendix B. The obtained results reveal that for SBB-treated materials, except for IP-PDMS, the laser power had to be increased to more than 50% to be able to visualize the cells and even then, the gain had to be increased to a degree where background noise obstructed efficient visualization of the stainings. This was especially a problem when visualizing paxillin (in the red channel) since focal adhesions can be a few hundred nanometres in size and increased noise substantially affects their measurement. Moreover, for IP-S for example, the microstructures were damaged when increasing the laser power of the 405 nm wavelength laser to 50% (data not shown).

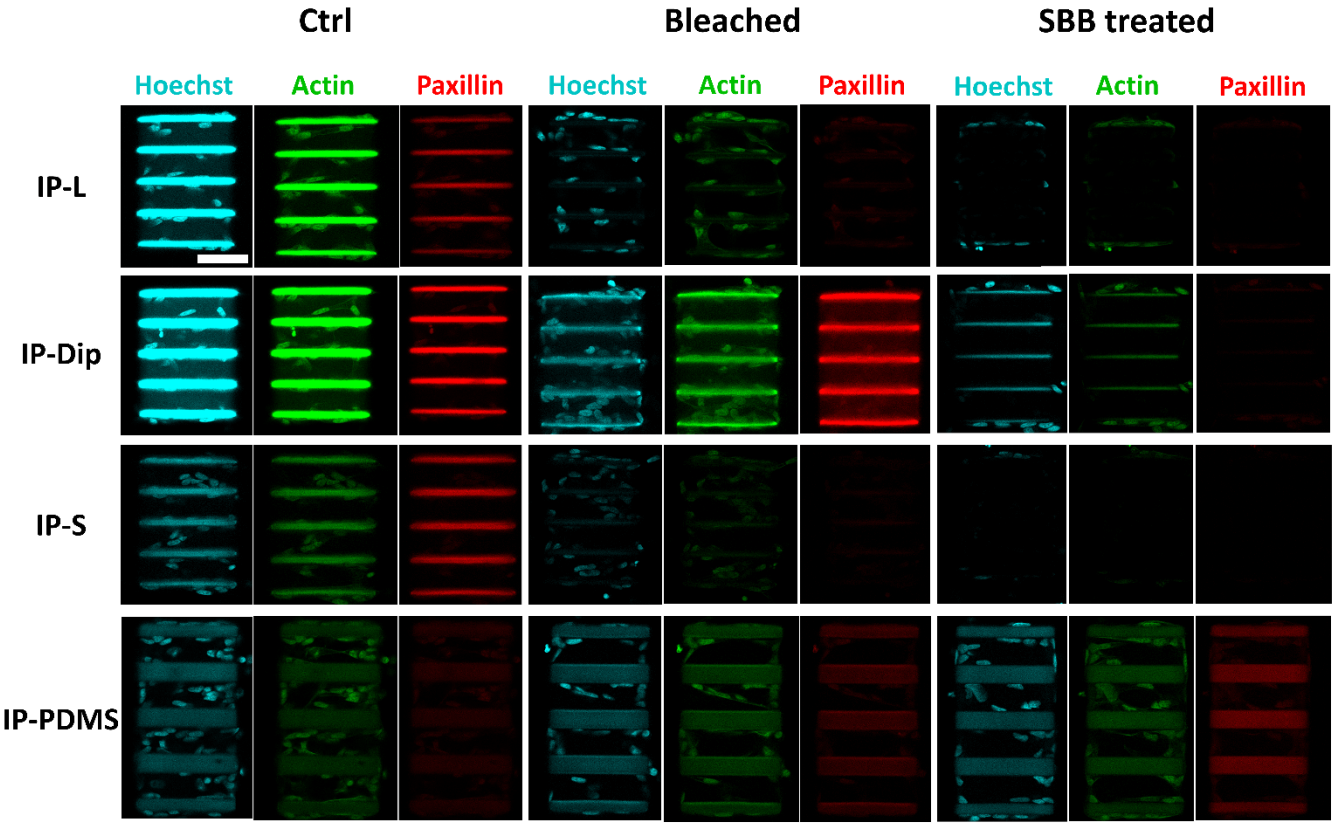

Fig. 3.7. Confocal images of stained SH-SY5Y cells in the 3D rectangular microchannels. The depicted images are of the mid-section of the rectangular microchannels. Blue is Hoechst staining (cells nuclei). Green is actin (cytoskeleton). Red is paxillin (focal adhesions). All images were taken at the same laser power and gain. These images were processed by Fiji. Scale bar = 50 µm.

Additionally, as already indicated previously, after bleaching, auto-fluorescence of IP-Dip decreased in the blue and green channels, but increased in the red channel, rendering the visualization of cells in that channel very difficult. Fig. B8 in Appendix B also depicts representative images of the intermediate section of treated and untreated microchannels acquired sequentially instead of in parallel for blue, green, and red channels. The observations made earlier were similar for images acquired via sequential scanning.

To further assess the efficiency of both solutions, SH-SY5Y cells were also cultured on 3D microcages and differentiated for 3 days as shown in Fig. 3.8. The structures represented in the figure are of IP-L only. All structures were imaged using the same laser powers and gain to facilitate the comparison. The acquisition was obtained via parallel scanning for all three channels (blue, green, and red). A clear difference can be observed in Fig. 3.8 between the untreated structure and the treated ones as the strong auto-fluorescence of the untreated structure especially in the blue channel hinders any meaningful analysis of cells within this complex 3D structure. Bleached and SBB-treated structures on the other hand showed a significant enhancement in visualization of the cells due to the decreased auto-fluorescence. Using these imaging parameters (i.e.: laser power and gain), no substantial difference between bleached or SBB-treated structures was noticed. However, upon attempting to optimize the imaging parameters to better visualize the middle and lower sections of the microcages, once again, SBB proved to be inferior to bleaching as the laser power had to be increased to 50% which resulted in substantial background noise (see Fig. B9 in Appendix B). It must be noted though that the results for bleached structures were not perfect due to the high structural density of the microcages, which results in scattering and absorbing emitted photons from the lower sections of the structure. An additional acquisition via sequential scanning of blue, green, and red channels of the microcages is shown in Fig. B10 in Appendix B to illustrate that the reported observations apply to that modality of confocal acquisition as well.

These results lead us to conclude that although both methods are effective in suppressing the auto-fluorescence of various materials, the preference of one over the other highly depends on the geometry of the structure. In our cell culture study, SBB coating did not perform as well as bleaching. It should be noted however that bleaching is also not a perfect solution since it can lead to unexpected behaviours like the increased auto-fluorescence of IP-Dip in the red region of the spectrum. Both solutions provide anyhow a path towards the suppression of auto-fluorescence of 2PP scaffolds.

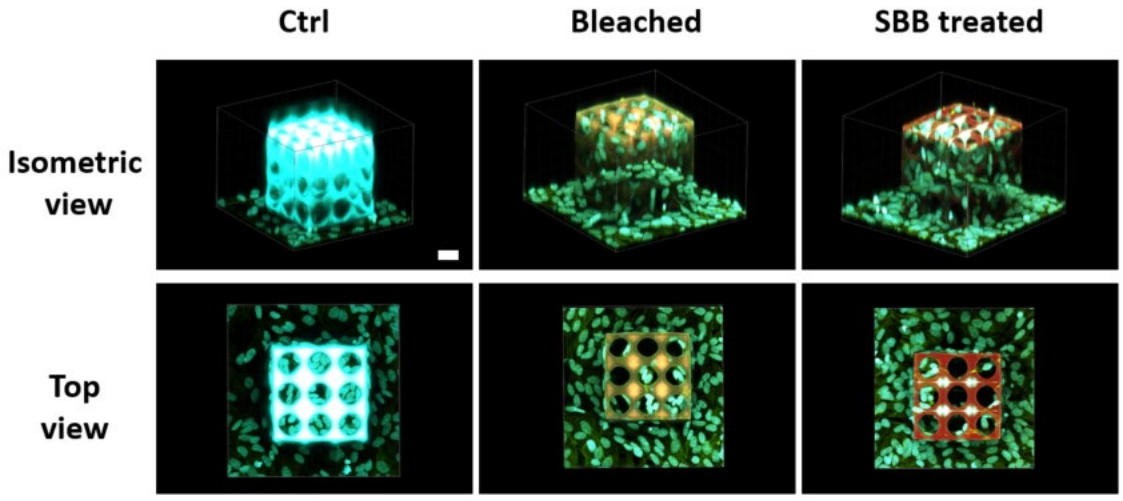

Fig. 3.8. 3D reconstruction of IP-L microcages with SH-SY5Y cells cultured on them. The images represent merged blue, green, and red channels. Blue is Hoechst staining (cells nuclei). Green is actin (cytoskeleton). Red is paxillin (focal adhesions). The top row shows an isometric view of the cages and the bottom one shows the top view. All z-stacks were acquired at the same laser power and gain. These images were created by Imaris Viewer software. Scale bar = 30 μm.

3.4. Conclusions

In the present study, we address the issue of auto-fluorescence of four commercial photoresins that are widely used in the field of 2PP. In the context of *in vitro* mechanobiological studies that involve the fabrication of 3D microscaffolds, auto-fluorescence of these structures interfere with the analysis of cells cultured onto them. Therefore, we proposed a systematic study and comparison between two solutions that are applied after the fabrication of the structures, namely, photo-bleaching and auto-fluorescence quenching. The proposed solutions can be performed with relative ease and with virtually any material, therefore they are not limited by the current selection of materials. Our results show that photo-bleaching consistently eliminates the auto-fluorescence of all materials and does not depend on the chemistry of the material. In some cases (such as with IP-Dip), it can result in the creation of a species that slightly increases the auto-fluorescence of the material in one region of the spectrum while simultaneously decreasing it in another region. Concerning quenching instead, we used SBB to coat the surface of the structures and obstruct photons emitted by them. SBB proved to be of equal efficiency or superior to bleaching with all materials used for this study except for IP-PDMS where it only reduced the fluorescence by 33%. This is attributed to the affinity of SBB to be adsorbed by one material rather than the other. Such affinity is likely affected by the hydrophobicity/philicity, charges, and roughness of a surface in relation to SBB. With an oxygen plasma pre-treatment, however, the IP-PDMS structures were activated and SBB achieved better adhesion resulting in a significant increase in auto-fluorescence suppression. In addition, we performed a study with the human neuroblastoma cell line (SH-SY5Y) to emphasize the efficiency of both solutions and compared them. Our results showed that bleaching is superior to quenching in the proposed scenarios, since in the case of rectangular microchannels and microcages within which cells migrate, SBB quenches not only the fluorescence of the structures, but also that of the stained cells inside the structures. Therefore, the choice of either one of these two solutions highly depends on the type of experiments planned and structures used. In summary, the present study provides a systematic comparison of solutions to suppress the auto-fluorescence of polymeric microstructures in order to increase the efficiency of analysis using fluorescence microscopy for cell biology applications.

4

Effect of confinement on the expression of YAP and neurite outgrowth of SH-SY5Y neuron-like cells and induced pluripotent stem cell derived neurons

The effect of mechanical cues on cellular behaviour has been reported in multiple studies so far, and a specific aspect of interest is the role of mechanotransductive proteins in neuronal development. Among these, yes associated protein (YAP) is responsible for multiple functions in neuronal development such as neuronal progenitor cells migration and differentiation while myocardin-related transcription factor A (MRTFA) facilitates neurite outgrowth and axonal pathfinding. Both proteins have indirectly intertwined fates via their signalling pathways. There is little literature investigating the roles of YAP and MRTFA in vitro concerning neurite outgrowth in mechanically confined microenvironments. Moreover, our understanding of their relationship in immature neurons cultured within engineered confined microenvironments is still lacking. In this study, we fabricated, via 2PP, 2.5D microgrooves and 3D polymeric microchannels, with a diameter range from 5 to 30 µm. We cultured SH-SY5Y cells and differentiated them into immature neuron-like cells on both 2.5D and 3D microstructures to investigate the effect of mechanical confinement on cell morphology and protein expression. In 2.5D microgrooves, both YAP and MRTFA nuclear/cytoplasmic (N/C) ratios exhibited maxima in the 10 µm grooves indicating a strong relation with mechanical-stress-inducing confinement. In 3D microchannels, both proteins' N/C ratio exhibited minima in presence of 5 or 10 µm channels, a behaviour that was opposite to the ones observed in the 2.5D microgrooves and that indicates how the geometry and mechanical confinement of 3D microenvironments are unique compared to 2.5D ones due to focal adhesion, actin, and nuclear polarization. Further, especially in presence of 2.5D microgrooves, cells featured an inversely proportional relationship between YAP N/C ratio and the average neurite length. Finally, we also cultured hiPSCs and differentiated them into cortical neurons on the microstructures for up to 2 weeks. Interestingly, YAP and MRTFA N/C ratios also showed a maximum around the 10 µm 2.5D microgrooves, indicating the physiological relevance of our study. Our results elucidate the possible differences induced by 2.5D and 3D confining microenvironments in neuronal development and paves the way for understanding the intricate interplay between mechanotransductive proteins and their effect on neural cell fate within engineered cell microenvironments.

The contents of this chapter have been published in:

- A. Sharaf, J.P. Frimat, A. Accardo, Mechanical confinement matters: Unveiling the effect of two-photon polymerized 2.5D and 3D microarchitectures on neuronal YAP expression and neurite outgrowth, Materials Today Bio 29 (2024) 101325.

4.1. Introduction

Decision making mechanisms and gene expression within cells are affected by multiple biochemical or physical cues. A collection of studies over the years have shown how mechanical cues have a vital role in a range of decision making processes within neuronal development ranging from the migration and differentiation of neuronal progenitor cells to the outgrowth and guidance of neurites [106]. As illustrated earlier, microstructures can be fabricated via 2PP for fundamental studies of neuromechanobiology.

While interacting with these microstructures, cells sense mechanical cues and translate them into relevant biochemical signals via a class of proteins named mechanotransductive proteins [107]. Among these, the Yes-associated protein (YAP), which is a Hippo pathway effector, normally resides in the cytoplasm and it shuttles to the nucleus primarily when the actin filaments of the cytoskeleton are under tension [108]. Studies revealed that factors affecting the activation of YAP can be a change in the stiffness of the ECM, the area and confinement of the cell body (i.e. cell spreading), cell density, shear flow, and cell stretching [109]. Once activated, YAP interacts with transcriptional enhanced associate domain (TEAD) transcription factors in the nucleus to regulate gene expression. YAP has an evident effect on the regulation of multiple aspects of cell fate in health and disease such as their survival, self-renewal, proliferation, and differentiation [108,110]. For example, YAP activation stimulates self-renewal of human embryonic stem cells [111] and promotes the proliferation of vascular smooth muscle cells [112]. It has been linked also to cell necrosis when drawn towards the cytoplasm in cortical neurons in Alzheimer's patients [113]. In addition, studies have shown that YAP is responsible for cancer cell metastasis and transformation [114,115]. Moreover, YAP plays an important role in neuronal development [116]. Musah et al. showed how human embryonic stem cells (hESCs) selectively differentiated into neurons within 10 days on soft polyacrylamide (PA) hydrogel substrates (Young's modulus (E) ~ 0.7 kPa) even though the culture medium promoted pluripotency. This was accompanied by YAP localization in the cytoplasm and not the nucleus. In comparison, stiffer PA hydrogel substrates of E ~ 10 kPa induced YAP to be located in the nucleus and was accompanied by much less pronounced neuronal differentiation [117]. Sun et al. showed similar results with compliant PDMS microposts' arrays (E = 3 kPa) vs. stiff ones (E = 1200 kPa) when used as substrates for hESCs for 3 days [118]. In addition to YAP, a highly relevant protein is myocardin-related transcription factor A (MRTFA/MAL/MKL1) which is a co-activator of serum response factor (SRF) in the nucleus. MRTFA acts as a sensor of the ratio of G-actin monomers to F-actin polymeric filaments [119]. In an unstimulated state, MRTFA resides in the cytoplasm and binds to G-actin monomers. When stimulated, the bond with G-actin is severed and it shuttles towards the nucleus to bind to SRF transcription factor and induces gene transcription. SRF in turn regulates the polymerization of actin in the cell. Within the nervous system, MRTFA is particularly located in the hippocampus and cerebral cortex [120]. It was shown in multiple studies that the absence of SRF has a negative effect on neurite outgrowth, axon pathfinding, and formation of neuronal circuitry [121]. Zhang et al. even illustrated that overexpression of MRTFA in the hippocampus of Alzheimer's-transfected mice reduces the accumulation of β-amyloid peptide and consequently decreases cognition defect [122]. There are multiple studies that suggest some crosstalk between the two pathways of YAP and MRTFA [123–125], since they are both related to actin in the cytoskeleton. Similar to YAP, MRTFA translocation from the cytoplasm to the nucleus and the subsequent activation of SRF transcription factor was shown to be manipulated by mechanical cues such as cell stretching and confinement of cellular growth volume [126,127]. Finally, within the complex of mechanotransduction, the anchor points at which the cell and ECM adhere, known as focal adhesions (FAs), play a major role. FAs are made up of multiprotein bundles and they directly and physically connect the ECM to the actin filaments of the cytoskeleton

[128]. FA proteins such as vinculin and paxillin were shown to have a relationship with YAP expression and its nuclear to cytoplasmic (N/C) ratio within multiple studies [88,110,129,130].

Among mechanical cues investigated by various research groups, confinement remains an especially interesting one due to its high relevance to the mechanics of migration of neuronal progenitor cells and immature neurons within the CNS [106]. Although a few studies have investigated the effect of confinement on YAP N/C ratio [129–133], very little research has been performed on immature neurons in this regard. In addition, unravelling the relationship between YAP and MRTFA with respect to the elongation and outgrowth of neuronal processes at early stages of neuronal development is still at its infancy. Moreover, past studies concerned with mechanical confinement mainly used biochemical patterns of proteins such as fibronectin or 2.5D microwells made from compliant materials such as PDMS. Therefore, a systematic comparison between 2.5D and 3D microenvironments has not been reported yet to the best of our knowledge. In the current study, we employed the 2PP technology to fabricate a set of 2.5D microgrooves and 3D microchannels with varying diameters (i.e. 5, 10, 20, and 30 µm) using IP-L photoresin. After which, we utilised the developed protocols in **Chapter 3** (as elaborated below) to suppress the autofluorescence of the microstructures. We then employed confocal microscopy and scanning electron microscopy (SEM) to investigate the effect of mechanical confinement on YAP and MRTFA N/C ratios as well as to identify the relationship between these ratios and the elongation of neuronal processes. Additionally, the effect of the microstructures on the early FA protein, paxillin, was studied. We cultured SH-SY5Y human neuroblastoma cells on the microstructures and differentiated them into immature neuron-like cells for 1 and 3 days. In addition, and as a proof of principle, we also cultured a more physiologically relevant hiPSC-derived neuronal model on the microgrooves and differentiated the cells for 7 and 14 days to investigate possible differences in YAP N/C ratio. Besides YAP and MRTFA, we investigated the overall expression of microtubule-associated protein 2 (MAP2) and beta-tubulin III (TUJ1) in the differentiated cells since these proteins are indicators of neuronal differentiation.

4.2. Materials and Methods

4.2.1. Design of the microstructures

The design of all 2.5D and 3D microstructures employed in this study were carried out using SOLIDWORKS (Dassault Systèmes). Two sets of microstructures were designed, namely 2.5D microgrooves and 3D microchannels. Both sets had 4 different gaps/diameters 5, 10, 20, or 30 µm. From this point onward, the 2.5D microgrooves are referred to as G5, G10, G20, and G30 and the 3D microchannels will be referred to as C5, C10, C20, and C30. In the case of the 3D microchannels, we designed two additional variants featuring diameters of 5 or 10 µm and featuring a 50 µm long truncated cone attached at both ends to provide a gradual decrease of the diameter of the channels from 30 µm down to either 5 or 10 µm. This alternative design was chosen to investigate the effect of gradual confinement on the colonization of the cells in the 10 µm and, especially, 5 µm microchannels. These two 3D microchannel designs are referred to as alternative design channels (ADC) of 5 or 10 µm diameters (i.e. ADC5 and ADC10). All 2.5D microgrooves and 3D microchannels were curved and not rectangular in shape. 2.5D microgroove arrays covered an area of 750 x 750 μm^2 and featured 15 µm high and 5 µm wide ridges. 3D microchannel arrays on the other hand covered an area of 250 x 250 μm^2. Both structures had a base of 1 µm thick pedestals to promote adhesion to the substrate. The full detailed designs are presented in Appendix C (Fig. C1,2).

4.2.2. Microfabrication of the 2.5D and 3D microarchitectures

The microstructures were printed via 2PP technology by employing a Nanoscribe Photonic Professional GT+ (PPGT+) printer (Nanoscribe GmbH & Co. KG). The substrates used to perform the printing were 25 x 25 x 0.7 mm^3 soda lime glass substrates coated with a nanometric layer of indium tin oxide (ITO) supplied by Nanoscribe GmbH & Co. KG. Prior to printing, the substrates were cleaned with acetone and IPA (Sigma-Aldrich) , dried, and then treated with oxygen plasma in a Diener Femto plasma cleaner for 5 min with an oxygen flowrate of 5.5 cm^3/min at a power of 100 W and ~0.24 mbar (40 kHz frequency). Afterwards, they were silanized with MAPTMS (TCI Chemicals) by dispensing a 30 µL droplet on a parafilm sheet and then placing the substrates face down on the droplet overnight. The silanized substrates were stored in the dark until further use. Immediately before printing, the substrates were rinsed with IPA and dried with an air gun. Afterwards, a droplet of IP-L resin was dispensed on the substrate to print the microstructures. IP-L is a proprietary acrylate-based photoresin of Nanoscribe GmbH & Co. KG and it was employed in combination with a 25x Zeiss objective (NA = 0.8) to 3D print the microstructures. This combination enabled the printing of large areas of microstructures required for biological studies with fine features (i.e. 5 µm diameter channels). The printing took place in DiLL mode and galvanometric mirrors-assisted scanning configuration. Printing via 2PP with the Nanoscribe PPGT+ takes place in a line-by-line fashion in the horizontal direction followed by cumulative printing of consecutive layers on top of each another. The hatching distance of the horizontal lines and the slicing distance of the vertical layers were chosen to be 0.2 and 0.7 µm respectively. The direction of the hatch lines was parallel to the walls of the microstructures to prevent the effect of any competing mechanical neuronal guidance cues that maybe created if their direction was perpendicular to the walls. The laser power was set to 20 mW (equivalent to a light intensity of 0.4 TW/cm^2 [63]) and the scanning speed was 90 mm/sec. After printing, the microstructures were developed in PGMEA (Sigma-Aldrich) for 30 min then transferred to a second bath of clean PGMEA for 2 h. Afterwards, they were placed in an IPA bath for 5 min before placing them in NOVEC™ 7100 (Mavom BV) for 30 sec to prevent structural deformation caused by capillary effect during drying. The samples were finally blow dried with an air gun.

4.2.3. Post treatment of the structures

After development, the microstructures were activated using oxygen plasma for 1 min (same parameters used in section 4.2.2). Immediately afterwards, they were coated with (3-Aminopropyl) triethoxysilane (APTES) (Sigma-Aldrich) by placing them in a bath of 3% APTES in ethanol (Sigma-Aldrich) overnight followed by cleaning in a DI water bath for 1 h. Coating with APTES was performed to increase the hydrophilicity of the microstructures thereby facilitating the delivery of nutrients to the cells. Amine terminated silanization was also proven to improve cell attachment and viability on 2PP acrylate-based photoresins [134]. Due to the high autofluorescence of IP-L, especially in the blue and green regions of the spectrum and since the samples were planned to be inspected via confocal microscopy after the culture of the cells, we applied a protocol to supress this autofluorescence previously developed by our group [135]. Briefly, the samples were bleached by a UV point source (Bluepoint 4 Ecocure Honle UV technology) with a wavelength range of 300 to 600 nm and a maximum of 375 nm for 30 min at a power of 100% (i.e. 10,000 mW/cm^2). The UV lamp was placed at a 1 cm distance from the samples.

The Young's modulus of the bleached microstructures was measured by compression testing with FEMTOTOOLS nanomechanical testing system (FT-NMT03) by utilising a 50 x 50 μm^2 Si probe with a flat punch head and a measurable force range of 200,000 ± 0.5 µN. Pedestals of 30 x 30 x 20 μm^3 (length x width x height) were used for these measurements.

4.2.4. Cell culture

4.2.4.1. SH-SY5Y human neuroblastomas-derived immature neuron-like cells

Prior to seeding on the samples, human neuroblastoma cell line SH-SY5Y cells (Sigma-Aldrich, #94030304) were cultured in Dulbecco's Modified Eagle's Medium (DMEM)/F-12 media (1:1) (Thermo Fisher Scientific, #10565018) in presence of 10% fetal bovine serum (FBS, Sigma-Aldrich F7524) and 1% penicillin/ streptomycin in an incubator at 37°C and 5% CO_2. Once the cells were confluent, they were harvested by the use of trypsin (x1) before centrifuging them at 900 rpm for 5 min. They were then seeded on the structures at a density of 10,000 cells/cm^2 before differentiating them into immature neuron-like cells by adding 10 µM of retinoic acid to the culture medium (Sigma-Aldrich, R2625) for 1 and 3 days.

4.2.4.2. hiPSC-derived immature neurons

hiPSC (LUMCi003-A) were thawed, resuspended in complete STEMdiff™ Neural Progenitor Media (Stem Cell Technologies, #05833) and plated on 0.1% matrigel coated 6 well plates in complete STEMdiff™ Neural Progenitor Media. Cells were harvested for differentiation when nearly confluent by visual inspection (80%), typically on day 7, with media refreshing every 2-3 days.

hiPSC-derived cortical neurons were generated using the STEMdiff™ midbrain neuron differentiation kit (stem cell technologies cat. No. #100-0038). Briefly, the cells were harvested using accutase (Stem Cell Technologies, #07920) and centrifuged at 400 rpm for 5 min prior to reseeding for differentiation on the 2PP samples. Cells were resuspended in full STEMdiff™ midbrain neuron differentiation media and seeded on poly-L-ornithine (100 µg/mL)(Sigma Aldrich P3655)/ laminin (100 µg/mL)(Sigma Aldrich L2020) coated 2PP samples at 75,000 cells/cm^2 in full STEMdiff™ midbrain neuron differentiation media for 7 days with daily media refreshing. After 7 days, cortical neurons were generated and half of the 2PP samples were fixed for the first time point. The remainder of the samples were further matured 1 week using the BrainPhys™ hPSC Neuron kit media (Stem Cell Technologies, #05795) with half media change every 3 days until day 14, after which samples were fixed for the second time point.

4.2.5. Immunocytochemistry

All samples were fixed in 4% paraformaldehyde (PFA) for 15 min at room temperature (RT) and then permeabilized using 0.1% Triton X- 100 in Phosphate Buffer Saline (PBS) solution. Blocking of the cells was done using 1% bovine serum albumin (BSA) in PBS for 30 min at RT. Mouse anti-YAP primary antibody (Santa Cruz, sc-101199, 1:200) was then applied for 2 h in PBS containing 1% BSA at RT. For MRTFA, we used mouse anti-MRTFA primary antibody (Santa Cruz, sc-398675, 1:200) also for 2 h in PBS containing 1% BSA at RT. Immature neurons were stained against anti-beta-Tubulin III (TUJ-1, Sigma-Aldrich, T2200; 1:100 in 1% BSA) and anti-MAP2 (Sigma-Aldrich, M9942; 1:200 in 1% BSA) to study their growing processes. To visualize focal adhesions, anti-paxillin primary antibodies (Sigma-Aldrich, SAB4502553, 1:200 in 1% BSA) were incubated for 2 h at RT. The secondary antibody (Sigma-Aldrich, SAB3700937-Anti- Rabbit IgG (H + L)-Texas Red® antibody, 1:500 in 1% BSA) was used to stain paxillin and TUJ-1 antibodies by incubation for 1.5 h at RT while visualization of YAP, MRTFA, and MAP2 took place via staining also for 1.5 h at RT with the secondary antibody (Thermo Fisher Scientific, A-21235-Goat anti-Mouse IgG (H+L) Cross-Adsorbed Secondary Antibody, Alexa Fluor™ 647). As for visualizing the cytoskeleton, we used phalloidin (Thermo Fisher Scientific, ActinGreen 488 ReadyProbes, R37110) to stain F-actin. We then used NucBlue™ (Thermo Fisher Scientific, Live ReadyProbes™ Reagent Hoechst 3334, R37605) as a stain for nuclei. For both actin and Hoechst, 2 drops per mL in PBS were added and incubated for 25 min. Samples were washed 3 times with PBS afterwards and stored in PBS in the dark until imaging. All samples were stored at 4°C in the dark until further use.

4.2.6. Confocal microscopy image acquisition

A spinning disk Dragonfly 200 High Speed Confocal microscope (Oxford Instruments Andor Ltd) was utilised to acquire all confocal images of the samples. We used a Nikon Apo LWD 25x Water Dipping objective (NA = 1.10) to acquire images of YAP, MRTFA, and TUJ-1. Imaging of these samples was carried out in PBS. A Nikon Apo total internal reflection fluorescence (TIRF) 60x oil immersion objective (NA = 1.49) was used for paxillin and MAP2 images in order to provide a higher feature resolution for the visualization of paxillin. These samples were mounted by using a ProLong™ Gold Antifade Mountant with DNA Stain DAPI (Thermo Fisher Scientific, P36941). An acquisition resolution of 1024 x 1024 px^2 was chosen for YAP and MRTFA images of SH-SY5Y-derived immature neuron-like cells in 2.5D microgrooves while for hiPSC-derived immature neurons, we used a resolution of 2048 x 2048 px^2. For all paxillin and 3D microchannel images, a 2048 x 2048 px^2 resolution was chosen. Laser sources with excitation wavelengths equal to 405, 488, 561, 640 nm were employed during the acquisition. The employed emission filters were 445/46 (Hoechst), 521/38 (Actin), 594/43 (TUJ-1 and paxillin), 685/47 nm (YAP, MRTFA, MAP2). Z-stacks were acquired at 0.5 µm step size.

After confocal microscopy acquisition, each 2.5D microgroove array (750 x 750 um^2) was split into four z-stacks since the imaging was carried out via stitching of each array. As for the 3D microchannels, each z-stack of images included one array of 3D microchannels (250 x 250 um^2). The z-stacks were imported into Fiji [65] and cut into areas (along the x-y direction) that only contained the required microstructures with the cells therein. Care was taken to discard z-slices that contained any cells residing on top of the grooves and not inside. Maximum z-projection images were then created from each z-stack. To identify the nuclei, the machine learning plugin Cellpose 2.0 was utilised [136]. In the case of the 3D microchannels, the plugin required some training runs to be able to identify nuclei. Once the images of the nuclei were generated and saved, they were imported in CellProfiler 4.2.6 [137] along with the relevant maximum z-projection images. Multiple pipelines were developed in CellProfiler to identify cell body, neurite length, FAs (i.e. paxillin), and MAP2 intensity per image. YAP N/C ratio was calculated by measuring the mean intensity of YAP in the nucleus and the cell body (minus the area of the nucleus) and dividing the former by the latter to obtain the result. MRTFA N/C ratio was calculated similarly. Visualizations of images throughout the manuscript were performed by using Imaris Viewer software (Oxford Instruments).

4.2.7. SEM imaging

Samples were dehydrated in order to prepare them for SEM imaging [95]. Briefly, following fixation, samples were placed in a bath of DI water 2 times for 5 min each. They were then placed in 50% ethanol in DI water followed by a bath in 70% and then 96% ethanol for 15 min each. For further dehydration, HMDS (Sigma Aldrich) was used in consecutive baths of 2:1, 1:1, and 1:2 (96% ethanol:HMDS) for 15 min each followed by 15 min of a 100% HMDS bath for 2 times. HMDS was used due to its low surface tension to preserve the membranes and processes of the cells [90–92]. Finally, the samples were left to air dry before imaging. Before imaging, dehydrated samples were sputter coated with a nanometric layer of gold (≈20 nm) using a JEOL JFC-1300 auto-fine sputter coater. Imaging and further morphological characterization was carried out via a JEOL JSM-6010LA SEM (JEOL (Europe) B. V.) in high vacuum at a voltage of 10 kV.

4.2.8. Statistical analysis

For calculating the cell colonization, cell alignment, nuclear minimum and maximum Feret diameters, cell area, and neurite length of SH-SY5Y-derived immature neuron-like cells, 6 samples were employed for each time point. For YAP and MRTFA N/C ratio and MAP2 intensity, 3 samples were used for each time point. For focal adhesion

number, area, and alignment, 3 samples were used for each time point. It should be noted that the 2.5D microgrooves and 3D microchannels were studied in two separate cultures. On the other hand, for the hiPSC-derived immature cortical neurons, 4 samples were used to calculate cell colonization, cell alignment, nuclear minimum and maximum Feret diameters, cell area, and neurite length. For YAP N/C ratio, 3 samples were used for each time point while for and MRTFA N/C ratio and MAP2 intensity focal adhesions number, area, and diameter, 1 sample was used for each time point. Further details of the analysis is shown in Fig. C3,4 in Appendix C. All data extracted from CellProfiler 4.2.6 were exported in Excel files while the analysis and presentation was performed by using an inhouse developed MATLAB (MathWorks®) code. All graphs in this study represent the mean with the standard deviation indicated therein. P-values were obtained by using two-tailed Student's t-test.

4.3. Results and Discussion

4.3.1. Morphological characterization of 2.5D and 3D microfabricated structures

2.5D microgrooves and 3D microchannels were printed via 2PP to investigate the effect of mechanical confinement in 2.5D and 3D microenvironments on the YAP N/C ratio. Both, the 2.5D microgrooves and 3D microchannels, had diameters in the range of 5 to 30 µm. This specific range was chosen to be in the same range of and slightly smaller than the size of cell body and nucleus especially since there are studies suggesting that the squeezing of the nucleus is the limiting factor when attempting to mechanically confine a cell [138,139]. All 2.5D microgrooves were fabricated with high reproducibility (Fig. 4.1) and structural stability. No detachment was observed from the substrates even after an extended period in culture media due to their strong adhesion to the substrates. In all structures, the hatch and slice lines could be observed and helped cell adhesion, since it is known how cells preferentially grow on rough substrates [140], as well as the alignment of their processes. The 2.5D microgrooves were printed with minimal shrinkage.

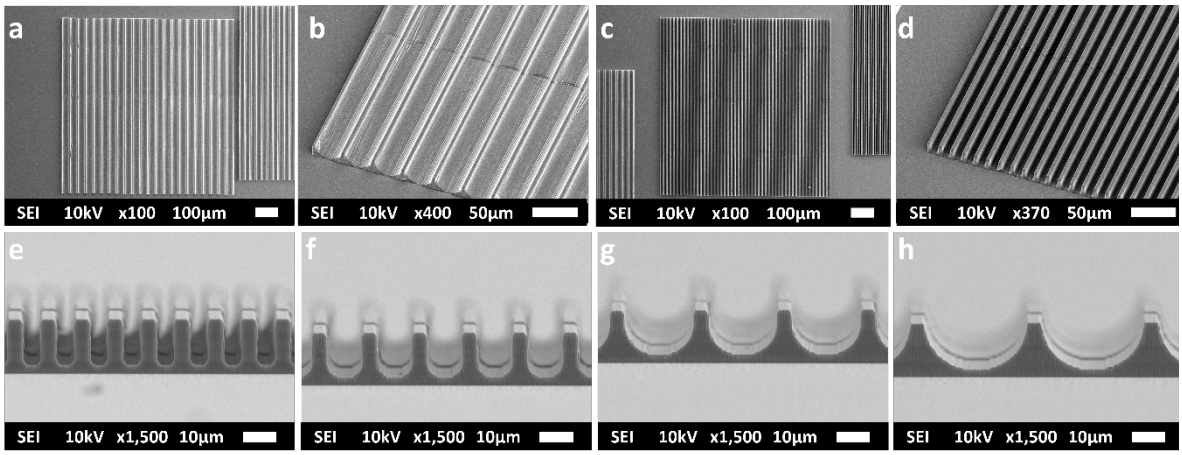

Fig. 4.1. Representative SEM images of (a) and (b) G30 arrays, (c) and (d) G10 arrays. SEM images taken at 90° tilt angle of (e) G5 arrays, (f) G10 arrays, (g) G20 arrays, and (h) G30 arrays. The dimensions of the arrays of microgrooves were 750 x 750 x 15 μm^3.

As for the 3D microchannels (Fig. 4.2), each array of 3D microchannels was 250 x 250 μm^2 and for each diameter of the microstructures, there were 4 arrays printed and placed next to each other longitudinally at a distance of 50 µm (Fig. 4.2a). An average shrinkage of 26% was noticed along the vertical axis (i.e. z-direction) of the microstructures. The shrinkage was at a minimum of 20% in the C30 microchannels (Fig. 4.2j) and increased to reach 38% for the C5 channels (Fig. 4.2e). The measured dimensions of the C5 microchannels were 5.4 µm in the

x-y direction and 3.3 µm in the z-direction. Shrinkage after development is considered normal due to the diffusion of the residual monomers and oligomers from the solidified resin to the solvent. A negligible amount of C5 and C10 channels still had residues from the printing process after the chemical development, thus indicating that at these diameters there was apparent residual polymerization or the possible need for a longer time of PGMEA treatment. The Young's modulus of the bleached microstructures was found to be ~ 3 GPa.

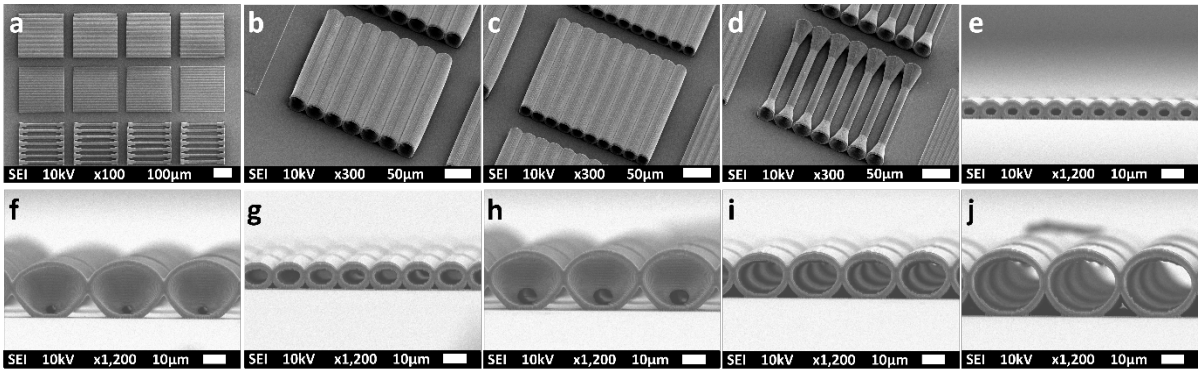

Fig. 4.2. Representative SEM images of (a) 250 x 250 µm^2 arrays of 3D microchannels, (b) C30 microchannels, (c) C20 microchannels, (d) ADC10 microchannels. SEM images taken at 90° angle of (e) C5 microchannels (f) ADC5 microchannels (g) C10 microchannels (h) ADC10 microchannels (i) C20 microchannels and (j) C30 microchannels.

4.3.2. Effect of confinement in 2.5D structures on differentiated SH-SY5Y cells

The human neuroblastoma cell line SH-SY5Y was cultured on the microgrooves and differentiated into early stage neuron-like cells for 1 day (D1) and 3 days (D3) of culture in medium containing 10 µM of retinoic acid. This experiment was performed to investigate the effect of confinement in 2.5D microgrooves on the expression of YAP, the outgrowth of neurites, and the behaviour of FA molecules identified by paxillin. In addition, the relationship between YAP, MRTFA, and MAP2 expression was also investigated.

All structures were colonized by cells, indicating good cell biocompatibility of all the microfabricated microstructures (Fig. 4.3a). With an initial seeding concentration of 10,000 cells/cm^2, the colonization percentage (calculated as the ratio between the total area of cell bodies with respect to the total area of the microgrooves) ranged from 12 to 20% for D1 of differentiation and increased in D3 to reach a range of 17 to 25% (Fig. 4.3b). The cells migrated inside the grooves and some of them were suspended on top between two ridges (Fig. 4.3c.i,ii). Cells exhibited also a high degree of alignment to the microgrooves compared to the cells grown on the flat ITO coated glass substrate (ctrl). There was a clear trend of alignment of the cells to the direction of the major axis of the microgrooves. This was observed by calculating the difference in the average angle of the major axis of the nuclei with respect to the major axis of the 2.5D microgrooves (Fig. 4.3c.iii). There was a clear interaction between the processes of the cells and the hatch lines of the microstructures which likely aided the alignment of the cells. Cells on D3 showed a higher degree of alignment than D1 which could be due to the continued interaction between cells and microstructures with time or the higher degree of maturation of the cells (Fig. 4.3d). Similar to cell alignment, the minimum Feret diameter [141] of the nucleus showed increasing trends from G5 to G30 (Fig. 4.3e). The elongation of the nuclei increased with time of differentiation, as is illustrated by the simultaneous increase of nuclear polarity (Fig. 4.3f). Fig. C10 in Appendix C depicts 3D renders of cells in the microchannels.

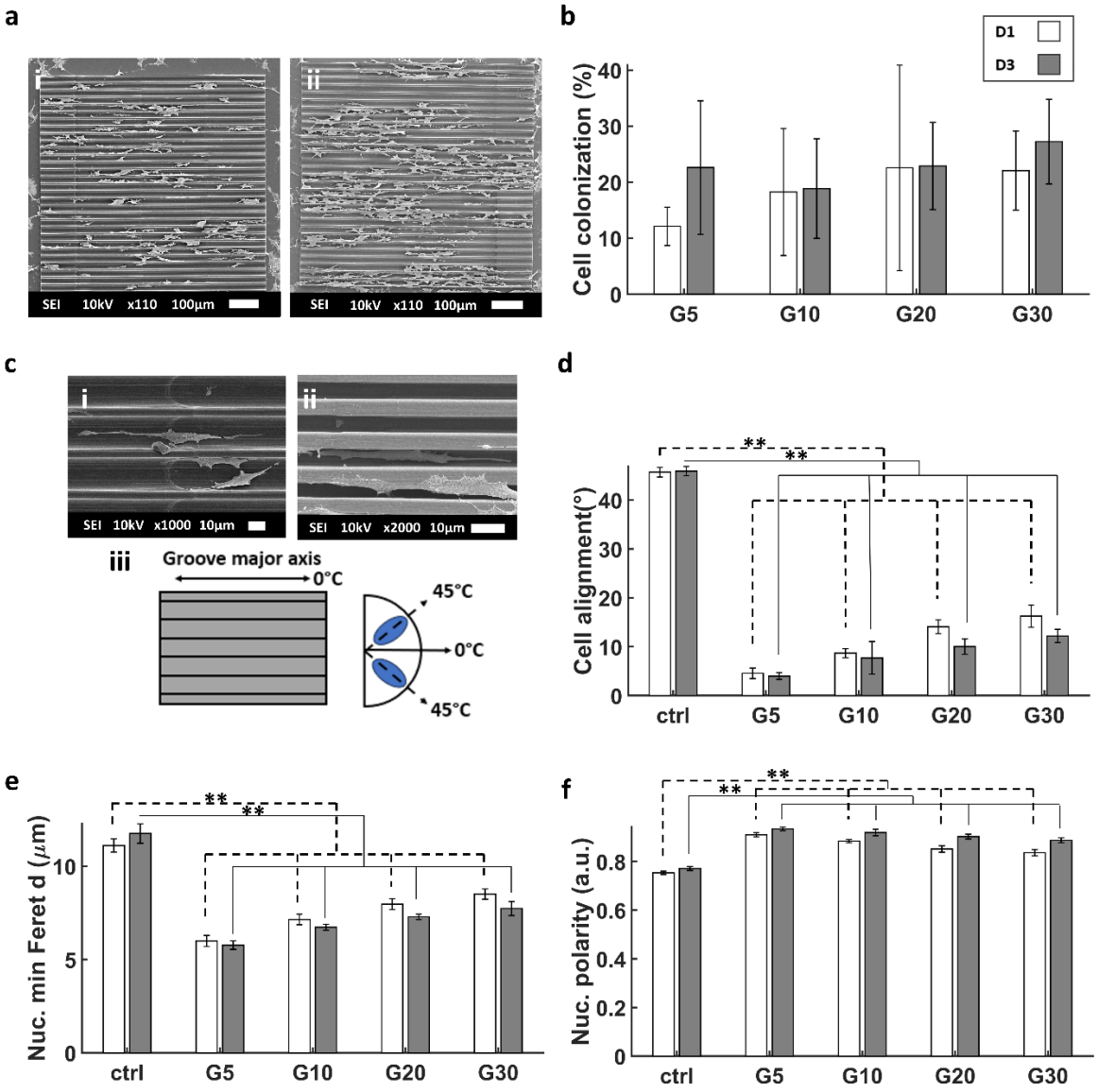

Fig. 4.3. (a) Representative SEM images of (i) cells at D1 in G20, (ii) cells at D3 in G20. (b) The percentage of SH-SY5Y cell colonization in the 2.5D microgrooves calculated as the ratio between the total area of cell bodies with respect to the total area of the microgrooves. (c) SEM images showing the alignment of cells at D1 in (i) G20, and D3 in (ii) G5. (c.iii) Illustration of the major axis of the microgroove which represents the angel zero. It also shows a schematic representation of nuclei at an angle of 45°C with respect to the major axis of the microgrooves. (d) Degree of cell alignment on the microgrooves. (e) Average minimum Feret diameter of the cells nuclei. (f) Nuclear polarity of the cells (where 0 signifies a perfect circle and 1 a straight line). The white and grey bars represent D1 and D3 respectively. * corresponds to a p-value < 0.05 and ** corresponds to a p-value < 0.01. P-values were obtained by two-tailed student's t-test. n = 6 samples for each timepoint.

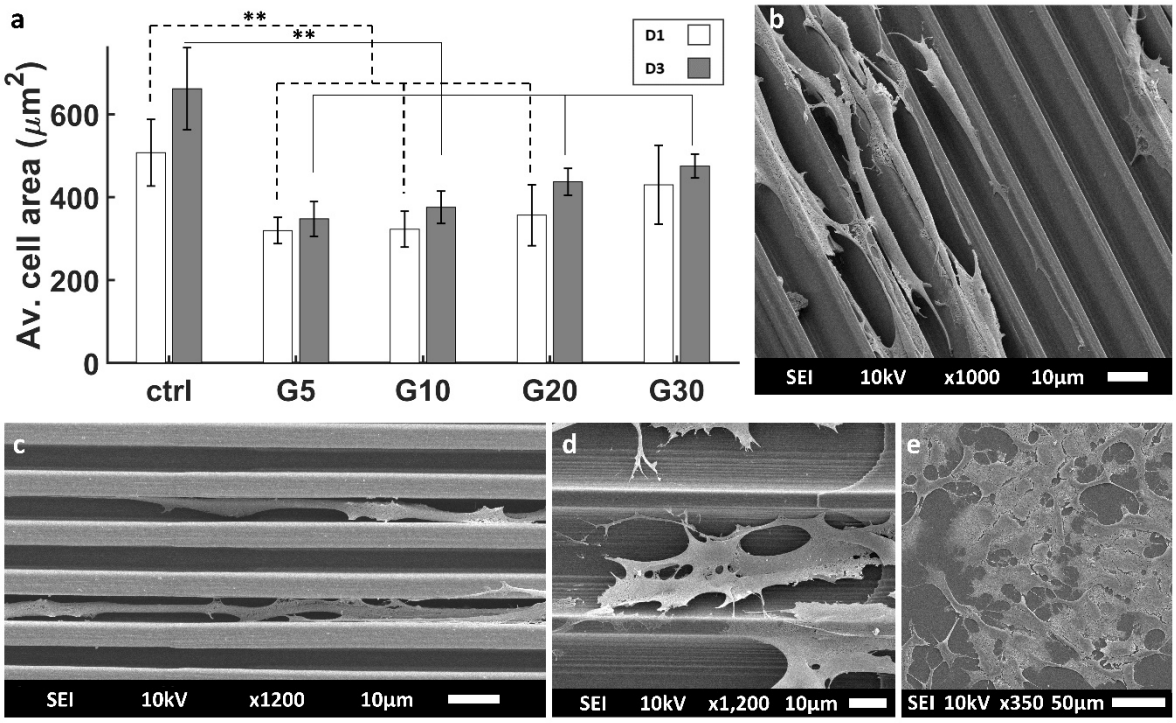

Fig. 4.4. (a) Average area of the cell body (calculated from actin staining of the cytoskeleton). SEM images of cells at D3 in (b) G10, (c) G5, (d) G30, and (e) on the flat ITO-coated glass substrate (ctrl). The white and grey bars represent D1 and D3 respectively. * corresponds to a p-value < 0.05 and ** corresponds to a p-value < 0.01. P-values were obtained by two-tailed student's t-test. n = 6 samples for each timepoint.

The average area of the cell body (i.e. cytoskeleton) (Fig. 4.4a) showed an increasing trend from G5 to G30 indicating the ability of the nuclei and cells to stretch and fit in 2.5D microgrooves as small as 5 µm. SEM imaging showed a clear difference in terms of cell morphology and area as the cell bodies were elongated and small in G5 and G10 (Fig. 4.4b,c) while they were spread out and much larger in G20 and G30 (Fig. 4.4d). Cells cultured on the flat control showed, as expected, the largest degree of spreading and consequently the largest area (Fig. 4.4e).
Expression of YAP was evident for the ctrl and all cells in the microgrooves for both time points (Fig. 4.5a), which may be due to the relatively high Young's modulus of bleached IP-L (E ~ 3 GPa) compared to the Young's modulus of brain tissue (E = 0.1 to 1 kPa) [3] as YAP has been shown to be concentrated in the nucleus in presence of substrates with relatively high Young's moduli in the range of tens of kPa [109,110,128,129]. Overall, the YAP N/C ratios were always greater than 1. The ratio increased from D1 to D3 for all conditions. YAP N/C ratio reached a maximum of 2 in the G10 microgrooves followed closely by G20 while the minimum (1.6) was on the flat ITO-coated glass ctrl (Fig. 4.5b). The trend for the average total neurite length was somewhat opposite to that of YAP since the maximum length was 34 µm on the ctrl and the minimum (20 µm) was in G5 followed by a value of 22 µm in G10 (Fig. 4.5c). The trend of YAP N/C ratio in relation to confined spaces goes against some literature using human mesenchymal stem cells (hMSCs) that suggest that the smaller the area of the cell body, the lower the YAP N/C ratio [129,130]. However, other studies employing mouse embryonic stem cells (mESCs) have shown that upon culturing single mESCs in 35 x 35 vs. 15 x 15 μm^2 wells made from PDMS, the YAP N/C ratio increased in the smaller wells [55] while the study of Wada et al. also reported a threshold of YAP N/C ratio based on cell area

when using NIH3T3 cells [131]. Our results show that within 2.5D microgrooves, there is a threshold of increase of the YAP N/C ratio around the 10-20 µm diameter microgrooves. The difference between our results and those mentioned in literature may be caused by a number of reasons. First, the type of cells used in the current study (SH-SY5Y human neuroblastomas) are different from those in the other mentioned studies. Second, the material used in the current study is different. The Young's modulus of bleached IP-L is 3 GPa while the one of PDMS is in the range of MPa. Third, in the studies conducted by Dupont et al. and Nardone et al., the confinement was applied by printing patterns of fibronectin squares to confine single cells [129,130]. On the other hand, in the current study and in the one of Bertels et al. [55], confinement was applied mechanically via culturing the cells in 2.5D microgrooves that are designed to contain them in small spaces comparable to that of the diameter of the nuclei. This difference in chemical vs. mechanical confinement was also observed by Rianna et al. when culturing U2OS cells in PDMS microchannels vs. fibronectin patterned lines of the same width (5 µm) [142]. Fourth, in the other studies, cells were confined in square-like wells (i.e. isotropic confinement) while in our study, the confinement took place in long aspect ratio (length/diameter) microgrooves which resulted in a highly polar configuration of the nuclei, the bodies of the cells, and the FAs (i.e. anisotropic confinement). This may suggest that isotropy also plays a role in the expression and behaviour of YAP N/C ratio. This observation is corroborated by other studies such as that of Li et al. in which they find a threshold of YAP N/C ratio of Dental pulp stem cells (DPSCs) that directly relates to the aspect ratio of the cells [133]. Finally, all mentioned studies focused on single cells while in the current study, cell-cell interaction is present, fostering network formation. In addition, YAP N/C ratio has been shown to be negatively affected by high density of cells [109,110].

As for the MRTFA N/C ratio, the maximum (1.6) was also at G10 and minimum (1.3) at the ctrl although it was different from YAP in the fact that the second largest ratio was at G5 (Fig. 4.5d and Fig. C5 in Appendix C). This proves how mechanical confinement can indeed affect the behaviour of MRTFA. A possible explanation of our results is that when the cells are under a relatively large amount of mechanical stress that is induced by confinement and/or high polarization (like in G5 and G10), MRTFA is mostly located in the nucleus since the polymerization of G-actin monomers into F-actin filaments increases significantly. The mean intensity of MAP2 showed a maximum at G30 followed by G10 with a minimum at G5. MAP2 intensity slightly increased from D1 to D3 for all conditions. However, the effect of confinement in the grooves on the expression of MAP2 was not statistically significant (Fig. 4.5e).

Similar to the behaviour of the nuclei, FAs exhibited a great deal of alignment within the grooves compared to the ctrl as shown in images acquired via confocal microscopy (Fig. 4.6a). The interaction between the filopodia of the growth cone (where most of the FAs are concentrated) and the hatch lines of the structures was evident when qualitatively investigating via SEM images (Fig. 4.6b.i-iii). This was contrary to the spread out filopodia exhibited on the flat ctrl (Fig. 4.6b.iv). As aforementioned, this interaction increased the alignment since the hatch line distances were of the same scale as that of the filopodia (100-300 nm in size) [71]. On the other hand, such directed growth was not noticed on the flat ctrl surface since the filopodia were widely spread across the substrate.

The number of FAs per cell showed a significant difference between the cells cultured on the flat ctrl and those in any of the microgrooves with a maximum at G10 and a minimum at G30 (Fig. 4.6c). This may be linked to the higher YAP N/C ratio since YAP was shown to be affected by the behaviour of FAs [88]. The average area of FAs per cell did not show a specific trend since it was comparable for all cases except for G30 where there was a maximum (Fig. 4.6d) at D1. As for their alignment along the major axis of the 2.5D microgrooves, FAs exhibited a clear trend where the highest alignment was in G5 (Fig. 4.6e).

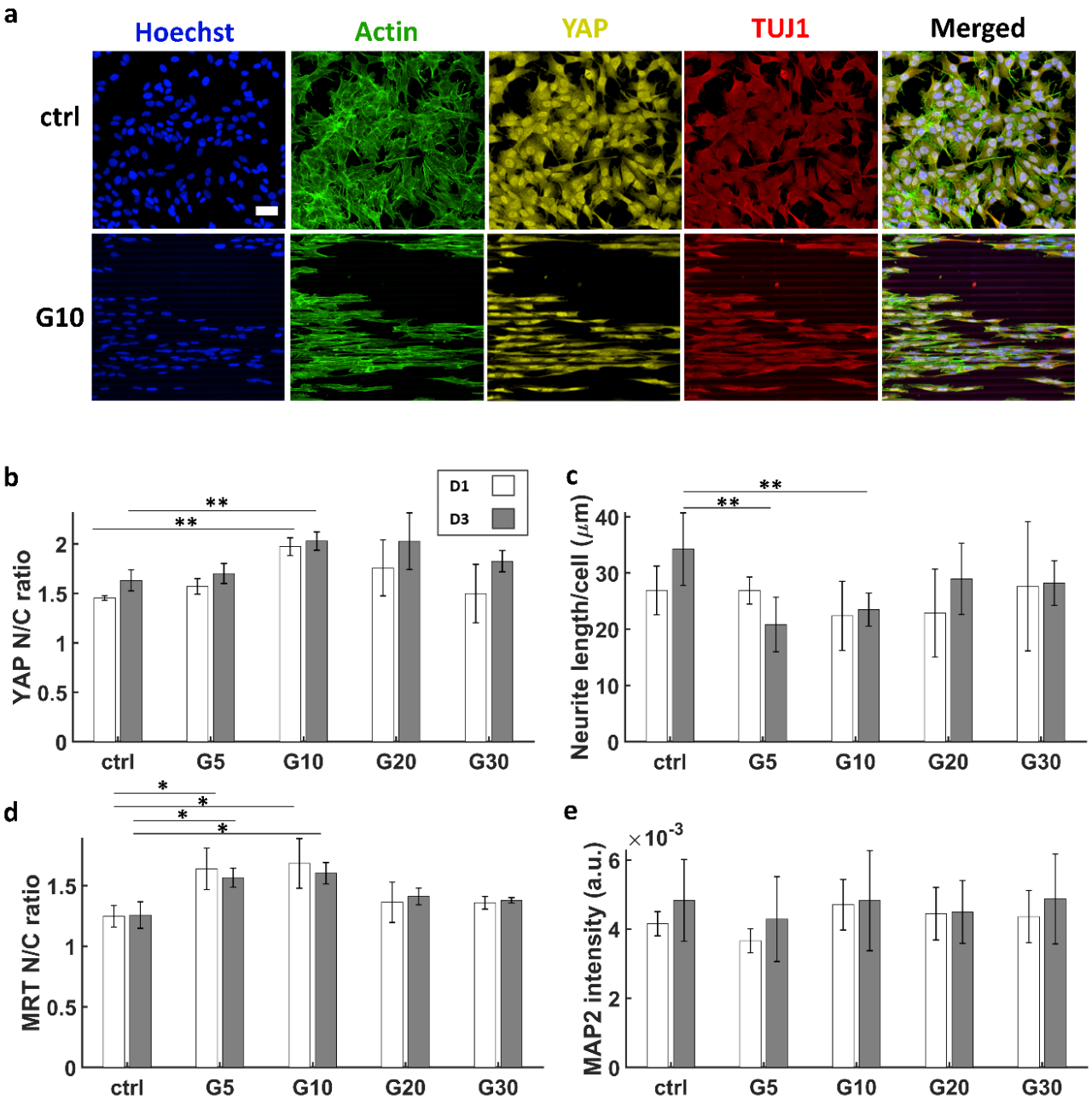

Fig. 4.5. (a) Maximum Z-projection images obtained via confocal microscopy of the SH-SY5Y cells at D3 of differentiation on ctrl and G10. (b) YAP N/C ratio. (c) Average total length of processes per cell. (d) MRTFA N/C ratio (e) MAP2 average intensity. The white and grey bars represent D1 and D3 respectively. * corresponds to a p-value < 0.05 and ** corresponds to a p-value < 0.01. P-values were obtained by two-tailed student's t-test. For YAP and MRTFA N/C ratios and MAP2 intensity, n = 3 samples for each time point. For neurite average length, n = 6 samples for each time point. Scale bar = 50 µm.

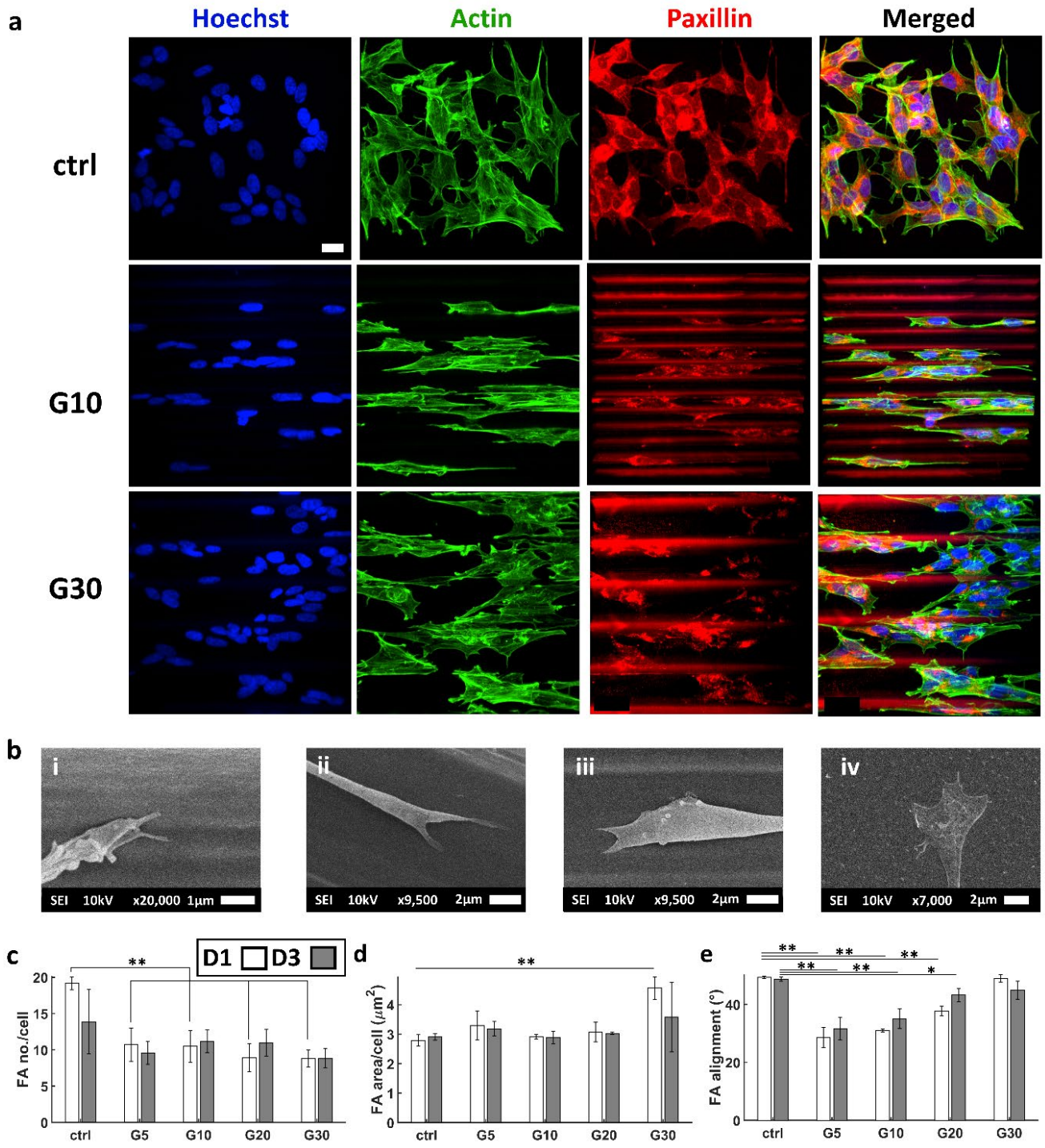

Fig. 4.6. (a) Confocal maximum Z-projection of SH-SY5Y cells at D3. (b) SEM images of filopodia adhering to 2.5D microgrooves (i), (ii), (iii) and the flat ITO-coated glass ctrl (iv). (c) The average number of FAs per cell. (d) Average FA area per cell. (e) Average alignment of FAs. The white and grey bars represent D1 and D3 respectively. * corresponds to a p-value < 0.05 and ** corresponds to a p-value < 0.01. P-values were obtained by two-tailed student's t-test. n = 3 samples for each time point. Scale bar = 20 µm.

4.3.3. Effect of confinement in 3D microchannels on differentiated SH-SY5Y cells

In order to assess the effect of fully confining 3D microenvironments, 3D microchannels of diameters ranging from 5 to 30 µm were printed via 2PP and, similar to the 2.5D microgrooves, SH-SY5Y cells were cultured and differentiated into immature neuron-like cells for 1 and 3 days. In order to determine the optimal length of the 3D microchannels, we performed an experiment in which SH-SY5Y cells were cultured on C30 microchannels and allowed to differentiate into neuron-like cells for 1 day. We tested channels of 250, 500, and 750 µm length. Our results showed that the 250 µm channels fostered the largest degree of cell colonization (Appendix C, Fig. C8). The reason for this behaviour can be attributed to the fact that the length of the longer channels hampered the diffusion of nutrients to the cells growing therein. It is also possible that the shorter channels fostered inter-cellular communication, thus having a direct influence on cell colonization.

An investigation of cell colonization showed that all structures were colonized by cells with the exception of C5 microchannels. Interestingly, the modified design of ADC5 and ADC10 improved the colonization of cells by 8 and 20% compared to the C5 and C10 designs respectively (Fig. 4.7a). Qualitative assessment via SEM imaging illustrated how cells probed the entrance of the 3D microchannels using their filopodia (Fig. 4.7b). The images show that the hatch line distances fostered the interaction between the filopodia and the microstructures thereby possibly increasing the chances of the cells colonizing the microchannels. Cell alignment showed the expected trend where the highest degree of alignment was in ADC5 and it decreased gradually until C30 (Fig. 4.7c,d). One particular observation was the significant elongation of nuclei in the ADC5 channels as shown by the maximum Feret diameter which reached 42 µm at D3 (Fig. 4.7e). This was accompanied by a decrease in the minimum Feret diameter to 5 µm (Fig. 4.7f). This phenomenon was also reflected in the area of the nuclei (Appendix C, Fig. C9) and the average cell area where the maximum was at ADC5 as well (Fig. 4.7g,h). Fig. C11 in Appendix C depicts 3D renders of cells in the microchannels.

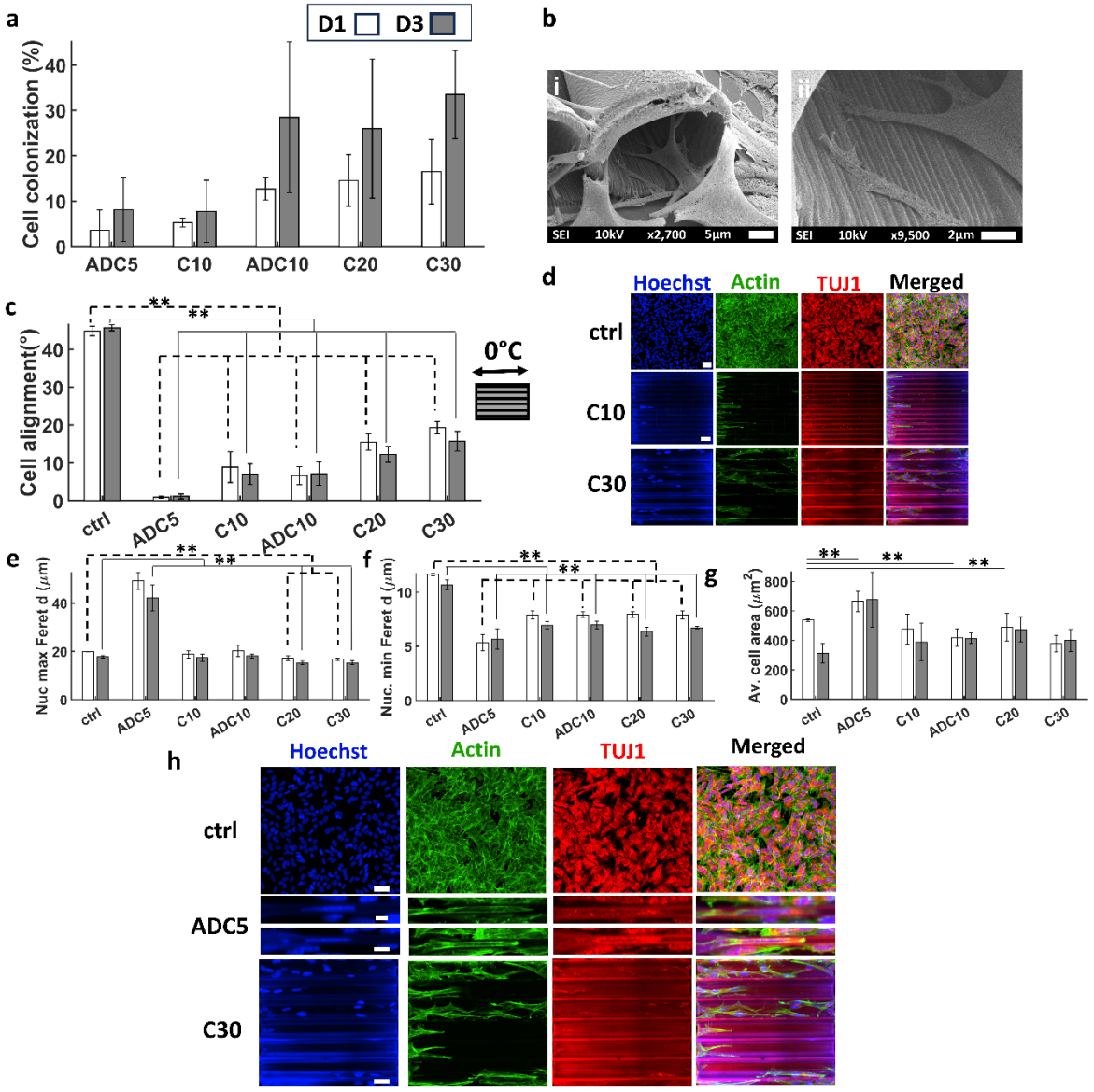

Fig. 4.7. (a) The percentage of cell colonization of SH-SY5Y in the 3D microchannels calculated as the ratio between the total area of cell bodies with respect to the total area of the 3D microchannels. (b) Representative SEM images of (i) and (ii) cells probing the entrance of the 3D microchannels via filopodia. (c) Degree of cell alignment on the microchannels. (d) Confocal maximum Z-projection images of the inner volume of the microchannels showing the alignment of cells at D3. Scale bar in the first row = 50 µm and the second row = 30 µm. (e) The average maximum Feret diameter of the cells. (f) The average minimum Feret diameter of the cells. (g) The average cell body area. (h) Confocal maximum Z-projection images of the inner volume of the channels exhibiting the substantial elongation of the cell nuclei in ADC5 compared to other channels and the flat substrate. The white and grey bars represent D1 and D3 respectively. Scale bars in the first, second, third, and fourth rows = 50, 10, 15 and 30 µm respectively. * corresponds to a p-value < 0.05 and ** corresponds to a p-value < 0.01. P-values were obtained by two-tailed student's t-test. n = 6 samples for each time point.

The ratio of YAP N/C was similar to that of the 2.5D microgrooves in the sense that it was larger than 1 for all cases and the ratios in D3 were larger than those in D1. We noticed that some cells in C10 and ADC10 showed very little expression of YAP altogether while most cells in ADC5 showed almost no expression of YAP (Fig. 4.8a). Interestingly, the trend observed here with the 3D microchannels was different from that of the 2.5D microgrooves. A minimal ratio of 1.1 lied at ADC5 followed by C10 while a maximum of 1.4 was found in the C20 channels followed by the flat ctrl and then C30 (Fig. 4.8b). As for the length of the processes of the cells, it increased from D1 to D3 (Fig. 4.8c). This was not the case for the ctrl due to the confluence of the cells. We also observed a maximum of 65 µm at C20 and a minimum of 12 µm on the flat ctrl. Almost no processes were observed for cells in ADC5 channels. Overall, both for the 2.5D microgrooves and the 3D microchannels, we observed that the YAP N/C ratio is inversely proportional to the total average length of processes per cell, which may be attributed to the degree of differentiation of the cells since it was shown that the lower the YAP N/C ratio, the further the cells are down the neuronal differentiation path [117,118]. An investigation of MRTFA N/C ratio showed that it was mostly at 1 and slightly below. The minimum was found at ADC5 and the maximum at C30 (Fig. 4.8d and Fig. C6 in Appendix C) which is contrary to the results of SH-SY5Y cells in 2.5D microgrooves. It is difficult to discern the reason behind this behaviour of MRTFA. As for MAP2 average intensity, it followed a similar trend of that of YAP N/C ratio with the exception that a slight decrease from D1 to D3 was noticed (Fig. 4.8e). For all three proteins, YAP, MRTFA, and MAP2, the trends showed a minimum at ADC5 which may suggest that the increase in cell polarity and 3D confinement has an adverse effect on tension in the cytoskeleton and hence the activation of these mechanotransductive pathways. The difference of results between the 2.5D microgrooves and 3D microchannels alludes to the fact that a 3D full confinement may have a different effect than a 2.5D partial one. This may be related to a number of reasons. First, differentiated cells cultured in C10, ADC10, and ADC5 3D microchannels exhibited a higher aspect ratio and polarity of nuclei compared to those cultured in G10 and G5 2.5D microgrooves. Second, a closed 3D microchannel creates a different microenvironment compared to 2.5D open grooves since nutrition is certainly more dependent on diffusion within the 3D microchannels due to the hindrance that the closed channel represents for the molecules of nutrients to flow to the cells through the medium. Naturally, this problem is expected to have been exacerbated for channels with smaller diameters (i.e. C10, ADC10, and ADC5). Finally, the density of cells in 3D microchannels was much lower than that in 2.5D microgrooves and cell density is known to have an effect on YAP N/C ratio [109]. The apparent difference in the behaviour of cells in 2.5D vs. 3D microenvironments has not been specifically investigated in literature and its exploitation may lead to furthering the understanding of fundamental behaviours of mechanotransductive proteins.

The terminal ends of the cells interacted with the hatch lines of the 3D microchannels to form FAs as depicted in Fig. 4.9a. Cells in ADC5 had very few FAs compared to all other 3D microchannels. The average FA number per cell at D3 showed a maximum at C10 and a minimum on the flat ITO-coated glass ctrl with no clear trend (Fig. 4.9b). On the other hand, the average FA area per cell had a maximum at C20 and a minimum at ADC5 (Fig. 4.9c) while the alignment of FAs increased (Fig. 4.9d) with the decrease of the diameter of the 3D microchannels proving the effect of the structures and especially the fine features of the hatch lines on the configuration of the FAs.

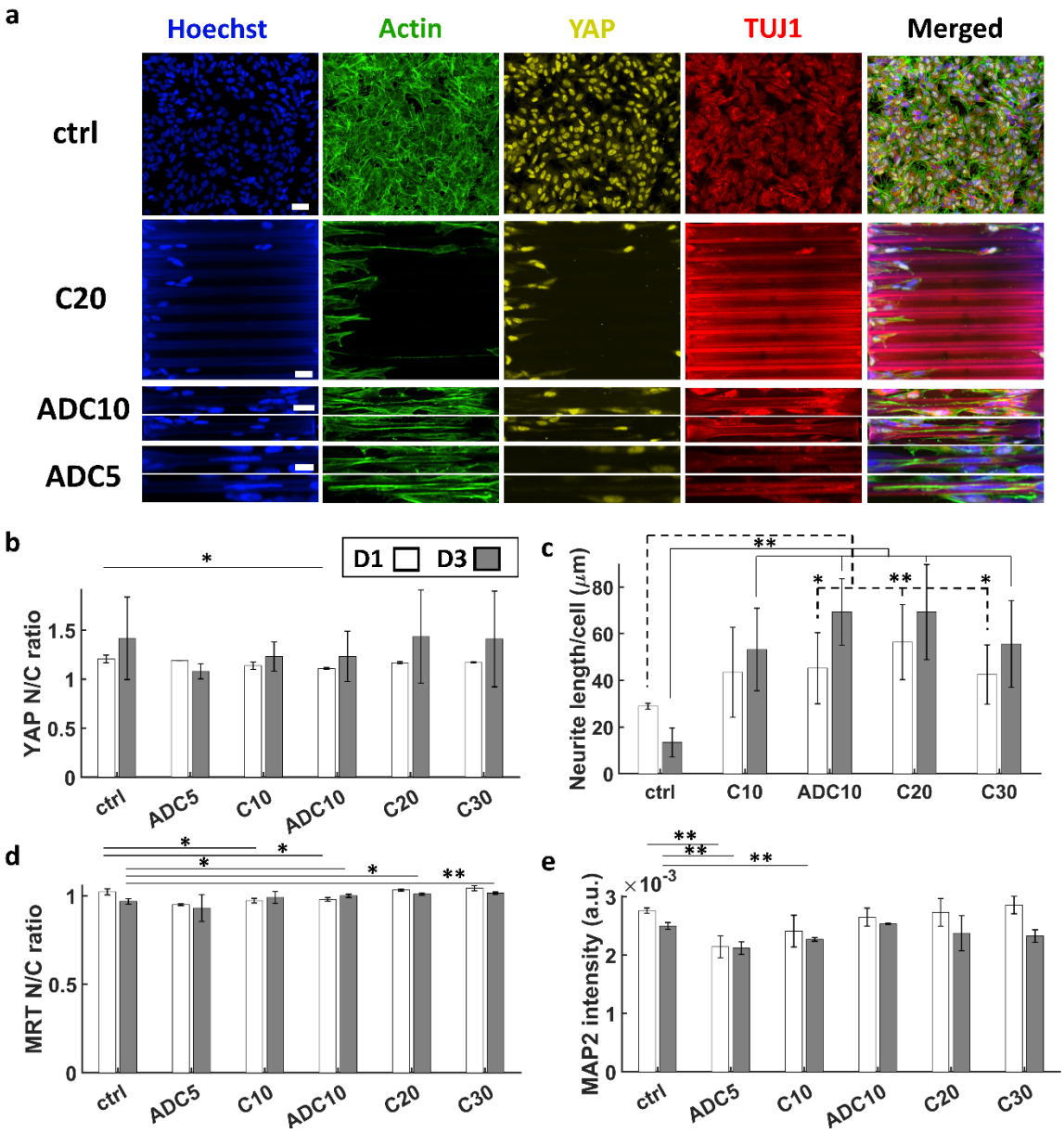

Fig. 4.8. (a) Maximum Z-projection images obtained via confocal microscopy of the SH-SY5Y cells at D3 of differentiation. Scale bars in the first, second, third, and fifth rows = 50, 30, 30 and 15 µm respectively. (b) YAP N/C ratio. (c) Average total length of processes per cell. (d) MRTFA N/C ratio. (e) MAP2 average intensity. The white and grey bars represent D1 and D3 respectively. * corresponds to a p-value < 0.05 and ** corresponds to a p-value < 0.01. P-values were obtained by two-tailed student's t-test. For YAP and MRTFA N/C ratios and MAP2 intensity, n = 3 samples for each time point. For neurite average length, n = 6 samples for each time point.

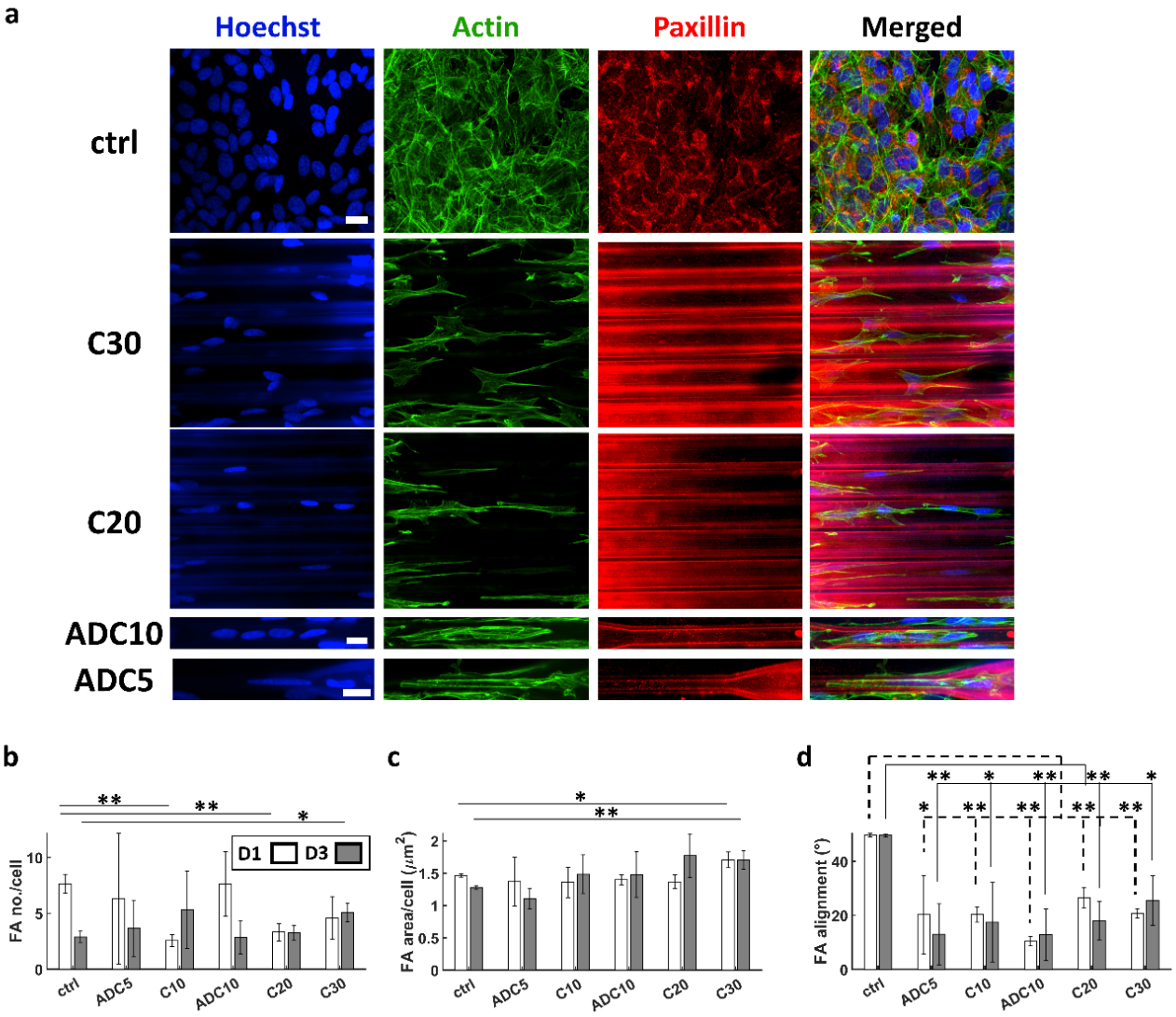

Fig. 4.9. (a) Confocal maximum Z-projection of SH-SY5Y cells at D3. Scale bars in the first, fourth and fifth rows = 20, 15 and 15 µm respectively. (b) The average number of FAs per cell. (c) Average FA area per cell. (d) Average alignment of FAs. The white and grey bars represent D1 and D3 respectively. * corresponds to a p-value < 0.05 and ** corresponds to a p-value < 0.01. P-values were obtained by two-tailed student's t-test. n = 3 samples for each time point.

4.3.4. Effect of confinement in 2.5D structures on hiPSC-derived neurons

Following the investigation conducted on SH-SY5Y differentiated cells in 2.5D microgrooves, we performed a twin study in presence of hiPSC-derived cortical neurons due to their higher physiological relevance in the field of neuro-mechanobiology and *in vitro* disease modelling [143–145]. 2.5D microgrooves of the same size range were employed and hiPSCs were differentiated into immature cortical neurons for 7 and 14 days (i.e. D7 and D14). Cells colonized all 2.5D microgrooves and formed complex networks (Fig. 4.10a and Fig. C12 in Appendix C), but interestingly, the degree of colonization decreased from D7 to D14 (Fig. 4.10b) which may indicate that upon

further maturation into neurons, these cells prefer to form unaligned clump-like networks (data not shown). As for alignment, qualitative investigation of the cells via SEM imaging showed a high degree of interaction between the cells and the microstructures. The processes of the cells aligned along the lines of the hatch lines and in some cases their filopodia probed in a parallel direction to the lines. The cells also aligned on top of the ridges and showed a high degree of connectivity (Fig. 4.10c). The variation of the angles of the nuclei with respect to the direction of the 2.5D microgrooves decreased for the smaller grooves as expected (Fig. 4.10d). The minimum Feret diameters of the nuclei decreased with the decrease of the size of the 2.5D microgrooves as well (Fig. 4.10e) while the cell area showed a maximum on the flat ctrl substrate and a minimum in the G20 microgrooves (Fig. 4.10f). In combination with the minimum Feret diameter, the maximum Feret diameter of the nuclei illustrated the high polarity of the cells in all 2.5D microgrooves compared to the ctrl (Fig. 4.10g,h). Fig. C13 in Appendix C depicts 3D renders of cells in the microchannels.

As for the YAP N/C ratio, similar to the SH-SY5Y cells, the ratio was always larger than 1 (Fig. 4.11a,b). There was an increase from D7 to D14 for all cases. At D14, the ratio was larger than 2. A minimum of 2.1 was at G5 and a maximum of 2.7 was at G20 (Fig. 4.11b). In relation to the cell body area, there seems to be an inversely proportional relationship of YAP N/C ratio. These results are similar to those reported for SH-SY5Y cells therefore the same argumentation for the possible reasons behind this correlation follows. A study of the average total neurite length per cell exhibited a minimum at G30 and a maximum at G5, although for the latter one a relatively high standard deviation was observed (Fig. 4.11c). However, no noticeable trend was observed nor could we deduce a relationship between this elongation and the YAP N/C ratio. For MRTFA N/C ratio, the maximum was 2.3 at G10 and a minimum of 1.6 was at G20 (Fig. 4.11d and Fig. C7 in Appendix C). Similar to SH-SY5Y cells in 2.5D microgrooves, differentiated hiPSC-derived neurons at D14 showed more MRTFA N/C ratio albeit with a much larger difference between the two time points in the case of hiPSCs. Having a maximum at G10 for MRTFA N/C ratio in hiPSCs illustrates that the relationship drawn between confinement and MRTFA due to increased mechanical stress can be carried over from SH-SY5Y cells to this more physiologically relevant model of hiPSCs. Since the study performed on hiPSCs here was a proof of principle, we would recommend further investigation into this particular phenomenon in the future with more samples to obtain statistically significant data. The mean intensity of MAP2 showed a maximum at G10 and a minimum at G5 with no clear trend relatable to YAP or FAs (Fig. 4.11e). This can be seen as contrary to the study of Ankam et al. where they showed that the expression of MAP2 of hESC-derived neurons increased when cultured on nanogratings of 250 nm width and height compared to flat PDMS substrates. This was accompanied by significant alignment of the cells as well [146].However, since MAP2 is an indicator of neuronal maturation, these results may suggest that confinement aids the differentiation of hiPSCs into neurons until a certain extent after which, confinement exhibits an adverse effect on neuronal maturation (i.e. in G5).

The average FA number per cell showed a substantial increase compared to the SH-SY5Y cells (Fig. 4.12a). This increase in number of FAs was accompanied by a significant decrease in the sizes of FAs for hiPSC-derived neurons (Fig. 4.12b-d). This is most probably due to the nature of FAs in hiPSC-derived neurons for which we observed how neuronal processes (supported by actin filaments) are much longer, much more branched and with finer protrusions than SH-SY5Y-derived neuron-like cells. In our observations, this lead to the formation of much finer and much more spread FAs in the case of hiPSCs. The maximum of the size of FAs was at G10, but no apparent relationship could be drawn between it and the N/C ratio of YAP, which suggests that the conformation of the cytoskeleton and the area of the cell body are the main effectors on the behaviour of YAP in hiPSC-derived cortical neurons.

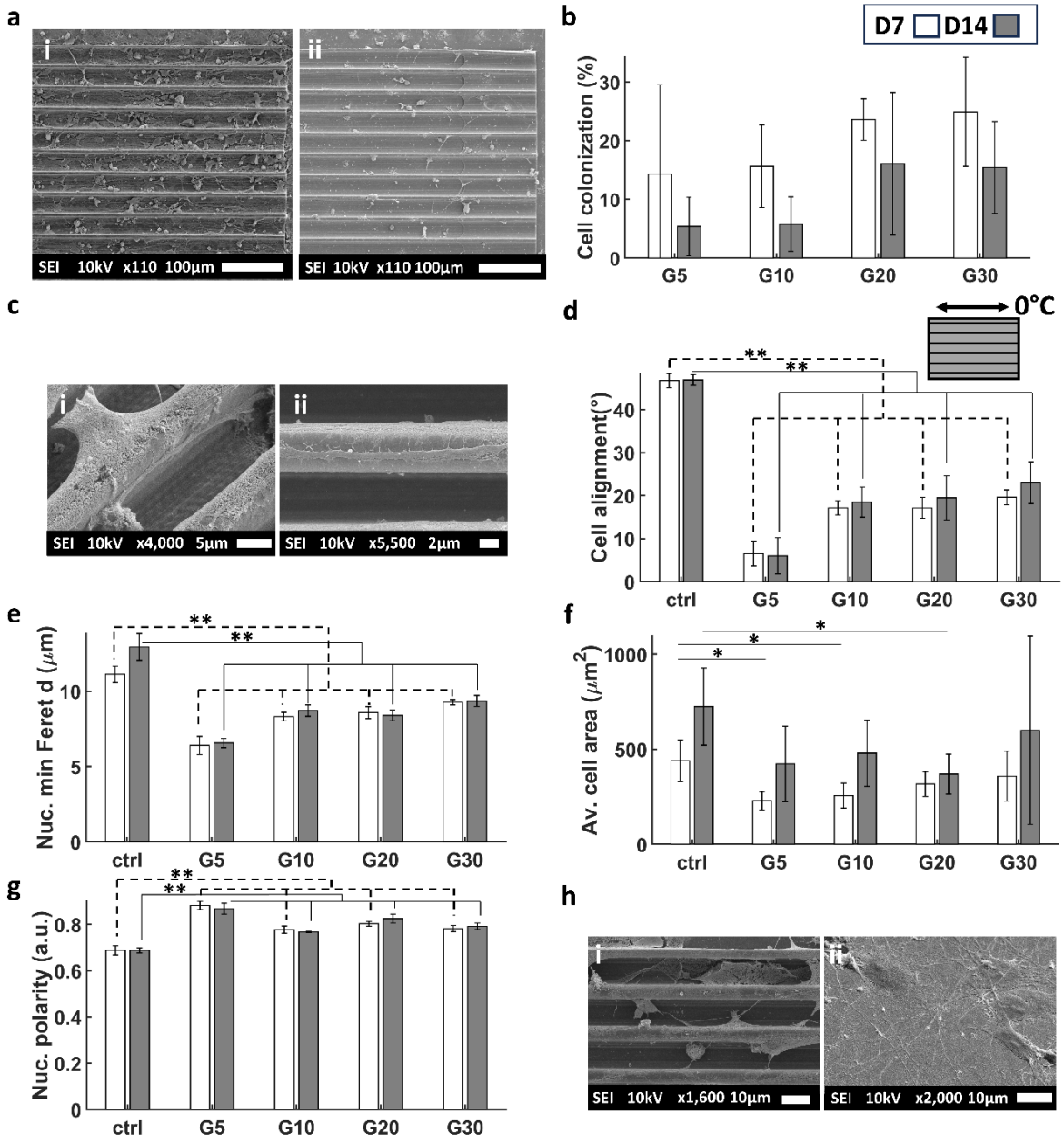

Fig. 4.10. (a) Representative SEM images of hiPSC-neurons (i) at D7 in G20 and (ii) at D14 in G20. (b) The percentage of cell colonization of hiPSC-derived neurons in the 2.5D microgrooves calculated as the ratio between the total area of cell bodies with respect to the total area of the microgrooves. (c) SEM images showing the alignment and connectivity of cells at D7 in (i) G10 and (ii) G5. (d) Degree of cell alignment in the 2.5D microgrooves. (e) The average minimum Feret diameter of the cells. (f) The average area of the cell bodies. (g) The average nuclear polarity (where 0 signifies a perfect circle and 1 a straight line). The white and grey bars represent D7 and D14 respectively. (h) SEM images illustrating the polarity of the cells at D7 in (i) G10 vs. (ii) the flat substrate (ctrl). The white and grey bars represent D7 and D14 respectively. * corresponds to a p-value < 0.05 and ** corresponds to a p-value < 0.01. P-values were obtained by two-tailed student's t-test. n = 3 samples for each time point.

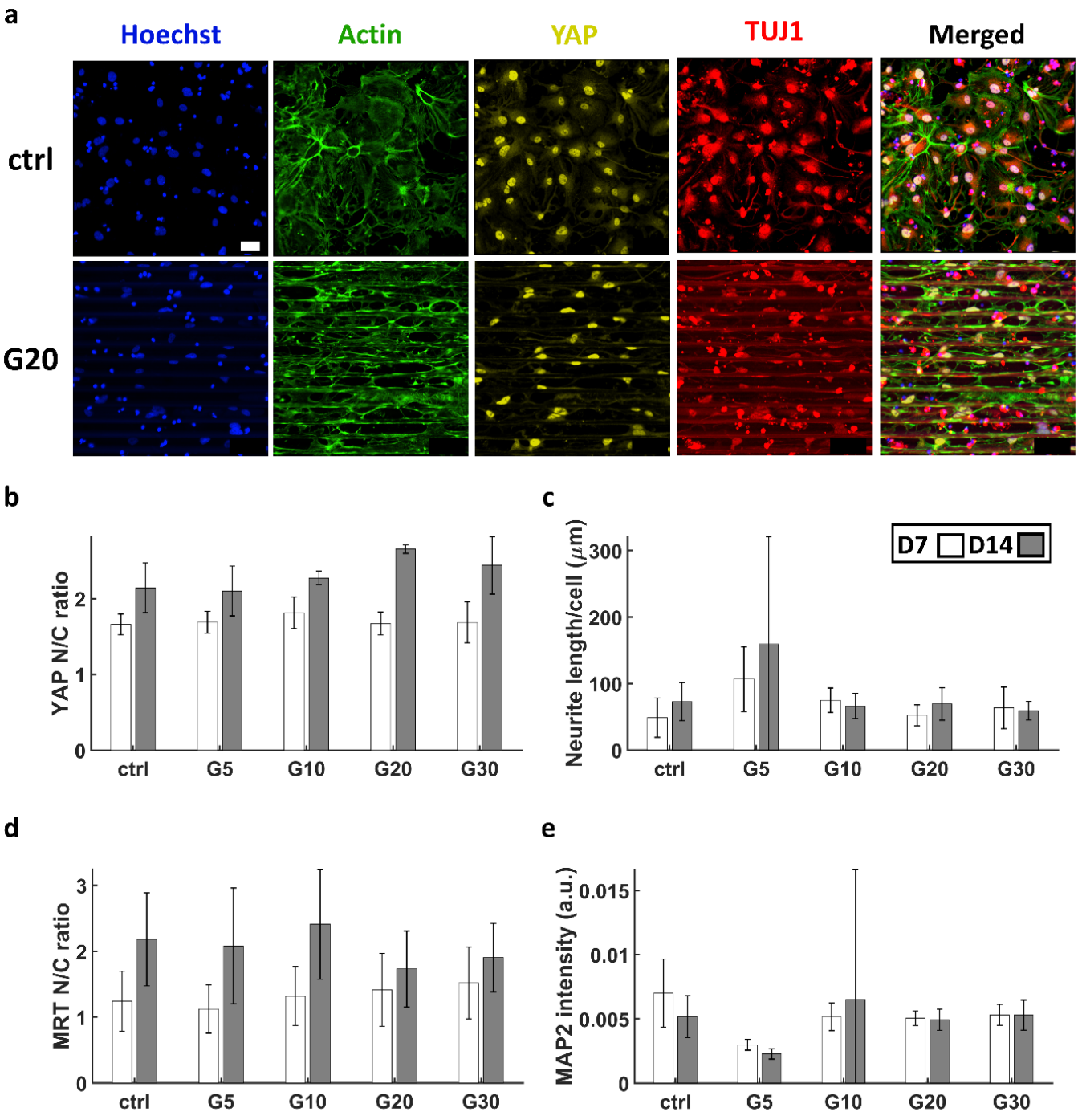

Fig. 4.11. (a) Maximum Z-projection images obtained via confocal microscopy of the hiPSC-neurons at D7 of differentiation. (b) YAP N/C ratio. (c) Average total length of processes per cell. (d) MRTFA N/C ratio. (e) MAP2 average intensity. The white and grey bars represent D7 and D14 respectively. For YAP N/C ratio, n = 3 samples for each time point. For neurite average length, n = 4 samples for each time point. For MRTFA N/C ratio and MAP2 intensity, n = 1 sample for each time point. Scale bar = 50 µm.

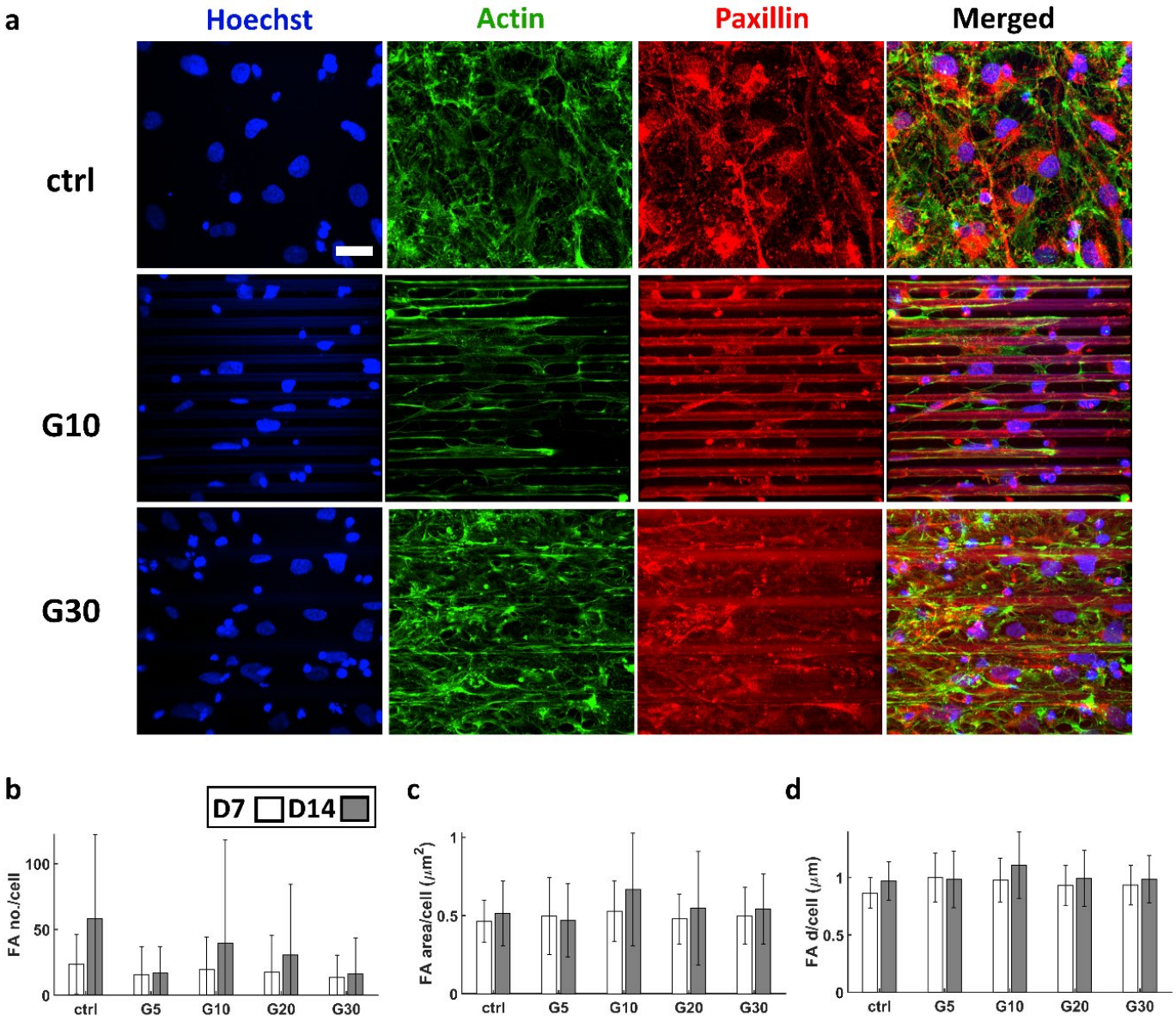

Fig. 4.12. (a) Confocal maximum Z-projection of hiPSC-derived neurons at D7. (b) The average number of FAs per cell. (c) Average FA area per cell. (d) Average FA diameter per cell. The white and grey bars represent D7 and D14 respectively. n = 1 sample for each time point. Scale bar = 30 μm.

4.4. Conclusions

Mechanotransductive proteins such as YAP and MRTFA play a vital role in neuronal development. They are in a constant dynamic state where they are affected by the conformation and polymerization of the actin filaments of the cytoskeleton. This is closely related to the formation and alignment of FAs on different substrates. One of the most interesting mechanical cues that has the ability to alter the conformation of the cytoskeleton is mechanical confinement. In this study, we investigated the effect of confinement, in 2.5D microgrooves and 3D microchannels

with diameters ranging from 5 to 30 µm, on YAP, MRTFA N/C ratio and neurite elongation. We cultured SH-SY5Y cells on the microstructures and differentiated them into immature neuron-like cells for 1 and 3 days. Our results showed that, in presence of 2.5D microgrooves, an increase in YAP N/C ratio was accompanied by a decrease in average neurite length. In the 2.5D microgrooves, maximum values of YAP and MRTFA N/C ratios were noticed in the 10 µm grooves at which a decrease was observed and can be tentatively attributed to the increased polarity of the cell or the nucleus in the 5 µm grooves. For MRTFA specifically, it seemed that the increased mechanical stress, and consequently F-actin formation, induced by the smaller grooves, increased its N/C ratio as expected. In the case of the 3D microchannels, the novel alternative designs of the 5 and 10 µm tapered channels substantially fostered cell colonization. YAP and MRTFA N/C ratios had similar trends for which the minimum was found at the 5 µm and the maximum at the 30 µm 3D microchannels. The trend was therefore different from the one observed in the 2.5D microgrooves. This depends on the effects of 3D microarchitecture on the actin in the cytoskeleton compared to 2.5D microgrooves, although further research must be carried out to confirm differences between these microenvironments. Focal adhesions showed a high degree of alignment for all microstructures. We also cultured hiPSCs on the 2.5D microgrooves and differentiated them into immature neurons for 7 and 14 days since this is a more physiologically relevant cell model compared to SH-SY5Y cells. Interestingly, the behaviour of hiPSC-derived cortical neurons was similar to SH-SY5Y cells since the maximum of YAP and MRTFA N/C ratios were observed at the 20 and 10 µm 2.5D microgrooves respectively. No evident relationship was observed between the proteins and the length of neurites. On average, the number of FAs per cell was substantially higher compared to SH-SY5Y cells and their sizes were much smaller. In summary, our results suggest a relationship between YAP and MRTFA in relation to mechanical confinement in 2.5D and 3D engineered microenvironments. A relationship between these proteins and neurite outgrowth could be drawn for SH-SY5Y cells. Most interestingly, the results were different from 2.5D and 3D microenvironments alluding to the fact that mechanical confinement is highly sensitive to geometrical changes in the microenvironment. Further, another reason for the difference between the results is that the supply of nutrients and oxygen can be different in 3D microchannels compared to 2.5D microgrooves. Therefore we suggest in future studies to investigate the expression of hypoxia indicators such as HIF-1α [147] in order to confirm this hypothesis. Future studies attempting to discover additional relationships between these types of mechanical confinement and neuro-mechanobiology could include: the investigation of nuclear mechanotransductive proteins such as Lamin A/C [127] and be extended to disease models (e.g. Alzheimer's disease [113,148]); and the fabrication of confining microarchitectures made of softer biomaterials (e.g. photocrosslinkable hydrogels [149] and elastomers [150] with a Young's modulus in the kPa-MPa range).

5

Fabrication of 3D microscaffolds featuring stiff core and soft hydrogel shell

The development and use of materials to mimic the mechanical properties of brain tissue is an integral part of the field of neuromechanobiology. One property of materials that specifically stands out is stiffness since it has a large influence on the behaviour and fate of neurons. Due to the softness of brain tissue (Young's modulus = 0.1-1 kPa), researchers usually resort to the class of materials known as hydrogels since they possess stiffness in a similar range to that of brain tissue. However, properties such as swelling and shrinking in addition to the effect of surface tension especially at the microscale substantially compromises the structural stability of microstructure fabricated from hydrogels. To solve this issue, in this study, we developed a protocol in which we fabricated microstructures via 2PP made from a stiff photoresin and then grew a micrometric layer of polyethylene glycol methacrylate (PEGMA) hydrogel on top of them. Utilising such a method to fabricate microstructures with a stiff core and a soft hydrogel-based shell provides the necessary biomimicry of neuronal tissue while at the same time ensuring the structural stability of the microstructures due to the presence of the stiff underlying skeleton of the photoresin. We succeeded in growing a 1 µm thick layer of PEGMA hydrogel on top of micro-pedestals fabricated from the acrylate-based photoresin IP-S. Additionally, we fabricated 3D microcages from IP-S and grew a hydrogel layer on the beams. The hydrogel growth was highly specific to the microcages, but we noticed clogging of their pores with hydrogel films, possibly due to the effect of surface tension. Our developed protocol advances the field of neuromechanobiology towards obtaining microenvironments that truly simulate brain tissue in order to be used for *in vitro* studies of neurons in health and disease.

This work was done in collaboration with Chihao Kuo.

5.1. Introduction

In previous chapters, the role of topography, geometry, and stiffness as mechanical cues in affecting the behaviour of neurons was explored. Relevant fabrication techniques were elaborated therein. Moving over, and focusing more keenly on the factor of stiffness (intended as Young's modulus (E)), in this chapter, we specifically explore the development of novel protocols coupled with traditionally employed soft materials to fabricate structures mimicking the Young's modulus of brain tissue (E = 0.1-1 kPa [3]). The effect of substrate stiffness on the behaviour and fate of neurons and the relevance of this mechanical factor in the field of neuromechanobiology is evident. As aforementioned, the vast difference between the E of brain tissue and that of polystyrene (E ~ 3 GPa) [5] or glass (E ~ 70 GPa) [4], which are traditionally used for neuronal studies *in vitro*, can lead to significant changes in the behaviour of neurons with respect to their *in vivo* counterparts. To solve this issue, many researchers resort to a class of materials known as hydrogels. These materials are made of polymeric hydrophilic chains with an ability to swell to multiple times their original volume [151]. Hydrogels are commonly recognized to be soft materials with E as low as tens of kPa [152]. For many years, researchers conducting neuronal *in vitro* studies used hydrogels such as Matrigel™ as a bench mark of soft materials [153]. Indeed, studies have shown that hydrogels promote neurite outgrowth and neural cell growth [154–156]. Nonetheless, until now, most studies utilizing hydrogels simply cure a precursor solution to form a layer of the polymer in a 2D petri dish that does not resemble the native cell environment with its 3D geometrical complexities. Also, Matrigel is well known for its batch to batch variability issues [157]. Various research groups have shown the difference in neuronal and glial behaviour when they are cultured on 2D substrates vs. 3D scaffolds. Differences include neuronal network formation [158], connectivity, and synchronicity [159], effect of proton therapy on glioblastoma [160]. One possible reason for this change in behaviour/phenotype is the conformation of the focal adhesions [161] and the cytoskeleton resulting in a more round and compact shape of cells in 3D networks [162,163]. In order to fabricate 3D microstructures with high precision, freedom of design, and reproducibility, two photon polymerization (2PP) has been widely employed with soft hydrogel materials. Many research groups tried to couple the favourable properties of 2PP as a fabrication method and the desired mechanical properties (i.e. low E) of hydrogels by attempting to fabricate 3D hydrogel microarchitectures from materials such as Poly(ethylene glycol) diacrylate (PEGDA) or Gelatine-Methacrylate (GelMA) [18,164–167]. While it is certainly possible to fabricate such 3D structures, there lie many challenges in doing so. The main challenge is the fragility of hydrogel structures due to their low E, which leads to mechanical instability of the fabricated structures, especially at the micrometric scale, due to the swelling/shrinking properties of such materials. Indeed, these 3D microstructures are prone to collapse during development and drying due to surface tension/capillary forces. Consequently, the development of a robust and reproducible method of fabrication of 3D microstructures with soft surfaces and higher structural integrity is deemed an urgent need in the field. This assumes a specific relevance if we consider that some research suggests how cells are able to sense the stiffness only of the first micrometres of the underlying materials [168,169], rendering the fabrication of the whole structure out of hydrogel unnecessary. We therefore aimed to develop a protocol in which 2PP would be employed to fabricate a stiff skeleton of a microstructure made from an acrylate-based photoresin from which a hydrogel layer would be grown via simple ultraviolet (UV) curing [170]. In this way, the structural integrity, and thereby handling, of the microstructures would increase significantly due to the presence of the stiff skeleton while the soft outer layer of the hydrogel would provide a biomimetic environment for prospective neuronal cell culture applications. Our method relies on the protocol developed by Yu et al. in which they grow micrometric layers of hydrogel on the surface of millimetric sized silicon-based 3D structures by exploiting the hydrophilic/phobic properties of the structures and water solubility of the photoinitiators [171]. Matching hydrophobic surfaces with photoinitiators of low water solubility allowed for their diffusion into the initial surface-layers of the structures, thereby initiating the polymerization process of the hydrogel in these layers and creating a strong physical bond with the structures. In our study, we rely on the same physical principles in which we coat the surfaces of the microstructures with a photoinitiator of low water solubility. Afterwards, a water-based hydrogel precursor solution would be drop casted on the structures and cured. Owing to the low

water solubility of the photoinitiator adsorbed on the microfabricated polymer, the photoinitiator would not diffuse into the water-based solution and the growth of the layer of hydrogel would be restricted only to the surfaces of the microstructures. The main problem to be tackled in our protocol was to ensure the specificity of hydrogel growth (i.e. growth only on the surfaces of microstructures and not the entire substrate). In the following sections, we outline the protocol developed and the results observed. Morphological characterization of the structures was carried out by scanning electron microscopy (SEM) and atomic force microscopy (AFM). In addition, the Young's modulus of the hydrogel layer was measured by nanoindentation.

5.2. Materials and methods

In this section, the methods employed for fabrication and post processing of the microstructures are outlined. The protocol of growing hydrogel layers is as well laid out along with the characterization techniques used. All materials were purchased from Sigma Aldrich unless otherwise specified.

5.2.1. Design of microstructures

All structures were designed using SOLIDWORKS (Dassault Systèmes) CAD software. Three types of microstructures were designed for this study. The first one was a pedestal of dimensions 100 x 100 x 50 μm^3 (length x width x height). The second one was a microcage of 80 x 80 x 80 μm^3 dimensions with cylindrical beams of 15 µm in diameter. The microcage served as the unit cell of the third structure which consisted of 18 unit cells (i.e. microcages) with total dimensions of 210 x 210 x 145 μm^3.

5.2.2. Fabrication of microstructures

The 2PP DLW PPGT+ Nanoscribe printer (Nanoscribe GmbH & Co. KG) was employed to fabricate all microstructures. First, the "stl" files of the designed microstructures were imported into Describe (a proprietary software of Nanoscribe) for slicing and hatching. In 2PP printing, the structures are printed in a line-by-line fashion in which each structure is "sliced" into multiple layers in the vertical direction and each slice is "hatched" into multiple lines horizontally. The microstructures were hence sliced and hatched in Describe before printing. Slicing and hatching distances were chosen to be 1 and 0.5 µm respectively. Structures were printed on a 25 x 25 x 0.7 mm^3 (length x width x thickness) soda lime glass substrates coated with a nanometric layer of Indium-Tin-Oxide (ITO) (purchased from Nanoscribe GmbH & Co. KG). Prior to printing, the ITO substrates were coated with MAPTMS to improve the adhesion of the structures to the substrates. Briefly, substrates were first cleaned with acetone and IPA and then blow dried with an airgun. Subsequently, they were further cleaned and activated for 10 min via oxygen plasma exposure (Diener Femto plasma cleaner) at a flowrate of 5.5 cm^3/min, power of 100 W, frequency of 40 kHz, and pressure of ~ 0.24 mbar. Afterwards, they were immediately dipped in a solution of 0.2% v/v MAPTMS in ethanol for 1 h. The substrates were then rinsed with DI water and acetone before drying with an airgun and stored until further use.

Printing was performed at a laser power of 40 mW (80% of the maximum laser power) which is equivalent to 0.9 TW/cm^2 [63] and scanning speed of 80 mm/s. A 25x Zeiss objective (NA = 0.8) was employed in the printing process which took place in DiLL mode in which the objective was submerged in the resin. We used the Galvo configuration to print the structures. IP-S (a proprietary resin of Nanoscribe GmbH & Co. KG) was the photoresin of choice due to its higher Young's modulus and structural stability and possibility to create relatively large scale structures (micro to millimetre range) [172]. Samples were developed in PGMEA for 25 min followed by an IPA bath for 5 min before drying with an airgun.

5.2.3. Hydrogel layer growth

The developed protocol was adapted from the one of Yu et al. [171]. After development and drying of the IP-S-fabricated microstructures, they were coated with a photoinitiator of relatively low water solubility [173], namely 1-Hydroxycyclohexyl phenyl ketone, more commonly known as Irgacure 184 (I184) (Sigma-Aldrich). The coating took place by placing the microstructures in a bath of IPA with 10% w/v I184 overnight. Afterwards, the samples were rinsed with IPA to remove residual I184 adsorbed on the glass substrate. The samples were then left to airdry overnight. A hydrogel precursor solution of 20% w/v Poly(ethylene glycol) methacrylate (PEGMA) (Sigma-Aldrich) (see Fig. D1 in Appendix D for the chemical structures of I184 and PEGMA) in DI water was prepared and drop casted on the samples. An ultraviolet (UV) point source (Bluepoint 4 Ecocure Honle UV technology) was then used for 5 min for curing in order to grow a layer of PEGMA hydrogel on top of the microstructures. The point source had a diameter of 8mm; a total power of 10,000 mW/cm^2 at the emitting surface; and a wavelength range of 300-600 with a maximum intensity at ~375 nm. The point source was placed at a distance of 3 cm from the microstructures. Finally, the hydrogel-grown structures were developed in DI water for 1 hr to remove the unpolymerized PEGMA precursor solution and left to airdry. Fig. 5.1 shows a depiction of the fabrication process.

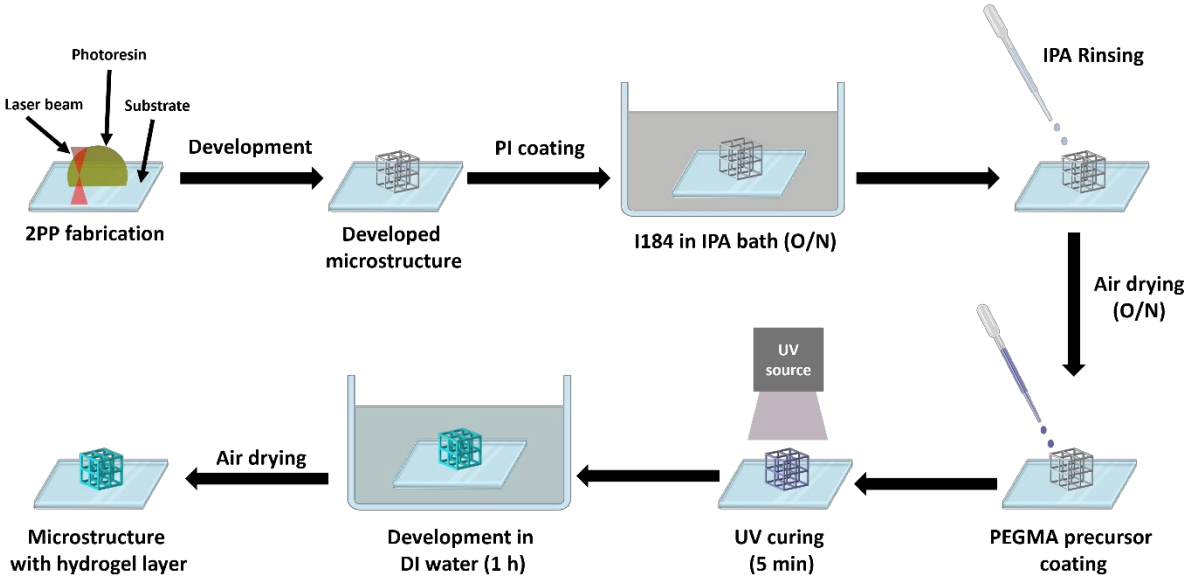

Fig. 5.1. A schematic representation of the process of growing a layer of PEGMA hydrogel on the surface of a stiff microstructure. PI = photoinitiator, IPA = Isopropanol, O/N = overnight, DI water = deionized water.

5.2.4. Contact angle measurement

The water contact angle of IP-S was measured to determine the degree of its hydrophilicity. In order to do that, IP-S was spin-coated on a glass substrate and then polymerized via a UV point source with the aforementioned properties in section 5.2.3 with a power of 80% and at a distance of 1 cm from the sample. The contact angle was measured by dispensing a droplet of Milli-Q water on the polymerized layer of photoresin and observing the angle of the droplet by a KSV CAM 200 (KSV Instruments) goniometer. The angle was then determined by a proprietary software of KSV Instruments.

5.2.5. Morphological characterization

5.2.5.1. Scanning electron microscope (SEM)

Prior to SEM morphological characterization, the microstructures were sputter coated with a thin nanometric layer of gold in a JEOL JFC-1300 auto-fine sputter coater. They were then visualized in a JEOL JSM-6010LA SEM

(JEOL (Europe) B.V.) scanning electron microscope at high-vacuum. Structures with hydrogel layers however were imaged in low-vacuum setting. The electron beam voltage range used was between 10 and 20 kV.

5.2.5.2. Atomic force microscopy (AFM)

The surface roughness of the hydrogel layers grown on the pedestals was measured by AFM. A Nanite B AFM (Nanosruf) was employed. The measurements were performed in non-contact dynamic force mode with a tip of Non-contact / Tapping™ mode - Long AFM Cantilever - Reflex coating (NCLR) type. All measurements were performed in DI water where the samples were pedestals with a hydrogel layer grown on them. Data was processed by Gwyddion software [174] to obtain the average of the height deviations from the mean line (R_a) and the root mean square average of the height deviations from the mean line (R_q).

5.2.6. Mechanical characterization

5.2.6.1. Compression testing

To determine the Young's modulus (E) of the IP-S microstructures, compression testing via a FEMTOTOOLS nanomechanical testing system FTNMT03 was employed. The tip was a flat punch Si tip of 50 x 50 μm^2 dimensions. The force range of the tip was 200,000 ± 0.5 µN. The microstructures used for measurement were pedestals.

5.2.6.2. Nanoindentation

The Young's modulus of the PEGMA hydrogel was measured by nanoindentation. A Piuma Nanoindenter (Optics11 Life) was used with a spherical probe of a 50 µm diameter and stiffness of 0.023 N/m. The samples were made from a PEGMA precursor solution of 20% w/v PEGMA in DI water with 0.1% w/v Lithium phenyl-2,4,6-trimethylbenzoylphosphinate (LAP) (Sigma-Aldrich) photoinitiator. The precursor solution was dispensed on a glass substrate and cured as mentioned in section 5.2.3. The measurement was performed in DI water and the indentation depth was 4 µm. A Hertzian contact model was chosen to calculate the Young's modulus of the hydrogel layer and the calculation was performed by using DataViewer, the Optics 11 proprietary software.

5.3. Results and discussion

5.3.1. Microstructures fabricated via 2PP

Two types of stiff microstructures were printed in order to grow a micrometric layer of hydrogel on their surfaces. The first ones were pedestals (Fig. 5.2a) and the second ones were microcages (Fig. 5.2b,c). All microstructures were printed with no issues using IP-S as the photoresin. They also exhibited minimal shrinkage.

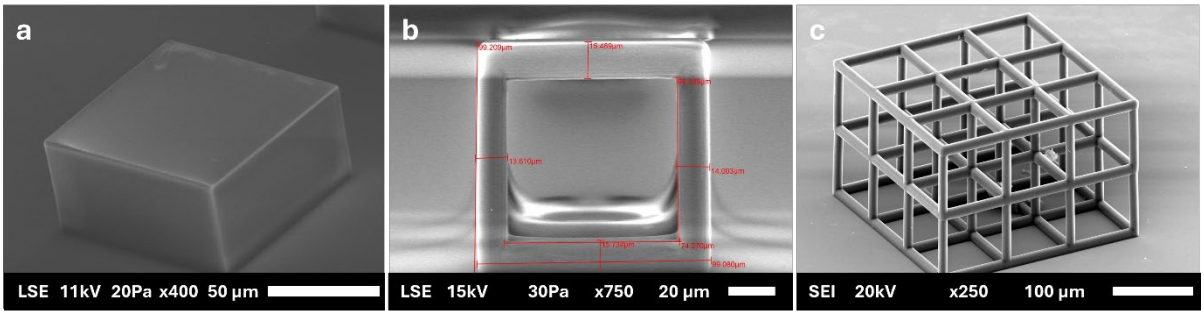

Fig. 5.2. Representative SEM figures of (a) the pedestal, (b) one unit cell of the microcage, and (c) the microcage composed of multiple unit cells.

Following printing, the Young's modulus (E) of the pedestals was measured by compression testing by employing the FEMTOTOOLS. E of IP-S was found to be 2.85 ± 0.58 GPa (n>3 samples). Contact angle measurement revealed IP-S to be hydrophilic after measuring the contact angle to be 77.7°± 0.1° (n>3 samples).

5.3.2. Hydrogel layer growth

5.3.2.1. Hydrogel layer growth on pedestals

The micro-pedestals were the structures used first to test the protocol of hydrogel growth that was elaborated in the Materials and Methods section. It is noteworthy to mention here that among our trials to reach a working protocol that would result in a local growth of the hydrogel layer, we attempted to use another photoinitiator simultaneously with I184. We chose LAP as a second photoinitiator and we mixed it with the PEGMA precursor solution at a concentration of 0.1% w/v (see Fig. D1 in Appendix D for the chemical structure of LAP). The rationale of LAP addition was centred around exploiting the differences in water solubility of I184 and LAP. Since I184 water solubility (1.1 mg/mL) is 40 fold less than that of LAP (40-47 mg/mL) [173], we hypothesized that after the precipitation of I184 on the surface of the microstructures, it will not transfer to the PEGMA water-based precursor solution drop casted on the substrate thereafter. On the other hand, LAP (mixed with the PEGMA precursor solution) would remain in the precursor water-based solution and avoid adsorption on the microstructures. Upon UV curing of the hydrogel precursor solution, the adsorbed layer of I184 would initiate the polymerization reaction at the surface of the microstructures thereby covalently and physically linking the polymer chains to the microstructures. Further growth of the hydrogel layer within the precursor solution would take place by utilising LAP as the photoinitiator which would eventually result in the formation of a micrometric hydrogel layer. Upon trying this protocol however, the results showed that the hydrogel layer lacked specificity since it formed on the entire substrate (Appendix D, Fig. D2.a). Additionally, the hydrogel formed on top of the pedestals showed the presence of hemispherical small clumps rather than a uniform layer (Appendix D, Fig. D2.b). Upon further investigation and in order to understand the reason behind this observation, we removed the step involving I184 from the protocol leaving LAP to be the only photoinitiator in the protocol. The result of this was the absence of polymerization of the hydrogel layer on any area of the substrate or the pedestal (Appendix D, Fig. D3). This led us to eventually remove LAP as a photoinitiator and use only I184 which resulted in the outcome elaborated below.

After employing the developed final protocol, thin layers of PEGMA hydrogel were grown on the pedestals (Fig. 5.3). The layers were thinnest on top of the pedestals and slightly thicker on the sides as depicted in the SEM figure. The layer thickness on top of the pedestals was roughly 1 µm (Appendix D, Fig. D4). The growth was highly localized onto the pedestals and a small circle around the microstructures. The reason behind the extension of hydrogel growth around the pedestals towards this micrometric circle is not clear, but may be due to the presence of residues of I184 photoinitiator around the pedestals that were left due to the formation of a meniscus around them during the photoinitiator coating stage in the protocol. Such meniscuses are expected to form during evaporation of the solvent due to surface tension forces between the solvent, the microstructures, and the glass substrate.

Further morphological characterization of the hydrogel layers formed on top of the pedestals was carried out via AFM. The surface roughness of the hydrogel layer was measured and the R_a and R_q values were 13.1 and 19.5 nm respectively. In an attempt to fully identify the hydrogel formed, we also measured its Young's modulus via nanoindentation. The value obtained was 429.3 Pa ± 93.7 Pa (n>3 samples).

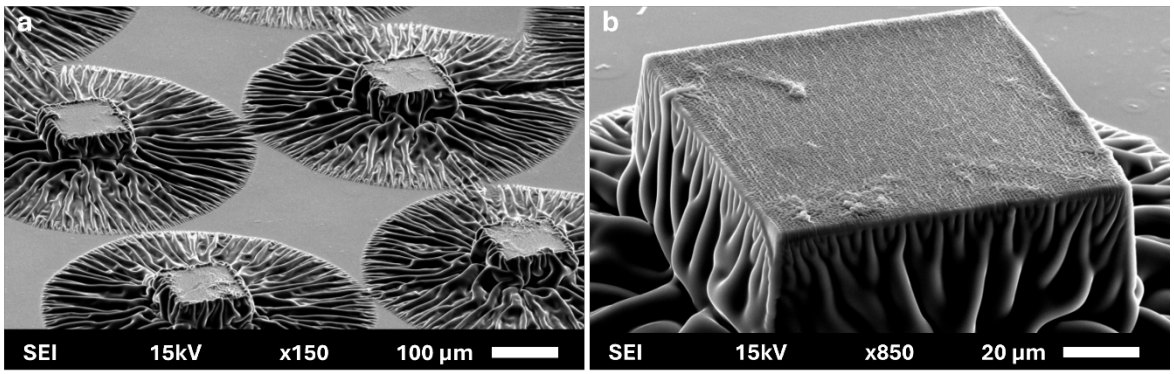

Fig. 5.3. (a) SEM image of pedestals with the hydrogel layer grown on top of them. (b) A zoomed in image showing the surface of one pedestal.

5.3.2.2. Hydrogel layer growth on 3D microcages

After developing a protocol that resulted in the uniform and local growth of hydrogel layers on stiff pedestals, we applied the same protocol on microcages made of single and multiple cells, since the future aim of our work was to culture neurons on 3D microstructures. In order to obtain a hydrogel layer that is restricted in growing specifically only to the beams of the microcages, we investigated the effect of two variables on the polymerization process. The first one was the concentration of PEGMA in the precursor solution. Concentrations of 1, 5, 10, and 20% PEGMA were used (Fig. 5.4). As shown in the figure, at 1% PEGMA the polymerization of the hydrogel was not sufficient to cover the beams of the microcage except for the base (Fig. 5.4a). At 5% PEGMA, the microcage was partially covered by the hydrogel layer (Fig. 5.4b) and at 10% PEGMA, the coverage of the hydrogel layer increased and clogged the pores of the microcage (Fig. 5.4c). Finally, at 20% PEGMA, there was, as expected, a large degree of over-polymerization of the hydrogel layer on and around the microcages (Fig. 5.4d).

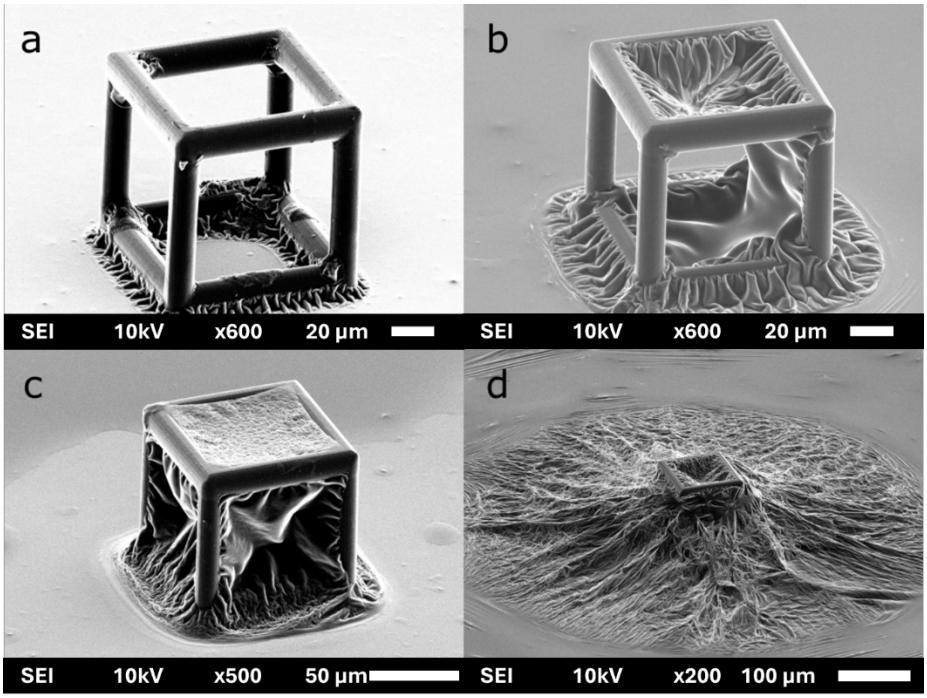

Fig. 5.4. SEM images exhibiting trials of hydrogel growth with different concentrations of PEGMA in the precursor solution. (a) 1%, (b) 5%, (c) 10%, and (d) 20% v/v PEGMA in DI water.

In all our attempts with various concentrations of PEGMA, the hydrogel layer never grew strictly on the beams of the microcages. A substantial amount of clogging in the pores of the cages was systematically observed. We tentatively attributed this to the surface tension effects which may have led to the formation of a film of the hydrogel precursor solution in the pores. During the UV curing phase, this film would then polymerize to form a layer of hydrogel within the pores.

The second variable under investigation was the time of UV curing. Instead of 5 min of UV curing, the time was scaled down to a range between 90 and 210 s. However, our results showed that there was not a clear correlation between the increase of UV curing time and the crosslinking increase or the hydrogel layer growth on the microcages (Appendix D, Fig. D5).

Finally, we investigated the adhesion strength of the hydrogel layers grown on the microcages by placing them in a DI water bath for 15, 30, 60 min and overnight. This investigation was performed to determine the possibility of utilising the structures we developed, after growing the layer of hydrogel on them, for neuronal mechanobiology studies, where they would be subject to culture media for extended periods of time. Fig. 5.5 exhibits the results of the investigation. After 15 min in a water bath, the hydrogel layer is still largely intact (Fig. 5.5a). Longer periods of time however resulted in the complete removal of the hydrogel layer (Fig. 5.5b-d). The reason for this may be the fact that the hydrogel layer poorly adhered to the surface of IP-S due to the poor swelling properties of microstructures fabricated from this photoresin. In other words, the I184 photoinitiator only adsorbed to the surface of the structures and did not diffuse in the surface-layers which in turn caused the hydrogel layer to only have a superficial weak bond on the surface of the microcages.

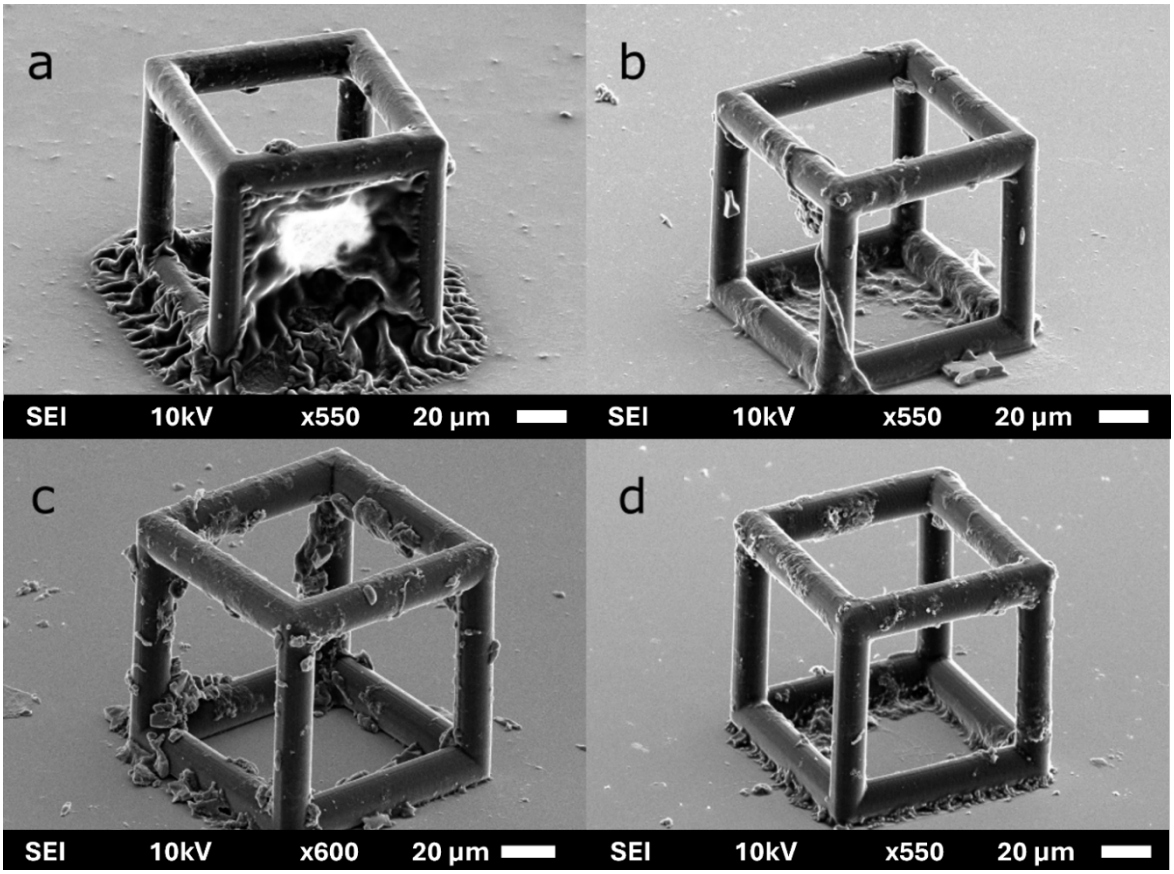

Fig. 5.5. Representative SEM images of the hydrogel coated microstructures after placing in a bath of DI water for (a) 15 min, (b) 30 min, (c) 60 min, and (d) overnight.

5.4. Conclusions

In light of recent exponential increase of studies on fundamental neuromechanobiology, the need for a simple and robust method of fabrication of soft microstructures has grown. In this study, we attempted to provide such a method by exploring different protocols of fabricating stiff microstructures via 2PP and then growing a micrometric layer of soft hydrogel wrapping them. We succeeded in growing a thin localized ~1 μm thick layer of PEGMA hydrogel on IP-S micro-pedestals. The Young's modulus of the hydrogel layers were as low as 0.4 kPa resembling the Young's modulus of the brain ECM. The hydrogel layers proved to grow only on the microstructures proving our protocol to have a high degree of specificity. Additionally, we investigated the growth of such layers on microcages to expand the use of our protocol towards other more complex geometries. The microcages proved to be more challenging than the pedestals as the hydrogel layers clogged their pores possibly due to the effect of surface tension. The low adhesion properties of the hydrogel layer after immersion in water proved to require further technical development. A possible reason for this behaviour may be the poor swelling properties of the IP-S photoresin from which the stiff microstructures were made. It is recommended therefore to use photoresins with better swelling properties such as IP-PDMS [150] in future studies to mitigate the problem of hydrogel layer adhesion. Nonetheless, our attempts to develop a robust protocol for the fabrication of a stiff/soft-core/shell structure represent a step into a new avenue that is much needed at the moment for the development of biomimetic platforms that can be efficiently produced and effectively used for studies in the field of (neuronal mechanobiology).

6

Conclusions & recommendations

This thesis reported a series of new fabrication protocols for the development of *in vitro* model employing physical cues such as geometry, topography and stiffness for the study of neuronal mechanobiology. This chapter presents the overall conclusions , which allowed to answer the main research question "*how to develop robust protocols for the fabrication of physiologically relevant and reproducible neural microenvironments by employing two-photon polymerization technique?",* along with future recommendations for endeavours to come.

1. **Two-photon polymerization of 2.5D and 3D microstructures fostering a ramified resting phenotype in primary microglia.**

   The technology of 2PP was employed to fabricate arrays of 2.5D nanopillars, micropillars, and 3D pillar-decorated-microcages for influencing the phenotypic expression of primary rhesus macaque-derived microglia. Overall, the results showed an increase in the phenotypic expression of ramified microglia when cultured on nanopillar arrays compared to those cultured on flat substrates, which is indicative of a homeostatic condition of these cells. On the other hand, we reported a simultaneous decrease in expression of the amoeboid phenotype. This result is hypothesized to have been due to the relatively low effective shear modulus of the nanopillar arrays (0.25 MPa), which is closer to the stiffness of brain tissue than to the one of conventional plastic or glass petri dishes. In addition, the unique topography of the arrays could have also had an effect on the cells since it more resembled the structure of the ECM, and the diameter of the pillars was of the same order of magnitude of that of filopodia, thereby increasing the probability of interaction of the cells with the structures. The results mentioned should be corroborated in future studies with investigations of gene and protein expression in order to confirm the functional nature of these phenotypes. Fabricating such structures with 2PP was of relative ease and high reproducibility in part due to the high stiffness of the resin of choice (IP-Dip, E~ 1 GPa). This specific method of fabricating micro and nanopillars using a relatively stiff resin provides both, a facile method of fabrication in addition to an innovative way of manipulating the effective shear modulus by altering the dimensions of the pillars.

   As for the microcages, we fabricated micro- and nanopillar-decorated cages. The function of these 3D decorated microscaffolds was to attempt mimicking the complex architecture of the ECM. While there was no apparent specific effect of the microcages on the phenotypic expression of the microglia, we did observe in particular for the smaller cages (i.e. cages with dimensions significantly smaller than the average cell size) that they were engulfed by the microglia in what seemed to be an attempt of phagocytosis. Microglia cultured on the microcages with sizes bigger than the average cell size exhibited significant interaction between the filopodia and the micro- or nanopillars. The results of this study indicated the possibility of the manipulation and control of phenotypic expression of primary primate-derived microglia via 2PP-fabricated microstructures. By utilising the proposed method of combining this fabrication technology with stiff resins, new avenues of investigation of healthy and diseased microglia may be opened in the future.

   It is noteworthy to mention that the effect of array topography and shear modulus should be differentiated from each other in future studies since it is not possible to claim one or the other as the main reason behind the observed results. Other recommendations include the focus on development of a robust method of performing gene expression studies of the cells cultured on the microstructures only. In other words, a protocol should be developed to prohibit the attachment of cells to the glass substrate upon which the structures are printed. This will facilitate carrying out relevant gene expression tests that will contribute to the confirmation of quantitative (based on immunochemistry studies) or qualitative (based on observations via SEM) results. Finally, a prominent bottleneck in the study appeared to be the

high autofluorescence of the polymer especially in the blue and green channels (445 and 521 nm respectively). It was substantially difficult to distinguish the nuclei of the cells from either the pillar arrays or the microcages. Moreover, this autofluorescence at times rendered one channel unusable. Due to this particular difficulty, we sought of a method to eliminate or supress the cumbersome feature of autofluorescence of microscaffolds while maintaining the possibility to use resins that would allow for printing with the highest possible resolution using 2PP, which is treated in the next paragraph.

2. **Suppression of auto-fluorescence from high-resolution 3D polymeric architectures fabricated via two-photon polymerization for cell biology applications.**

As indicated in previously, autofluorescence is a specifically problematic feature of 2PP-fabricated microstructures in the context of mechanobiological studies. Autofluorescence of microscaffolds negatively affects studies in which visualization and quantification of cells cultured on these structures and proteins expressed therein is carried out.

We investigated two methods of suppression of autofluorescence in an attempt to develop a universal protocol that can be used with any material regardless of its chemical composition. The two methods proposed were photobleaching and autofluorescence quenching. Four widely used commercial photoresins for 2PP were investigated in this study, namely IP-Dip, IP-L, IP-S, and IP-PDMS. Both methods proposed for autofluorescence suppression worked with all materials. Photobleaching using a powerful UV light source was indeed very effective with all four materials. Reduction in autofluorescence ranged from 61.7-92.5% for an emission range of 410-750 nm. One clear observation, however, was that for IP-Dip, specifically, bleaching resulted in a reduction in the blue and green regions of the emission spectrum, but an increase in the red one. This indicates the possible creation of a new species that is particularly autofluorescent in that region of the spectrum. On the other hand, quenching via coating the structures with Sudan Black B (SBB) resulted in a reduction of autofluorescence in the range of 33-95.4% for the same emission range. On average, the results from the two methods were comparable, however, quenching proved to be more sensitive to the surface properties of the material (e.g. hydrophilicity and roughness) since it is an adsorption-based process. This was evident specifically with the large increase in suppression of the fluorescence of IP-PDMS (33% to 53.7%) when treated a short oxygen plasma treatment before SBB coating.

As a proof of concept, we cultured SH-SY5Y neuroblastoma cells on microchannels and microcages fabricated from all four materials and performed an immunochemistry study to test the effectiveness of both methods in suppressing the autofluorescence of the structures. The cells were differentiated for 3 days on the microstructures to obtain immature neuron-like cells. They were stained for nuclei (blue channel), cytoskeleton (green channel) and focal adhesions (red channel). Our results showed an advantage of bleaching over quenching for our specific geometries. The main reason is that SBB quenched all photons coming from the structures as well as the stained cells. We also report that, after UV bleaching, an (expected) overall increase of Young's modulus was reported via compression (for IP-Dip, IP-L, IP-S) and nanoindentation (for IP-PDMS) characterization.

In conclusion, it must be noted that either one of these two solutions should be handled with caution. Even though there is a great deal of universality to their application, the choice of optimal method among them does depend on the material and geometry of the microstructure.

3. **Effect of confining 2.5D and 3D microarchitectures on neuronal YAP expression and neurite outgrowth**

The aim of this study was to utilize 2PP in combination with photobleaching for suppression of autofluorescence in order to study the effect of spatial confinement on neurons, and the expression of the mechanotransductive yes-associated protein (YAP).

In particular, we reported the combination of laser-assisted 3D printing and neuromechanobiology to unveil the effect of mechanical confinement on neuronal mechanotransductive proteins and neurite outgrowth. Polymeric 2.5D microgrooves or 3D microchannels were manufactured via 2PP and cultured with SH-SY5Y differentiated neuronlike cells or human induced hiPSCs derived neurons, due to their physiological relevance. We showed that: Yes-associated protein (YAP), responsible for multiple functions in neuronal development; Myocardin-related transcription factor A (MRTFA), involved in neurite outgrowth and axonal pathfinding; as well as neurite length, are directly linked and affected by the different types of mechanical confinement. Specifically, SH-SY5Y differentiated cells cultured in 2.5D microgrooves, featured an increase in YAP nuclear/cytoplasmic (N/C) ratio accompanied by a decrease in average neurite length. Both YAP and MRTFA N/C ratios exhibited maxima in 10 µm grooves indicating a strong relation with mechanical-stress-inducing confinement. hiPSCs-derived neurons showed a similar trend, as the maxima of YAP and MRTFA N/C ratios were observed at the 20 and 10 µm microgrooves respectively. In 3D microchannels on the other hand, both proteins' N/C ratio exhibited minima in presence of 5 or 10 µm channels, a behavior that was opposite to the ones observed in the 2.5D microgrooves and that indicates how the geometry and mechanical confinement of 3D microenvironments are unique compared to 2.5D ones due to focal adhesion, actin, and nuclear polarization. In summary, our results suggest a relationship between YAP, MRTFA, neurite length and mechanical confinement in 2.5D and 3D microstructures and pave the way for understanding the intricate interplay between mechanotransductive proteins and their effect on neural cell fate within engineered cell microenvironments. The developed engineered in-vitro neuromechanobiology platform can therefore propel the development of prospective in-vitro disease models for neurodegenerative disorders (e.g. Alzheimer's) where YAP plays a major role.

4. **Fabrication of neuronal stiff 3D microscaffolds covered with soft hydrogel micrometric layers**

This study was an attempt to further the efforts of providing innovative ways and protocols for the community of mechanobiological studies to manipulate the stiffness of microstructures. In this study, we targeted the fabrication of 2.5D pedestal structures and 3D microcages with a soft outer layer composed of a hydrogel material while having a stiff inner core constructed via 2PP. This protocol was attractive to pursue owing to the relative ease of fabrication of the inner stiff core using a commercial 2PP photoresin while having the benefit of a softer shell on the outside that would be beneficial in mechanobiological studies that require the simulation of softer tissues in the human body (e.g. brain tissue). The resin of choice in this study was IP-S and the hydrogel used to synthesize the outer softer shell was polyethylene glycol methacrylate (PEGMA). The method adopted for fabricating the structures included first coating the IP-S structures by a photoinitiator (Irgacure 184). After which, the structures were submersed in a PEGMA precursor solution. Finally, they were exposed to UV light to create the hydrogel layer via free radical polymerization that was initiated at the surface of the structures. Our results showed the possibility of fabricating 2.5D pedestals (dimensions = 100x100x50 um^3) of IP-S with a thin micrometric layer (thickness ≈ 1 µm) of soft PEGMA (E = 0.43 kPa) on top of it in a sustainable and reproducible manner. On 3D microcages (dimensions = 80x80x80 um^3), however, the process faced an obstacle of a lack of homogeneity and reproducibility. Hydrogel films noticeably clogged the pores of the microcages possibly

due to a multitude of reasons. The first of which is surface tension since it is plausible that these films may have been formed at the thresholds of the cages due to these forces. Another possible reason is the distribution of the photoinitiator across the structure which may have not been homogenous, thereby leading to over-polymerization at one place at the expense of another. In addition, a general issue for all structures, whether 2.5D or 3D ones, was the detachment of the hydrogel layer from the surface of the structures when submersed in water for over 15 min. This particular issue draws its relevance from the fact that mechanobiological studies require the stability of the structure in cell culture media for days. The reason for such poor adhesion of the hydrogel layer maybe the poor swelling properties of microstructures fabricated from IP-S which lead to the adsorption of the photoinitiator on the surface of the structures and not their diffusion in the layers under the surface. This may have resulted in a weak bond between the hydrogel and the structures.

Although the feasibility of using this method is evident, there are certainly multiple issues that need to be tackled in future studies. Therefore, we recommend using different photoresins (such as IP-PDMS) due to its superior swelling properties compared to IP-S [150] which would lead to the diffusion of the photoinitiator inside the microstructures, thereby securing a stronger bond with the hydrogel layer. In conclusion, our results provide a stepping stone in providing a facile protocol for fabricating a stiff/soft-core/shell structure in an innovative manner for mechanobiological studies, but the road still lies ahead for optimizing this protocol.

Appendix A

The contents of this chapter have been published as supplementary information in:

- A. Sharaf, B. Roos, R. Timmerman, G.-J. Kremers, J.J. Bajramovic, A. Accardo, *Two-Photon Polymerization of 2.5D and 3D Microstructures Fostering a Ramified Resting Phenotype in Primary Microglia*, Frontiers in Bioengineering and Biotechnology 10 (2022)

3D CAD models of a pedestal, a pillar array, and a pillar-decorated cage.

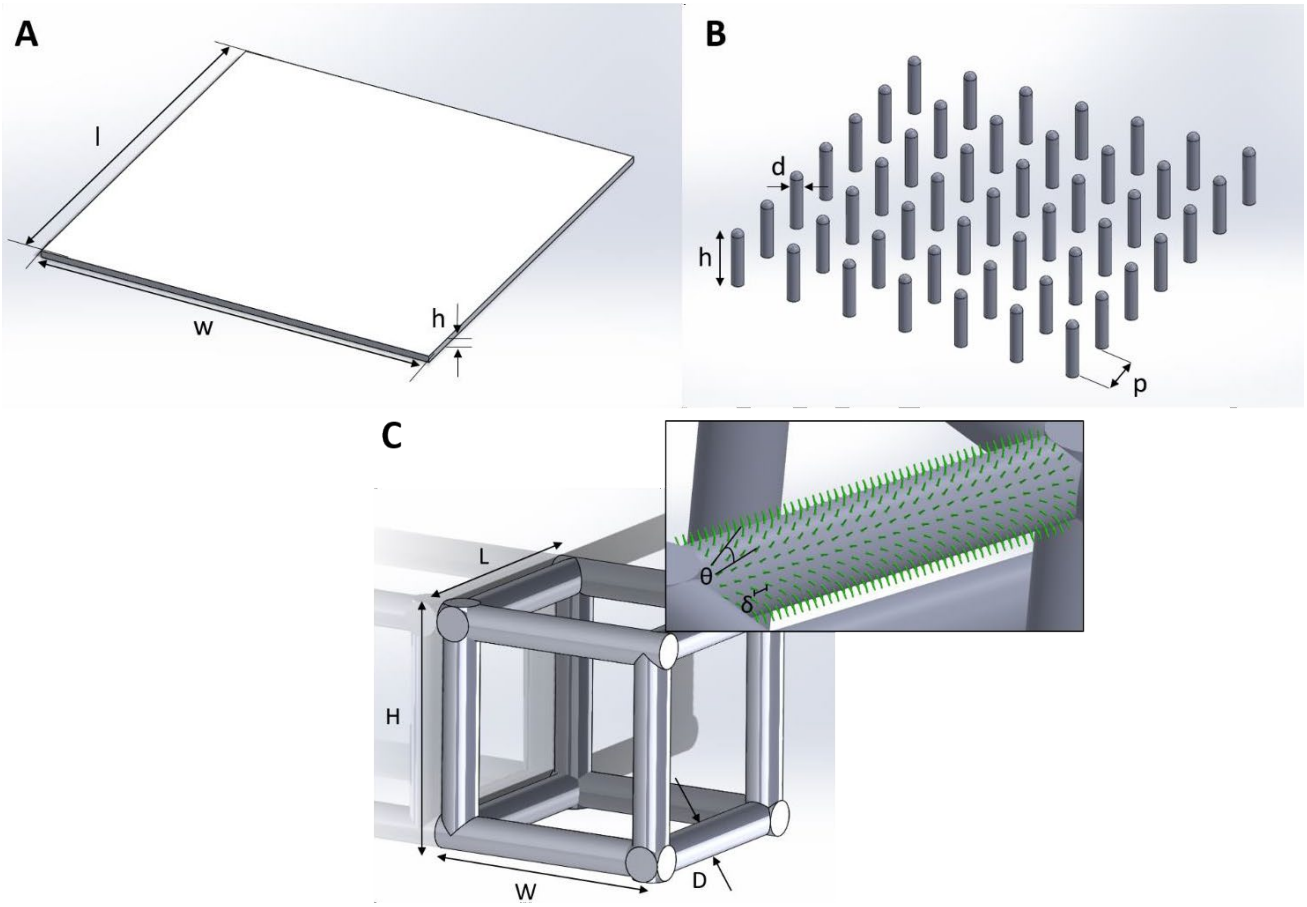

Fig. A1. 3D CAD models of 2D, 2.5D, and 3D structures created by SOLIDWORKS (DASSAULT SYSTEMES). (A) Pedestal (2D) design. l is the length, h is the height and w is the width. (B) 2.5D pillar array design. d, h and p are the pillar diameter, height and spacing between pillars, respectively. (C) 3D CAD model of a cage design with pillar decoration. H represents the height, W represents the width, L represents the length, and D represents the beam diameter. For the pillar decorations, θ = angular spacing between pillars and δ = lateral spacing between pillars

Schematic representation of mechanical strength characterization using FEMTOTOOLS nanomechanical testing system FT-NMT03 and AFM.

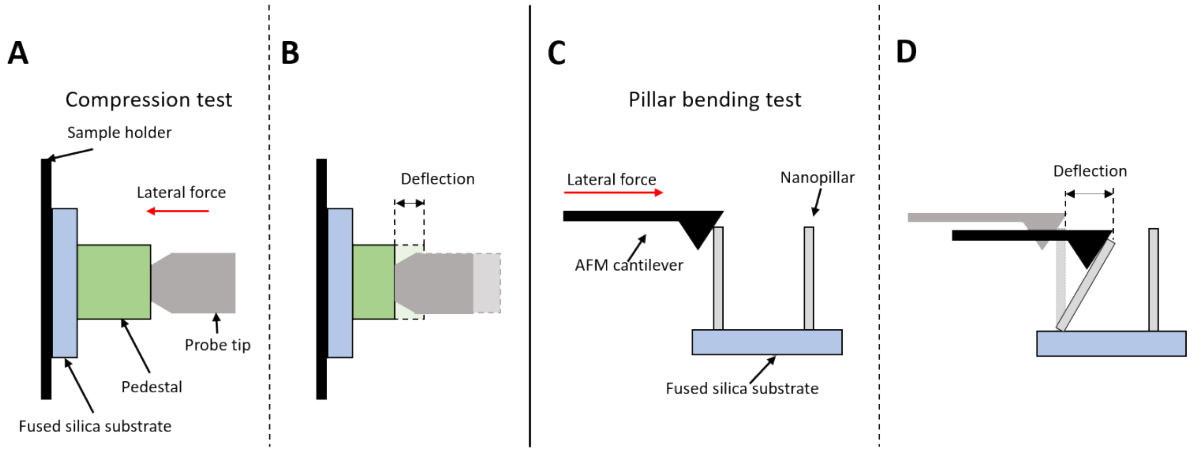

Fig. A2. (A), (B) Schematic of the compression test using the Femtotools. (A) Femtotools probe tip applies a lateral force on the pedestal. (B) Deflection of pedestal caused by the applied force of the tip of the probe. (C), (D) Schematic of the AFM pillar bending test. (C) AFM probe tip applies a lateral force on the nano-pillar. (D) Deflection of nano-pillar caused by the applied force of the tip of the AFM.

SEM characterization of micro-pillars and nano-pillars on cuboidal cages.

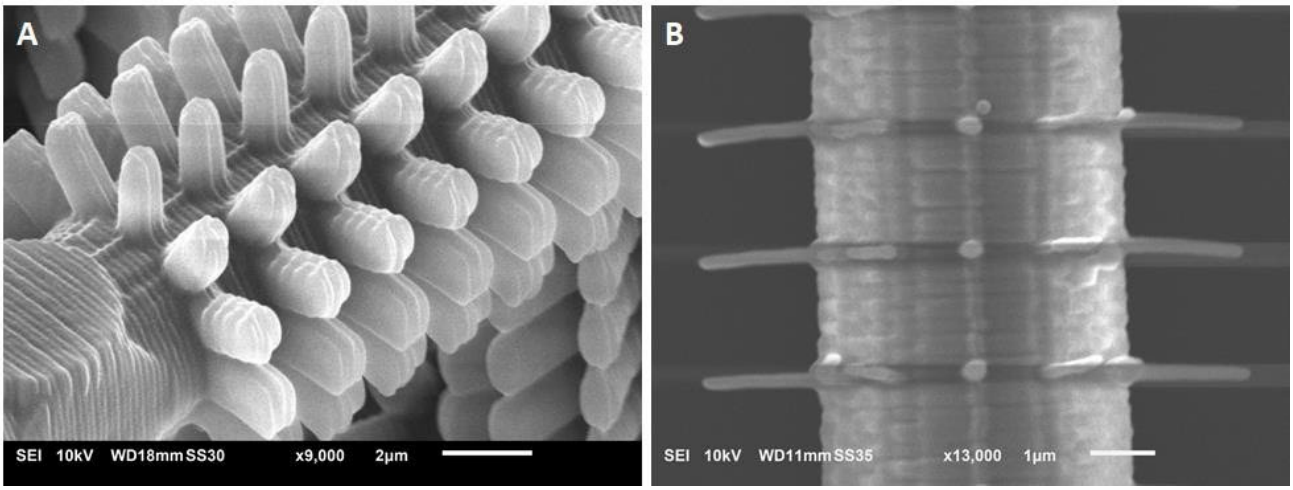

Fig. A3. SEM micrograph of the micro- (A) and nano-pillars (B) decorating the cuboidal cages.

***In vitro* classification of primary microglia.**

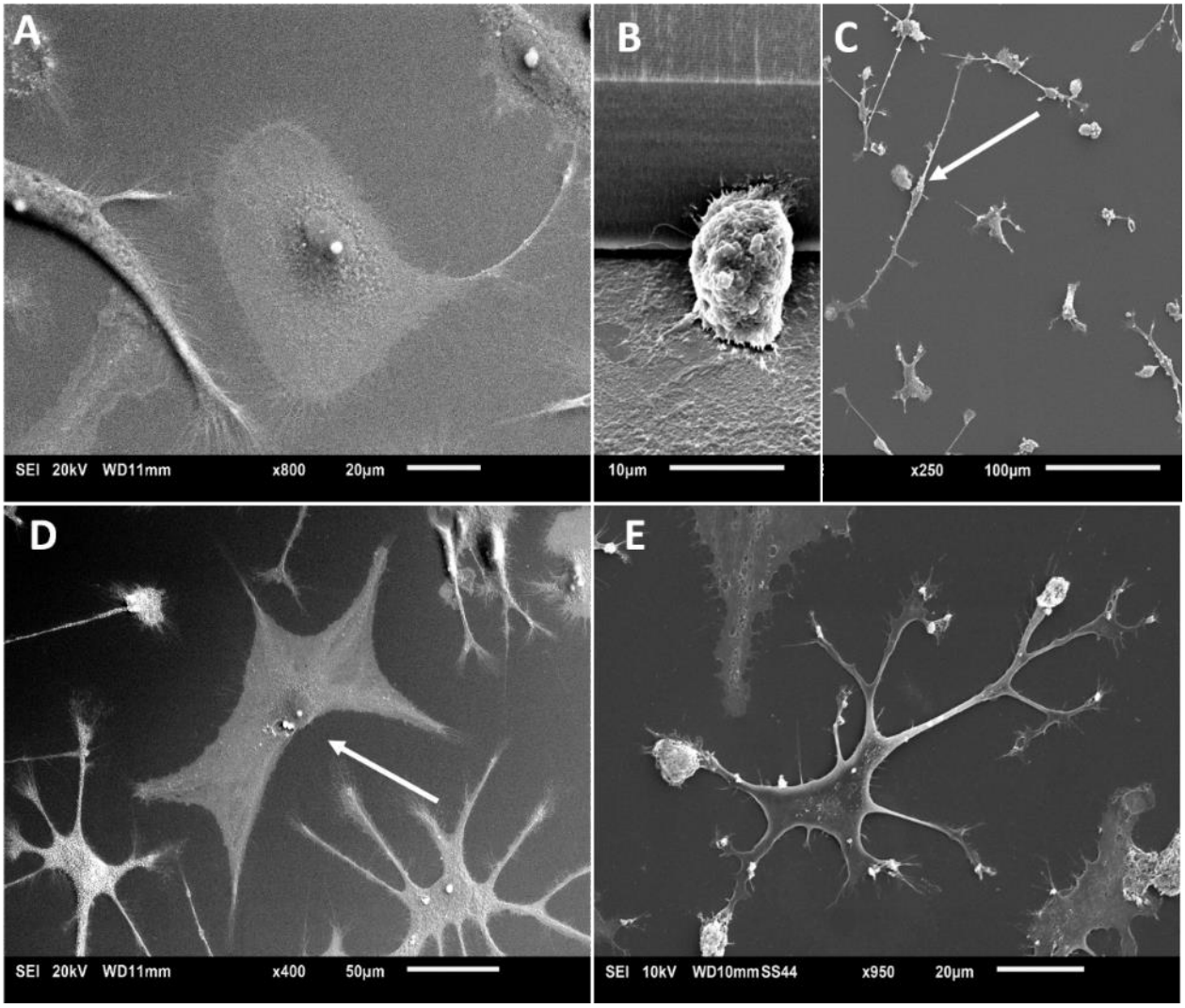

Fig. A4. SEM images of the phenotypes of primary microglia *in vitro*. (A) Flat amoeboid cell, a round cell with a flattened cell body. (B) Globular cell, spherically shaped cell with a small soma. (C) Bi-polar phenotype is a long rod-shaped cell with two poles extending from each side of the soma (white arrow). (D), (E) Non-amoeboid phenotype. (D) Non-ramified cell with short underdeveloped branches (white arrow). (E) Ramified phenotype, showing 6 primary branches with side branches and a relatively small soma

Effect of laminin on the phenotypic expression of primary microglia.

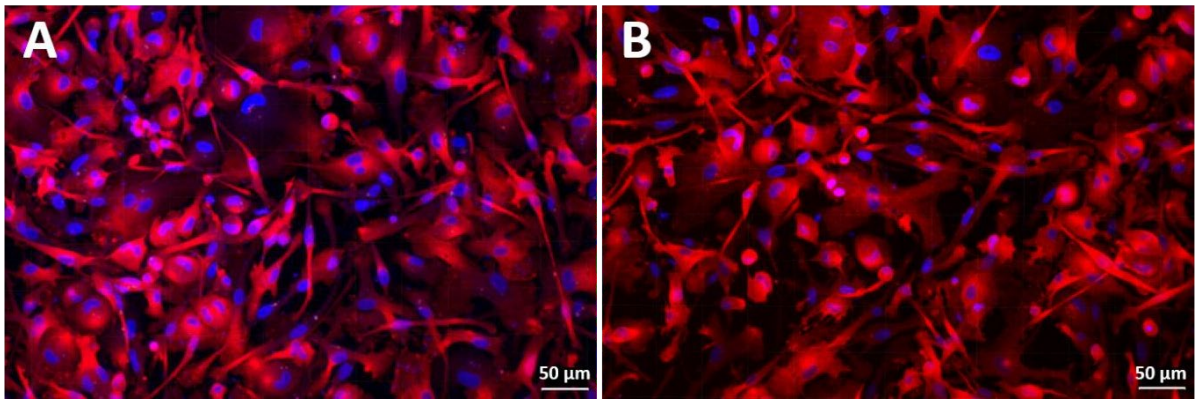

Fig. A5. Representative confocal microscopy images of primary microglia on (A) an uncoated fused silica substrate and (B) laminin-coated substrate.

Effect of micro- and nano-pillar arrays on the phenotype, morphology and network formation of primary microglia.

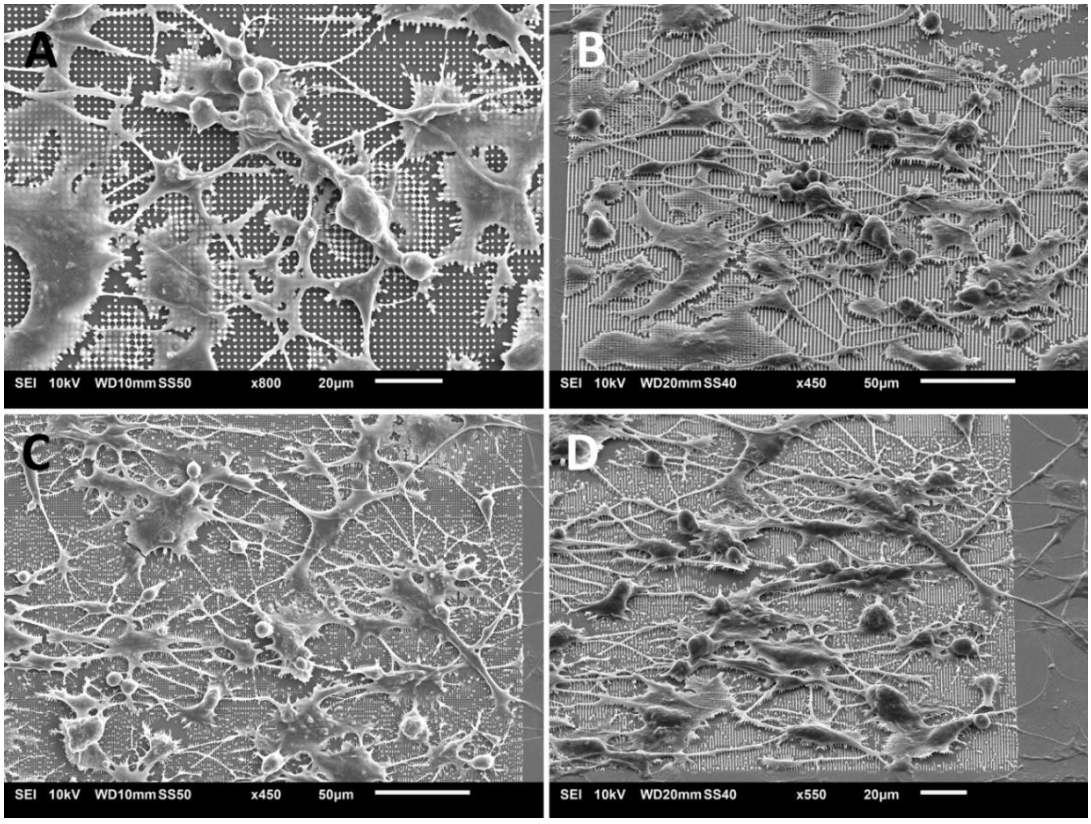

Fig. A6. Representative SEM images of primary microglia on (A), (B) MP1 micro- pillar arrays and (C), (D) NP1 nano-pillar arrays. The images show the heavy interconnection and networks formed between the microglia. B and D are taken at a 45° angle.

Light intensity values

The light intensity values corresponding to the laser power values (35 and 42.5 mW) employed to print the structures were calculated using the following equation [63].

$$I = \frac{2PT}{Rw_0^2\pi\tau}$$

Where *I* is the light intensity of the laser, *P* is the laser power, *T* is the transmittance of the employed objective, *R* is the pulse repetition rate of the laser, w_0 is the waist radius of the laser beam, and τ is the pulse duration of the laser source.

Table A1. Calculated light intensities. All values pertaining to the properties of the laser source were provided by Nanoscribe GmbH & Co. KG.

Objective transmittance (T)	0.75	
Pulse repetition rate (R) [MHz]	70.15	
Radius at beam waist (w_0) [nm]	340	
Pulse duration (τ) [fs]	95.3	
Laser power (P) [mW]	35	42.5
Light Intensity (I) [TW/cm^2]	1.89	2.29

Information of rhesus macaque donors from which primary microglia were isolated.

Table A2. Information of rhesus macaques microglia donors

Donor	Age [year]	Gender	Weight [kg]	Origin
D1	13	Female	7.6	India
D2	13	Male	10.7	India
D3	19	Male	13.1	India
D4	3	Male	7.85	India
D5	5	Female	4.6	India
D6	11	Male	17.4	India

Measured dimensions of the 2D, 2.5D. and 3D structures.

Table A3. Measured dimensions of 2D and 2.5D structures.

Measured dimensions	Pedestal	MP1	MP2	NP1	NP2
Width (w) [µm]	121±1.07	-	-	-	-
Diameter (d) [µm]	-	0.97±0.04	1.06±0.07	0.39±0.02	0.29±0.01
Height (h) [µm]	19.4±0.36	1.97±0.04	1.87±0.05	1.90±0.07	1.82±0.06
Spacing (p) [µm]	-	1.01±0.02	0.97±0.05	0.83±0.04	0.76±0.03

Table A4. Measured dimensions of 3D structures.

Measured dimensions	SC	SC-MP	BC	BC-MP	BC-NP
Width (W) or Length (L) [µm]	24.2±0.09	24.1±0.15	49.0±0.07	46.9±0.44	46.1±0.33
Beam diameter (D) [µm]	4.92±0.05	4.90±0.05	4.98±0.05	4.75±0.06	4.89±0.03
Height (H) [µm]	24.3±0.04	23.7±0.20	48.8±0.11	43.7±0.68	46.0±0.34
Pillar diameter [µm]	-	1.01±0.04	-	0.88±0.05	0.24±0.02
Pillar height [µm]	-	2.20±0.02	-	2.27±0.03	1.86±0.02
Angular spacing (θ) [◦]	-	29.4±0.22	-	30.1±0.52	31.0±0.88
Lateral spacing (δ) [µm]	-	0.97±0.02	-	1.00±0.08	0.83±0.02

Additional considerations on the data analysis

We considered different statistical analytical test methods to handle the large donor-donor variability that we encounter using outbred animals. A standard paired t-test could be used to analyse differences within the same animal, assuming that the distribution of these differences is normal. If one assumes that these differences are not normally distributed, a Welch's test can be considered. Either way, the combination of high standard deviations and low donor numbers precluded meaningful statistical analysis

Appendix B

The contents of this chapter have been published as supplementary information in:

- A. Sharaf, J.P. Frimat, G.J. Kremers, A. Accardo, Suppression of auto-fluorescence from high-resolution 3D polymeric architectures fabricated via two-photon polymerization for cell biology applications, Micro and Nano Engineering 19 (2023) 100188.

3D renderings of designed structures with all dimensions therein.

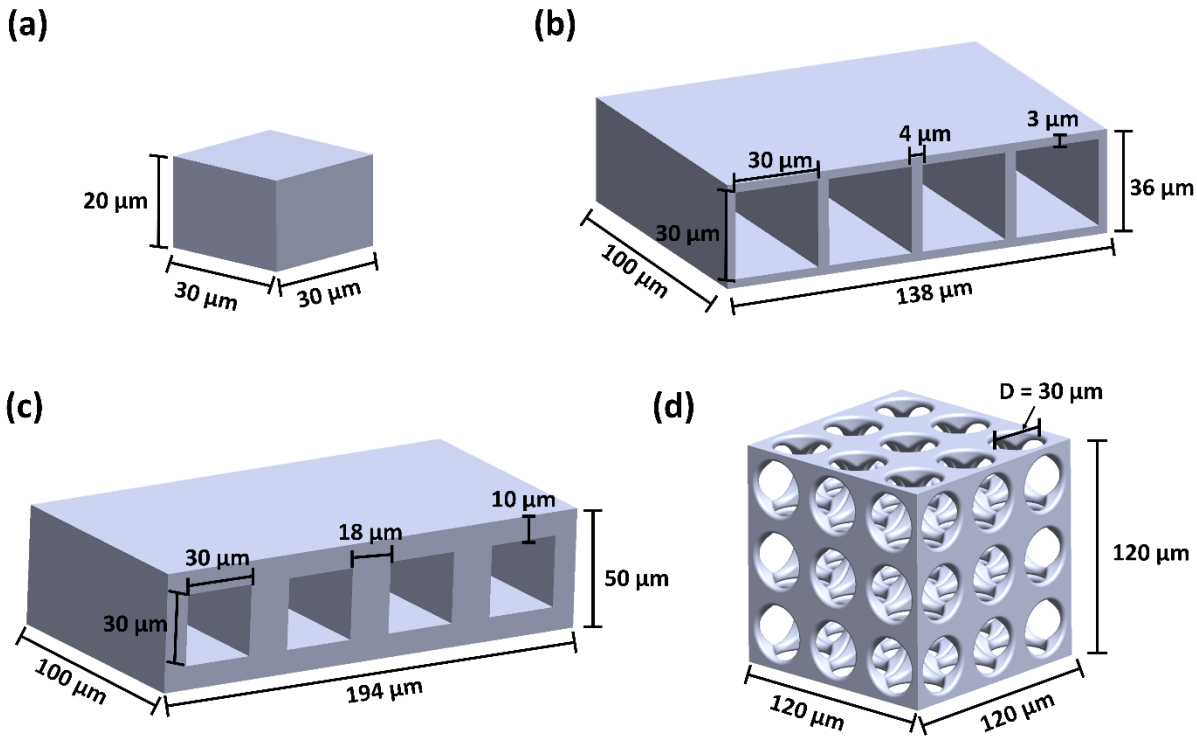

Fig. B1. 3D renderings of (a) Pedestals used for measurement of fluorescence and mechanical characterization. (b) Rectangular microchannels fabricated using IP-L, IP-Dip, IP-S and used for cell studies. (c) Rectangular microchannels fabricated using IP-PDMS. (d) 3D microcages.

Printing parameters of all materials and structures

All printing parameters are mentioned in Table B1. For IP-S, different parameters were used for the pedestals compared to those employed for the 3D microstructures. The reason was that when employing the parameters used for the 3D microstructures to print the pedestals, microbubbles were noticed indicating over-polymerization. Laser light intensity (I_{las}) values were calculated using the equation $I_{las} = \frac{2PT}{Rw_0^2\pi\tau}$ where I_{las} is the light intensity of the laser in W/cm^2, P is the laser power in W, T is the objective transmittance (0.75 for the 63x objective and 0.84 for the 25x objective), R is the pulse repetition rate of the laser (79618466 Hz), w_0 is the waist radius of the laser beam (340 nm for the 63x objective and 595 nm for the 25x objective), and τ is the pulse duration of the laser source (84.8 fs) [63].

Table B1. Printing parameters of all structures

Material	Hatching distance (µm)	Slicing distance (µm)	Laser power (mW)	Scanning speed (µm/s)	Laser light intensity (I_{las}) (TW/cm^2)
IP-L	0.2	0.7	20	90,000	0.4
IP-Dip	0.2	0.3	35	60,000	2.1
IP-S pedestals	0.5	1	40	100,000	0.9
IP-S 3D structures	0.5	1	50	100,000	1.1
IP-PDMS	0.3	0.3	50	100,000	1.1

IP structures treated with SBB

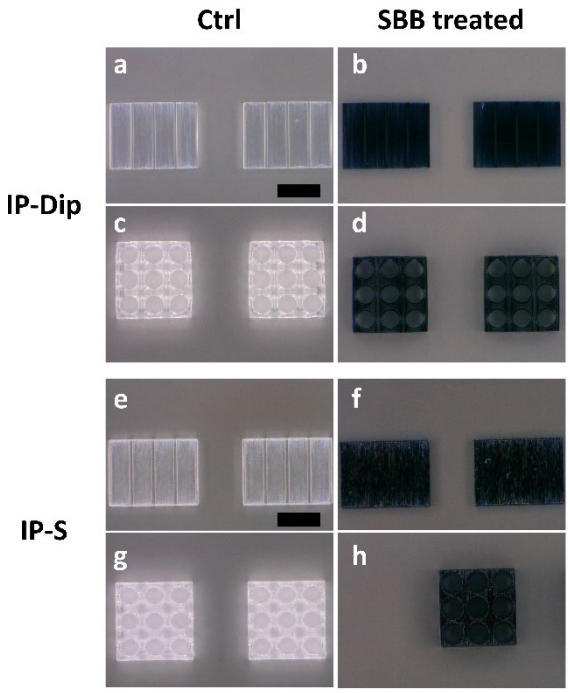

Fig. B2. Optical microscope images of (a,c) untreated IP-Dip fabricated structures (i.e. controls), (b,d) SBB treated IP-Dip structures, (e,g) Untreated IP-S fabricated structures, (f,h) SBB treated IP-S structures.

SEM characterization of untreated and SBB-treated samples

Images acquired by the SEM of untreated and SBB-treated samples did not provide conclusive results to be easily interpreted since the layer of SBB was likely too thin to be observed via SEM imaging.

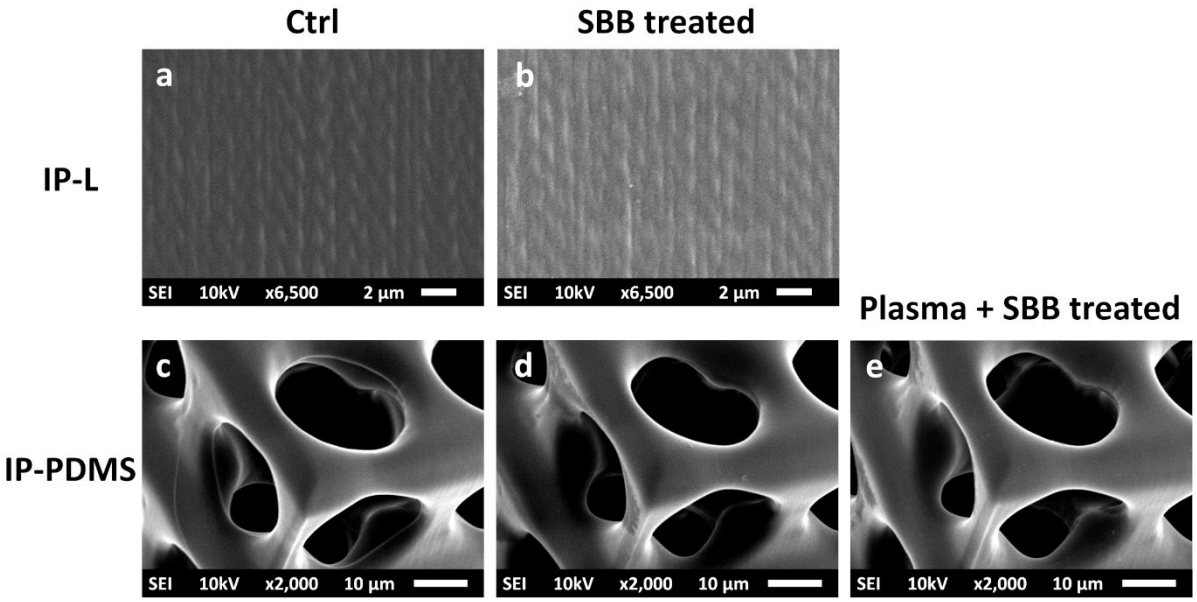

Fig. B3. SEM zoomed in images of untreated IP-L (ctrl) (a), SBB-treated IP-L (b), untreated IP-PDMS (ctrl) (c), SBB-treated IP-PDMS (d), and IP-PDMS that was treated with oxygen plasma for 30 s before treatment with SBB (e).

Comparison between the auto-fluorescence of IP materials

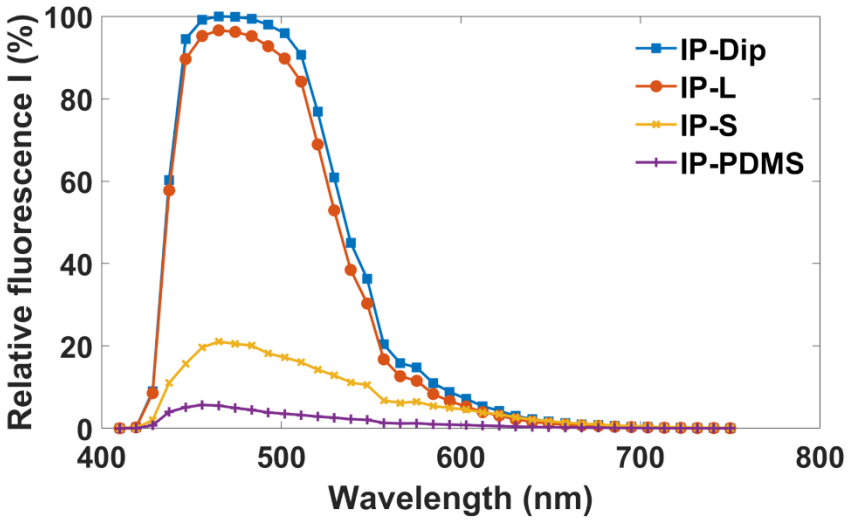

Fig. B4. A comparison between the auto-fluorescence of IP-Dip, IP-L, IP-S, and IP-PDMS measured as a relative fluorescence intensity (I) where 100% fluorescence intensity is equivalent to the highest signal.

Effect of aging after bleaching on the auto-fluorescence of IP materials

To determine whether the IP materials exhibit reversible bleaching or not, we measured the auto-fluorescence of the materials, 1, 4, and 6 days after UV-bleaching. The results showed no significant change in auto-fluorescence intensity.

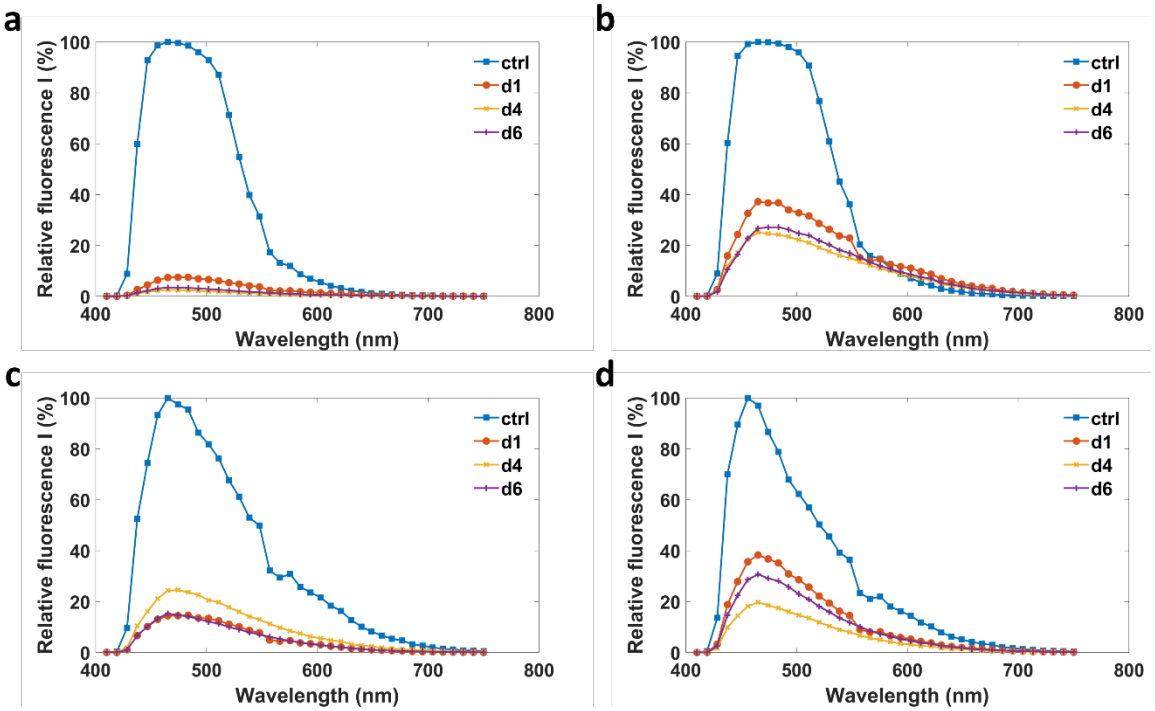

Fig. B5. Relative fluorescence intensity measurements of untreated samples (ctrl), samples after 1 (d1), 4 (d4), and 6 days (d6) of bleaching of (a) IP-L, (b) IP-Dip, (c) IP-S, (d) IP-PDMS. For each sample, n = 5 pedestals.

Optimized confocal images of microchannels and microcages

To showcase the difference between the untreated samples and the treated ones, we optimized the imaging parameters (i.e. Laser power and gain) of each configuration (i.e. untreated (ctrl), bleached, or SBB-treated) using confocal microscopy. Fig. B6, B7, and B9 only show IP-L structures as an example. When we attempted decreasing the laser power to reduce the auto-fluorescence of the untreated (ctrl) samples, observing the cells was extremely difficult. On the other hand, for SBB-treated structures, the laser power and gain had to be substantially increased to be able to visualize the cells inside the structures. This resulted in the creation of too much background noise to the extent that analysis was practically impossible. Bleached samples gave the best results upon optimizing their imaging parameters due to the inherent lower auto-fluorescence of the material after bleaching. This held especially true for visualizing the focal adhesions due to their small size (Fig. B7). Moreover, we highlight confocal images acquired via sequential scanning in Fig. B8 and B10 to illustrate the difference between untreated and treated structures in terms of visualization of the cells. In this imaging modality, bleached samples once again proved to provide better visualization of the cells compared to untreated and SBB treated samples.

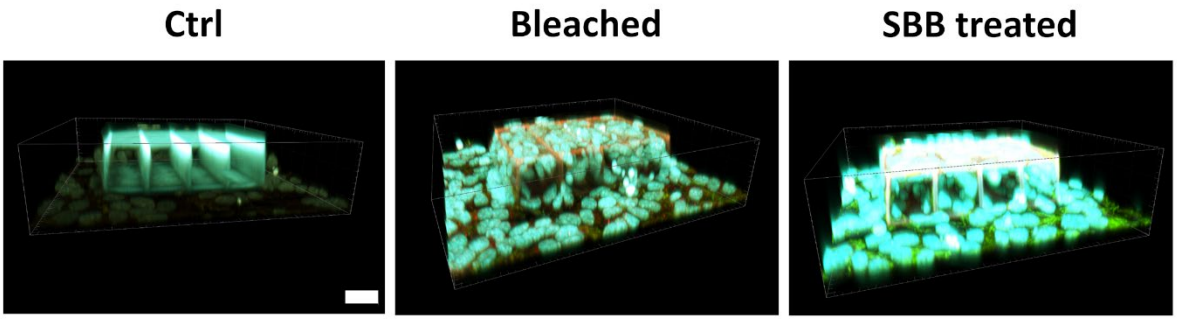

Fig. B6. Representative 3D reconstructions acquired by confocal microscopy of SH-SY5Y cells cultured on untreated and treated IP-L microchannels. These images were acquired at optimized imaging parameters for each configuration. The images represent merged blue, green, and red channels. Blue is Hoechst staining (cells nuclei). Green is actin (cytoskeleton). Red is paxillin (focal adhesions). The brightness levels in these images were adjusted to obtain the best visualization of the cells. These images were processed and created by Imaris Viewer software. Scale bar = 30 µm.

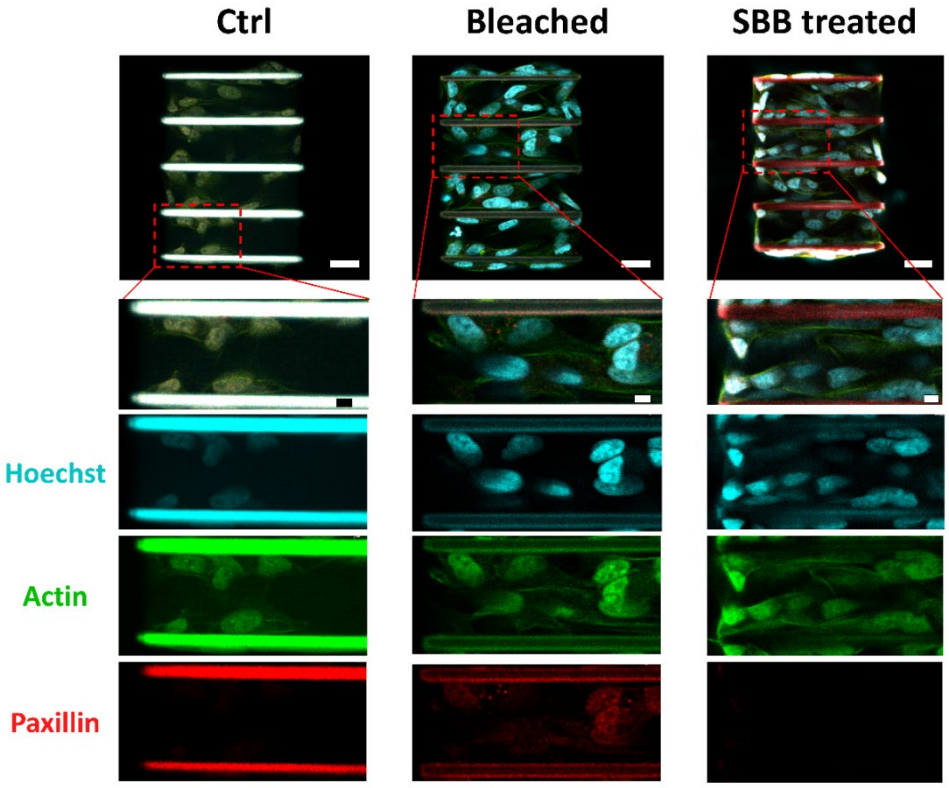

Fig. B7. Representative images of an intermediate section of IP-L microchannels with the SH-SY5Y cells shown inside the channels acquired at optimized imaging parameters for each configuration by confocal imaging. The first two rows represent images of merged channels (blue, green, and red). The rows underneath represent separate channels. Blue is Hoechst staining (cells nuclei). Green is actin (cytoskeleton). Red is paxillin (focal adhesions). The brightness levels in these images were adjusted to obtain the best visualization of the cells. These images were processed and created by Imaris Viewer software. Top row scale bar = 20 µm. Bottom row scale bar = 5 µm.

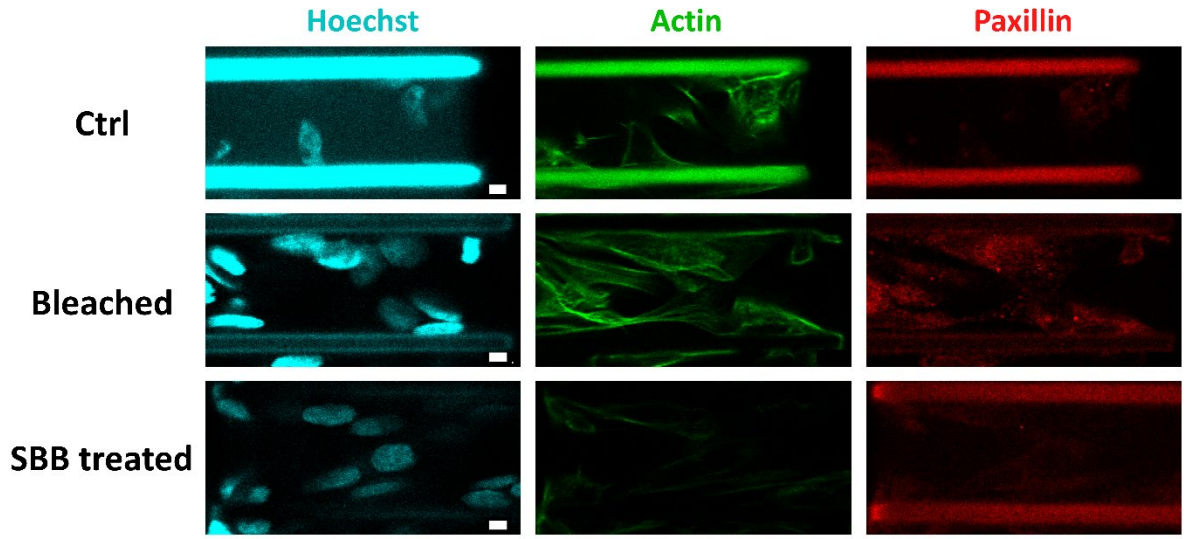

Fig. B8. Representative images of a zoomed in part within an intermediate section of IP-L microchannels with the SH-SY5Y cells shown inside the channels acquired at optimized imaging parameters for each configuration by confocal imaging. These images were acquired via sequential scanning for all 3 channels (blue, green, and red). Blue is Hoechst staining (cells nuclei). Green is actin (cytoskeleton). Red is paxillin (focal adhesions). These images were processed and created by Imaris Viewer software. Scale bars = 5 µm.

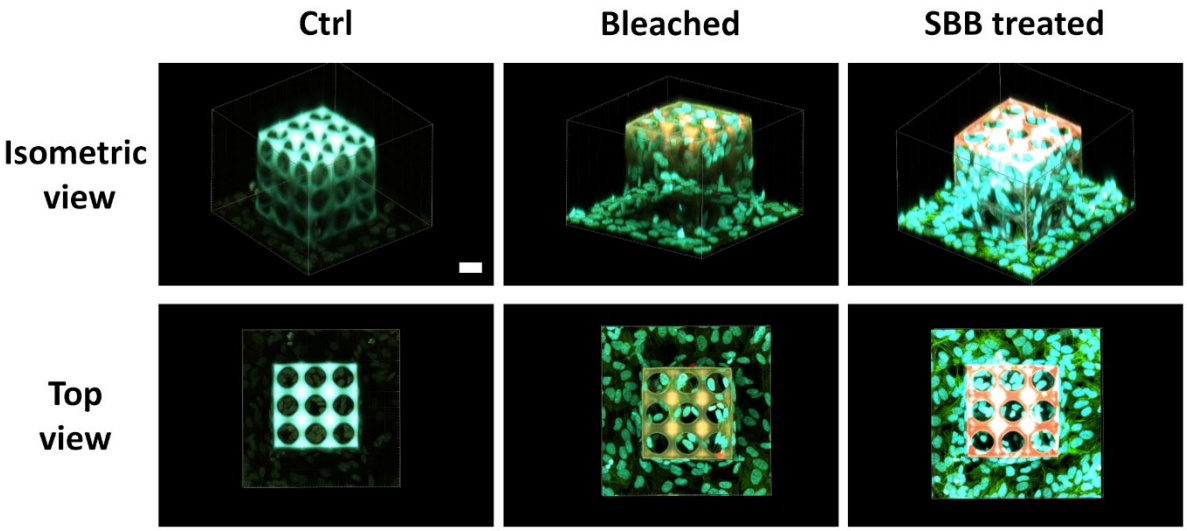

Fig. B9. Representative 3D reconstructions acquired by confocal microscopy of SH-SY5Y cells cultured on untreated and treated IP-L microcages. These images were acquired at optimized imaging parameters for each configuration. The images represent merged blue, green, and red channels. Blue is Hoechst staining (cells nuclei). Green is actin (cytoskeleton). Red is paxillin (focal adhesions). The brightness levels in these images were adjusted to obtain the best visualization of the cells. These images were processed and created by Imaris Viewer software. Scale bar = 30 µm.

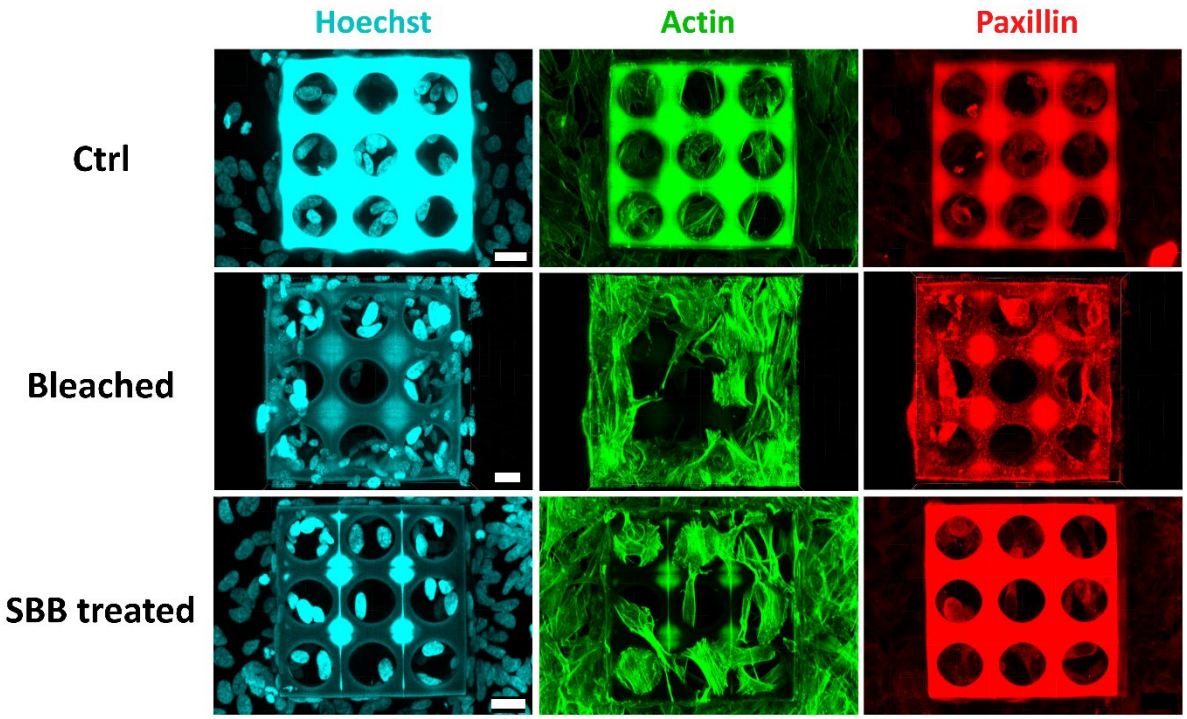

Fig. B10. Representative confocal microscopy images of the top view of IP-L microcages colonized by SH-SY5Y cells acquired via sequential scanning at optimized imaging parameters for each configuration. Blue is Hoechst staining (cells nuclei). Green is actin (cytoskeleton). Red is paxillin (focal adhesions). These images were processed and created by Imaris Viewer software. Scale bars = 20 µm.

Appendix C

The contents of this chapter have been published as supplementary information in:

- A. Sharaf, J.P. Frimat, A. Accardo, Mechanical confinement matters: Unveiling the effect of two-photon polymerized 2.5D and 3D microarchitectures on neuronal YAP expression and neurite outgrowth, Materials Today Bio 29 (2024) 101325.

CAD renderings and dimensions of all microstructures.

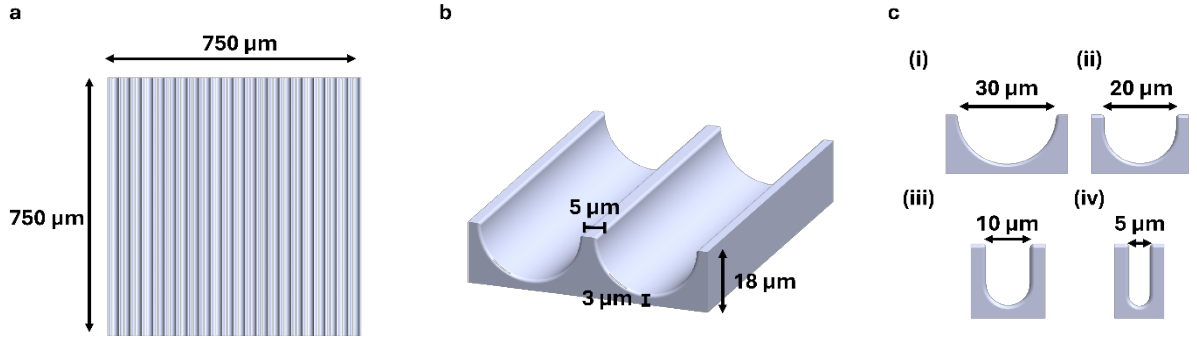

Fig. C1. CAD renderings of the 2.5D microgrooves created by SOLIDWORKS. (a) Top view and dimensions of a representative array. (b) Isometric zoomed in view and detailed dimensions of the microgrooves. (c) Front view and diameters of each array.

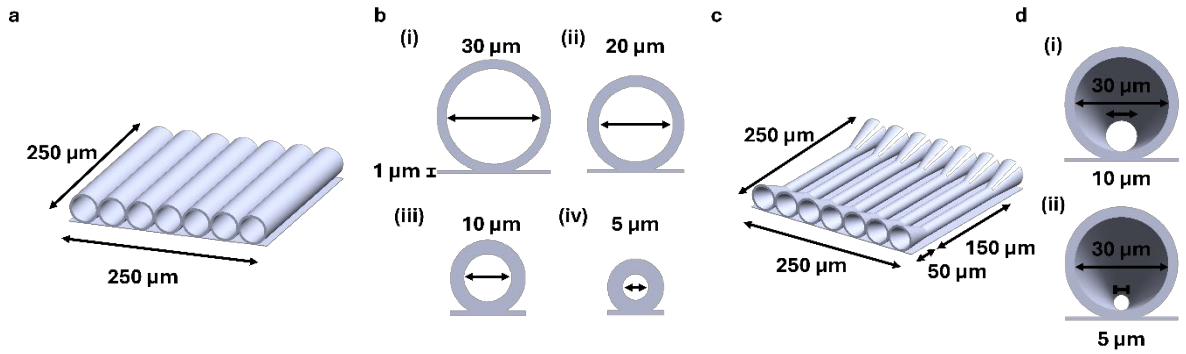

Fig. C2. CAD renderings of the 3D microchannels created by SOLIDWORKS. (a) Isometric view and dimensions of one C30 array of microchannels. (b) Front view and diameters of (i) C30, (ii) C20, (iii) C10, and (iv) C5. (c) Isometric view and dimensions of one ADC10 array of microchannels. (d) Front view and dimensions of (i) ADC10 and (ii) ADC5.

Elaboration of analysis pipelines.

Fig. S3 shows the pipeline for identifying cell bodies and neurites (processes). After obtaining maximum z-projection images by Fiji (Fig. S3a), Cellpose was employed to identify nuclei via machine learning (Fig. S3b). Consequently, the identified nuclei were imported into CellProfiler as primary objects (Fig. S3c) to be used as seeds for identifying the bodies of the cells by using the F-actin staining (Fig. Sd). Cell bodies were identified by using an Otsu thresholding method. Afterwards, identified cell bodies were turned into objects (Fig. S3e) to perform further analysis such as calculating cell area. Nuclei were also used as seeds to identify processes of the cells (Fig. S3f). For this step, nuclei had to be dilated in order to account for the cell body area that must be excluded from the calculation of the length of the processes.

Focal adhesions (FAs) were identified as shown in Fig. S4. First, the cell bodies were identified as already mentioned (Fig. S4a,b). FAs were then identified in CellProfiler as primary objects (Fig. S4c) based on the paxillin channel (Fig. S4d). The Robust Background thresholding method was employed to identify FAs. Finally, FAs were related to the relevant cell body as shown in Fig. S4e.

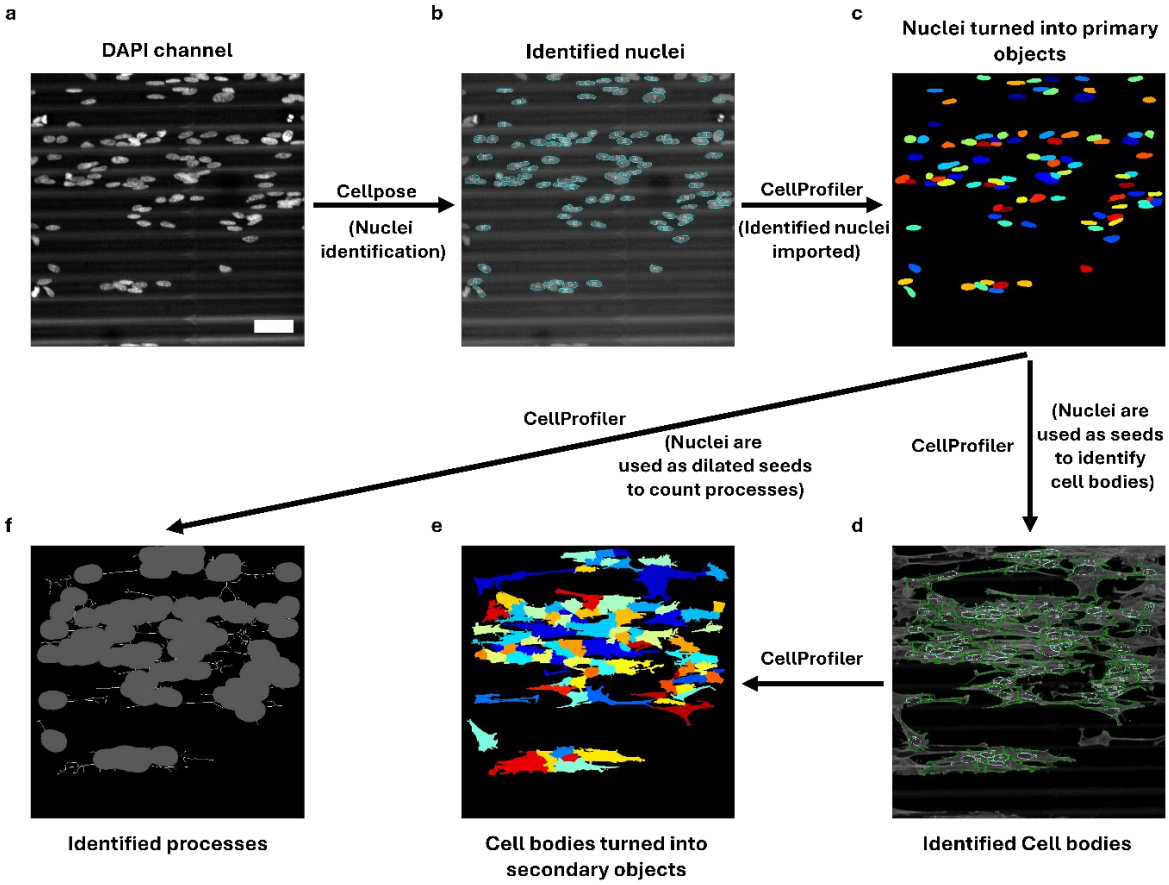

Fig. C3. Analysis pipeline for identification of cell bodies and neurites (processes). (a) Representative maximum z-projection of a DAPI channel of C20 (created by using Fiji). (b) Identified nuclei via Cellpose machine learning-based plugin are indicated by the blue contours. (c) Identified nuclei were imported into CellProfiler as primary objects. (d) Identified cell bodies shown as green contours and overlayed on the actin channel. (e) Identified cell bodies were transformed into objects in CellProfiler for further analysis. (f) Neurites (processes) of cells (as indicated by the white branched lines) were identified by using nuclei as seeds after their dilation. Scale bar = 50 µm.

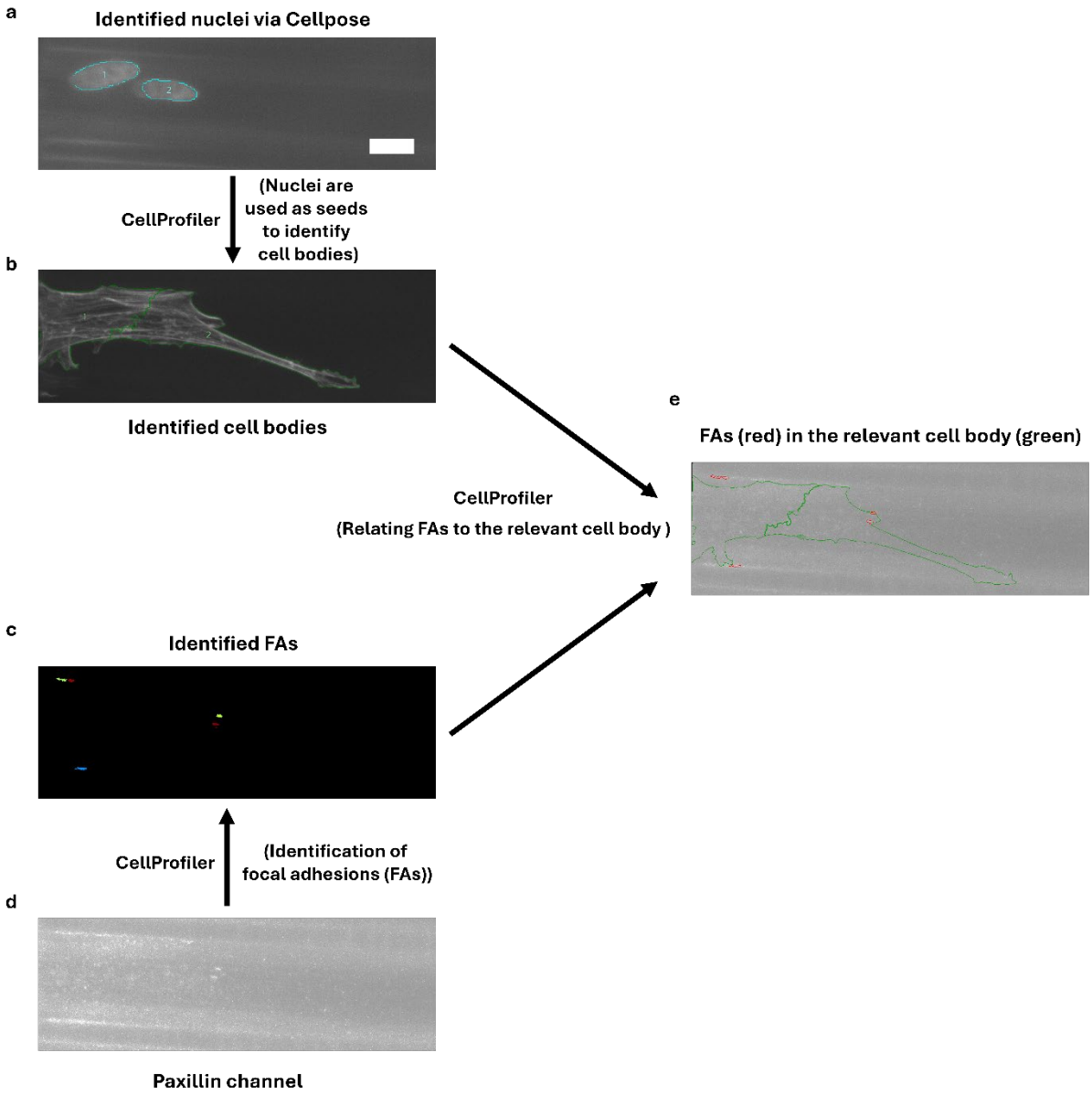

Fig. C4. Analysis pipeline for identification of focal adhesions (FAs). (a) Identified nuclei via Cellpose as mentioned earlier. (b) Identified nuclei were imported into CellProfiler and used as seeds to identify cell bodies as mentioned earlier. (c) FAs were identified in CellProfiler by using the paxillin channel (d). (e) identified FAs (red contours) were related to the relevant cell body (green contours) in CellProfiler for further analysis. Scale bar = 10 µm.

Fluorescence images of MRTFA.

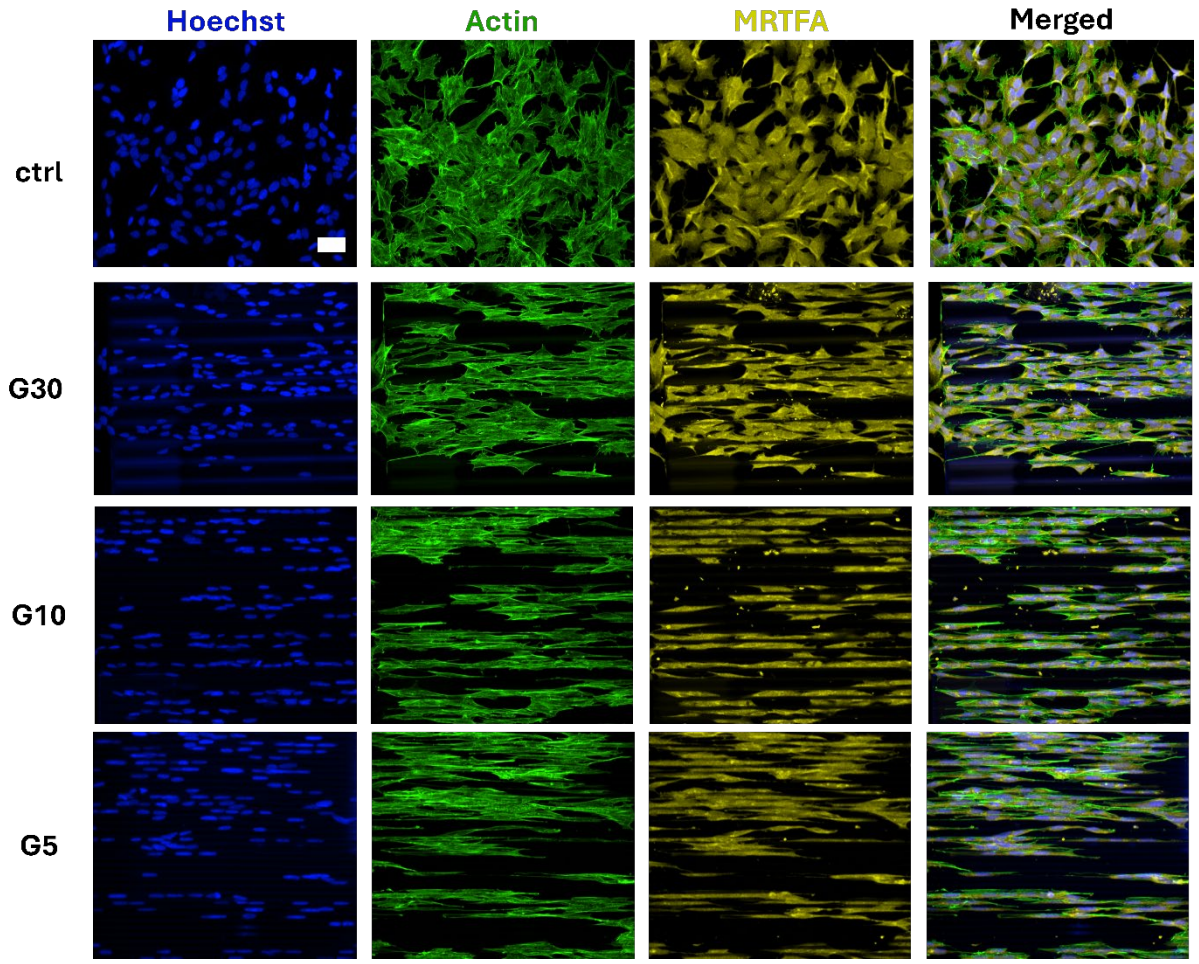

Fig. C5. Maximum Z-projection images obtained via confocal microscopy of the SH-SY5Y cells at D3 of differentiation on ctrl, G30, G10 and G5 showcasing the expression of MRTFA in the cells. Scale bar = 50 µm.

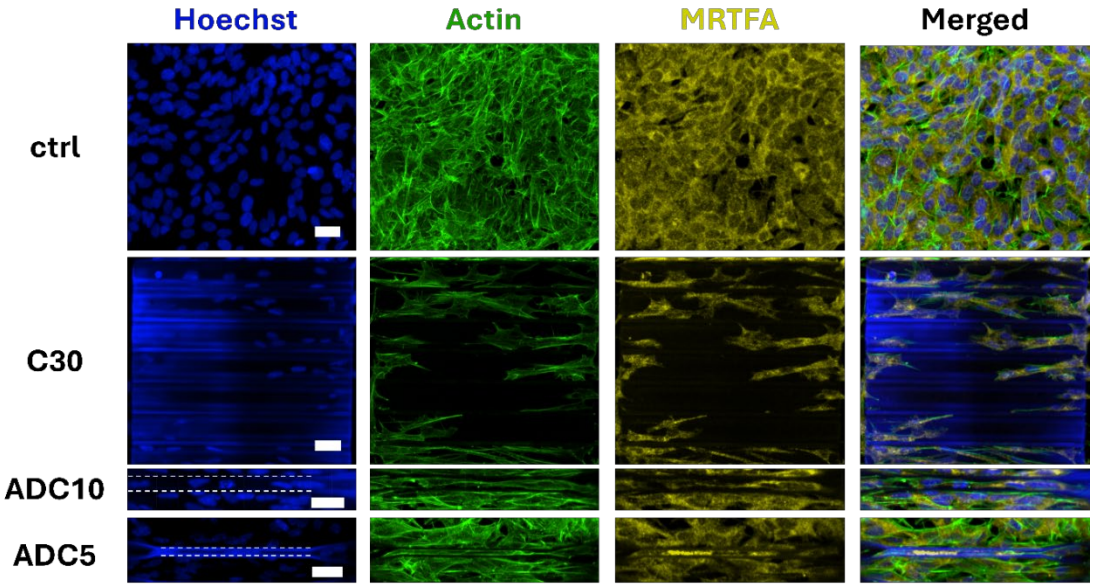

Fig. C6. Maximum Z-projection images obtained via confocal microscopy of the SH-SY5Y cells at D3 of differentiation on ctrl, C30, ADC10 and ADC5 showcasing the expression of MRTFA in the cells. The dashes white lines in ADC10 and ADC5 represent the channel walls. Scale bar = 30 µm.

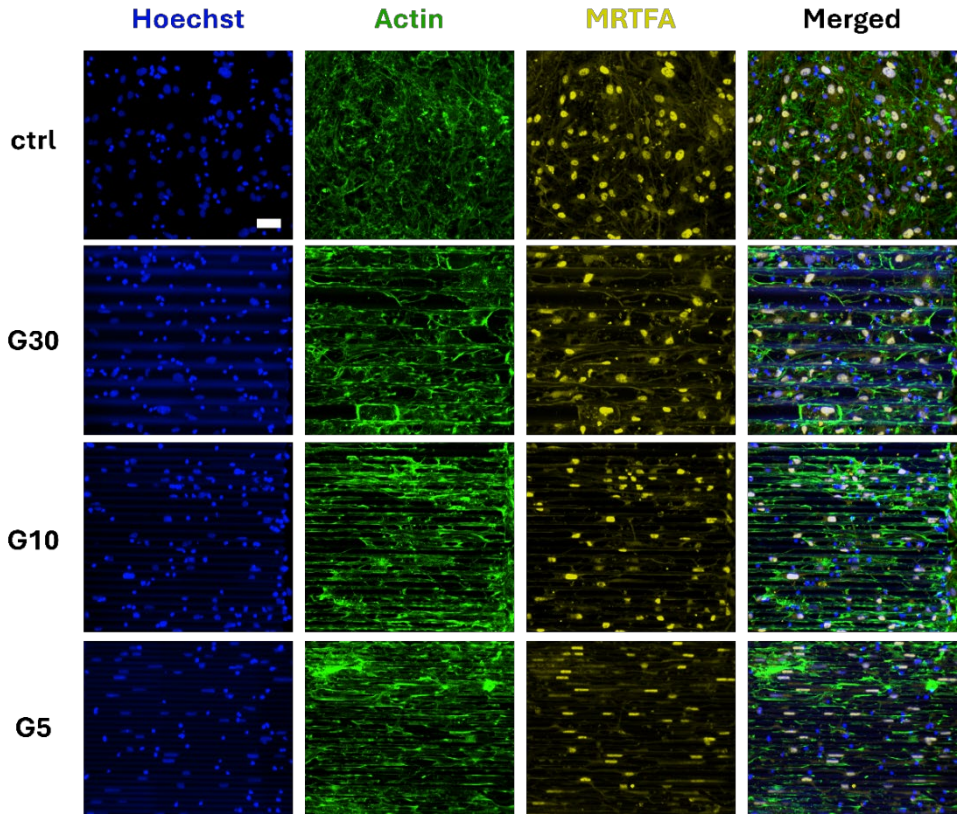

Fig. C7. Maximum Z-projection images obtained via confocal microscopy of the hiPSC cells at D14 of differentiation on ctrl, G30, G10 and G5 showcasing the expression of MRTFA in the cells. Scale bar = 50 µm.

Channels length determination.

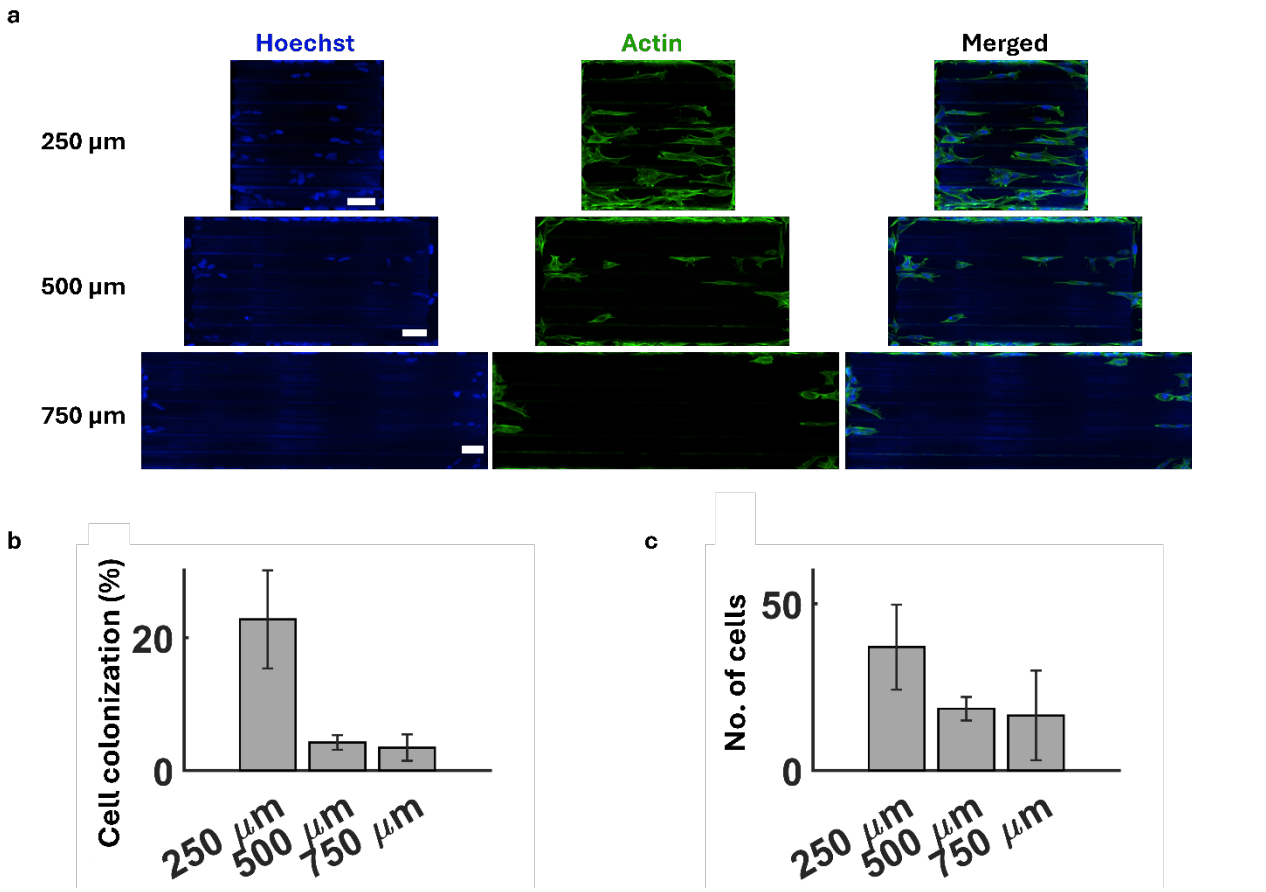

Fig. C8. (a) Maximum Z-projection images obtained via confocal microscopy of the SH-SY5Y cells at D1 of differentiation in channels of 30 µm diameter and lengths of 250, 500, and 750 µm. (b) Percentage of cell colonization calculated as the ratio of the summation of the areas of cell bodies to the area of the arrays of microchannels. (c) The average number of cells per array of channels. Scale bar = 50 µm.

Average area of nuclei in microchannels.

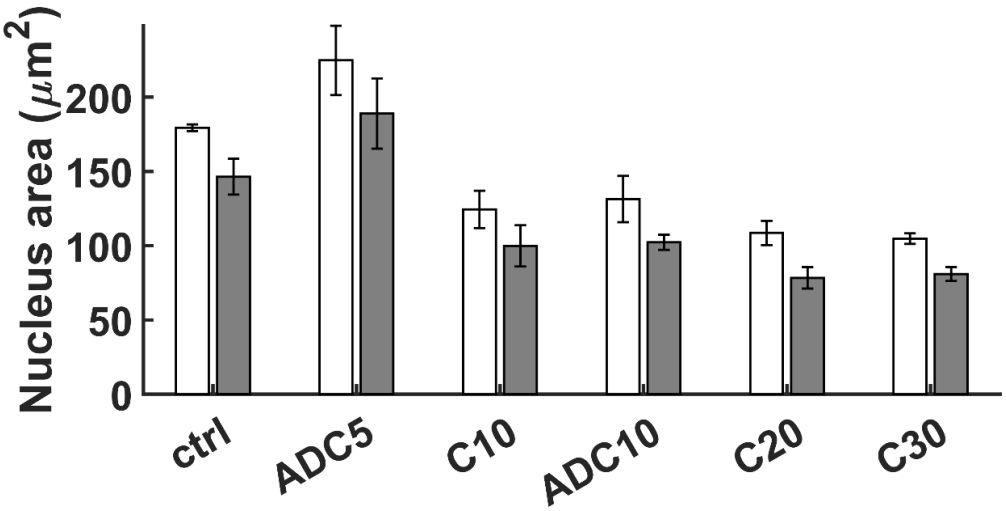

Fig. C9. Average area of nuclei of SH-SY5Y-differentiated cells in the microchannels.

3D renderings of confocal images of SH-SY5Y derived immature neurons.

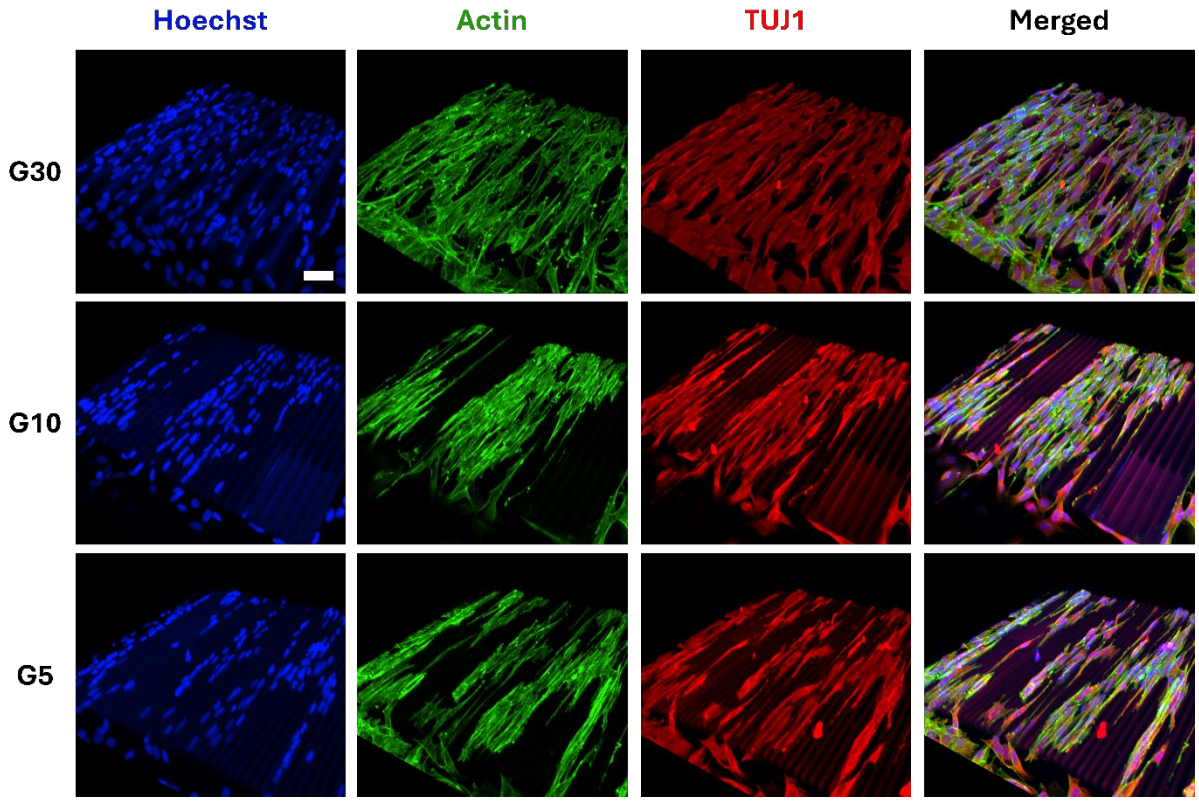

Fig. C10. Representative 3D reconstructions obtained via confocal microscopy of SH-SY5Y cells in microgrooves at D3 of differentiation. Scale bar = 50 µm.

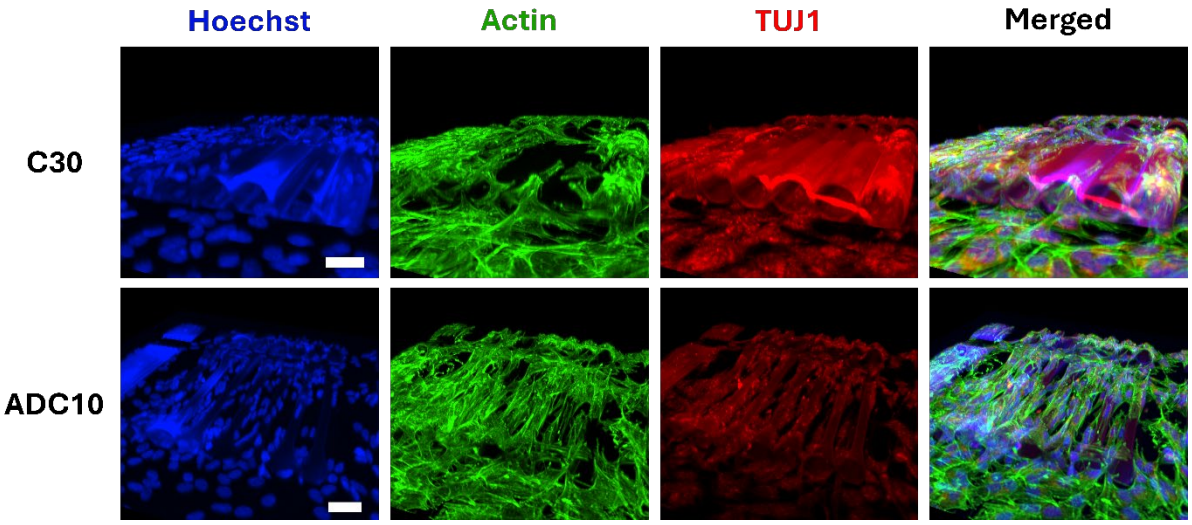

Fig. C11. Representative 3D reconstructions obtained via confocal microscopy of SH-SY5Y cells in microchannels at D3 of differentiation. Scale bar = 50 µm.

Illustration of networks formed between hiPSC derived immature neurons in the microgrooves.

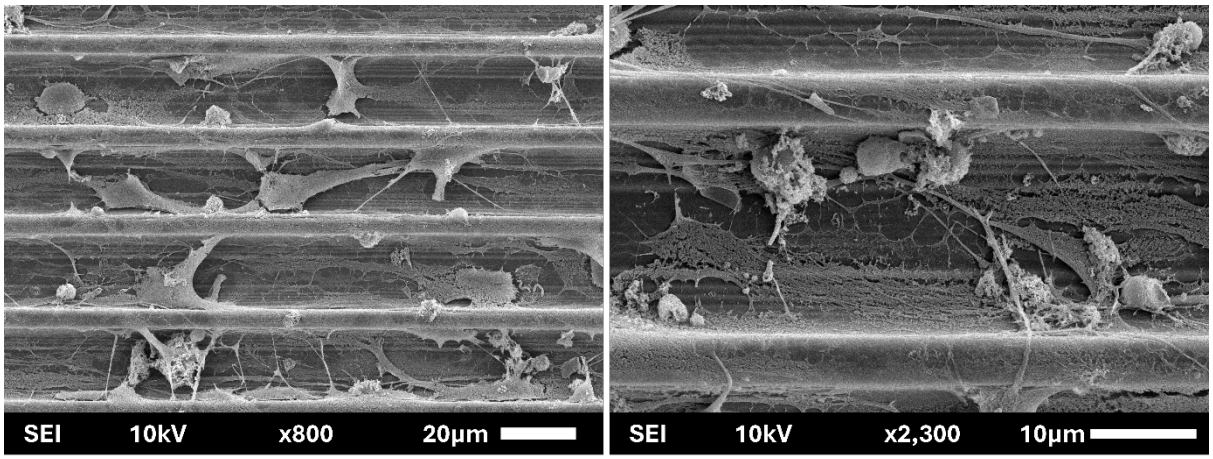

Fig. C12. Representative SEM images of hiPSC derived immature neurons in G20 at D7 illustrating the connectivity and complex networks formed between the cells.

3D renderings of confocal images of hiPSC derived immature neurons.

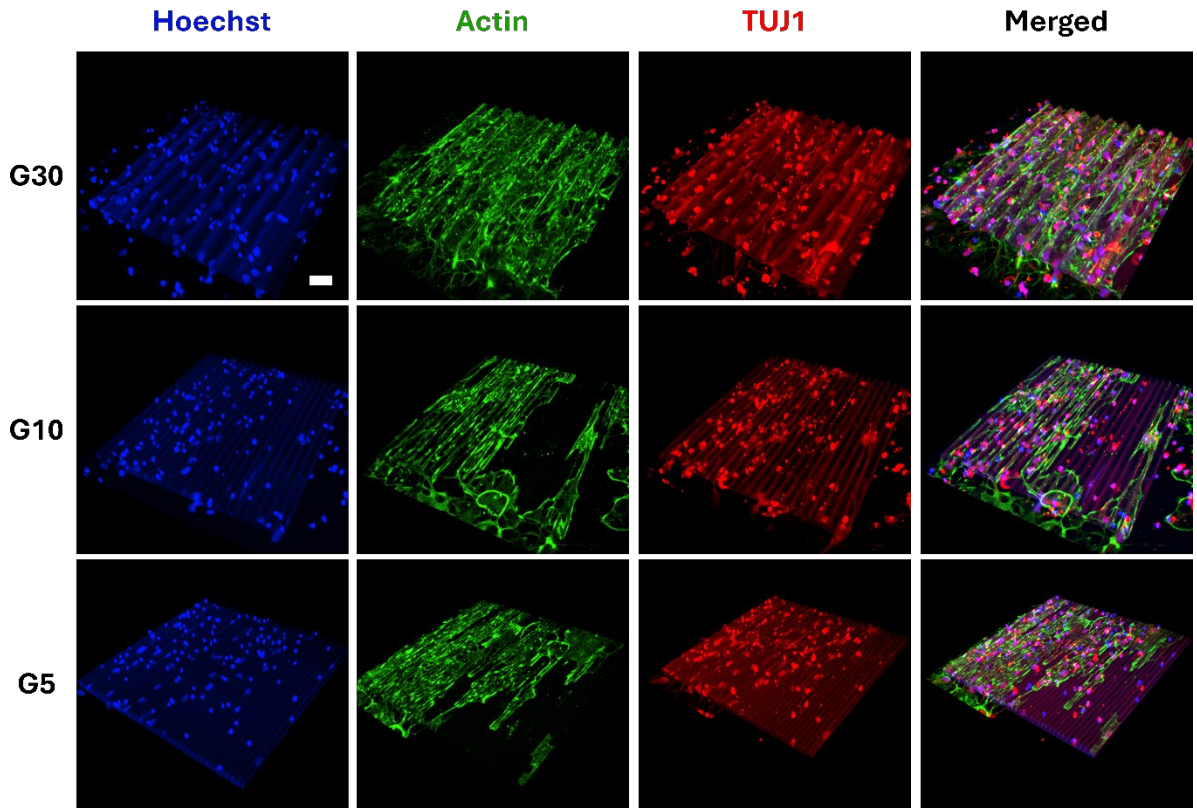

Fig. C13. Representative 3D reconstructions obtained via confocal microscopy of hiPSC cells in microgrooves at D14 of differentiation. Scale bar = 50 µm

Appendix D

This work was done in collaboration with Chihao Kuo.

Chemical structures of the compounds used.

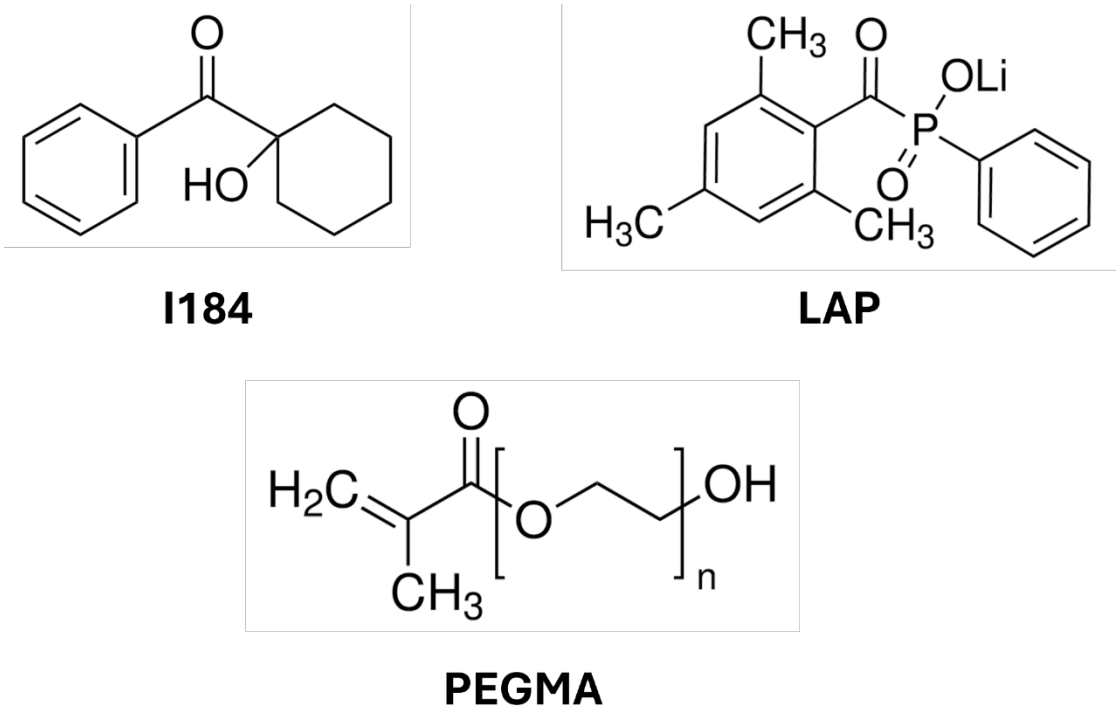

Fig. D1. Chemical structures of the photoinitiators and the hydrogel oligomer [175–177].

Hydrogel growth after implementing protocol using both LAP and I184 as photoinitiators.

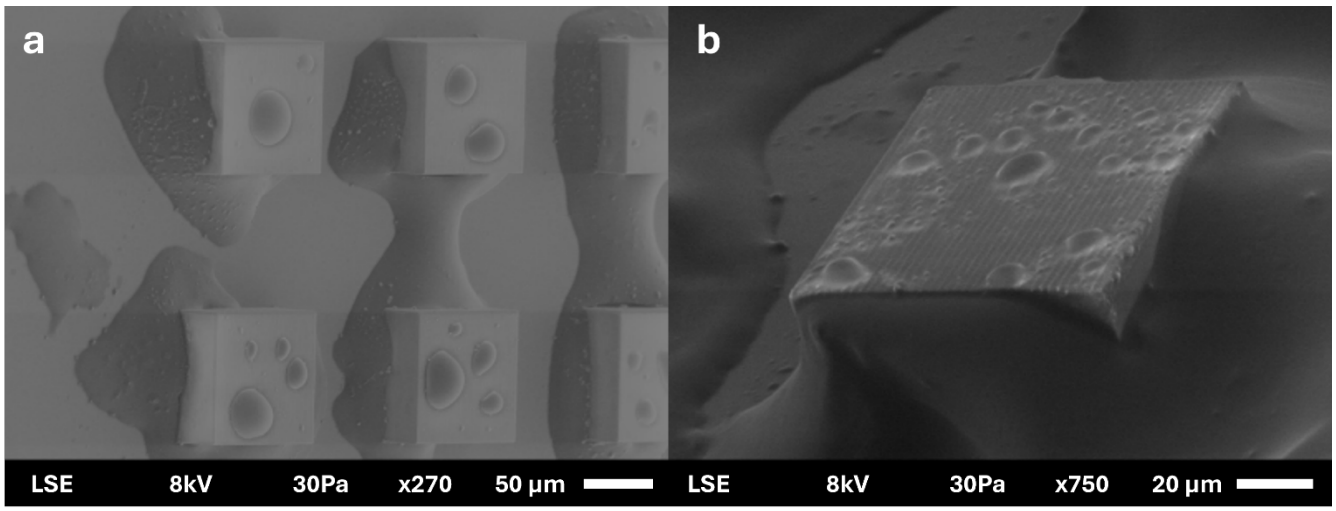

Fig. D2. (a) Hydrogel layer lacking specificity and growing between pedestals. (b) Hydrogel bubbles growing on top of the pedestals due to an issue with the clumping of photoinitiators.

SEM images of pedestals after removing I184 from the protocol.

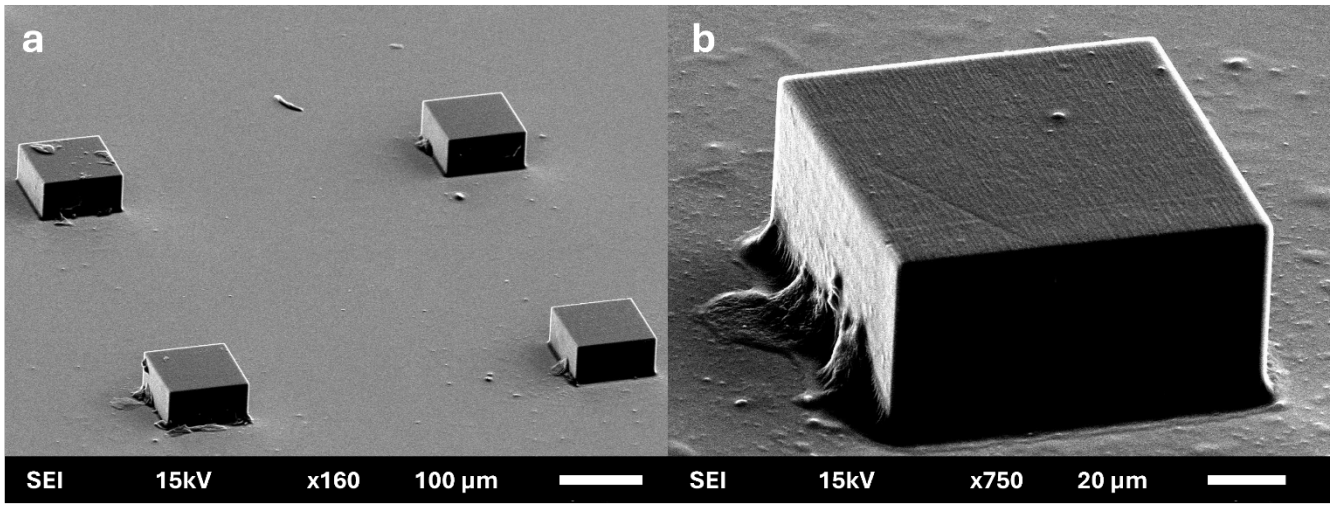

Fig. D3. (a) Multiple pedestals after removing I184 from the protocol while keeping LAP. (b) A zoomed in image of one pedestal showing very little hydrogel growth and only on the sidewalls

Hydrogel layer thickness on the pedestals

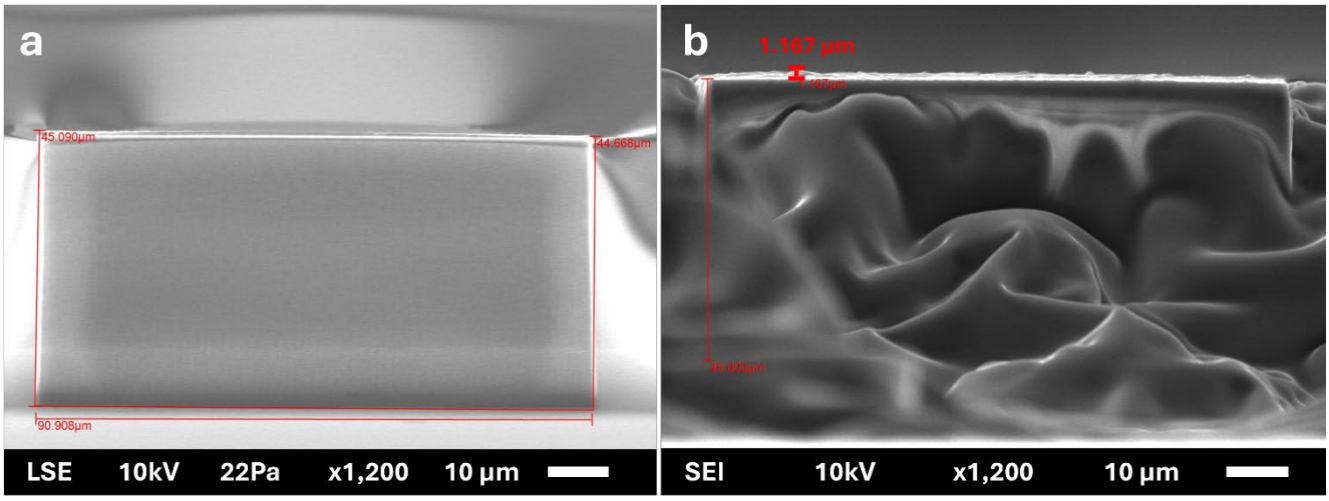

Fig. D4. 90° angled SEM images of (a) A pedestal made from IP-S with no hydrogel coating, and (b) A pedestal after the growth of the hydrogel layer. The thickness of the layer is shown to be ~ 1 µm.

Effect of UV curing time on the growth of the hydrogel.

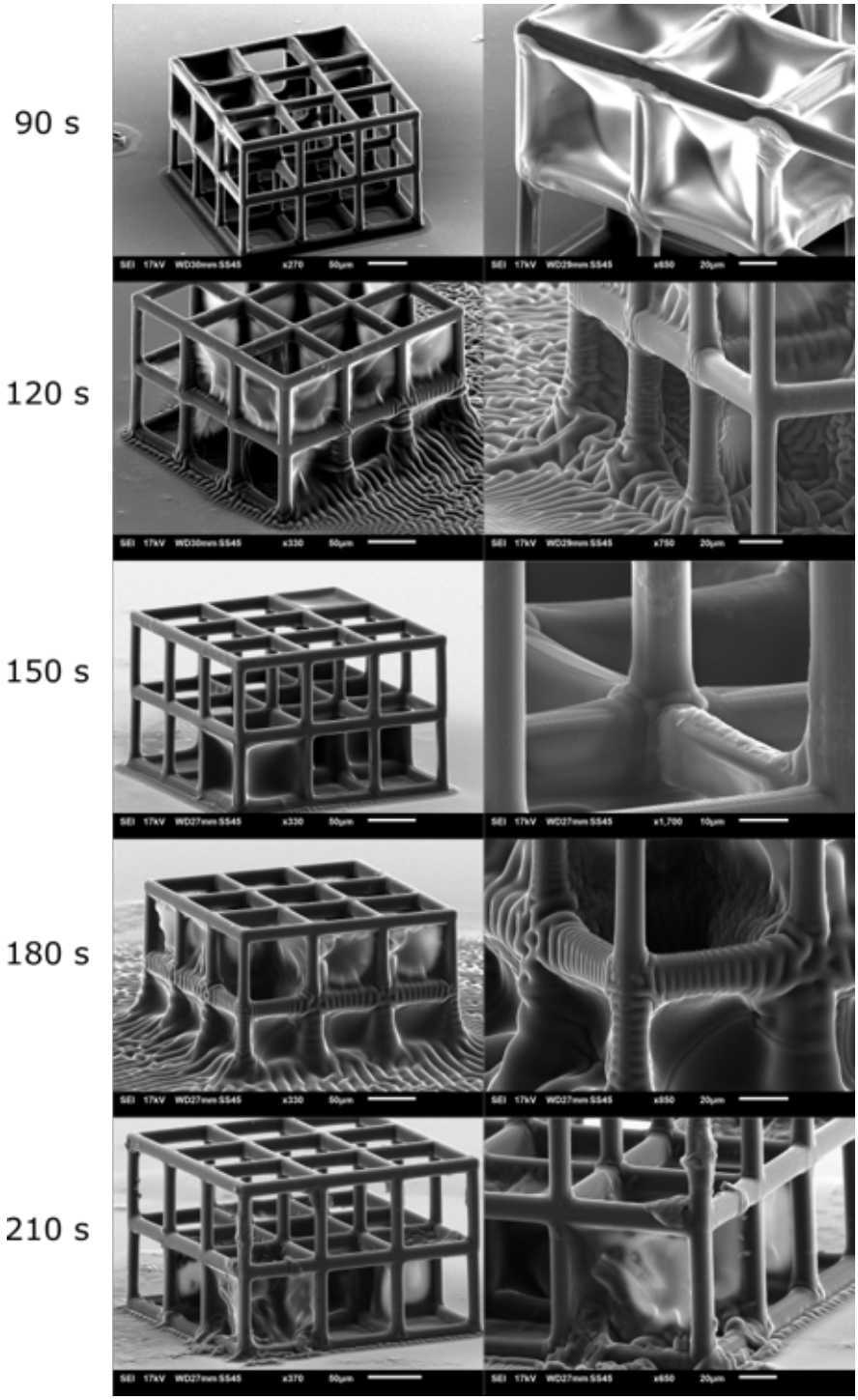

Fig. D5. SEM images depicting the cages with hydrogel layers after different UV curing durations ranging from 90 s to 210 s.

References

[1] C. Koch, I. Segev, The role of single neurons in information processing, Nat Neurosci 3 (2000) 1171–1177. https://doi.org/10.1038/81444.

[2] K.R. Jessen, Glial cells, The International Journal of Biochemistry & Cell Biology 36 (2004) 1861–1867. https://doi.org/10.1016/j.biocel.2004.02.023.

[3] Y.-B. Lu, K. Franze, G. Seifert, C. Steinhauser, F. Kirchhoff, H. Wolburg, J. Guck, P. Janmey, E.-Q. Wei, J. Kas, A. Reichenbach, Viscoelastic properties of individual glial cells and neurons in the CNS, Proceedings of the National Academy of Sciences 103 (2006) 17759–17764. https://doi.org/10.1073/pnas.0606150103.

[4] D. Espinosa-Hoyos, A. Jagielska, K.A. Homan, H. Du, T. Busbee, D.G. Anderson, N.X. Fang, J.A. Lewis, K.J. Van Vliet, Engineered 3D-printed artificial axons, Scientific Reports 8 (2018). https://doi.org/10.1038/s41598-017-18744-6.

[5] N. Fekete, A.V. Béland, K. Campbell, S.L. Clark, C.A. Hoesli, Bags versus flasks: a comparison of cell culture systems for the production of dendritic cell–based immunotherapies, Transfusion 58 (2018) 1800–1813. https://doi.org/10.1111/trf.14621.

[6] J.C. Mateus, S. Weaver, D. van Swaay, A.F. Renz, J. Hengsteler, P. Aguiar, J. Vörös, Nanoscale Patterning of In Vitro Neuronal Circuits, ACS Nano 16 (2022) 5731–5742. https://doi.org/10.1021/acsnano.1c10750.

[7] R.L. Wilmoth, V.L. Ferguson, S.J. Bryant, A 3D, Dynamically Loaded Hydrogel Model of the Osteochondral Unit to Study Osteocyte Mechanobiology, Advanced Healthcare Materials 9 (2020) 2001226. https://doi.org/10.1002/adhm.202001226.

[8] D. Kim, S.-M. Kim, S. Lee, M.-H. Yoon, Investigation of neuronal pathfinding and construction of artificial neuronal networks on 3D-arranged porous fibrillar scaffolds with controlled geometry, Scientific Reports 7 (2017) 7716. https://doi.org/10.1038/s41598-017-08231-3.

[9] G. Silvani, C. Basirun, H. Wu, C. Mehner, K. Poole, P. Bradbury, J. Chou, A 3D-Bioprinted Vascularized Glioblastoma-on-a-Chip for Studying the Impact of Simulated Microgravity as a Novel Pre-Clinical Approach in Brain Tumor Therapy, Advanced Therapeutics 4 (2021) 2100106. https://doi.org/10.1002/adtp.202100106.

[10] E.D. Lemma, B. Spagnolo, M. De Vittorio, F. Pisanello, Studying Cell Mechanobiology in 3D: The Two-Photon Lithography Approach, Trends in Biotechnology 37 (2019) 358–372. https://doi.org/10.1016/j.tibtech.2018.09.008.

[11] M. Malinauskas, A. Žukauskas, G. Bičkauskaitė, R. Gadonas, S. Juodkazis, Mechanisms of three-dimensional structuring of photo-polymers by tightly focussed femtosecond laser pulses, Opt. Express, OE 18 (2010) 10209–10221. https://doi.org/10.1364/OE.18.010209.

[12] M. Emons, K. Obata, T. Binhammer, A. Ovsianikov, B.N. Chichkov, U. Morgner, Two-photon polymerization technique with sub-50 nm resolution by sub-10 fs laser pulses, Opt. Mater. Express, OME 2 (2012) 942–947. https://doi.org/10.1364/OME.2.000942.

[13] A. Marino, G. Ciofani, C. Filippeschi, M. Pellegrino, M. Pellegrini, P. Orsini, M. Pasqualetti, V. Mattoli, B. Mazzolai, Two-Photon Polymerization of Sub-micrometric Patterned Surfaces: Investigation of Cell-Substrate Interactions and Improved Differentiation of Neuron-like Cells, ACS Appl. Mater. Interfaces 5 (2013) 13012–13021. https://doi.org/10.1021/am403895k.

[14] C. Fendler, J. Harberts, L. Rafeldt, G. Loers, R. Zierold, R. H. Blick, Neurite guidance and neuro-caging on steps and grooves in 2.5 dimensions, Nanoscale Advances (2020). https://doi.org/10.1039/D0NA00549E.

[15] S. Turunen, T. Joki, M.L. Hiltunen, T.O. Ihalainen, S. Narkilahti, M. Kellomäki, Direct Laser Writing of Tubular Microtowers for 3D Culture of Human Pluripotent Stem Cell-Derived Neuronal Cells, ACS Appl. Mater. Interfaces 9 (2017) 25717–25730. https://doi.org/10.1021/acsami.7b05536.

[16] C. Fendler, C. Denker, G. Loers, J.I. Harberts, R. Zierold, M. Münzenberg, R.H. Blick, 3D Micro Scaffolds for Tailor-Made Three-Dimensional Neural Network Studies, Biophysical Journal 114 (2018) 672a–673a. https://doi.org/10.1016/j.bpj.2017.11.3626.
[17] F. Larramendy, S. Yoshida, D. Maier, Z. Fekete, S. Takeuchi, O. Paul, 3D arrays of microcages by two-photon lithography for spatial organization of living cells, Lab on a Chip 19 (2019) 875–884. https://doi.org/10.1039/C8LC01240G.
[18] A. Accardo, M.-C. Blatché, R. Courson, I. Loubinoux, C. Vieu, L. Malaquin, Direct laser fabrication of free-standing PEGDA-hydrogel scaffolds for neuronal cell growth, Materials Today 21 (2018) 315–316. https://doi.org/10.1016/j.mattod.2018.02.004.
[19] J. Abu Shihada, M. Jung, S. Decke, L. Koschinski, S. Musall, V. Rincón Montes, A. Offenhäusser, Highly Customizable 3D Microelectrode Arrays for In Vitro and In Vivo Neuronal Tissue Recordings, Advanced Science 11 (2024) 2305944. https://doi.org/10.1002/advs.202305944.
[20] T. Koch, W. Zhang, T.T. Tran, Y. Wang, A. Mikitisin, J. Puchhammer, J.R. Greer, A. Ovsianikov, F. Chalupa-Gantner, M. Lunzer, Approaching Standardization: Mechanical Material Testing of Macroscopic Two-Photon Polymerized Specimens, Advanced Materials 36 (2024) 2308497. https://doi.org/10.1002/adma.202308497.
[21] Q. Hu, G.A. Rance, G.F. Trindade, D. Pervan, L. Jiang, A. Foerster, L. Turyanska, C. Tuck, D.J. Irvine, R. Hague, R.D. Wildman, The influence of printing parameters on multi-material two-photon polymerisation based micro additive manufacturing, Additive Manufacturing 51 (2022) 102575. https://doi.org/10.1016/j.addma.2021.102575.
[22] A. Maggi, H. Li, J.R. Greer, Three-dimensional nano-architected scaffolds with tunable stiffness for efficient bone tissue growth, Acta Biomaterialia 63 (2017) 294–305. https://doi.org/10.1016/j.actbio.2017.09.007.
[23] Y. Kim, S.M. Meade, K. Chen, H. Feng, J. Rayyan, A. Hess-Dunning, E.S. Ereifej, Nano-Architectural Approaches for Improved Intracortical Interface Technologies, Frontiers in Neuroscience 12 (2018) 456. https://doi.org/10.3389/fnins.2018.00456.
[24] J.B. Zuchero, B.A. Barres, Glia in mammalian development and disease, Development 142 (2015) 3805–3809. https://doi.org/10.1242/dev.129304.
[25] K. Saijo, C.K. Glass, Microglial cell origin and phenotypes in health and disease, Nat Rev Immunol 11 (2011) 775–787. https://doi.org/10.1038/nri3086.
[26] R. Timmerman, S.M. Burm, J.J. Bajramovic, An Overview of in vitro Methods to Study Microglia, Front. Cell. Neurosci. 12 (2018) 242. https://doi.org/10.3389/fncel.2018.00242.
[27] X. Jin, T. Yamashita, Microglia in central nervous system repair after injury, The Journal of Biochemistry 159 (2016) 491–496. https://doi.org/10.1093/jb/mvw009.
[28] S. Hickman, S. Izzy, P. Sen, L. Morsett, J. El Khoury, Microglia in neurodegeneration, Nat Neurosci 21 (2018) 1359–1369. https://doi.org/10.1038/s41593-018-0242-x.
[29] E. Uribe-Querol, C. Rosales, Phagocytosis: Our Current Understanding of a Universal Biological Process, Frontiers in Immunology 11 (2020) 1066. https://doi.org/10.3389/fimmu.2020.01066.
[30] H.-K. Jeong, K. Ji, K. Min, E.-H. Joe, Brain Inflammation and Microglia: Facts and Misconceptions, Exp Neurobiol 22 (2013) 59–67. https://doi.org/10.5607/en.2013.22.2.59.
[31] S. Lund, K.V. Christensen, M. Hedtjärn, A.L. Mortensen, H. Hagberg, J. Falsig, H. Hasseldam, A. Schrattenholz, P. Pörzgen, M. Leist, The dynamics of the LPS triggered inflammatory response of murine microglia under different culture and in vivo conditions, Journal of Neuroimmunology 180 (2006) 71–87. https://doi.org/10.1016/j.jneuroim.2006.07.007.
[32] J.A. Smith, A. Das, S.K. Ray, N.L. Banik, Role of pro-inflammatory cytokines released from microglia in neurodegenerative diseases, Brain Research Bulletin 87 (2012) 10–20. https://doi.org/10.1016/j.brainresbull.2011.10.004.

[33] S.G. Torres-Platas, S. Comeau, A. Rachalski, G. Bo, C. Cruceanu, G. Turecki, B. Giros, N. Mechawar, Morphometric characterization of microglial phenotypes in human cerebral cortex, J Neuroinflammation 11 (2014) 12. https://doi.org/10.1186/1742-2094-11-12.
[34] A. Sharaf, R. Timmerman, J. Bajramovic, A. Accardo, In vitro microglia models: the era of engineered cell microenvironments, Neural Regeneration Research 18 (2023) 1709. https://doi.org/10.4103/1673-5374.363828.
[35] L.R. Pires, D.N. Rocha, L. Ambrosio, A.P. Pêgo, The role of the surface on microglia function: implications for central nervous system tissue engineering, Journal of The Royal Society Interface 12 (2015) 20141224. https://doi.org/10.1098/rsif.2014.1224.
[36] T.B. Wissing, V. Bonito, E.E. van Haaften, M. van Doeselaar, M.M.C.P. Brugmans, H.M. Janssen, C.V.C. Bouten, A.I.P.M. Smits, Macrophage-Driven Biomaterial Degradation Depends on Scaffold Microarchitecture, Frontiers in Bioengineering and Biotechnology 7 (2019) 87. https://doi.org/10.3389/fbioe.2019.00087.
[37] D. Venugopal, S. Vishwakarma, I. Kaur, S. Samavedi, Electrospun meshes intrinsically promote M2 polarization of microglia under hypoxia and offer protection from hypoxia-driven cell death, Biomed. Mater. 16 (2021) 045049. https://doi.org/10.1088/1748-605X/ac0a91.
[38] Z. Jiang, Q. Song, M. Tang, L. Yang, Y. Cheng, M. Zhang, D. Xu, G. Cheng, Enhanced Migration of Neural Stem Cells by Microglia Grown on a Three-Dimensional Graphene Scaffold, ACS Appl. Mater. Interfaces 8 (2016) 25069–25077. https://doi.org/10.1021/acsami.6b06780.
[39] S. Varapnickas, M. Malinauskas, Processes of Laser Direct Writing 3D Nanolithography, in: K. Sugioka (Ed.), Handbook of Laser Micro- and Nano-Engineering, Springer International Publishing, Cham, 2020: pp. 1–31. https://doi.org/10.1007/978-3-319-69537-2_32-1.
[40] S. Persheyev, Y. Fan, A. Irving, M.J. Rose, BV-2 microglial cells sense micro-nanotextured silicon surface topology, Journal of Biomedical Materials Research Part A 99A (2011) 135–140. https://doi.org/10.1002/jbm.a.33159.
[41] T.U. Luu, S.C. Gott, B.W.K. Woo, M.P. Rao, W.F. Liu, Micro- and Nanopatterned Topographical Cues for Regulating Macrophage Cell Shape and Phenotype, ACS Appl. Mater. Interfaces 7 (2015) 28665–28672. https://doi.org/10.1021/acsami.5b10589.
[42] J.V. Small, T. Stradal, E. Vignal, K. Rottner, The lamellipodium: where motility begins, Trends in Cell Biology 12 (2002) 112–120. https://doi.org/10.1016/S0962-8924(01)02237-1.
[43] G.-E. Choi, Importance of Microglial Cytoskeleton and the Actin-interacting Proteins in Alzheimer's Disease, Biomed Sci Letters 26 (2020) 1–7. https://doi.org/10.15616/BSL.2020.26.1.1.
[44] Y. Chen, L. Ju, M. Rushdi, C. Ge, C. Zhu, Receptor-mediated cell mechanosensing, MBoC 28 (2017) 3134–3155. https://doi.org/10.1091/mbc.e17-04-0228.
[45] R. Sridharan, E.J. Ryan, C.J. Kearney, D.J. Kelly, F.J. O'Brien, Macrophage Polarization in Response to Collagen Scaffold Stiffness Is Dependent on Cross-Linking Agent Used To Modulate the Stiffness, ACS Biomater. Sci. Eng. 5 (2019) 544–552. https://doi.org/10.1021/acsbiomaterials.8b00910.
[46] S.J. Blaschke, S. Demir, A. König, J.-A. Abraham, S.U. Vay, M. Rabenstein, D.N. Olschewski, C. Hoffmann, M. Hoffmann, N. Hersch, R. Merkel, B. Hoffmann, M. Schroeter, G.R. Fink, M.A. Rueger, Substrate Elasticity Exerts Functional Effects on Primary Microglia, Front Cell Neurosci 14 (2020) 590500. https://doi.org/10.3389/fncel.2020.590500.
[47] T. Dudiki, J. Meller, G. Mahajan, H. Liu, I. Zhevlakova, S. Stefl, C. Witherow, E. Podrez, C.R. Kothapalli, T.V. Byzova, Microglia control vascular architecture via a TGFβ1 dependent paracrine mechanism linked to tissue mechanics, Nat Commun 11 (2020) 986. https://doi.org/10.1038/s41467-020-14787-y.

[48] M. Chen, Y. Zhang, P. Zhou, X. Liu, H. Zhao, X. Zhou, Q. Gu, B. Li, X. Zhu, Q. Shi, Substrate stiffness modulates bone marrow-derived macrophage polarization through NF-κB signaling pathway, Bioactive Materials 5 (2020) 880–890. https://doi.org/10.1016/j.bioactmat.2020.05.004.
[49] C.H. Rasmussen, P.M. Reynolds, D.R. Petersen, M. Hansson, R.M. McMeeking, M. Dufva, N. Gadegaard, Enhanced Differentiation of Human Embryonic Stem Cells Toward Definitive Endoderm on Ultrahigh Aspect Ratio Nanopillars, Adv. Funct. Mater. 26 (2016) 815–823. https://doi.org/10.1002/adfm.201504204.
[50] L. Moroni, T. Boland, J.A. Burdick, C. De Maria, B. Derby, G. Forgacs, J. Groll, Q. Li, J. Malda, V.A. Mironov, C. Mota, M. Nakamura, W. Shu, S. Takeuchi, T.B.F. Woodfield, T. Xu, J.J. Yoo, G. Vozzi, Biofabrication: A Guide to Technology and Terminology, Trends in Biotechnology 36 (2018) 384–402. https://doi.org/10.1016/j.tibtech.2017.10.015.
[51] A. Accardo, M.-C. Blatché, R. Courson, I. Loubinoux, C. Thibault, L. Malaquin, C. Vieu, Multiphoton Direct Laser Writing and 3D Imaging of Polymeric Freestanding Architectures for Cell Colonization, Small 13 (2017) 1700621. https://doi.org/10.1002/smll.201700621.
[52] J. Maciulaitis, S. Rekštytė, M. Bratchikov, R. Gudas, M. Malinauskas, A. Pockevicius, A. Usas, A. Rimkunas, V. Jankauskaite, V. Grigaliunas, R. Maciulaitis, Customization of direct laser lithography-based 3D scaffolds for optimized in vivo outcome, Applied Surface Science 487 (2019) 692–702. https://doi.org/10.1016/j.apsusc.2019.05.065.
[53] C. Fendler, C. Denker, J. Harberts, P. Bayat, R. Zierold, G. Loers, M. Münzenberg, R.H. Blick, Microscaffolds by Direct Laser Writing for Neurite Guidance Leading to Tailor-Made Neuronal Networks, Advanced Biosystems 3 (2019) 1800329. https://doi.org/10.1002/adbi.201800329.
[54] M. Babi, R. Riesco, L. Boyer, A. Fatona, A. Accardo, L. Malaquin, J. Moran-Mirabal, Tuning the Nanotopography and Chemical Functionality of 3D Printed Scaffolds through Cellulose Nanocrystal Coatings, ACS Appl. Bio Mater. (2021). https://doi.org/10.1021/acsabm.1c00970.
[55] S. Bertels, M. Jaggy, B. Richter, S. Keppler, K. Weber, E. Genthner, A.C. Fischer, M. Thiel, M. Wegener, A.M. Greiner, T.J. Autenrieth, M. Bastmeyer, Geometrically defined environments direct cell division rate and subcellular YAP localization in single mouse embryonic stem cells, Sci Rep 11 (2021) 9269. https://doi.org/10.1038/s41598-021-88336-y.
[56] J. Maciulaitis, M. Miskiniene, S. Rekštytė, M. Bratchikov, A. Darinskas, A. Simbelyte, G. Daunoras, A. Laurinaviciene, A. Laurinavicius, R. Gudas, M. Malinauskas, R. Maciulaitis, Osteochondral Repair and Electromechanical Evaluation of Custom 3D Scaffold Microstructured by Direct Laser Writing Lithography, CARTILAGE 13 (2021) 615S-625S. https://doi.org/10.1177/1947603519847745.
[57] M. Nouri-Goushki, A. Isaakidou, B.I. M. Eijkel, M. Minneboo, Q. Liu, P. E. Boukany, M. J. Mirzaali, L. E. Fratila-Apachitei, A. A. Zadpoor, 3D printed submicron patterns orchestrate the response of macrophages, Nanoscale 13 (2021) 14304–14315. https://doi.org/10.1039/D1NR01557E.
[58] Q. Akolawala, M. Rovituso, H.H. Versteeg, A.M.R. Rondon, A. Accardo, Evaluation of Proton-Induced DNA Damage in 3D-Engineered Glioblastoma Microenvironments, ACS Appl. Mater. Interfaces (2022). https://doi.org/10.1021/acsami.2c03706.
[59] B.N.L. Costa, R.M.R. Adão, C. Maibohm, A. Accardo, V.F. Cardoso, J.B. Nieder, Cellular Interaction of Bone Marrow Mesenchymal Stem Cells with Polymer and Hydrogel 3D Microscaffold Templates, ACS Appl. Mater. Interfaces (2022). https://doi.org/10.1021/acsami.1c23442.
[60] B. Chamak, M. Mallat, Fibronectin and laminin regulate thein vitro differentiation of microglial cells, Neuroscience 45 (1991) 513–527. https://doi.org/10.1016/0306-4522(91)90267-R.

[61] W.Y. Tam, N.P.B. Au, C.H.E. Ma, The association between laminin and microglial morphology in vitro, Scientific Reports 6 (2016) 28580. https://doi.org/10.1038/srep28580.
[62] D. Torres-Torres, J. Muñoz-Saldaña, L.A.G.-L. Guevara, A. Hurtado-Macías, M.V. Swain, Geometry and bluntness tip effects on elastic–plastic behaviour during nanoindentation of fused silica: experimental and FE simulation, Modelling Simul. Mater. Sci. Eng. 18 (2010) 075006. https://doi.org/10.1088/0965-0393/18/7/075006.
[63] E. Skliutas, M. Lebedevaite, E. Kabouraki, T. Baldacchini, J. Ostrauskaite, M. Vamvakaki, M. Farsari, S. Juodkazis, M. Malinauskas, Polymerization mechanisms initiated by spatio-temporally confined light, Nanophotonics 10 (2021) 1211–1242. https://doi.org/10.1515/nanoph-2020-0551.
[64] L. Angeloni, M. Ganjian, M. Nouri-Goushki, M.J. Mirzaali, C.W. Hagen, A.A. Zadpoor, L.E. Fratila-Apachitei, M.K. Ghatkesar, Mechanical characterization of nanopillars by atomic force microscopy, Additive Manufacturing 39 (2021) 101858. https://doi.org/10.1016/j.addma.2021.101858.
[65] J. Schindelin, I. Arganda-Carreras, E. Frise, V. Kaynig, M. Longair, T. Pietzsch, S. Preibisch, C. Rueden, S. Saalfeld, B. Schmid, J.-Y. Tinevez, D.J. White, V. Hartenstein, K. Eliceiri, P. Tomancak, A. Cardona, Fiji: an open-source platform for biological-image analysis, Nat Methods 9 (2012) 676–682. https://doi.org/10.1038/nmeth.2019.
[66] M. Goraus, D. Pudis, P. Urbancova, I. Martincek, P. Gaso, Surface-relief Bragg grating waveguides based on IP-Dip polymer for photonic applications, Applied Surface Science 461 (2018) 113–116. https://doi.org/10.1016/j.apsusc.2018.05.185.
[67] E.D. Lemma, F. Rizzi, T. Dattoma, B. Spagnolo, L. Sileo, A. Qualtieri, M. De Vittorio, F. Pisanello, Mechanical Properties Tunability of Three-Dimensional Polymeric Structures in Two-Photon Lithography, IEEE Transactions on Nanotechnology 16 (2017) 23–31. https://doi.org/10.1109/TNANO.2016.2625820.
[68] C.C. Chao, S. Hu, T.W. Molitor, E.G. Shaskan, P.K. Peterson, Activated microglia mediate neuronal cell injury via a nitric oxide mechanism., The Journal of Immunology 149 (1992) 2736–2741.
[69] A. Nimmerjahn, F. Kirchhoff, F. Helmchen, Resting Microglial Cells Are Highly Dynamic Surveillants of Brain Parenchyma in Vivo, Science 308 (2005) 1314–1318. https://doi.org/10.1126/science.1110647.
[70] G. Pietrogrande, N. Mabotuwana, Z. Zhao, M. Abdolhoseini, S.J. Johnson, M. Nilsson, F.R. Walker, Chronic stress induced disturbances in Laminin: A significant contributor to modulating microglial pro-inflammatory tone?, Brain, Behavior, and Immunity 68 (2018) 23–33. https://doi.org/10.1016/j.bbi.2017.09.012.
[71] P.K. Mattila, P. Lappalainen, Filopodia: molecular architecture and cellular functions, Nature Reviews Molecular Cell Biology 9 (2008) 446–454. https://doi.org/10.1038/nrm2406.
[72] O.Y. Antonova, O.Y. Kochetkova, Y.M. Shlyapnikov, ECM-Mimetic Nylon Nanofiber Scaffolds for Neurite Growth Guidance, Nanomaterials (Basel) 11 (2021). https://doi.org/10.3390/nano11020516.
[73] S.I. Fraley, Y. Feng, R. Krishnamurthy, D.-H. Kim, A. Celedon, G.D. Longmore, D. Wirtz, A distinctive role for focal adhesion proteins in three-dimensional cell motility, Nature Cell Biology 12 (2010) 598–604. https://doi.org/10.1038/ncb2062.
[74] J. Zonderland, I.L. Moldero, S. Anand, C. Mota, L. Moroni, Dimensionality changes actin network through lamin A/C and zyxin, Biomaterials 240 (2020) 119854. https://doi.org/10.1016/j.biomaterials.2020.119854.
[75] J. Zonderland, L. Moroni, Steering cell behavior through mechanobiology in 3D: A regenerative medicine perspective, Biomaterials 268 (2021) 120572. https://doi.org/10.1016/j.biomaterials.2020.120572.

[76] C. Schulte, M. Ripamonti, E. Maffioli, M.A. Cappelluti, S. Nonnis, L. Puricelli, J. Lamanna, C. Piazzoni, A. Podestà, C. Lenardi, G. Tedeschi, A. Malgaroli, P. Milani, Scale Invariant Disordered Nanotopography Promotes Hippocampal Neuron Development and Maturation with Involvement of Mechanotransductive Pathways, Frontiers in Cellular Neuroscience 10 (2016) 267. https://doi.org/10.3389/fncel.2016.00267.
[77] J. Selvakumaran, J.L. Keddie, D.J. Ewins, M.P. Hughes, Protein adsorption on materials for recording sites on implantable microelectrodes, J Mater Sci: Mater Med 19 (2008) 143–151. https://doi.org/10.1007/s10856-007-3110-x.
[78] K. Yang, K. Jung, E. Ko, J. Kim, K.I. Park, J. Kim, S.-W. Cho, Nanotopographical Manipulation of Focal Adhesion Formation for Enhanced Differentiation of Human Neural Stem Cells, ACS Appl. Mater. Interfaces 5 (2013) 10529–10540. https://doi.org/10.1021/am402156f.
[79] Y.-H. Yang, Z. Khan, C. Ma, H.J. Lim, L.A. Smith Callahan, Optimization of adhesive conditions for neural differentiation of murine embryonic stem cells using hydrogels functionalized with continuous Ile-Lys-Val-Ala-Val concentration gradients, Acta Biomaterialia 21 (2015) 55–62. https://doi.org/10.1016/j.actbio.2015.04.031.
[80] S. Chen, J.A. Jones, Y. Xu, H.-Y. Low, J.M. Anderson, K.W. Leong, Characterization of topographical effects on macrophage behavior in a foreign body response model, Biomaterials 31 (2010) 3479–3491. https://doi.org/10.1016/j.biomaterials.2010.01.074.
[81] Q. Song, S. Pifferi, L. Shi, C. Chen, R. Proietti Zaccaria, A. Menini, J. Cao, Q. Zhang, V. Torre, Textured nanofibrils drive microglial phenotype, Biomaterials 257 (2020) 120177. https://doi.org/10.1016/j.biomaterials.2020.120177.
[82] Q. Song, Z. Jiang, N. Li, P. Liu, L. Liu, M. Tang, G. Cheng, Anti-inflammatory effects of three-dimensional graphene foams cultured with microglial cells, Biomaterials 35 (2014) 6930–6940. https://doi.org/10.1016/j.biomaterials.2014.05.002.
[83] Z. Xia, J.T. Triffitt, A review on macrophage responses to biomaterials, Biomed. Mater. 1 (2006) R1–R9. https://doi.org/10.1088/1748-6041/1/1/R01.
[84] S. Mitragotri, J. Lahann, Physical approaches to biomaterial design, Nature Mater 8 (2009) 15–23. https://doi.org/10.1038/nmat2344.
[85] T. Tylek, C. Blum, A. Hrynevich, K. Schlegelmilch, T. Schilling, P.D. Dalton, J. Groll, Precisely defined fiber scaffolds with 40 µm porosity induce elongation driven M2-like polarization of human macrophages, Biofabrication 12 (2020) 025007. https://doi.org/10.1088/1758-5090/ab5f4e.
[86] R. Liang, D. Fang, W. Lin, Y. Wang, Z. Liu, Y. Wang, Y. Zeng, M. He, J. Li, F. Luo, J. Li, H. Liu, J. Xu, H. Tan, Macrophage Polarization in Response to Varying Pore Sizes of 3D Polyurethane Scaffolds, Journal of Biomedical Nanotechnology 14 (2018) 1744–1760. https://doi.org/10.1166/jbn.2018.2629.
[87] S. Jiang, C. Lyu, P. Zhao, W. Li, W. Kong, C. Huang, G.M. Genin, Y. Du, Cryoprotectant enables structural control of porous scaffolds for exploration of cellular mechano-responsiveness in 3D, Nat Commun 10 (2019) 3491. https://doi.org/10.1038/s41467-019-11397-1.
[88] I. Tonazzini, C. Masciullo, E. Savi, A. Sonato, F. Romanato, M. Cecchini, Neuronal contact guidance and YAP signaling on ultra-small nanogratings, Scientific Reports 10 (2020). https://doi.org/10.1038/s41598-020-60745-5.
[89] S. Fujita, M. Ohshima, H. Iwata, Time-lapse observation of cell alignment on nanogrooved patterns, Journal of The Royal Society Interface 6 (2009) S269–S277. https://doi.org/10.1098/rsif.2008.0428.focus.
[90] J.T.Y. Lee, K.L. Chow, SEM sample preparation for cells on 3D scaffolds by freeze-drying and HMDS: SEM sample preparation for cells, Scanning 34 (2012) 12–25. https://doi.org/10.1002/sca.20271.

[91] Y. Jusman, S.C. Ng, N.A. Abu Osman, Investigation of CPD and HMDS Sample Preparation Techniques for Cervical Cells in Developing Computer-Aided Screening System Based on FE-SEM/EDX, The Scientific World Journal 2014 (2014) 1–11. https://doi.org/10.1155/2014/289817.
[92] A. Katsen-Globa, N. Puetz, M.M. Gepp, J.C. Neubauer, H. Zimmermann, Study of SEM preparation artefacts with correlative microscopy: Cell shrinkage of adherent cells by HMDS-drying, Scanning 38 (2016) 625–633. https://doi.org/10.1002/sca.21310.
[93] C. Leclech, M. Renner, C. Villard, C. Métin, Topographical cues control the morphology and dynamics of migrating cortical interneurons, Biomaterials 214 (2019) 119194. https://doi.org/10.1016/j.biomaterials.2019.05.005.
[94] G. Bugnicourt, J. Brocard, A. Nicolas, C. Villard, Nanoscale Surface Topography Reshapes Neuronal Growth in Culture, Langmuir 30 (2014) 4441–4449. https://doi.org/10.1021/la5001683.
[95] A. Sharaf, B. Roos, R. Timmerman, G.-J. Kremers, J.J. Bajramovic, A. Accardo, Two-Photon Polymerization of 2.5D and 3D Microstructures Fostering a Ramified Resting Phenotype in Primary Microglia, Frontiers in Bioengineering and Biotechnology 10 (2022). https://www.frontiersin.org/articles/10.3389/fbioe.2022.926642 (accessed July 22, 2022).
[96] A. Maggi, H. Li, J.R. Greer, Three-dimensional nano-architected scaffolds with tunable stiffness for efficient bone tissue growth, Acta Biomaterialia 63 (2017) 294–305. https://doi.org/10.1016/j.actbio.2017.09.007.
[97] G. Flamourakis, G. Flamourakis, A. Kordas, A. Kordas, G.D. Barmparis, A. Ranella, A. Ranella, M. Farsari, M. Farsari, Low-autofluorescence, transparent composite for multiphoton 3D printing, Opt. Mater. Express, OME 11 (2021) 801–813. https://doi.org/10.1364/OME.418269.
[98] I.H. Jaafar, C.E. LeBlon, M.-T. Wei, D. Ou-Yang, J.P. Coulter, S.S. Jedlicka, Improving fluorescence imaging of biological cells on biomedical polymers, Acta Biomaterialia 7 (2011) 1588–1598. https://doi.org/10.1016/j.actbio.2010.12.007.
[99] G.-J. Kremers, K.L. Hazelwood, C.S. Murphy, M.W. Davidson, D.W. Piston, Photoconversion in orange and red fluorescent proteins, Nat Methods 6 (2009) 355–358. https://doi.org/10.1038/nmeth.1319.
[100] E.A. Protasova, A.S. Mishin, K.A. Lukyanov, E.G. Maksimov, A.M. Bogdanov, Chromophore reduction plus reversible photobleaching: how the mKate2 “photoconversion” works, Photochem Photobiol Sci 20 (2021) 791–803. https://doi.org/10.1007/s43630-021-00060-8.
[101] B. Turkowyd, A. Balinovic, D. Virant, H.G.G. Carnero, F. Caldana, M. Endesfelder, D. Bourgeois, U. Endesfelder, A General Mechanism of Photoconversion of Green-to-Red Fluorescent Proteins Based on Blue and Infrared Light Reduces Phototoxicity in Live-Cell Single-Molecule Imaging, Angewandte Chemie International Edition 56 (2017) 11634–11639. https://doi.org/10.1002/anie.201702870.
[102] D. Sinnecker, P. Voigt, N. Hellwig, M. Schaefer, Reversible Photobleaching of Enhanced Green Fluorescent Proteins, Biochemistry 44 (2005) 7085–7094. https://doi.org/10.1021/bi047881x.
[103] S. Khetan, M. Guvendiren, W.R. Legant, D.M. Cohen, C.S. Chen, J.A. Burdick, Degradation-mediated cellular traction directs stem cell fate in covalently crosslinked three-dimensional hydrogels, Nature Materials 12 (2013) 458–465. https://doi.org/10.1038/nmat3586.
[104] T.-Y. Chang, C. Chen, M. Lee, Y.-C. Chang, C.-H. Lu, S.-T. Lu, D.-Y. Wang, A. Wang, C.-L. Guo, P.-L. Cheng, Paxillin facilitates timely neurite initiation on soft-substrate environments by interacting with the endocytic machinery, eLife 6 (2017) e31101. https://doi.org/10.7554/eLife.31101.

[105] A.J.G. Otuka, B.B.M. Torres, J. Dipold, D.T. Balogh, V. Tribuzi, L.D. Boni, C.R. Mendonça, Three-dimensional structures fabricated after laser-induced free radical generation in azoaromatic compounds, Opt. Mater. Express, OME 10 (2020) 1792–1800. https://doi.org/10.1364/OME.397716.
[106] H. Abuwarda, M.M. Pathak, Mechanobiology of neural development, Current Opinion in Cell Biology 66 (2020) 104–111. https://doi.org/10.1016/j.ceb.2020.05.012.
[107] B.D. Hoffman, C. Grashoff, M.A. Schwartz, Dynamic molecular processes mediate cellular mechanotransduction, Nature 475 (2011) 316–323. https://doi.org/10.1038/nature10316.
[108] X. Cai, K.-C. Wang, Z. Meng, Mechanoregulation of YAP and TAZ in Cellular Homeostasis and Disease Progression, Front. Cell Dev. Biol. 9 (2021). https://doi.org/10.3389/fcell.2021.673599.
[109] T. Panciera, L. Azzolin, M. Cordenonsi, S. Piccolo, Mechanobiology of YAP and TAZ in physiology and disease, Nat Rev Mol Cell Biol 18 (2017) 758–770. https://doi.org/10.1038/nrm.2017.87.
[110] S. Dupont, Role of YAP/TAZ in cell-matrix adhesion-mediated signalling and mechanotransduction, Experimental Cell Research 343 (2016) 42–53. https://doi.org/10.1016/j.yexcr.2015.10.034.
[111] M. Ohgushi, M. Minaguchi, Y. Sasai, Rho-Signaling-Directed YAP/TAZ Activity Underlies the Long-Term Survival and Expansion of Human Embryonic Stem Cells, Cell Stem Cell 17 (2015) 448–461. https://doi.org/10.1016/j.stem.2015.07.009.
[112] X. Feng, P. Liu, X. Zhou, M.-T. Li, F.-L. Li, Z. Wang, Z. Meng, Y.-P. Sun, Y. Yu, Y. Xiong, H.-X. Yuan, K.-L. Guan, Thromboxane A2 Activates YAP/TAZ Protein to Induce Vascular Smooth Muscle Cell Proliferation and Migration *, Journal of Biological Chemistry 291 (2016) 18947–18958. https://doi.org/10.1074/jbc.M116.739722.
[113] H. Tanaka, H. Homma, K. Fujita, K. Kondo, S. Yamada, X. Jin, M. Waragai, G. Ohtomo, A. Iwata, K. Tagawa, N. Atsuta, M. Katsuno, N. Tomita, K. Furukawa, Y. Saito, T. Saito, A. Ichise, S. Shibata, H. Arai, T. Saido, M. Sudol, S. Muramatsu, H. Okano, E.J. Mufson, G. Sobue, S. Murayama, H. Okazawa, YAP-dependent necrosis occurs in early stages of Alzheimer's disease and regulates mouse model pathology, Nat Commun 11 (2020) 507. https://doi.org/10.1038/s41467-020-14353-6.
[114] J.M. Lamar, P. Stern, H. Liu, J.W. Schindler, Z.-G. Jiang, R.O. Hynes, The Hippo pathway target, YAP, promotes metastasis through its TEAD-interaction domain, Proceedings of the National Academy of Sciences 109 (2012) E2441–E2450. https://doi.org/10.1073/pnas.1212021109.
[115] A.P.Z.P. Fiore, P. de F. Ribeiro, A. Bruni-Cardoso, Sleeping Beauty and the Microenvironment Enchantment: Microenvironmental Regulation of the Proliferation-Quiescence Decision in Normal Tissues and in Cancer Development, Front. Cell Dev. Biol. 6 (2018). https://doi.org/10.3389/fcell.2018.00059.
[116] M. Chighizola, T. Dini, C. Lenardi, P. Milani, A. Podestà, C. Schulte, Mechanotransduction in neuronal cell development and functioning, Biophys Rev 11 (2019) 701–720. https://doi.org/10.1007/s12551-019-00587-2.
[117] S. Musah, P.J. Wrighton, Y. Zaltsman, X. Zhong, S. Zorn, M.B. Parlato, C. Hsiao, S.P. Palecek, Q. Chang, W.L. Murphy, L.L. Kiessling, Substratum-induced differentiation of human pluripotent stem cells reveals the coactivator YAP is a potent regulator of neuronal specification, Proceedings of the National Academy of Sciences 111 (2014) 13805–13810. https://doi.org/10.1073/pnas.1415330111.
[118] Y. Sun, K.M.A. Yong, L.G. Villa-Diaz, X. Zhang, W. Chen, R. Philson, S. Weng, H. Xu, P.H. Krebsbach, J. Fu, Hippo/YAP-mediated rigidity-dependent motor neuron differentiation of human pluripotent stem cells, Nature Mater 13 (2014) 599–604. https://doi.org/10.1038/nmat3945.

[119] B. Knöll, Actin-mediated gene expression in neurons: the MRTF-SRF connection, 391 (2010) 591–597. https://doi.org/10.1515/bc.2010.061.
[120] J. Shiota, M. Ishikawa, H. Sakagami, M. Tsuda, J.M. Baraban, A. Tabuchi, Developmental expression of the SRF co-activator MAL in brain: role in regulating dendritic morphology, Journal of Neurochemistry 98 (2006) 1778–1788. https://doi.org/10.1111/j.1471-4159.2006.03992.x.
[121] M.H. Mokalled, A. Johnson, Y. Kim, J. Oh, E.N. Olson, Myocardin-related transcription factors regulate the Cdk5/Pctaire1 kinase cascade to control neurite outgrowth, neuronal migration and brain development, Development 137 (2010) 2365–2374. https://doi.org/10.1242/dev.047605.
[122] W. Zhang, Y. Yang, Z. Xiang, J. Cheng, Z. Yu, W. Wang, L. Hu, F. Ma, Y. Deng, Z. Jin, X. Hu, MRTF-A-mediated protection against amyloid-β-induced neuronal injury correlates with restoring autophagy via miR-1273g-3p/mTOR axis in Alzheimer models, Aging (Albany NY) 14 (2022) 4305–4325. https://doi.org/10.18632/aging.203883.
[123] C.T. Foster, F. Gualdrini, R. Treisman, Mutual dependence of the MRTF–SRF and YAP–TEAD pathways in cancer-associated fibroblasts is indirect and mediated by cytoskeletal dynamics, Genes Dev. 31 (2017) 2361–2375. https://doi.org/10.1101/gad.304501.117.
[124] T. Kim, D. Hwang, D. Lee, J. Kim, S. Kim, D. Lim, MRTF potentiates TEAD-YAP transcriptional activity causing metastasis, The EMBO Journal 36 (2017) 520–535. https://doi.org/10.15252/embj.201695137.
[125] M. Finch-Edmondson, M. Sudol, Framework to function: mechanosensitive regulators of gene transcription, Cell Mol Biol Lett 21 (2016) 28. https://doi.org/10.1186/s11658-016-0028-7.
[126] B. Blomme, C. Deroanne, A. Hulin, C. Lambert, J.-O. Defraigne, B. Nusgens, M. Radermecker, A. Colige, Mechanical strain induces a pro-fibrotic phenotype in human mitral valvular interstitial cells through RhoC/ROCK/MRTF-A and Erk1/2 signaling pathways, Journal of Molecular and Cellular Cardiology 135 (2019) 149–159. https://doi.org/10.1016/j.yjmcc.2019.08.008.
[127] I.L. Chin, S.E. Amos, J.H. Jeong, L. Hool, Y. Hwang, Y.S. Choi, Volume adaptation of neonatal cardiomyocyte spheroids in 3D stiffness gradient GelMA, Journal of Biomedical Materials Research Part A 111 (2023) 801–813. https://doi.org/10.1002/jbm.a.37456.
[128] G. Halder, S. Dupont, S. Piccolo, Transduction of mechanical and cytoskeletal cues by YAP and TAZ, Nat Rev Mol Cell Biol 13 (2012) 591–600. https://doi.org/10.1038/nrm3416.
[129] S. Dupont, L. Morsut, M. Aragona, E. Enzo, S. Giulitti, M. Cordenonsi, F. Zanconato, J. Le Digabel, M. Forcato, S. Bicciato, N. Elvassore, S. Piccolo, Role of YAP/TAZ in mechanotransduction, Nature 474 (2011) 179–183. https://doi.org/10.1038/nature10137.
[130] G. Nardone, J. Oliver-De La Cruz, J. Vrbsky, C. Martini, J. Pribyl, P. Skládal, M. Pešl, G. Caluori, S. Pagliari, F. Martino, Z. Maceckova, M. Hajduch, A. Sanz-Garcia, N.M. Pugno, G.B. Stokin, G. Forte, YAP regulates cell mechanics by controlling focal adhesion assembly, Nat Commun 8 (2017) 15321. https://doi.org/10.1038/ncomms15321.
[131] K.-I. Wada, K. Itoga, T. Okano, S. Yonemura, H. Sasaki, Hippo pathway regulation by cell morphology and stress fibers, Development 138 (2011) 3907–3914. https://doi.org/10.1242/dev.070987.
[132] O.Y. Dudaryeva, A. Bucciarelli, G. Bovone, F. Huwyler, S. Jaydev, N. Broguiere, M. al-Bayati, M. Lütolf, M.W. Tibbitt, 3D Confinement Regulates Cell Life and Death, Advanced Functional Materials 31 (2021) 2104098. https://doi.org/10.1002/adfm.202104098.
[133] C. Li, F. Meng, Z. Yang, J. Peng, Y. Guo, J. Na, Q. Shi, Y. Liu, Y. Wang, L. Zheng, Y. Fan, Micropattern-Based Stem Cell Gym: Mechanical Memory Enhanced Stemness Maintenance of Human Dental Pulp Stem Cells and Nerve Regeneration, Advanced Functional Materials 33 (2023) 2302829. https://doi.org/10.1002/adfm.202302829.

[134] J. Zhang, H. Ding, X. Liu, H. Gu, M. Wei, X. Li, S. Liu, S. Li, X. Du, Z. Gu, Facile Surface Functionalization Strategy for Two-Photon Lithography Microstructures, Small 17 (2021) 2101048. https://doi.org/10.1002/smll.202101048.
[135] A. Sharaf, J.P. Frimat, G.J. Kremers, A. Accardo, Suppression of auto-fluorescence from high-resolution 3D polymeric architectures fabricated via two-photon polymerization for cell biology applications, Micro and Nano Engineering 19 (2023) 100188. https://doi.org/10.1016/j.mne.2023.100188.
[136] M. Pachitariu, C. Stringer, Cellpose 2.0: how to train your own model, Nat Methods 19 (2022) 1634–1641. https://doi.org/10.1038/s41592-022-01663-4.
[137] D.R. Stirling, M.J. Swain-Bowden, A.M. Lucas, A.E. Carpenter, B.A. Cimini, A. Goodman, CellProfiler 4: improvements in speed, utility and usability, BMC Bioinformatics 22 (2021) 433. https://doi.org/10.1186/s12859-021-04344-9.
[138] A.L. McGregor, C.-R. Hsia, J. Lammerding, Squish and squeeze—the nucleus as a physical barrier during migration in confined environments, Current Opinion in Cell Biology 40 (2016) 32–40. https://doi.org/10.1016/j.ceb.2016.01.011.
[139] J.A. Crowe, A. El-Tamer, D. Nagel, A.V. Koroleva, J. Madrid-Wolff, O.E. Olarte, S. Sokolovsky, E. Estevez-Priego, A.-A. Ludl, J. Soriano, P. Loza-Alvarez, B.N. Chichkov, E.J. Hill, H.R. Parri, E.U. Rafailov, Development of two-photon polymerised scaffolds for optical interrogation and neurite guidance of human iPSC-derived cortical neuronal networks, Lab Chip 20 (2020) 1792–1806. https://doi.org/10.1039/C9LC01209E.
[140] F. Gentile, L. Tirinato, E. Battista, F. Causa, C. Liberale, E.M. di Fabrizio, P. Decuzzi, Cells preferentially grow on rough substrates, Biomaterials 31 (2010) 7205–7212. https://doi.org/10.1016/j.biomaterials.2010.06.016.
[141] Q. Gao, D. Yan, D. Wang, S. Gao, S. Zhao, S. Wang, Y. Liu, Variations in Nuclear Number and Size in Vegetative Hyphae of the Edible Mushroom Lentinula edodes, Front. Microbiol. 10 (2019). https://doi.org/10.3389/fmicb.2019.01987.
[142] C. Rianna, M. Radmacher, S. Kumar, Direct evidence that tumor cells soften when navigating confined spaces, MBoC 31 (2020) 1726–1734. https://doi.org/10.1091/mbc.E19-10-0588.
[143] P. Rivetti di Val Cervo, D. Besusso, P. Conforti, E. Cattaneo, hiPSCs for predictive modelling of neurodegenerative diseases: dreaming the possible, Nat Rev Neurol 17 (2021) 381–392. https://doi.org/10.1038/s41582-021-00465-0.
[144] A. Sharma, S. Sances, M.J. Workman, C.N. Svendsen, Multi-lineage Human iPSC-Derived Platforms for Disease Modeling and Drug Discovery, Cell Stem Cell 26 (2020) 309–329. https://doi.org/10.1016/j.stem.2020.02.011.
[145] S. Turunen, E. Käpylä, M. Lähteenmäki, L. Ylä-Outinen, S. Narkilahti, M. Kellomäki, Direct laser writing of microstructures for the growth guidance of human pluripotent stem cell derived neuronal cells, Optics and Lasers in Engineering 55 (2014) 197–204. https://doi.org/10.1016/j.optlaseng.2013.11.003.
[146] S. Ankam, C.K. Lim, E.K.F. Yim, Actomyosin contractility plays a role in MAP2 expression during nanotopography-directed neuronal differentiation of human embryonic stem cells, Biomaterials 47 (2015) 20–28. https://doi.org/10.1016/j.biomaterials.2015.01.003.
[147] T. Roitbak, Z. Surviladze, L.A. Cunningham, Continuous Expression of HIF-1α in Neural Stem/Progenitor Cells, Cell Mol Neurobiol 31 (2011) 119–133. https://doi.org/10.1007/s10571-010-9561-5.
[148] X. Xu, Y. Wang, Z. Huang, YAP: a novel target for Alzheimer's disease, Aging (Albany NY) 14 (2022) 3724–3725. https://doi.org/10.18632/aging.204045.
[149] A.I. Ciuciu, P.J. Cywiński, Two-photon polymerization of hydrogels – versatile solutions to fabricate well-defined 3D structures, RSC Adv. 4 (2014) 45504–45516. https://doi.org/10.1039/C4RA06892K.

[150] P.F.J. van Altena, A. Accardo, Micro 3D Printing Elastomeric IP-PDMS Using Two-Photon Polymerisation: A Comparative Analysis of Mechanical and Feature Resolution Properties, Polymers 15 (2023) 1816. https://doi.org/10.3390/polym15081816.
[151] E.M. Ahmed, Hydrogel: Preparation, characterization, and applications: A review, Journal of Advanced Research 6 (2015) 105–121. https://doi.org/10.1016/j.jare.2013.07.006.
[152] B.D. Johnson, D.J. Beebe, W.C. Crone, Effects of swelling on the mechanical properties of a pH-sensitive hydrogel for use in microfluidic devices, Materials Science and Engineering: C 24 (2004) 575–581. https://doi.org/10.1016/j.msec.2003.11.002.
[153] F. Absalan, M.S. Pasandi, H. Ghasemi Hamidabadi, S. Saeednia, M.N. Bojnordi, M. Zahiri, R. Alizadeh, Z. Bagher, Matrigel enhances differentiation of human adipose tissue-derived stem cells into dopaminergic neuron, Neuroscience Letters 760 (2021) 136070. https://doi.org/10.1016/j.neulet.2021.136070.
[154] P.C. Georges, W.J. Miller, D.F. Meaney, E.S. Sawyer, P.A. Janmey, Matrices with Compliance Comparable to that of Brain Tissue Select Neuronal over Glial Growth in Mixed Cortical Cultures, Biophysical Journal 90 (2006) 3012–3018. https://doi.org/10.1529/biophysj.105.073114.
[155] A.I. Teixeira, S. Ilkhanizadeh, J.A. Wigenius, J.K. Duckworth, O. Inganäs, O. Hermanson, The promotion of neuronal maturation on soft substrates, Biomaterials 30 (2009) 4567–4572. https://doi.org/10.1016/j.biomaterials.2009.05.013.
[156] A.P. Balgude, X. Yu, A. Szymanski, R.V. Bellamkonda, Agarose gel stiffness determines rate of DRG neurite extension in 3D cultures, Biomaterials 22 (2001) 1077–1084. https://doi.org/10.1016/S0142-9612(00)00350-1.
[157] E.A. Aisenbrey, W.L. Murphy, Synthetic alternatives to Matrigel, Nat Rev Mater 5 (2020) 539–551. https://doi.org/10.1038/s41578-020-0199-8.
[158] L. Agrawal, M. Saidani, L. Guillaud, M. Terenzio, Development of 3D culture scaffolds for directional neuronal growth using 2-photon lithography, Materials Science and Engineering: C 131 (2021) 112502. https://doi.org/10.1016/j.msec.2021.112502.
[159] F.P. Ulloa Severino, J. Ban, Q. Song, M. Tang, G. Bianconi, G. Cheng, V. Torre, The role of dimensionality in neuronal network dynamics, Scientific Reports 6 (2016) 1–14. https://doi.org/10.1038/srep29640.
[160] Q. Akolawala, F. Keuning, M. Rovituso, W. van Burik, E. van der Wal, H.H. Versteeg, A.M.R. Rondon, A. Accardo, Micro-Vessels-Like 3D Scaffolds for Studying the Proton Radiobiology of Glioblastoma-Endothelial Cells Co-Culture Models, Advanced Healthcare Materials 13 (2024) 2302988. https://doi.org/10.1002/adhm.202302988.
[161] F. Grinnell, C.-H. Ho, E. Tamariz, D.J. Lee, G. Skuta, Dendritic Fibroblasts in Three-dimensional Collagen Matrices, MBoC 14 (2003) 384–395. https://doi.org/10.1091/mbc.e02-08-0493.
[162] M. Laplaca, V. Vernekar, J. Shoemaker, D.K. Cullen, W. Coulter, Three-Dimensional Neuronal Cultures, Methods in Bioengineering: 3D Tissue Engineering (2010).
[163] J.-P. Frimat, S. Xie, A. Bastiaens, B. Schurink, F. Wolbers, J. den Toonder, R. Luttge, Advances in 3D neuronal cell culture, Journal of Vacuum Science & Technology B 33 (2015) 06F902. https://doi.org/10.1116/1.4931636.
[164] A. Ovsianikov, A. Deiwick, S. Van Vlierberghe, M. Pflaum, M. Wilhelmi, P. Dubruel, B. Chichkov, Laser Fabrication of 3D Gelatin Scaffolds for the Generation of Bioartificial Tissues, Materials 4 (2011) 288–299. https://doi.org/10.3390/ma4010288.
[165] F. Claeyssens, E.A. Hasan, A. Gaidukeviciute, D.S. Achilleos, A. Ranella, C. Reinhardt, A. Ovsianikov, X. Shizhou, C. Fotakis, M. Vamvakaki, B.N. Chichkov, M. Farsari, Three-Dimensional Biodegradable Structures Fabricated by Two-Photon Polymerization, Langmuir 25 (2009) 3219–3223. https://doi.org/10.1021/la803803m.
[166] J. Van Hoorick, P. Gruber, M. Markovic, M. Tromayer, J. Van Erps, H. Thienpont, R. Liska, A. Ovsianikov, P. Dubruel, S. Van Vlierberghe, Cross-Linkable Gelatins with Superior

Mechanical Properties Through Carboxylic Acid Modification: Increasing the Two-Photon Polymerization Potential, Biomacromolecules 18 (2017) 3260–3272. https://doi.org/10.1021/acs.biomac.7b00905.
[167] O. Dadras-Toussi, M. Khorrami, M.R. Abidian, Femtosecond Laser 3D-printing of Conductive Microelectronics for Potential Biomedical Applications, in: 2021 43rd Annual International Conference of the IEEE Engineering in Medicine Biology Society (EMBC), 2021: pp. 1197–1200. https://doi.org/10.1109/EMBC46164.2021.9630885.
[168] S. He, Y. Su, B. Ji, H. Gao, Some basic questions on mechanosensing in cell–substrate interaction, Journal of the Mechanics and Physics of Solids 70 (2014) 116–135. https://doi.org/10.1016/j.jmps.2014.05.016.
[169] C.G. Tusan, Y.-H. Man, H. Zarkoob, D.A. Johnston, O.G. Andriotis, P.J. Thurner, S. Yang, E.A. Sander, E. Gentleman, B.G. Sengers, N.D. Evans, Collective Cell Behavior in Mechanosensing of Substrate Thickness, Biophysical Journal 114 (2018) 2743–2755. https://doi.org/10.1016/j.bpj.2018.03.037.
[170] C. Kuo, Fabrication methods of a novel 3D hybrid stiffness scaffold for neuron mechanosensing, (2023). https://repository.tudelft.nl/record/uuid:6905c6c3-e074-4652-a5ee-1e137927a9d0 (accessed March 3, 2025).
[171] Y. Yu, H. Yuk, G.A. Parada, Y. Wu, X. Liu, C.S. Nabzdyk, K. Youcef-Toumi, J. Zang, X. Zhao, Multifunctional “Hydrogel Skins” on Diverse Polymers with Arbitrary Shapes, Advanced Materials 31 (2019) 1807101. https://doi.org/10.1002/adma.201807101.
[172] Y. Liu, J.H. Campbell, O. Stein, L. Jiang, J. Hund, Y. Lu, Deformation Behavior of Foam Laser Targets Fabricated by Two-Photon Polymerization, Nanomaterials 8 (2018) 498. https://doi.org/10.3390/nano8070498.
[173] F. Dumur, Recent advances on photobleachable visible light photoinitiators of polymerization, European Polymer Journal 186 (2023) 111874. https://doi.org/10.1016/j.eurpolymj.2023.111874.
[174] D. Nečas, P. Klapetek, Gwyddion: an open-source software for SPM data analysis, Open Physics 10 (2012) 181–188. https://doi.org/10.2478/s11534-011-0096-2.
[175] Poly(ethylene glycol) methyl ether methacrylate average Mn 500, MEHQ 100ppm inhibitor, BHT 200ppm inhibitor 26915-72-0, (n.d.). http://www.sigmaaldrich.com/ (accessed November 17, 2024).
[176] Lithium phenyl-2,4,6-trimethylbenzoylphosphinate = 95 85073-19-4, (n.d.). http://www.sigmaaldrich.com/ (accessed November 17, 2024).
[177] 1-Hydroxycyclohexyl phenyl ketone 99 947-19-3, (n.d.). http://www.sigmaaldrich.com/ (accessed November 17, 2024).

Curriculum Vitae

Ahmed Sharaf

Personal Information

- **Date of Birth:** 31/10/1991.
- **Born in:** Giza, Egypt.

Language

1. **Arabic:** mother tongue.
2. **English:** Excellent (spoken and written).
3. **Dutch (Nederlands)**: Intermediate.

Education

1. **PhD** from Delft University of Technology, the Netherlands.
    - **Date of graduation:** March 2025.
    - **Thesis title:** Development of two-photon polymerization-based protocols for the investigation of neuronal mechanobiology.
2. **Master of Chemical Engineering** (Product Development Track) from Delft University of Technology, the Netherlands.
    - **Date of graduation:** November 2019.
    - **Thesis title:** Synthesis of soft polymeric pillars for simulation of neuronal axons.
3. **Bachelor of Petrochemical Engineering** from Cairo University, Egypt.
    - **Date of graduation:** June 2013.

Professional Experience

1. Postdoctoral researcher at TU Delft (Delft, the Netherlands) (1/6/2024-present).
2. PhD candidate at TU Delft (Delft, the Netherlands) (1/4/2020-1/4/2024).
3. Process Simulation Engineer at Schneider Electric (Cairo, Egypt) (1/1/2015-15/8/2016).
    - **Main Job Responsibilities:** Simulate chemical production processes using the company's software such as PRO II and DYNSIM.
4. Sales Support Engineer at Systems & Technology Co. (Cairo, Egypt) (1/10/2014-1/12/2014).
    - **Main Job Responsibilities:** Provide technical assistance to existing customers and try to establish contact with new ones.
5. Process Engineer at Cairo Oil & Soap Corporation (Cairo, Egypt) (22/2/2014-30/6/2014)
    - **Main Job Responsibilities:** Assisting in the startup of the oil splitting and distillation units and responsible for keeping them operational.

List of publications

1) A. Sharaf, J.P. Frimat, A. Accardo, Mechanical confinement matters: Unveiling the effect of two-photon polymerized 2.5D and 3D microarchitectures on neuronal YAP expression and neurite outgrowth, Materials Today Bio 29 (2024) 101325.

2) A. Sharaf, J.P. Frimat, G.J. Kremers, A. Accardo, Suppression of auto-fluorescence from high-resolution 3D polymeric architectures fabricated via two-photon polymerization for cell biology applications, Micro and Nano Engineering 19 (2023) 100188.

3) A. Sharaf, R. Timmerman, J. Bajramovic, A. Accardo, In vitro microglia models: the era of engineered cell microenvironments, Neural Regeneration Research, 18(8): 1709-1710 (2023). (Invited perspective article)

4) A. Sharaf, B. Roos, R. Timmerman, G.-J. Kremers, J.J. Bajramovic, A. Accardo, Two-Photon Polymerization of 2.5D and 3D Microstructures Fostering a Ramified Resting Phenotype in Primary Microglia, Frontiers in Bioengineering and Biotechnology 10 (2022).

Acknowledgements

First and foremost, I thank **God** for helping me through this four year journey of my PhD. If I did anything right, it is because of **Him** and **His** blessing and if I did anything wrong, it is from me.
To my beautiful and most supportive family, my **mother, father, sister**, **Mona,** and little nieces **Sedra and Misk,** the support you gave me is immeasurable and the time I got to spend with you was the fuel that got me through all the tough moments. You are a gift from **God** in my life and I only hope you forgive me if I was ever not fully appreciative of this gift.
To my copromoter and daily supervisor, **Angelo Accardo**, thank you for all the lessons taught on a personal and professional level. Thank you for all the cappuccinos we had and your listening when things were not going well and thank you for not making this journey feel like a job, rather a journey of growth. To my promoter, **Urs Staufer**, thank you for being the calm sound of wisdom during those four years. Thank you for taking utter care of the details that most miss. Thank you for making me always look at the big picture when I lose focus. From now on, whenever I have an idea, your voice will always be in my mind asking the most important question "*but why?*". To **Eduardo Mendes and Hendrik Hubbe**, my MSc supervisors, thank you because all of this started with you. Thank you to all my professors and anyone who once was my teacher.
I would also like to immensely thank our collaborators throughout the PhD, **Raissa**, **Jeffrey**, **Gert-Jan**. Thank you so much for your time, effort, dedication, and passion that you put in the projects we worked on together. To my friend **JP**, the man with enough passion to move mountains; I cannot emphasize enough how much I enjoyed our discussions. Thank you for always being a beacon of hope and for your understanding and kind words whenever I needed them.
To my students/friends, **Dian**, **Brian**, **Chihao**, and **Himanshu**. Thank you for all of your hard work and for trusting me as a supervisor. I am incredibly proud of each and every one of you and it was wonderful to see you grow both your technical and personal skills throughout your respective journeys of your MSc. I am sure you will all go on to do great things.
To my friends all over PME and TU Delft, thank you for providing this amazing work environment. To my tribe in the funfun office, **Ruben, Hava, Giulio, Serena, George, Stavros, Daria, Santiago and Zhiwei,** thank you for making this office feel like home. Thank you for all the riveting discussions we had about life, religion, politics, and science. To **Frederike, Pierre, and Hande**, thank you for all the coffee breaks. To **Martin, Giovanni, Michał, Yang, and Hadi**, thank you for all the support you gave me at the beginning of my journey. To **Daniel Fan**, my mentor from many years ago, thank you for putting things in perspective especially at the tough times. To my fellow Accardo group colleagues, **Qais, Nastaran, Pieter, Ebrahim, and Jurga**, I thank you for being my friends and for always making my life interesting. To **Francesco La Malfa**, the wonderful Sicilian, thank you for all the chats we had and for never ceasing to make me laugh even at the toughest of times.
I thank all my friends from MSA Ibn Firnas, **Rihan, Arish, Musaab, Irum** and all of them. You were and continue to be an anchor for me in life to let me see right from wrong. To **Ahmed Elghandour** (elomda), thank you for creating this community and for being our superman. To my friends back home, **Moataz and AbdelAziz** (our minister of foreign affairs), thank you for being a beacon of light in my life. To **Salah**, thank you for the wonderful overseas calls; thank you for all the advice; and thank you for the wisdom.
I ask **God** to always bless all of you.